Open problems in the microscopic theory of large-amplitude collective motion

2010 J. Phys. G: Nucl. Part. Phys. 37 064018

(http://iopscience.iop.org/0954-3899/37/6/064018)

IOP PUBLISHING JOURNAL OF PHYSICS G: NUCLEAR AND PARTICLE PHYSICS

J. Phys. G: Nucl. Part. Phys. **37** (2010) 064018 (16pp) doi:10.1088/0954-3899/37/6/064018

Open problems in the microscopic theory of large-amplitude collective motion

K Matsuyanagi[1,2], M Matsuo[3], T Nakatsukasa[1], N Hinohara[1] and K Sato[1,4]

[1] Theoretical Nuclear Physics Laboratory, RIKEN Nishina Center, Wako 351-0198, Japan
[2] Yukawa Institute for Theoretical Physics, Kyoto University, Kyoto 606-8502, Japan
[3] Department of Physics, Faculty of Science, Niigata University, Niigata 950-2181, Japan
[4] Department of Physics, Graduate School of Science, Kyoto University, Kyoto 606-8502, Japan

E-mail: matsuyanagi@riken.jp

Received 25 December 2009
Published 8 April 2010
Online at stacks.iop.org/JPhysG/37/064018

Abstract

Construction of the microscopic theory of large-amplitude collective motion, capable of describing a wide variety of quantum collective phenomena in nuclei, is a long-standing and fundamental subject in the study of nuclear many-body systems. The present status of the challenge toward this goal is discussed taking the shape coexistence/mixing phenomena as typical manifestations of the large-amplitude collective motion at zero temperature. Some open problems in rapidly rotating cold nuclei are also briefly discussed in this connection.

1. Introduction

Low-frequency collective modes of excitation in cold nuclei near the yrast line exhibit a number of unique features of the nucleus as a finite quantum many-body system. To understand the nature of these collective excitations, we need to develop a microscopic theory of large-amplitude collective motion (LACM), which has sound theoretical basis and, at the same time, is practical enough for applications to a wide variety of nuclear collective phenomena. This is a very broad and long-term pursuit in nuclear structure physics. Through the attempts up to now to construct the microscopic theories of LACM, promising new concepts and methods have been proposed and developed (see [1] for a review), but it may be fair to say that the challenge is still in its infancy. In this paper, we discuss the present status of the challenge taking mainly the shape coexistence/mixing phenomena as typical manifestations of LACM at zero temperature. Open problems in the theoretical formulation of microscopic LACM theory and collective phenomena awaiting its application are listed including those in rapidly rotating cold nuclei. This paper is not intended to be a comprehensive review of this broad field of nuclear structure physics, and we apologize that the selection of topics and references is leaning to our personal interest. Certainly, microscopic description of spontaneous fission from the viewpoint of nonlinear/non-equilibrium physics is one of the major goals, but this

subject will be discussed by other contributors to this special issue on *open problems in nuclear structure*.

2. Shape coexistence/mixings as large-amplitude collective phenomena

2.1. Shape coexistence phenomena

In recent years, new experimental data exhibiting coexistence of different shapes (like spherical, prolate, oblate and triaxial shapes) in the same energy region (of the same nucleus) have been obtained in low-energy spectra of nuclei in various regions of a nuclear chart (see [2, 3] for reviews and [4–6] for examples of recent data). These data indicate that the shape coexistence is a universal phenomenon representing essential features of the nucleus.

2.2. Necessity of going beyond the small-amplitude approximation

Let us define 'shape of the nucleus' as a semi-classical, macroscopic concept introduced by a self-consistent mean-field approximation, such as the Hartree–Fock–Bogoliubov (HFB) approximation, to the quantum-mechanical many-nucleon system. Needless to say, any HFB equilibrium shape inevitably accompanies quantum zero-point oscillations. If only one HFB equilibrium state exists, we can describe various kinds of vibrational mode about this point using the standard many-body methods like the random-phase approximation (RPA) or the boson-expansion methods [7, 8]. In the situations where two different HFB equilibrium shapes coexist in the same energy region, however, the large-amplitude shape vibrations tunneling through the potential barrier between the two HFB local minima may take place. To describe such LACM, we need to go beyond the perturbative approaches based on an expansion about one of the local minima.

2.3. Quantum field theory point of view

Different from the well-known tunneling of a single particle through the barrier created by an external field, the shape mixing of interest between different HFB local minima is a macroscopic tunneling phenomenon where the potential barrier itself is generated as a consequence of the dynamics of the self-bound quantum system. A HFB local minimum corresponds to a vacuum for quasiparticles in the quantum field-theoretical formulation. In contrast to infinite systems, different vacua in a finite quantum system are not exactly orthogonal to each other. Thus, the shape coexistence phenomena provide us precious opportunities to make a detailed study of the many-body dynamics of LACM connecting different vacua in terms of quantum spectra and electromagnetic transition properties associated with them.

2.4. Unique feature of the oblate–prolate coexistence

When the self-consistent mean field breaks the reflection symmetry (like the pear shape), parity doublets appear as the symmetric and anti-symmetric superpositions of two degenerate states associated with the two local minima. In contrast, there is no exact symmetry like parity when two local minima having the oblate and prolate shapes coexist. In this case, we do not know the relevant collective degree(s) of freedom through which the two shapes mix. It is obviously needed to develop a microscopic theory capable of describing the shape mixing dynamics of this kind.

2.5. Mysterious 0^+ *states*

There are only a few nuclei in which the first excited 0^+ state appears below the first excited 2^+ state. A well-known example is the 0^+ state at 0.69 MeV in ^{72}Ge which appears below the 2^+ state at 0.83 MeV. The nature of this state is poorly understood. Experimental systematics including neighboring nuclei indicates that the excitation energy of the 0^+ state takes the minimum around $N = 40$ where the neutron pairs start to occupy the $g_{9/2}$ shell. Microscopic calculations [9, 10] using the boson expansion method indicate that the mode–mode coupling between the quadrupole anharmonic vibration and the neutron pairing vibration plays an indispensable role in bringing about the peculiar behavior of the excited 0^+ states. On the other hand, these states are often interpreted in terms of the phenomenological shape coexistence picture [11]. Relations between the two interpretations are not well understood. Closely examining the properties of the excited 0^+ states in a wide region of nuclear chart, one finds that they exhibit features that cannot be understood in terms of the traditional concepts alone (see [12] for an example of recent data).

3. Characteristics of low-frequency collective excitations in nuclei

As is well known, shell structure and pairing correlations play essential roles for the emergence of low-frequency collective modes of excitation in medium–heavy and heavy nuclei. They exhibit unique features of the nucleus as a finite quantum many-body system and their amplitudes of vibration tend to become large. In this section, we discuss their characteristics in a wider perspective including the shape mixing phenomena and argue for the need of a microscopic theory capable of describing them.

3.1. Deformed shell structure

Nuclei exhibit quite rich shell structures comprising a variety of single-particle motions in the mean field localized in space. Let us define the shell structure as a regular oscillating pattern in the single-particle level density coarse-grained in energy. The nucleus gains an extra binding energy, called the shell energy, when the level density at the Fermi surface is low. The shell structure changes as a function of deformation. If the level density at the Fermi surface is high at the spherical shape, the nucleus prefers a deformed shape with lower level density. When different deformed shell structures give almost the same energy gain, we may obtain approximately degenerate HFB equilibrium shapes.

3.2. Pairing correlations and quasiparticles

It should be emphasized that both the mean field and the single-particle modes are collective phenomena. Needless to say, the nuclear mean field is self-consistently generated as a result of cooperative motion of strongly interacting nucleons. We learned from the BCS theory of superconductivity that the single-particle picture emerges as a consequence of collective phenomena: the Bogoliubov quasiparticles are nothing but the elementary modes of excitation in the presence of the Cooper pair condensate, and they have a gap in their excitation spectra (become 'massive'). As is well known, this idea has been greatly extended to understand dynamical mechanisms for generating the masses of 'elementary' particles [13]. The HFB theory is a generalized mean field theory taking into account both the pair condensation and the HF mean field in a unified manner [7, 8, 14].

3.3. Spontaneous breaking of symmetry

The self-consistent mean field of a finite quantum system inevitably breaks some symmetries. Even the spherical mean field breaks the translational symmetry. When the mean field breaks another symmetry of a higher order, the concept of single-particle motion is generalized accordingly. For instance, the Bogoliubov quasiparticle is introduced by breaking the number conservation. Struggles for finding a better concept of single-particle motion comprise the heart of nuclear structure study. When the mean field breaks some continuous symmetries, collective modes (Nambu–Goldstone modes) restoring the broken symmetries emerge. Nuclear rotations are typical examples: they restore the rotational symmetries broken by the mean field [15]. In this way, the (generalized) single-particle picture and the symmetry-restoring collective motions are inextricably linked like 'two sides of the same coin'. This fact has been beautifully demonstrated by the success of the 'rotating (cranked) shell model' [16], which describes the interplay of the rotational motions and 'the single-particle motions in the rotating mean field' in a simple manner. One of the fascinations of nuclear structure physics is that we can study the microscopic dynamics of symmetry breaking and restoration by means of a detailed study of quantum spectra. Finite quantum systems localized in space, such as the nucleus, provide us with such unique and invaluable opportunities.

3.4. Origin of oblate–prolate asymmetry

It should be noted that breaking of the spherical symmetry does not necessarily lead to the regular rotational band structure. For instance, even when the HFB mean field has an equilibrium point at a prolate shape which is deep with respect to the axial deformation parameter β, it should be deep also with respect to the axially asymmetric deformation parameter γ. In HFB calculations restricted to the axially symmetric shapes, we often obtain two solutions having the prolate and oblate shapes, but the oblate solution might be unstable with respect to γ. Even if both minima are stable, a strong mixing of the two shapes might occur through quantum mechanical large-amplitude collective vibrations in the γ degree of freedom. To suppress such a mixing, we need a sufficient amount of the potential barrier and the energy difference between the oblate and prolate solutions. Otherwise, identities of the rotational bands built on the oblate and prolate shapes will be easily lost due to the large-amplitude γ vibrations. These problems point to the critical need for the microscopic theory of LACM capable of describing such γ-soft situations, the oblate–prolate shape coexistence (where two rotational bands built on them can be identified) and various intermediate situations in a unified manner. In spite of the obvious importance for understanding low-energy collective spectra, the microscopic origin of the oblate–prolate asymmetry in nuclear structure (the reason why the prolate shapes are energetically more favored in many cases than the oblate shapes) still remains as one of the long-standing and fundamental problems. On this issue, quite recently, Hamamoto and Mottelson suggested that the surface diffuseness plays a key role in bringing about the asymmetry [17]. A useful approach to investigate the dynamical origin of appearance of the deformed shell structure is the semi-classical theory of the shell structure [18–20]. It may be interesting to apply this approach to the problem in question for a deeper understanding of the oblate–prolate asymmetry.

3.5. Collective motion as moving mean field

Nuclear rotational and vibrational motions can be described as moving self-consistent fields. This is one of the basic ideas of the unified model of Bohr and Mottelson [21, 22]. The time-dependent HFB (TDHFB) mean field is a generalized coherent state and its time

development can be described as a trajectory in the large-dimensional TDHFB phase space. Such a formulation of the TDHFB theory as a Hamilton dynamical system provides a microscopic foundation for using a classical picture of rotating and vibrating mean fields [23–25]. Thus, nuclear collective motions are beautiful examples of emergence of classical properties in genuine quantum many-body systems. For small-amplitude vibrations around a HFB equilibrium point, one can make the linear approximation to the TDHFB equations and obtain the quasiparticle RPA (QRPA). One of the merits of the QRPA is that it determines the microscopic structures of the normal modes (collective coordinates) without postulating them from the outset. The small-amplitude approximation is valid for giant resonances (high-frequency collective vibrations), and the (Q)RPA is used as the standard method for their microscopic descriptions.

3.6. Need for a microscopic theory of LACM

In contrast to giant resonances, the small-amplitude approximation is often insufficient for low-frequency collective modes. This is especially the case for the quadrupole collective modes in open-shell nuclei. The oblate–prolate shape coexistences/mixings are typical examples. It is also well known that the amplitude of the quadrupole vibration becomes very large in transient situations of the quantum phase transition from spherical to deformed, where the spherical mean field is barely stable or the spherical symmetry is broken only weakly. Many nuclei are situated in such a transitional region. It seems that this is one of the characteristic features of the quantum phase transition in the nucleus as a finite quantum many-body system. We need to go beyond the QRPA for describing such low-frequency quadrupole collective excitations. In view of the crucial role that the deformed shell structure and the pairing correlation play in generating the collectivity and determining the characters of these modes, it is desirable to construct a microscopic theory of LACM as an extension of the QRPA keeping its merit of deriving the collective coordinates from a huge number of microscopic degrees of freedom. Another important merit of the QRPA is that it is a quantum theory derived also with a new Tamm–Dancoff approximation in quantum field theory. Because we aim at constructing, on the basis of the TDHFB picture, a quantum theory of LACM capable of describing quantum spectra, it may be imperative, for justification of quantization of the collective coordinate, to formulate the quantum theory in such a way that it reduces to the QRPA in the small amplitude limit. In the next section, we briefly review various attempts toward this goal.

4. Problems in microscopic theories of collective motions

4.1. Boson expansion method

One of the microscopic approaches to treat nonlinear vibrations is the boson expansion method [26]. For describing the quadrupole vibrations in transitional nuclei, the collective QRPA normal modes at the spherical shape are represented as boson operators and anharmonic effects ignored in the QRPA are evaluated in terms of a power series of the boson creation and annihilation operators. The boson expansion methods have been widely used for the investigation of low-frequency quadrupole collective phenomena. This approach is perturbative in the sense that the microscopic structures of the collective coordinates and momenta are fixed at the spherical shape and nonlinear effects are evaluated by a power-series expansion in terms of these collective variables. To treat situations where the collective vibrations become increasingly larger amplitude and the nonlinear effects grow to such a degree that the microscopic structures of the collective variables themselves may change

during the vibrational motion, it is desirable to develop a microscopic theory which can treat the nonlinear effects in a non-perturbative way.

4.2. Generator coordinate method (GCM)

In the application of the GCM to quadrupole collective phenomena, quantum eigenstates are described as superpositions of mean-field (generalized Slater determinant) states parametrized by the generator coordinates. This microscopic approach is widely used in conjunction with the angular momentum and number projections [14]. A long-standing open problem in the GCM is the reliability of the collective masses (inertial functions) evaluated with the real generator coordinates. For the center of mass motion, complex generator coordinates are needed to reproduce the correct mass, indicating that we have to explicitly treat the collective momenta in addition to the coordinates [7]. Another important problem in the GCM is the choice of the generator coordinates. Holzwarth and Yukawa [27] once tried to find an optimal collective path by variationally determining the generator coordinate. This work stimulated the attempts to construct the microscopic theory of LACM.

4.3. Time-dependent HF (TDHF) method

Needless to say, the TDHF is a powerful tool to microscopically describe the LACM taking place in heavy-ion collisions [23]. The TDHF is insufficient for the description of quantum spectra of low-lying states, however, because of its semi-classical feature. On the other hand, as emphasized in section 3.6, its small-amplitude approximation, the RPA, can be formulated as a quantum theory and gives us a physical insight how the collective modes are generated as coherent superpositions of a large number of particle-hole excitations. It is thus desirable to extend the idea of deriving the RPA from the TDHF to large amplitude motions.

4.4. Adiabatic TDHF (ATDHF) method

Challenges for constructing microscopic theory of LACM can be traced back to the pioneering works by Belyaev [28], Baranger and Kumar [29] in which the collective potential and collective masses (inertial functions) appearing in the quadrupole collective Hamiltonian of Bohr and Mottelson are microscopically calculated on the basis of the time-dependent mean-field picture and with the use of the pairing-plus-quadrupole force [30]. In the ATDHF theories, developed by Baranger and Véneroni [31], Brink *et al* [32], Goeke and Reinhard [33], more general schemes applicable to general effective interactions are given. There, under the assumption that the LACM is slow, the time-dependent density matrix is expanded in terms of the collective momentum, and the collective coordinate is introduced as a parameter describing the time dependence of the density matrix. Another ATDHF theory by Villars [34] resembles the above approaches, but it is more ambitious in that it provides a set of equations to self-consistently determine the collective coordinates. It turned out, however, that these equations are insufficient to uniquely determine the collective coordinates. This problem was solved by properly treating the second-order equation (with respect to the collective momentum) in the time-dependent variational principle (see Mukherjee and Pal [35] and the series of papers by Klein, Do Dang, Bulgac and Walet, reviewed in [36]). It was also clarified through these works that the optimal collective path maximally decoupled from non-collective degrees of freedom coincides in a very good approximation with the valley in the large-dimensional configuration space associated with the TDHF states.

4.5. Self-consistent collective coordinate (SCC) method

Attempts to construct the LACM theory without assuming the adiabaticity and treating the collective coordinates and momenta on the same footing were initiated by Rowe [37] and Marumori [38]. The problems remaining in these early works were solved in the SCC method formulated by Marumori *et al* [39]. The major aim of this approach is to extract the optimal collective path (collective submanifold), maximally decoupled from non-collective degrees of freedom, in the TDHF phase space of large dimension. The collective submanifold is a geometrical object independent of the choice of the canonical coordinate system. This idea was developed also by Rowe [40], Yamamura and Kuriyama [41]. These works yield a new insight into the fundamental concepts of collective motion. The SCC method was extended [42] to include the pairing correlations and applied to anharmonic quadrupole vibrations [43–45]. In these works, a perturbative method of solving its basic equations was adopted and it remained as an open task to develop a non-perturbative method of solution for genuine LACM. This task was attained by the adiabatic SCC (ASCC) method [46], in which the basic equations of the SCC method is solved using an expansion with respect to the collective momentum. Therefore, the method is applicable to the change of the system in a wide range of the collective coordinate. This new method may also be regarded as a modern version of the ATDHF method initiated by Villars [34]. Another approach similar to the ASCC method has been developed also by Almehed and Walet [47] although the method of restoring the gauge invariance (number conservation) broken in the TDHFB states is not given there. In the next section, we briefly summarize the basic ideas of the microscopic theory of LACM along the lines of the ASCC method which is formulated respecting the gauge invariance.

5. Basic concepts of the microscopic theory of LACM

5.1. Extraction of the collective submanifold

As mentioned in the previous sections, the TDHFB theory can be formulated as a Hamilton dynamical system: the dimension of the phase space is quite large (twice the number of all possible two quasiparticle states). The major aim of the microscopic theory of LACM is to extract the collective submanifold from the TDHFB space, which is describable in terms of a few numbers of collective coordinates and momenta. The collective Hamiltonian is then derived and requantized yielding the collective Schrödinger equation.

5.2. Basic equations of the microscopic theory of LACM

Let us assume that the time development of the TDHFB state is describable in terms of the single collective coordinate $q(t)$ and momentum $p(t)$. To describe the superfluidity, we need to introduce also the number variable $n(t)$ and the gauge angle $\varphi(t)$ conjugate to it (for both protons and neutrons in applications to nuclei). We assume that the TDHFB state can be written in the following form:

$$|\phi(q, p, \varphi, n)\rangle = \mathrm{e}^{-\mathrm{i}\varphi\tilde{N}}|\phi(q, p, n)\rangle, \tag{1}$$

$$|\phi(q, p, n)\rangle = \mathrm{e}^{\mathrm{i}p\hat{Q}(q)+\mathrm{i}n\hat{\Theta}(q)}|\phi(q)\rangle. \tag{2}$$

Here $|\phi(q, p, n)\rangle$ is an intrinsic state for the pairing rotational degree of freedom parametrized by φ, $|\phi(q)\rangle$ represents a non-equilibrium HFB state called *moving-frame HFB state*, $\hat{Q}(q)$ and $\hat{\Theta}(q)$ are one-body operators called *infinitesimal generators* and $\tilde{N}$ and n are defined by

$\tilde{N} \equiv \hat{N} - \langle\phi(q)|\hat{N}|\phi(q)\rangle \equiv \hat{N} - N_0$ and $n \equiv \langle\phi(q,\, p, n)|\hat{N}|\phi(q,\, p, n)\rangle - N_0 \equiv N - N_0$, $\hat{N}$ being the number operator.

We determine the microscopic structure of the infinitesimal generators $\hat{Q}(q)$, $\hat{\Theta}(q)$ and the moving-frame HFB state $|\phi(q)\rangle$ on the basis of the time-dependent variational principle:

$$\delta\langle\phi(q,\, p, \varphi, n)|\mathrm{i}\frac{\partial}{\partial t} - \hat{H}|\phi(q,\, p, \varphi, n)\rangle = 0, \tag{3}$$

where $\hat{H}$ is a microscopic many-body Hamiltonian. Expanding in powers of p and n and keeping terms up to the second order in p, we obtain *the moving-frame HFB equation*

$$\delta\langle\phi(q)|\hat{H}_M(q)|\phi(q)\rangle = 0, \tag{4}$$

where $\hat{H}_M(q)$ is the moving-frame Hamiltonian defined by

$$\hat{H}_M(q) = \hat{H} - \lambda(q)\tilde{N} - \frac{\partial V}{\partial q}\hat{Q}(q), \tag{5}$$

and *the moving-frame QRPA equations* also called *local harmonic equations*

$$\delta\langle\phi(q)|[\hat{H}_M(q),\, \hat{Q}(q)] - \frac{1}{\mathrm{i}}B(q)\hat{P}(q)|\phi(q)\rangle = 0, \tag{6}$$

$$\delta\langle\phi(q)|\left[\hat{H}_M(q),\, \frac{1}{\mathrm{i}}\hat{P}(q)\right] - C(q)\hat{Q}(q) - \frac{1}{2B(q)}\left[\left[\hat{H}_M(q),\, \frac{\partial V}{\partial q}\hat{Q}(q)\right],\, \hat{Q}(q)\right] - \frac{\partial\lambda}{\partial q}\tilde{N}|\phi(q)\rangle = 0, \tag{7}$$

where $\hat{P}(q)$ is the displacement operator defined by

$$|\phi(q + \delta q)\rangle = \mathrm{e}^{-\mathrm{i}\delta q\hat{P}(q)}|\phi(q)\rangle, \tag{8}$$

and

$$C(q) = \frac{\partial^2 V}{\partial q^2} + \frac{1}{2B(q)}\frac{\partial B}{\partial q}\frac{\partial V}{\partial q}. \tag{9}$$

The quantities $C(q)$ and $B(q)$ are related to the eigenfrequency $\omega(q)$ of the local normal mode obtained by solving the moving-frame QRPA equations through $\omega^2(q) = B(q)C(q)$. Note that these equations are valid also for regions with a negative curvature ($C(q) < 0$) where $\omega(q)$ takes an imaginary value. The double commutator term in (7) stems from the q derivative of $\hat{Q}(q)$ and represents the curvature of the collective path.

Solving the above set of equations, the microscopic structure of the infinitesimal generators, $\hat{Q}(q)$ and $\hat{P}(q)$, are determined: they are explicitly expressed as bilinear superpositions of the quasiparticle creation and annihilation operators locally defined with respect to the moving-frame HFB state $|\phi(q)\rangle$. The collective Hamiltonian is given by

$$\mathcal{H}(q,\, p, n) = \langle\phi(q,\, p, n)|\hat{H}|\phi(q,\, p, n)\rangle = V(q) + \tfrac{1}{2}B(q)p^2 + \lambda(q)n, \tag{10}$$

where $V(q)$, $B(q)$ and $\lambda(q)$ represent the collective potential, inverse of the collective mass and the chemical potential, respectively. Note that they are functions of the collective coordinate q. The basic equations, (4), (6) and (7), reduce to the well-known HFB and QRPA equations at the equilibrium points where $\partial V/\partial q = 0$. Thus, the LACM theory outlined above is a natural extension of the HFB-QRPA theory to non-equilibrium states.

5.3. Relation to the constrained HFB approach

The moving-frame HFB equation (4) looks like the constrained HFB (CHFB) equation, but it is essentially different from the CHFB in that the infinitesimal generator $\hat{Q}(q)$ (corresponding to the constraint operator) is self-consistently determined together with $\hat{P}(q)$ as a solution of the moving-frame QRPA equations, (6) and (7), locally at every point of the collective coordinate q. Therefore, unlike the constraint operator in the CHFB method, its microscopic structure changes as a function of q. In other words, the LACM takes place choosing the locally optimal 'constraint operator' at every point of q along the collective path. When the LACM of interest is described by more than one collective coordinates, we try to extract the collective hypersurface embedded in the large-dimensional TDHFB space by extending the above equations to the multi-dimensional cases and derive the collective Schrödinger equation by requantization. This attempt has some features in common with the problem of *quantization of a constrained dynamical system* [40]. It is interesting to discuss the microscopic foundation of the so-called Pauli prescription (frequently used in quantizing phenomenological collective Hamiltonians) from this point of view. In discussing this issue, it is important to note that the LACM is constrained on the collective hypersurface not by external constraining forces but by the dynamics of itself. Namely, the collective hypersurface is generated as a consequence of the dynamics of the quantum many-body system under consideration. It seems that this is a unique and quite attractive feature of the subject under discussion.

5.4. Gauge invariance with respect to the pairing rotational angle

An important problem in formulating the microscopic LACM theory based on the TDHFB approximation is how to respect the number conservation. As is well known, one of the merits of the QRPA is that the zero-frequency Nambu–Goldstone mode restoring the number conservation is decoupled from other normal modes of vibration [48]. Our problem is how to generalize this concept to non-equilibrium HFB states. A clue for solving this problem is obtained by noting that the basic equations, (4), (6) and (7), are invariant against rotations of the gauge angle φ at every point of q. Actually, we can determine the infinitesimal generator $\hat{\Theta}(q)$ associated with the pairing-rotational degree of freedom in the same way as $\hat{Q}(q)$ and $\hat{P}(q)$, and obtain the pairing rotational energy proportional to n^2 as an additional term to the collective Hamiltonian (10). Although this term vanishes by setting $N = N_0$ to respect the number conservation, the consideration of the gauge invariance is essential for correctly treating the LACM in systems with superfluidity. Specifically, we need to set up a gauge fixing condition in practical calculations (see [49] for details).

6. Open problems in the microscopic theory of LACM

6.1. Contributions of the time-odd mean field to the collective mass

In the microscopic calculation of the collective mass (inertial function), the cranking mass is widely used. It is obtained through the adiabatic perturbation treatment of the time development of the mean field. As stressed by Belyaev [28], Baranger and Véneroni [31], the effects of the time-odd components (breaking the time-reversal invariance) induced by the time evolution of the mean field are ignored in the cranking mass. These effects are self-consistently taken into account in the ASCC collective mass obtained by solving equations (6) and (7). On the other hand, one can derive the collective Schrödinger equation from the GCM equation by making the Gaussian overlap approximation (GOA). It is not clear, however, to what extent the time-odd mean-field effects are taken into account in the GCM-GOA mass evaluated in this

way with real generator coordinates. In view of the importance of the collective mass in the dynamics of LACM, the time-odd mean-field effects have been studied extensively (see e.g. [50]). In spite of these efforts, it may be fair to say that we are still far from a full understanding of the time-odd effects. Thus, it remains as a great subject for future to evaluate the time-odd mean-field effects on the collective mass using energy density functionals currently under active development.

6.2. Different meaning of 'adiabatic'

There is another important difference between the ASCC collective mass and the cranking mass. Let us first note that the meaning of the adjective 'adiabatic' in the ASCC method is different from that of the adiabatic perturbation theory. In the ASCC method, it just means that the collective kinetic energy term higher than the second order in the power-series expansion with respect to the collective momentum is omitted and, in contrast to the adiabatic perturbation, the smallness of the collective kinetic energy in comparison with the intrinsic two-quasiparticle excitation energies is not indispensable. Recalling that the ASCC collective mass coincides with the QRPA collective mass at the HFB equilibrium point, one can easily confirm this difference by considering the spherical QRPA limit in the pairing-plus-quadrupole force model, where the time-odd mean-field effect is absent. At the spherical HFB equilibrium point, in fact, the QRPA collective mass reduces to the cranking mass in the limit that the frequency of the QRPA normal mode vanishes [30]. In this connection, it may be pertinent to emphasize the difference between the ASCC collective mass and the ATDHFB collective mass of Baranger and Véneroni. Specifically, the former is determined by the local QRPA mode and reduces to the QRPA collective mass at the HFB equilibrium point, while the latter is related to the cubic inverse energy-weighted sum rule [51] and does not reduce to the QRPA collective mass in this limit. Therefore, it is also interesting to make a systematic comparison between different collective masses including the ASCC, cranking, GCM-GOA and ATDHFB collective masses.

6.3. Deeper understanding of the pair-hopping mechanism

The collective mass represents the inertia of the many-body system against an infinitesimal change of the collective coordinate q during the time evolution of the mean field. It is a local quantity and varies as a function of q. What is the microscopic mechanism that determines the collective mass? This is one of the central questions in our study of many-body dynamics of the LACM. Concerning this question, it is well known that the pairing correlation plays a crucial role. Because the single-particle-energy spectrum in the mean field changes as a function of q, the level crossing at the Fermi energy successively occurs during the LACM. In the presence of the pairing correlation, the many-body system can easily rearrange to take the lowest energy configurations at every value of q, i.e. the system can easily change q. The easiness/hardness of the configuration rearrangements at the level crossings determines the adiabaticity/diabaticity of the system. Since the inertia represents a property of the system trying to keep a definite configuration, we expect that the stronger the pairing correlation, the smaller the collective mass. The nucleon-pair hopping mechanism at the successive level crossings at the Fermi surface is modeled by Barranco *et al* [52]. It yields the collective mass, called hopping mass, which has been applied to the exotic decays and the tunneling phenomena between the superdeformed (SD) and normal deformed states [52, 53]. Of course, smooth changes of single-particle wavefunctions as functions of q also contribute to the collective mass in addition to the configuration changes. To deepen our understanding of the collective mass

of LACM, it is desirable to make a comprehensive analysis of the microscopic mechanism determining it. A systematic comparison between the hopping mass and other collective masses discussed above will certainly serve for this purpose.

6.4. Application to the shape coexistence/mixing phenomena

As discussed in section 2, one of the most interesting LACM phenomena is the oblate–prolate shape coexistence/mixing in the proton-rich ^{68}Se and ^{72}Kr region. Quite recently, we have applied the ASCC method to them and successfully determined the collective path which runs through the triaxially deformed valley and connects the oblate and prolate HFB minima. Evaluating the rotational moments of inertia on the collective path and requantizing the collective Hamiltonian, we have derived the collective Schrödinger equation describing the coupled motion of the large-amplitude shape vibrations and the three-dimensional (3D) rotational motions [54, 55]. We have thus found a number of interesting features which change when going from nucleus to nucleus. For instance, the ^{68}Se nucleus exhibits intermediate features between the oblate–prolate shape coexistence and the γ-soft rotors, while in the neighboring $N = Z$ nucleus ^{72}Kr, we have found that the localization of the collective wavefunction in the (β, γ) plane significantly develops with increasing rotational angular momentum. It is certainly desirable to carry out this kind of microscopic analysis for a wide variety of shape coexistence/mixing phenomena. We believe that theoretical and experimental investigations of these phenomena will be very fruitful and bring about plenty of new ideas on nuclear structure and dynamics.

6.5. Microscopic derivation of the Bohr–Mottelson collective Hamiltonian

Extending the one-dimensional (1D) collective path to the two-dimensional (2D) hypersurface and mapping it on the (β, γ) plane, we shall be able to microscopically derive the five-dimensional (5D) quadrupole collective Hamiltonian of Bohr and Mottelson [15]. In this derivation, the moments of inertia of the 3D rotation may be evaluated at every point of the 2D hypersurface generalizing the Thouless–Valatin equations to those at non-equilibrium points. The microscopic derivation of the Bohr–Mottelson collective Hamiltonian is a well-known long-standing subject in nuclear structure physics, but we are still on the way to the goal (see [56, 57] for examples of recent works and [58] for a review). We illustrate in figure 1 the basic concepts of the microscopic LACM theory and the result of a recent calculation.

6.6. Extension to high-spin states

In the above approach, variations of intrinsic structure due to rotation are not taken into account. Therefore, the range of its applicability is limited to low-spin states. A promising way of constructing LACM theory applicable to high-spin states is to adopt the rotating mean-field picture. Specifically, it is interesting to develop LACM theory on the basis of the HFB approximation in a rotating frame (it is possible to formulate the SCC method in a form suitable for treating the rotational motions [59, 60]). Such an approach was once tried in [47]. It remains as a future challenge to construct the microscopic theory of LACM at high spin, which is capable of self-consistently taking into account variation of intrinsic structure due to rapid rotation.

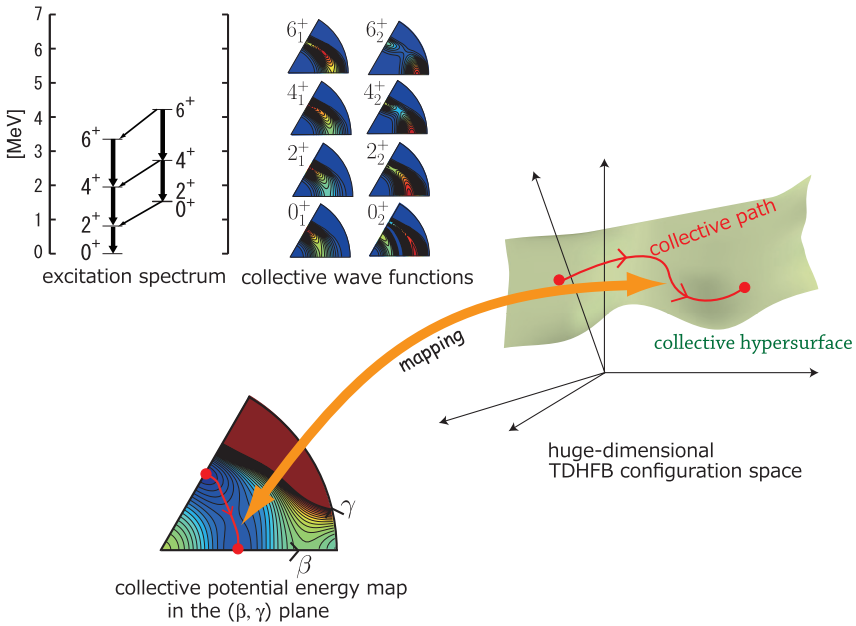

Figure 1. Illustration of basic concepts of LACM. The collective path and the collective hypersurface embedded in the huge-dimensional TDHFB configuration space (*right-hand side*). Mapping of the collective path and the hypersurface into the (β, γ) plane and the collective potential energy on it (*lower part on the left-hand side*). The excitation spectrum and collective wavefunctions obtained by solving the collective Schrödinger equation (*upper part on the left-hand side*). In this illustration, the result of a microscopic calculation for the oblate–prolate shape coexistence/mixing phenomenon in ^{68}Se is used, where the collective path is self-consistently determined by solving the ASCC equations while the collective potential and the collective masses are evaluated by solving the CHFB and the moving-frame QRPA equations, respectively, with the pairing-plus-quadrupole force (the quadrupole pairing is also taken into account). This calculation may be regarded as a first step toward a fully self-consistent microscopic derivation of the 5D quadrupole collective Hamiltonian starting from modern density functionals.

(This figure is in colour only in the electronic version)

6.7. Combining with better density functionals

As seen in a number of contributions to this special issue on open problems in nuclear structure, very active works are going on to build a universal nuclear energy density functional. It is certainly a great challenge to make a systematic microscopic calculation for LACM phenomena using better energy density functionals. For carrying out such ambitious calculations, it is certainly necessary to develop efficient numerical algorithms to solve the basic equations of the LACM theory. In practical applications, for instance, we need to iteratively solve the moving-frame HFB equation and the moving-frame QRPA equations at every point on the collective path. When we extend these equations to 2D hypersurfaces, the numerical calculation grows to a large scale. Especially, an efficient method of solving the moving-frame QRPA equations is needed. An extension of the finite amplitude method [61] into a form suitable for this purpose may be promising. It may also be worthwhile to examine the applicability of the separable approximation [62] to the effective interaction derived from the energy density functionals.

6.8. LACM in odd-A nuclei

So far we have limited our discussions to LACM in doubly even nuclei only. In fact, microscopic description of LACM in odd-A nuclei remains as a vast unexplored field. Needless to say, unified treatment of the seemingly contradictory concepts of single-particle and collective modes of motion is the central theme of the phenomenological Bohr–Mottelson model of nuclear structure. Low-lying states in odd-A nuclei provide a wealth of data exhibiting their interplay. In view of the great success of the Bohr–Mottelson approach, it is extremely important to develop a microscopic theory capable of treating the single-particle and collective modes in a unified manner. In fact, various microscopic theories of particle–vibration coupling have been developed: e.g. the nuclear field theory [63] and the boson-expansion method for odd-A nuclei [26]. These available theories treat the particle–vibration couplings in a perturbative manner starting from the small-amplitude approximation (RPA/QRPA) for collective excitations at an equilibrium point of the mean field. Non-perturbative method capable of treating LACM in odd-A nuclei (generally speaking, LACM in the presence of several quasiparticles) is lacking, however. This is an extremely difficult but challenging subject for future.

7. Large-amplitude collective phenomena at high spin

The nucleus exhibits a rich variety of nonlinear collective phenomena awaiting applications of the microscopic LACM theory. Certainly, microscopic description of spontaneous fission from the viewpoint of nonlinear/non-equilibrium physics is one of the major goals. Another vast unexplored field is the microscopic study of LACM at finite temperature. Microscopic mechanism of damping and dissipation of various kinds of LACM is a long-term subject. It seems particularly interesting to explore both theoretically and experimentally how the character of LACM changes when going from the yrast to the compound-nucleus regions. These subjects are outside the scope of the present paper, however. Restricting our scope to the LACM at zero temperature, in this section, we discuss a few open problems in rapidly rotating nuclei (see [64] for a review on high-spin states).

7.1. Tunneling decay of superdeformed (SD) states and high-K isomers

It is quite interesting to apply the microscopic LACM theory to the quantum tunneling phenomena from the SD states (with an axis ratio of about 2:1) to the compound-nucleus states [53], because the tunneling probability depends quite sensitively on the collective mass and the collective path connecting the initial and final states. The tunneling decay from high-K to low-K isomers is also interesting [65], because it poses a unique question as to which of the two competing decay paths dominates; one through LACM in the triaxial shape degree of freedom and the other in the orientation degree of freedom of the angular momentum vector (with respect to the principal axes of the body-fixed frame).

7.2. Large-amplitude wobbling motions and chiral vibrations

A new mode of 3D rotation associated with the spontaneous breaking of the axial symmetry is called wobbling motion; it is describable as a boson (small-amplitude vibration-like) excitation from the yrast line [15, 66]. The observed rotational band associated with the double excitations of the wobbling mode indicates, however, the presence of significant anharmonicity [67]. It is an interesting open problem to explore what will happen when the amplitude of the wobbling mode increases and the uniformly rotating nucleus becomes unstable against this collective

rotational degree of freedom [68, 69]. Another interesting issue concerning new modes of 3D rotation is the possibility of doublet rotational bands called chiral band [16, 70, 71]. In triaxially deformed nucleus, one can define *chirality* in terms of the directions of the collective rotational angular momentum and those of the quasiparticle angular momenta of both protons and neutrons. When the rotating HFB mean field involves such an intrinsic structure, the two solutions corresponding to the right-handed and left-handed configurations are degenerate. Then, a chiral doublet pattern is expected to appear in the rotational band structure. In a transient situation, where the barrier separating the two HFB solutions is still in an early stage of development, the large-amplitude vibrations connecting the two configurations, called chiral vibrations, may occur [16, 70, 71]. It remains for the future to apply the microscopic LACM theory to these phenomena unique to rapidly rotating nuclei with triaxial shape.

7.3. Large-amplitude vibrations associated with the reflection symmetry breaking

Rich experimental data exhibiting the parity-doublet pattern are available, indicating that the reflection symmetry is broken in their mean fields [72]. The energy splitting of the doublet changes as a function of rotational angular momentum [73]. Thus, it is quite interesting to investigate, on the basis of the microscopic LACM theory, how the quantum tunneling motion between the left- and right-configurations is affected by rapid rotation. Also interesting in this connection is the recent observation of alternating parity bands [74, 75] that exhibit a transitional feature toward the static octupole deformation. A considerable number of SD states are expected to be very soft with respect to the shape vibrational degrees of freedom simultaneously breaking the reflection and axial symmetries. In fact, the soft octupole vibrations built on the SD yrast states have been observed [76, 77]. When the SD mean field becomes unstable against this kind of vibrations, a new class of SD states having exotic shapes (like a banana) may appear [78, 79]. In transitional situations, the large-amplitude vibrations associated with the instability toward such exotic shapes may take place. Possible appearance of exotic shapes is not restricted to SD high-spin states. For example, the symmetry-unrestricted HFB calculation [80] yields a local minimum with the tetrahedral shape near the ground state of ^{80}Zr. The potential energy surface is shallow, however, indicating that we need to take into account the large-amplitude tetrahedral shape fluctuation [81]. Generally speaking, microscopic LACM theories are required for describing collective motions in transitional regions of quantum phase transition, where some symmetry is weakly broken or tends to be broken.

8. Concluding remarks

One of the fundamental questions of nuclear structure physics is why and how a variety of LACM emerges in consequence of quantum many-body dynamics. The nucleus provides us valuable opportunities to make a detailed study of the microscopic dynamics generating the collectivities. The microscopic derivation of the quadrupole collective Hamiltonian started more than half a century ago, but the challenge to construct a fully self-consistent microscopic theory of LACM has encountered a number of serious difficulties. Finally, however, these long-term efforts have yielded the new concept of *collective submanifold* and a deeper understanding of what is *collectivity*. At the same time, new efficient methods of numerical calculation are now under active development. Thus, in the coming years, fruitful applications to low-frequency collective phenomena are envisaged. This means that a new era in the microscopic study of nuclear collective dynamics is opening.

Acknowledgments

This work is supported by the grant-in-aid for Scientific Research(B) (no 21340073). One of the authors (NH) is supported by the Special Postdoctoral Researcher Program of RIKEN.

References

[1] Do Dang G, Klein A and Walet N R 2000 *Phys. Rep.* **335** 93
[2] Åberg S, Flocard H and Nazarewicz W 1990 *Annu. Rev. Nucl. Part. Sci.* **40** 439
[3] Wood J L *et al* 1992 *Phys. Rep.* **215** 101
[4] Andreyev A N *et al* 2000 *Nature (London)* **405** 430
[5] Fischer S M *et al* 2000 *Phys. Rev. Lett.* **84** 4064
Fischer S M *et al* 2003 *Phys. Rev.* C **67** 064318
[6] Clément E *et al* 2007 *Phys. Rev.* C **75** 054313
[7] Ring P and Schuck P 1980 *The Nuclear Many-Body Problem* (Berlin: Springer)
[8] Blaizot J-P and Ripka G 1986 *Quantum Theory of Finite Systems* (Cambridge, MA: MIT Press)
[9] Takada K and Tazaki S 1986 *Nucl. Phys.* A **448** 56
[10] Weeks K J *et al* 1981 *Phys. Rev.* C **24** 703
[11] Kotliński B *et al* 1990 *Nucl. Phys.* A **519** 646
[12] Garrett P E *et al* 2009 *Phys. Rev. Lett.* **103** 062501
[13] Nambu Y 1960 *Phys. Rev* **117** 648
[14] Bender M, Heenen P-H and Reinhard P-G 2003 *Rev. Mod. Phys.* **75** 121
[15] Bohr A and Mottelson B R 1975 *Nuclear Structure* vol 2 (New York: Benjamin)
[16] Frauendorf S 2001 *Rev. Mod. Phys.* **73** 463
[17] Hamamoto I and Mottelson B R 2009 *Phys. Rev.* C **79** 034317
[18] Brack M and Bhaduri R K 1997 *Semiclassical Physics* (Reading, MA: Addison-Wesley)
[19] Frisk H 1990 *Nucl. Phys.* A **511** 309
[20] Arita K, Sugita A and Matsuyanagi K 1998 *Prog. Theor. Phys.* **100** 1223
[21] Bohr A 1976 *Rev. Mod. Phys.* **48** 365
[22] Mottelson B 1976 *Rev. Mod. Phys.* **48** 375
[23] Negele J W 1982 *Rev. Mod. Phys.* **54** 913
[24] Abe A and Suzuki T (eds) 1983 *Prog. Theor. Phys. Suppl.* **74-75** special issue
[25] Kuriyama A *et al* (eds) 2001 *Prog. Theor. Phys. Suppl.* **141** special issue
[26] Klein A and Marshalek E R 1991 *Rev. Mod. Phys.* **63** 375
[27] Holzwarth G and Yukawa T 1974 *Nucl. Phys.* A **219** 125
[28] Belyaev S T 1965 *Nucl. Phys.* **64** 17
[29] Baranger M and Kumar K 1968 *Nucl. Phys.* A **122** 241
Baranger M and Kumar K 1968 *Nucl. Phys.* A **122** 273
[30] Bes D R and Sorensen R A 1969 *Advances in Nuclear Physics* vol 2 (New York: Plenum) p 129
[31] Baranger M and Véneroni M 1978 *Ann. Phys.* **114** 123
[32] Brink D M, Giannoni M J and Veneroni M 1976 *Nucl. Phys.* A **258** 237
[33] Goeke K and Reinhard P-G 1978 *Ann. Phys.* **112** 328
[34] Villars F 1977 *Nucl. Phys.* A **285** 269
[35] Mukherjee A K and Pal M K 1981 *Phys. Lett.* B **100** 457
Mukherjee A K and Pal M K 1982 *Nucl. Phys.* A **373** 289
[36] Klein A, Walet N R and Do Dang G 1991 *Ann. Phys.* **208** 90
[37] Rowe D J and Bassermann R 1976 *Can. J. Phys.* **54** 1941
[38] Marumori T 1977 *Prog. Theor. Phys.* **57** 112
[39] Marumori T *et al* 1980 *Prog. Theor. Phys.* **64** 1294
[40] Rowe D J 1982 *Nucl. Phys.* A **391** 307
[41] Yamamura M and Kuriyama A 1987 *Prog. Theor. Phys. Suppl.* **93** special issue
[42] Matsuo M 1986 *Prog. Theor. Phys.* **76** 372
[43] Matsuo M and Matsuyanagi K 1985 *Prog. Theor. Phys.* **74** 1227
Matsuo M and Matsuyanagi K 1986 *Prog. Theor. Phys.* **76** 93
Matsuo M and Matsuyanagi K 1987 *Prog. Theor. Phys.* **78** 591
[44] Matsuo M, Shimizu Y R and Matsuyanagi K 1985 *Proc. of the Niels Bohr Centennial Conf. on Nuclear Structure* (Amsterdam: North-Holland) p 161

[45] Yamada K 1993 *Prog. Theor. Phys.* **89** 995
[46] Matsuo M, Nakatsukasa T and Matsuyanagi K 2000 *Prog. Theor. Phys.* **103** 959
[47] Almehed D and Walet N R 2004 *Phys. Rev.* C **69** 024302
Almehed D and Walet N R 2004 *Phys. Lett.* B **604** 163
[48] Brink D M and Broglia R A 2005 *Nuclear Superfluidity, Pairing in Finite Systems* (Cambridge: Cambridge University Press)
[49] Hinohara N *et al* 2007 *Prog. Theor. Phys.* **117** 451
[50] Dobaczewski J and Dudek J 1995 *Phys. Rev.* C **52** 1827
[51] Giannoni M J and Quentin P 1980 *Phys. Rev.* C **21** 2060
[52] Barranco F *et al* 1990 *Nucl. Phys.* A **512** 253
[53] Yoshida K, Shimizu Y R and Matsuo M 2001 *Nucl. Phys.* A **696** 85
[54] Hinohara N *et al* 2008 *Prog. Theor. Phys.* **119** 59
[55] Hinohara N *et al* 2009 *Phys. Rev.* C **80** 014305
[56] Bender M and Heenen P-H 2008 *Phys. Rev.* C **78** 024309
[57] Nikšić T *et al* 2009 *Phys. Rev.* C **79** 034303
[58] Próchniak L and Rohoziński S G 2009 *J. Phys. G: Nucl. Part. Phys.* **36** 123101
[59] Shimizu Y R and Matsuyanagi K 2001 *Prog. Theor. Phys. Suppl.* **141** 285
[60] Kaneko K 1994 *Phys. Rev.* C **49** 3014
[61] Nakatsukasa T, Inakura T and Yabana K 2007 *Phys. Rev.* C **76** 024318
[62] Kleinig W *et al* 2008 *Phys. Rev.* C **78** 044313
[63] Bortignon P F *et al* 1977 *Phys. Rep.* **30** 305
[64] Satula W and Wyss R A 2005 *Rep. Prog. Phys.* **68** 131
[65] Narimatsu K, Shimizu Y R and Shizuma T 1996 *Nucl. Phys.* A **601** 69
[66] Shoji T and Shimizu Y R 2009 *Prog. Theor. Phys.* **121** 319
[67] Jensen D R *et al* 2002 *Phys. Rev. Lett.* **89** 142503
[68] Matsuzaki M and Ohtsubo S I 2004 *Phys. Rev.* C **69** 064317
[69] Olbratowski P *et al* 2004 *Phys. Rev. Lett.* **93** 052501
[70] Koike T, Starosta K and Hamamoto I 2004 *Phys. Rev. Lett.* **93** 172502
[71] Mukhopadhyay S *et al* 2007 *Phys. Rev. Lett.* **99** 172501
[72] Butler P A and Nazarewicz W 1996 *Rev. Mod. Phys.* **68** 349
[73] Jolos R V and von Brentano P 1999 *Phys. Rev.* C **60** 064317
[74] Reviol W *et al* 2006 *Phys. Rev.* C **74** 044305
[75] Frauendorf S 2008 *Phys. Rev.* C **77** 021304
[76] Nakatsukasa T *et al* 1996 *Phys. Rev.* C **53** 2213
[77] Roßbach D *et al* 2001 *Phys. Lett.* B **513** 9
[78] Nakatsukasa T, Mizutori S and Matsuyanagi K 1992 *Prog. Theor. Phys.* **87** 607
[79] Inakura T *et al* 2002 *Nucl. Phys.* A **710** 261
[80] Yamagami M, Matsuyanagi K and Matsuo M 2001 *Nucl. Phys.* A **693** 579
[81] Zberecki K, Heenen P-H and Magierski P 2009 *Phys. Rev.* C **79** 014319

Microscopic description of large-amplitude shape-mixing dynamics with inertial functions derived in local quasiparticle random-phase approximation

Nobuo Hinohara,[1] Koichi Sato,[1,2] Takashi Nakatsukasa,[1] Masayuki Matsuo,[3] and Kenichi Matsuyanagi[1,4]
[1]*Theoretical Nuclear Physics Laboratory, RIKEN Nishina Center, Wako 351-0198, Japan*
[2]*Department of Physics, Graduate School of Science, Kyoto University, 606-8502 Kyoto, Japan*
[3]*Department of Physics, Faculty of Science, Niigata University, Niigata 950-2181, Japan*
[4]*Yukawa Institute for Theoretical Physics, Kyoto University, Kyoto 606-8502, Japan*
(Received 30 April 2010; revised manuscript received 19 August 2010; published 23 December 2010)

On the basis of the adiabatic self-consistent collective coordinate method, we develop an efficient microscopic method of deriving the five-dimensional quadrupole collective Hamiltonian and illustrate its usefulness by applying it to the oblate-prolate shape coexistence/mixing phenomena in proton-rich ^{68,70,72}Se. In this method, the vibrational and rotational collective masses (inertial functions) are determined by local normal modes built on constrained Hartree-Fock-Bogoliubov states. Numerical calculations are carried out using the pairing-plus-quadrupole Hamiltonian including the quadrupole-pairing interaction within the two major-shell active model spaces both for neutrons and protons. It is shown that the time-odd components of the moving mean-field significantly increase the vibrational and rotational collective masses in comparison with the Inglis-Belyaev cranking masses. Solving the collective Schrödinger equation, we evaluate excitation spectra, quadrupole transitions, and moments. The results of the numerical calculation are in excellent agreement with recent experimental data and indicate that the low-lying states of these nuclei are characterized as an intermediate situation between the oblate-prolate shape coexistence and the so-called γ unstable situation where large-amplitude triaxial-shape fluctuations play a dominant role.

DOI: 10.1103/PhysRevC.82.064313 PACS number(s): 21.60.Ev, 21.10.Re, 21.60.Jz, 27.50.+e

I. INTRODUCTION

The major purpose of this article is to develop an efficient microscopic method of deriving the five-dimensional (5D) quadrupole collective Hamiltonian [1–4] and illustrate its usefulness by applying it to the oblate-prolate shape coexistence/mixing phenomena in proton-rich Se isotopes [5–8]. As is well known, the quadrupole collective Hamiltonian, also called the general Bohr-Mottelson Hamiltonian, contains six collective inertia masses (three vibrational masses and three rotational moments of inertia) as well as the collective potential. These seven quantities are functions of the quadrupole deformation variables β and γ, which represent the magnitude and triaxiality of the quadrupole deformation, respectively. Therefore, we also call the collective inertial masses "inertial functions." They are usually calculated by means of the adiabatic perturbation treatment of the moving mean field [9], and the version taking into account nuclear superfluidity [10] is called the Inglis-Belyaev (IB) cranking mass or the IB inertial function. Its insufficiency has been repeatedly emphasized, however (see, e.g., Refs. [11–14]). The most serious shortcoming is that the time-odd terms induced by the moving mean field are ignored, which breaks the self-consistency of the theory [15,16]. In fact, one of the most important motives of constructing microscopic theory of large-amplitude collective motion was to overcome such a shortcoming of the IB cranking mass [15].

As fruits of long-term efforts, advanced microscopic theories of inertial functions are now available (see Refs. [15–26] for original articles and Refs. [27,28] for reviews). These theories of large-amplitude collective motion have been tested for schematic solvable models and applied to heavy-ion collisions and giant resonances [18,26]. For nuclei with pairing correlations, Dobaczewski and Skalski studied the quadrupole vibrational mass with use of the adiabatic time-dependent Hartree-Fock-Bogoliubov (ATDHFB) theory and concluded that the contributions from the time-odd components of the moving mean-field significantly increase the vibrational mass compared to the IB cranking mass [16]. Somewhat surprisingly, however, to the best of our knowledge, the ATDHFB vibrational masses have never been used in realistic calculations for low-lying quadrupole spectra of nuclei with superfluidity. For instance, in recent microscopic studies [29–34] by means of the 5D quadrupole Hamiltonian, the IB cranking formula are still used in actual numerical calculation for vibrational masses. This situation concerning the treatment of the collective kinetic energies is in marked contrast with the remarkable progress in microscopic calculation of the collective potential using modern effective interactions or energy density functionals (see Ref. [35] for a review).

In this article, on the basis of the adiabatic self-consistent collective coordinate (ASCC) method [36], we formulate a practical method of deriving the 5D quadrupole collective Hamiltonian. The central concept of this approach is local normal modes built on constrained Hartree-Fock-Bogoliubov (CHFB) states [37] defined at every point of the (β,γ) deformation space. These local normal modes are determined by the local QRPA (LQRPA) equation that is an extension of the well-known quasiparticle random-phase approximation (QRPA) to nonequilibrium HFB states determined by the CHFB equations. We therefore use an abbreviation "CHFB + LQRPA method" for this approach. This method may be used in

conjunction with any effective interaction or energy density functional. In this article, however, we use, for simplicity, the pairing-plus-quadrupole (P + Q) force [38,39] including the quadrupole-pairing force. Inclusion of the quadrupole-pairing force is essential because it produces the time-odd component of the moving field [40].

To examine the feasibility of the CHFB + LQRPA method, we apply it to the oblate-prolate shape coexistence/mixing phenomena in proton-rich ^{68,70,72}Se [5–8,41,42]. These phenomena are taken up because we obviously need to go beyond the traditional framework of describing small-amplitude vibrations around a single HFB equilibrium point to describe them; that is, they are very suitable targets for our purpose. We shall show in this article that this approach successfully describes large-amplitude collective vibrations extending from the oblate to the prolate HFB equilibrium points (and vice versa). In particular, it will be demonstrated that we can describe very well the transitional region between the oblate-prolate shape coexistence and the γ unstable situation where large-amplitude triaxial-shape fluctuations play a dominant role.

This article is organized as follows. In Sec. II, we formulate the CHFB + LQRPA as an approximation of the ASCC method and derive the 5D quadrupole collective Hamiltonian. In Sec. III, we calculate the vibrational and rotational masses by solving the LQRPA equations, and discuss their properties in comparison with those calculated by using the IB cranking formula. In Sec. IV, we calculate excitation spectra, $B(E2)$, and spectroscopic quadrupole moments of low-lying states in ^{68,70,72}Se and discuss properties of the oblate-prolate shape coexistence/mixing in these nuclei. Conclusions are given in Sec. V.

II. MICROSCOPIC DERIVATION OF THE 5D QUADRUPOLE COLLECTIVE HAMILTONIAN

A. 5D quadrupole collective Hamiltonian

Our aim in this section is to formulate a practical method of microscopically deriving the 5D quadrupole collective Hamiltonian [1–4]

$$\mathcal{H}_{\rm coll} = T_{\rm vib} + T_{\rm rot} + V(\beta,\gamma), \tag{1}$$

$$T_{\rm vib} = \frac{1}{2}D_{\beta\beta}(\beta,\gamma)\dot{\beta}^2 + D_{\beta\gamma}(\beta,\gamma)\dot{\beta}\dot{\gamma} + \frac{1}{2}D_{\gamma\gamma}(\beta,\gamma)\dot{\gamma}^2, \tag{2}$$

$$T_{\rm rot} = \frac{1}{2}\sum_{k=1}^{3}\mathcal{J}_k(\beta,\gamma)\omega_k^2, \tag{3}$$

starting from an effective Hamiltonian for finite many-nucleon systems. Here, $T_{\rm vib}$ and $T_{\rm rot}$ denote the kinetic energies of vibrational and rotational motions, while $V(\beta,\gamma)$ represents the collective potential. The velocities of the vibrational motion are described in terms of the time derivatives $(\dot{\beta},\dot{\gamma})$ of the quadrupole deformation variables (β,γ) representing the magnitude and the triaxiality of the quadrupole deformation, respectively. The three components ω_k of the rotational angular velocity are defined with respect to the intrinsic axes associated with the rotating nucleus. The inertial functions for vibrational motions (vibrational masses), $D_{\beta\beta}$, $D_{\beta\gamma}$, and $D_{\gamma\gamma}$, and the rotational moments of inertia $\mathcal{J}_k$ are functions of β and γ.

As seen in the recent review by Próchniak and Rohoziński [4], there are numerous articles on microscopic approaches to the 5D quadrupole collective Hamiltonian; among them, we should quote at least early articles by Belyaev [2], Baranger-Kumar [43,44], Pomorski *et al.* [12,13], and recent articles by Girod *et al.* [33], Nikšić *et al.* [29,30], and Li *et al.* [31,32]. In all these works, the IB cranking formula is used for the vibrational inertial functions. In the following, we outline the procedure of deriving the vibrational and rotational inertial functions on the basis of the ASCC method.

B. Basic equations of the ASCC method

To derive the 5D quadrupole collective Hamiltonian $\mathcal{H}_{\rm coll}$ starting from a microscopic Hamiltonian $\hat{H}$, we use the ASCC method [36,45]. This method enables us to determine a collective submanifold embedded in the large-dimensional TDHFB configuration space. We can use this method in conjunction with any effective interaction or energy density functional to microscopically derive the collective masses taking into account time-odd mean-field effects. For our present purpose, we here recapitulate a two-dimensional (2D) version of the ASCC method. We suppose the existence of a set of two collective coordinates (q^1, q^2) that has a one-to-one correspondence to the quadrupole deformation variable set (β,γ) and try to determine a 2D collective hypersurface associated with the large-amplitude quadrupole shape vibrations. We thus assume that the TDHFB states can be written on the hypersurface in the following form:

$$\begin{aligned}|\phi(\boldsymbol{q},\boldsymbol{p},\boldsymbol{\varphi},\boldsymbol{n})\rangle &= e^{-i\sum_\tau \varphi^{(\tau)}\tilde{N}^{(\tau)}}\,|\phi(\boldsymbol{q},\boldsymbol{p},\boldsymbol{n})\rangle \\ &= e^{-i\sum_\tau \varphi^{(\tau)}\tilde{N}^{(\tau)}} e^{i\hat{G}(\boldsymbol{q},\boldsymbol{p},\boldsymbol{n})}\,|\phi(\boldsymbol{q})\rangle\,,\end{aligned} \tag{4}$$

with

$$\hat{G}(\boldsymbol{q},\boldsymbol{p},\boldsymbol{n}) = \sum_{i=1,2} p_i\hat{Q}^i(\boldsymbol{q}) + \sum_{\tau=n,p} n^{(\tau)}\hat{\Theta}^{(\tau)}(\boldsymbol{q}), \tag{5}$$

$$\begin{aligned}\hat{Q}^i(\boldsymbol{q}) &= \hat{Q}^A(\boldsymbol{q}) + \hat{Q}^B(\boldsymbol{q}) \\ &= \sum_{\alpha\beta}\left[Q^A_{\alpha\beta}(\boldsymbol{q})a^\dagger_\alpha a^\dagger_\beta + Q^{A*}_{\alpha\beta}(\boldsymbol{q})a_\beta a_\alpha\right. \\ &\quad \left. + Q^B_{\alpha\beta}(\boldsymbol{q})a^\dagger_\alpha a_\beta\right],\end{aligned} \tag{6}$$

$$\hat{\Theta}^{(\tau)}(\boldsymbol{q}) = \sum_{\alpha\beta}\left[\Theta^{(\tau)A}_{\alpha\beta}(\boldsymbol{q})a^\dagger_\alpha a^\dagger_\beta + \Theta^{(\tau)A*}_{\alpha\beta}(\boldsymbol{q})a_\beta a_\alpha\right]. \tag{7}$$

For a gauge-invariant description of nuclei with superfluidity, we need to parametrize the TDHFB state vectors, as previously, not only by the collective coordinates $\boldsymbol{q} = (q^1, q^2)$ and conjugate momenta $\boldsymbol{p} = (p_1, p_2)$, but also by the gauge angles $\boldsymbol{\varphi} = (\varphi^{(n)}, \varphi^{(p)})$ conjugate to the number variables $\boldsymbol{n} = (n^{(n)}, n^{(p)})$ representing the pairing-rotational degrees of freedom (for both neutrons and protons). In the above equations, $\hat{Q}^i(\boldsymbol{q})$ and $\hat{\Theta}^{(\tau)}(\boldsymbol{q})$ are infinitesimal generators that are written in terms of the quasiparticle creation and annihilation operators $(a^\dagger_\alpha, a_\alpha)$ locally defined with respect to the moving-frame HFB states $|\phi(\boldsymbol{q})\rangle$. Note that the number operators are defined as

$\widetilde{N}^{(\tau)} \equiv \hat{N}^{(\tau)} - N_0^{(\tau)}$ subtracting the expectation values $(N_0^{(n)}, N_0^{(p)})$ of the neutron and proton numbers at $|\phi(\boldsymbol{q})\rangle$. In this article, we use units with $\hbar = 1$.

The moving-frame HFB states $|\phi(\boldsymbol{q})\rangle$ and the infinitesimal generators $\hat{Q}^i(\boldsymbol{q})$ are determined as solutions of the moving-frame HFB equation

$$\delta \langle\phi(\boldsymbol{q})| \hat{H}_M(\boldsymbol{q}) |\phi(\boldsymbol{q})\rangle = 0, \tag{8}$$

and the moving-frame QRPA equations

$$\begin{aligned}
&\delta\langle\phi(\boldsymbol{q})|[\hat{H}_M(\boldsymbol{q}), \hat{Q}^i(\boldsymbol{q})] - \frac{1}{i}\sum_k B^{ik}(\boldsymbol{q})\hat{P}_k(\boldsymbol{q}) \\
&\quad + \frac{1}{2}\left[\sum_k \frac{\partial V}{\partial q^k}\hat{Q}^k(\boldsymbol{q}), \hat{Q}^i(\boldsymbol{q})\right]|\phi(\boldsymbol{q})\rangle = 0, \qquad (9) \\
&\delta\langle\phi(\boldsymbol{q})|\left[\hat{H}_M(\boldsymbol{q}), \frac{1}{i}\hat{P}_i(\boldsymbol{q})\right] - \sum_j C_{ij}(\boldsymbol{q})\hat{Q}^j(\boldsymbol{q}) \\
&\quad - \frac{1}{2}\left[\left[\hat{H}_M(\boldsymbol{q}), \sum_k \frac{\partial V}{\partial q^k}\hat{Q}^k(\boldsymbol{q})\right], \sum_j B_{ij}(\boldsymbol{q})\hat{Q}^j(\boldsymbol{q})\right] \\
&\quad - \sum_\tau \frac{\partial \lambda^{(\tau)}}{\partial q^i}\widetilde{N}^{(\tau)}|\phi(\boldsymbol{q})\rangle = 0, \qquad (10)
\end{aligned}$$

which are derived from the time-dependent variational principle. Here, $\hat{H}_M(\boldsymbol{q})$ is the moving-frame Hamiltonian given by

$$\hat{H}_M(\boldsymbol{q}) = \hat{H} - \sum_\tau \lambda^{(\tau)}(\boldsymbol{q})\widetilde{N}^{(\tau)} - \sum_i \frac{\partial V}{\partial q^i}\hat{Q}^i(\boldsymbol{q}), \tag{11}$$

and

$$C_{ij}(\boldsymbol{q}) = \frac{\partial^2 V}{\partial q^i \partial q^j} - \sum_k \Gamma^k_{ij}\frac{\partial V}{\partial q^k}, \tag{12}$$

with

$$\Gamma^k_{ij}(\boldsymbol{q}) = \frac{1}{2}\sum_l B^{kl}\left(\frac{\partial B_{li}}{\partial q^j} + \frac{\partial B_{lj}}{\partial q^i} - \frac{\partial B_{ij}}{\partial q^l}\right). \tag{13}$$

The infinitesimal generators $\hat{P}_i(\boldsymbol{q})$ are defined by

$$\hat{P}_i(\boldsymbol{q})|\phi(\boldsymbol{q})\rangle = i\frac{\partial}{\partial q^i}|\phi(\boldsymbol{q})\rangle, \tag{14}$$

with

$$\hat{P}_i(\boldsymbol{q}) = i\sum_{\alpha\beta}[P_{i\alpha\beta}(\boldsymbol{q})a^\dagger_\alpha a^\dagger_\beta - P^*_{i\alpha\beta}(\boldsymbol{q})a_\beta a_\alpha], \tag{15}$$

and determined as solutions of the moving-frame QRPA equations.

The collective Hamiltonian is given as the expectation value of the microscopic Hamiltonian with respect to the TDHFB state

$$\begin{aligned}
\mathcal{H}(\boldsymbol{q}, \boldsymbol{p}, \boldsymbol{n}) &= \langle\phi(\boldsymbol{q}, \boldsymbol{p}, \boldsymbol{n})|\hat{H}|\phi(\boldsymbol{q}, \boldsymbol{p}, \boldsymbol{n})\rangle \\
&= V(\boldsymbol{q}) + \sum_{ij}\frac{1}{2}B^{ij}(\boldsymbol{q})p_i p_j + \sum_\tau \lambda^{(\tau)}(\boldsymbol{q})n^{(\tau)},
\end{aligned} \tag{16}$$

where

$$V(\boldsymbol{q}) = \mathcal{H}(\boldsymbol{q}, \boldsymbol{p}, \boldsymbol{n})|_{\boldsymbol{p}=\boldsymbol{0},\boldsymbol{n}=\boldsymbol{0}}, \tag{17}$$

$$B^{ij}(\boldsymbol{q}) = \left.\frac{\partial^2\mathcal{H}}{\partial p_i \partial p_j}\right|_{\boldsymbol{p}=\boldsymbol{0},\boldsymbol{n}=\boldsymbol{0}}, \tag{18}$$

$$\lambda^{(\tau)}(\boldsymbol{q}) = \left.\frac{\partial\mathcal{H}}{\partial n^{(\tau)}}\right|_{\boldsymbol{p}=\boldsymbol{0},\boldsymbol{n}=\boldsymbol{0}}, \tag{19}$$

represent the collective potential, inverse of the collective mass, and the chemical potential, respectively. Note that the last term in Eq. (10) can be set to zero adopting the QRPA gauge-fixing condition $d\lambda^{(\tau)}/dq^i = 0$ [45].

The basic equations of the ASCC method are invariant against point transformations of the collective coordinates (q^1, q^2). The $B^{ij}(\boldsymbol{q})$ and $C_{ij}(\boldsymbol{q})$ can be diagonalized simultaneously by a linear coordinate transformation at each point of $\boldsymbol{q} = (q^1, q^2)$. We assume that we can introduce the collective coordinate system in which the diagonal form is kept globally. Then, we can choose, without losing generality and for simplicity, the scale of the collective coordinates $\boldsymbol{q} = (q^1, q^2)$ such that the vibrational masses become unity. Consequently, the vibrational kinetic energy in the collective Hamiltonian (16) is written as

$$T_{\rm vib} = \frac{1}{2}\sum_{i=1,2}(p_i)^2 = \frac{1}{2}\sum_{i=1,2}(\dot{q}^i)^2. \tag{20}$$

C. CHFB + LQRPA equations

The basic equations of the ASCC method can be solved with an iterative procedure. This task was successfully carried out for extracting a one-dimensional (1D) collective path embedded in the TDHFB configuration space [46,47]. To determine a 2D hypersurface, however, the numerical calculation becomes too demanding at the present time. We therefore introduce practical approximations as follows: First, we ignore the curvature terms [the third terms in Eqs. (9) and (10)], which vanish at the HFB equilibrium points where $dV/dq^i = 0$, assuming that their effects are numerically small. Second, we replace the moving-frame HFB Hamiltonian $\hat{H}_M(\boldsymbol{q})$ and the moving-frame HFB state $|\phi(q^1, q^2)\rangle$ with a CHFB Hamiltonian $\hat{H}_{\rm CHFB}(\beta,\gamma)$ and a CHFB state $|\phi(\beta,\gamma)\rangle$, respectively, on the assumption that the latter two terms are good approximations to the former two terms.

The CHFB equations are given by

$$\delta\langle\phi(\beta,\gamma)|\hat{H}_{\rm CHFB}(\beta,\gamma)|\phi(\beta,\gamma)\rangle = 0, \tag{21}$$

$$\begin{aligned}
\hat{H}_{\rm CHFB}(\beta,\gamma) &= \hat{H} - \sum_\tau \lambda^{(\tau)}(\beta,\gamma)\widetilde{N}^{(\tau)} \\
&\quad - \sum_{m=0,2}\mu_m(\beta,\gamma)\hat{D}^{(+)}_{2m},
\end{aligned} \tag{22}$$

with four constraints

$$\langle\phi(\beta,\gamma)|\hat{N}^{(\tau)}|\phi(\beta,\gamma)\rangle = N_0^{(\tau)}, \quad (\tau = n, p), \tag{23}$$

$$\langle\phi(\beta,\gamma)|\hat{D}^{(+)}_{2m}|\phi(\beta,\gamma)\rangle = D^{(+)}_{2m}, \quad (m = 0, 2), \tag{24}$$

where $\hat{D}^{(+)}_{2m}$ denotes the Hermitian quadrupole operators $\hat{D}_{20}$ and $(\hat{D}_{22}+\hat{D}_{2-2})/2$ for $m=0$ and 2, respectively (see Ref. [46] for their explicit expressions). We define the quadrupole deformation variables (β,γ) in terms of the expectation values of the quadrupole operators

$$\beta\cos\gamma = \eta D^{(+)}_{20} = \eta\,\langle\phi(\beta,\gamma)|\,\hat{D}^{(+)}_{20}\,|\phi(\beta,\gamma)\rangle\,, \quad (25)$$

$$\frac{1}{\sqrt{2}}\beta\sin\gamma = \eta D^{(+)}_{22} = \eta\,\langle\phi(\beta,\gamma)|\,\hat{D}^{(+)}_{22}\,|\phi(\beta,\gamma)\rangle\,, \quad (26)$$

where η is a scaling factor (to be discussed in Sec. III A).

The moving-frame QRPA Eqs. (9) and (10) then reduce to

$$\delta\,\langle\phi(\beta,\gamma)|\,[\hat{H}_{\rm CHFB}(\beta,\gamma),\,\hat{Q}^i(\beta,\gamma)] - \frac{1}{i}\hat{P}_i(\beta,\gamma)\,|\phi(\beta,\gamma)\rangle = 0, \quad (i=1,2), \quad (27)$$

and

$$\delta\,\langle\phi(\beta,\gamma)|\left[\hat{H}_{\rm CHFB}(\beta,\gamma),\,\frac{1}{i}\hat{P}_i(\beta,\gamma)\right] - C_i(\beta,\gamma)\hat{Q}^i(\beta,\gamma)|\phi(\beta,\gamma)\rangle = 0. \quad (i=1,2) \quad (28)$$

Here the infinitesimal generators, $\hat{Q}^i(\beta,\gamma)$ and $\hat{P}_i(\beta,\gamma)$, are local operators defined at (β,γ) with respect to the CHFB state $|\phi(\beta,\gamma)\rangle$. These equations are solved at each point of (β,γ) to determine $\hat{Q}^i(\beta,\gamma)$, $\hat{P}_i(\beta,\gamma)$, and $C_i(\beta,\gamma)=\omega_i^2(\beta,\gamma)$. Note that these equations are valid also for regions with negative curvature $[C_i(\beta,\gamma)<0]$ where the QRPA frequency $\omega_i(\beta,\gamma)$ takes an imaginary value. We call the above equations "local QRPA (LQRPA) equations." There exist more than two solutions of LQRPA Eqs. (27) and (28) and we need to select relevant solutions. A useful criterion for selecting two collective modes among many LQRPA modes will be given in Sec. III C with numerical examples. Concerning the accuracy of the CHFB + LQRPA approximation, some arguments will be given in Sec. III F.

D. Derivation of the vibrational masses

Once the infinitesimal generators $\hat{Q}^i(\beta,\gamma)$ and $\hat{P}_i(\beta,\gamma)$ are obtained, we can derive the vibrational masses appearing in the 5D quadrupole collective Hamiltonian (1). We rewrite the vibrational kinetic energy $T_{\rm vib}$ given by Eq. (20) in terms of the time derivatives $\dot{\beta}$ and $\dot{\gamma}$ of the quadrupole deformation variables in the following way. We first note that an infinitesimal displacement of the collective coordinates (q^1,q^2) brings about a corresponding change

$$dD^{(+)}_{2m} = \sum_{i=1,2}\frac{\partial D^{(+)}_{2m}}{\partial q^i}dq^i, \quad (m=0,2), \quad (29)$$

in the expectation values of the quadrupole operators. The partial derivatives can be easily evaluated as

$$\frac{\partial D^{(+)}_{20}}{\partial q^i} = \frac{\partial}{\partial q^i}\langle\phi(\beta,\gamma)|\hat{D}^{(+)}_{20}|\phi(\beta,\gamma)\rangle = \langle\phi(\beta,\gamma)|\left[\hat{D}^{(+)}_{20},\,\frac{1}{i}\hat{P}_i(\beta,\gamma)\right]|\phi(\beta,\gamma)\rangle, \quad (30)$$

$$\frac{\partial D^{(+)}_{22}}{\partial q^i} = \frac{\partial}{\partial q^i}\langle\phi(\beta,\gamma)|\hat{D}^{(+)}_{22}|\phi(\beta,\gamma)\rangle = \langle\phi(\beta,\gamma)|\left[\hat{D}^{(+)}_{22},\,\frac{1}{i}\hat{P}_i(\beta,\gamma)\right]|\phi(\beta,\gamma)\rangle\,, \quad (31)$$

without the need of numerical derivatives. Accordingly, the vibrational kinetic energy can be written

$$T_{\rm vib} = \tfrac{1}{2}M_{00}[\dot{D}^{(+)}_{20}]^2 + M_{02}\dot{D}^{(+)}_{20}\dot{D}^{(+)}_{22} + \tfrac{1}{2}M_{22}[\dot{D}^{(+)}_{22}]^2, \quad (32)$$

with

$$M_{mm'}(\beta,\gamma) = \sum_{i=1,2}\frac{\partial q^i}{\partial D^{(+)}_{2m}}\frac{\partial q^i}{\partial D^{(+)}_{2m'}}. \quad (33)$$

Taking the time derivative of the definitional equations of (β,γ), Eqs. (25) and (26), we can straightforwardly transform expression (32) to the form in terms of $(\dot{\beta},\dot{\gamma})$. The vibrational masses $(D_{\beta\beta},\,D_{\beta\gamma},\,D_{\gamma\gamma})$ are then obtained from $(M_{00},\,M_{02},\,M_{22})$ through the following relations:

$$D_{\beta\beta} = \eta^{-2}\left(M_{00}\cos^2\gamma + \sqrt{2}M_{02}\sin\gamma\cos\gamma + \frac{1}{2}M_{22}\sin^2\gamma\right), \quad (34)$$

$$D_{\beta\gamma} = \beta\eta^{-2}\left[-M_{00}\sin\gamma\cos\gamma + \frac{1}{\sqrt{2}}M_{02}(\cos^2\gamma-\sin^2\gamma) + \frac{1}{2}M_{22}\sin\gamma\cos\gamma\right], \quad (35)$$

$$D_{\gamma\gamma} = \beta^2\eta^{-2}\left(M_{00}\sin^2\gamma - \sqrt{2}M_{02}\sin\gamma\cos\gamma + \frac{1}{2}M_{22}\cos^2\gamma\right). \quad (36)$$

E. Calculation of the rotational moments of inertia

We calculate the rotational moments of inertia $\mathcal{J}_k(\beta,\gamma)$ using the LQRPA equation for the collective rotation [46] at each CHFB state

$$\delta\,\langle\phi(\beta,\gamma)|\,[\hat{H}_{\rm CHFB},\,\hat{\Psi}_k] - \frac{1}{i}(\mathcal{J}_k)^{-1}\hat{I}_k\,|\phi(\beta,\gamma)\rangle = 0, \quad (37)$$

$$\langle\phi(\beta,\gamma)|\,[\hat{\Psi}_k(\beta,\gamma),\,\hat{I}_{k'}]\,|\phi(\beta,\gamma)\rangle = i\delta_{kk'}, \quad (38)$$

where $\hat{\Psi}_k(\beta,\gamma)$ and $\hat{I}_k$ represent the rotational angle and the angular momentum operators with respect to the principal axes associated with the CHFB state $|\phi(\beta,\gamma)\rangle$. This is an extension of the Thouless-Valatin equation [48] for the HFB equilibrium state to nonequilibrium CHFB states. The three moments of inertia can be written as

$$\mathcal{J}_k(\beta,\gamma) = 4\beta^2 D_k(\beta,\gamma)\sin^2\gamma_k \quad (k=1,2,3), \quad (39)$$

with $\gamma_k=\gamma-(2\pi k/3)$. If the inertial functions $D_k(\beta,\gamma)$ above are replaced with a constant, then $\mathcal{J}_k(\beta,\gamma)$ reduces to the well-known irrotational moments of inertia. In fact, however, we shall see that their (β,γ) dependence is very important. We call $\mathcal{J}_k(\beta,\gamma)$ and $D_k(\beta,\gamma)$ determined by the above equation "LQRPA moments of inertia" and "LQRPA rotational masses," respectively.

F. Collective Schrödinger equation

Quantizing the collective Hamiltonian (1) with the Pauli prescription, we obtain the collective Schrödinger equation [2]

$$\{\hat{T}_{\rm vib} + \hat{T}_{\rm rot} + V\}\Psi_{\alpha IM}(\beta,\gamma,\Omega) = E_{\alpha I}\Psi_{\alpha IM}(\beta,\gamma,\Omega), \quad (40)$$

where

$$\begin{aligned}\hat{T}_{\rm vib} = &-\frac{1}{2\sqrt{WR}}\left\{\frac{1}{\beta^4}\left[\left(\partial_\beta\beta^2\sqrt{\frac{R}{W}}D_{\gamma\gamma}\partial_\beta\right)\right.\right.\\ &\left.-\partial_\beta\left(\beta^2\sqrt{\frac{R}{W}}D_{\beta\gamma}\partial_\gamma\right)\right]\\ &+\frac{1}{\beta^2\sin 3\gamma}\left[-\partial_\gamma\left(\sqrt{\frac{R}{W}}\sin 3\gamma D_{\beta\gamma}\partial_\beta\right)\right.\\ &\left.\left.+\partial_\gamma\left(\sqrt{\frac{R}{W}}\sin 3\gamma D_{\beta\beta}\partial_\gamma\right)\right]\right\}, \quad (41)\end{aligned}$$

$$\hat{T}_{\rm rot} = \sum_{k=1}^{3}\frac{\hat{I}_k^2}{2\mathcal{J}_k}, \quad (42)$$

with

$$R(\beta,\gamma) = D_1(\beta,\gamma)D_2(\beta,\gamma)D_3(\beta,\gamma), \quad (43)$$

$$W(\beta,\gamma) = \{D_{\beta\beta}(\beta,\gamma)D_{\gamma\gamma}(\beta,\gamma) - [D_{\beta\gamma}(\beta,\gamma)]^2\}\beta^{-2}. \quad (44)$$

The collective wave function in the laboratory frame $\Psi_{\alpha IM}(\beta,\gamma,\Omega)$ is a function of β, γ, and a set of three Euler angles Ω. It is specified by the total angular momentum I, its projection onto the z axis in the laboratory frame M, and α that distinguishes the eigenstates possessing the same values of I and M. With the rotational wave function $\mathcal{D}^I_{MK}(\Omega)$, it is written as

$$\Psi_{\alpha IM}(\beta,\gamma,\Omega) = \sum_{K={\rm even}}\Phi_{\alpha IK}(\beta,\gamma)\langle\Omega|IMK\rangle, \quad (45)$$

where

$$\langle\Omega|IMK\rangle = \sqrt{\frac{2I+1}{16\pi^2(1+\delta_{k0})}}\left[\mathcal{D}^I_{MK}(\Omega) + (-)^I\mathcal{D}^I_{M-K}(\Omega)\right]. \quad (46)$$

The vibrational wave functions in the body-fixed frame $\Phi_{\alpha IK}(\beta,\gamma)$ are normalized as

$$\int d\beta d\gamma|\Phi_{\alpha I}(\beta,\gamma)|^2|G(\beta,\gamma)|^{\frac{1}{2}} = 1, \quad (47)$$

where

$$|\Phi_{\alpha I}(\beta,\gamma)|^2 \equiv \sum_{K={\rm even}}|\Phi_{\alpha IK}(\beta,\gamma)|^2, \quad (48)$$

and the volume element $|G(\beta,\gamma)|^{\frac{1}{2}}d\beta d\gamma$ is given by

$$|G(\beta,\gamma)|^{\frac{1}{2}}d\beta d\gamma = 2\beta^4\sqrt{W(\beta,\gamma)R(\beta,\gamma)}\sin 3\gamma d\beta d\gamma. \quad (49)$$

Thorough discussions of their symmetries and the boundary conditions for solving the collective Schrödinger equation are given in Refs. [1–3].

III. CALCULATION OF THE COLLECTIVE POTENTIAL AND THE COLLECTIVE MASSES

A. Details of numerical calculation

The CHFB + LQRPA method outlined in the preceding section may be used in conjunction with any effective interaction (e.g., density-dependent effective interactions like Skyrme forces or modern nuclear density functionals). In this article, as a first step toward such calculations, we use a version of the P + Q force model [38,39] that includes the quadrupole-pairing interaction in addition to the monopole-pairing interaction. Inclusion of the quadrupole-pairing is essential because neither the monopole-pairing nor the quadrupole particle-hole interaction contributes to the time-odd mean-field effects on the collective masses [16]; that is, only the quadrupole-pairing interaction induces the time-odd contribution in the present model. Note that the quadrupole-pairing effects were not considered in Ref. [16]. In the numerical calculation for ^{68,70,72}Se presented in the following, we use the same notations and parameters as in our previous work [47]. The shell model space consists of two major shells ($N_{\rm sh} = 3, 4$) for neutrons and protons and the spherical single-particle energies are calculated using the modified oscillator potential [49,50]. The monopole-pairing interaction strengths (for neutrons and protons) $G_0^{(\tau)}$ and the quadrupole-particle-hole interaction strength χ are determined such that the magnitudes of the quadrupole deformation β and the monopole-pairing gaps (for neutrons and protons) at the oblate and prolate local minima in ^{68}Se approximately reproduce those obtained in the Skyrme-HFB calculations [51]. The interaction strengths for ^{70}Se and ^{72}Se are then determined assuming simple mass-number dependence [39]; $G_0^{(\tau)} \sim A^{-1}$ and $\chi' \equiv \chi b^4 \sim A^{-\frac{5}{3}}$ (b denotes the oscillator-length parameter). For the quadrupole-pairing interaction strengths (for neutrons and protons), we use the Sakamoto-Kishimoto prescription [52] to derive the self-consistent values. Following the conventional treatment of the P + Q model [53], we ignore the Fock term so that we use the abbreviation HB (Hartree-Bogoliubov) in place of HFB in the following. In the case of the conventional P + Q model, the HB equation reduces to a simple Nilsson + BCS equation (see, e.g., Ref. [37]). The presence of the quadrupole-pairing interaction in our case does not allow such a reduction, however, and we directly solve the HB equation. In the P + Q model, the scaling factor η in Eqs. (25) and (26) is given by $\eta = \chi'/\hbar\omega_0 b^2$, where ω_0 denotes the frequency of the harmonic-oscillator potential. Effective charges $(e_n, e_p) = (0.4, 1.4)$ are used in the calculation of quadrupole transitions and moments.

To solve the CHB + LQRPA equations on the (β,γ) plane, we employ a 2D mesh consisting of 3600 points in the region $0 < \beta < 0.6$ and $0^\circ < \gamma < 60^\circ$. Each mesh point (β_i, γ_j) is represented as

$$\beta_i = (i - 0.5) \times 0.01, \quad (i = 1, \ldots, 60), \quad (50)$$

$$\gamma_j = (j - 0.5) \times 1^\circ, \quad (j = 1, \ldots, 60). \quad (51)$$

One of the advantages of the present approach is that we can solve the CHB + LQRPA equations independently at each

mesh point on the (β,γ) plane, so that it is suited to parallel computation.

Finally, we summarize the most important differences between the present approach and the Baranger-Kumar approach [43]. First, as repeatedly emphasized, we introduce the LQRPA collective massess in place of the cranking masses. Second, we take into account the quadrupole-pairing force (in addition to the monopole-pairing force), which brings about the time-odd effects on the collective masses. Third, we exactly solve the CHB self-consistent problem, Eq. (21), at every point on the (β, γ) plane using the gradient method, while in the Baranger-Kumar works the CHB Hamiltonian is replaced with a Nilsson-like single-particle model Hamiltonian. Fourth, we do not introduce the so-called core contributions to the collective masses, although we use the effective charges to renormalize the core polarization effects (outside of the model space consisting of two major shells) into the quadrupole operators, We shall see that we can well reproduce the major characteristics of the experimental data without introducing such core contributions to the collective masses. Fifth, most importantly, the theoretical framework developed in this article is quite general, that is, it can be used in conjunction with modern density functionals going far beyond the P + Q force model.

B. Collective potentials and pairing gaps

We show in Fig. 1 the collective potentials $V(\beta,\gamma)$ calculated for ^{68,70,72}Se. It is seen that two local minima always appear both at the oblate ($\gamma = 60^\circ$) and prolate ($\gamma = 0^\circ$) shapes and, in all these nuclei, the oblate minimum is lower than the prolate minimum. The energy difference between them is, however, only several hundred keV and the potential barrier is low in the direction of the triaxial shape (with respect to γ) indicating the γ-soft character of these nuclei. In Fig. 1 we also show the collective paths (connecting the oblate and prolate minima) determined by using the 1D version of the ASCC method [47]. It is seen that they always run through the triaxial valley and never go through the spherical shape.

In Fig. 2, the monopole-pairing and quadrupole-pairing gaps calculated for ^{68}Se are displayed. They show a significant (β,γ) dependence. Broadly speaking, the monopole pairing decreases while the quadrupole pairing increases as β increases.

C. Properties of the LQRPA modes

In Fig. 3 the frequencies squared $\omega_i^2(\beta,\gamma)$ of various LQRPA modes calculated for ^{68}Se are plotted as functions of β and γ. In the region of the (β,γ) plane where the collective potential energy is less than about 5 MeV, we can easily identify two collective modes among many LQRPA modes, whose $\omega_i^2(\beta,\gamma)$ are much lower than those of other modes. Therefore we adopt the two lowest-frequency modes to derive the collective Hamiltonian. This result of the numerical calculation supports our assumption that there exists a 2D hypersurface associated with large-amplitude quadrupole shape vibrations, which is approximately decoupled from other degrees of freedom. The situation changes when the collective potential energy exceeds about 5 MeV and/or the monopole-pairing gap becomes small. A typical example is presented in the bottom panel of Fig. 3. It becomes hard to identify two collective modes that are well separated from other modes when $\beta > 0.4$, where the collective potential energy is high (see Fig. 1) and the monopole-pairing gap becomes small (see Fig. 2). In this example, the second-lowest LQRPA mode in the $0.4 < \beta < 0.5$ region has pairing-vibrational character, but becomes noncollective for $\beta > 0.5$. In fact, many noncollective two-quasiparticle modes appear in its neighborhood. This region in the (β,γ) plane is not important, however, because only tails of the collective wave function enter into this region.

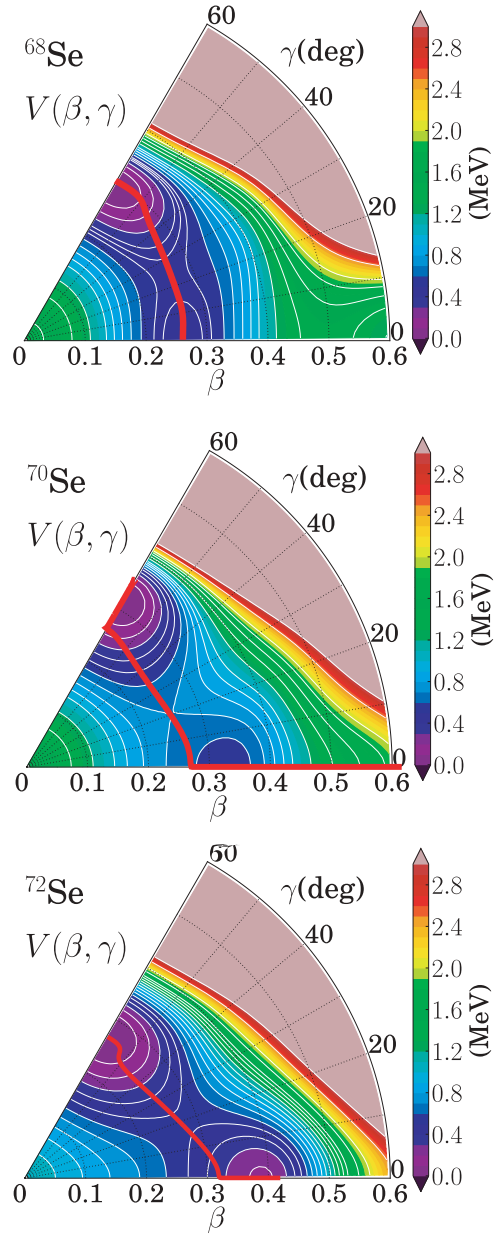

FIG. 1. (Color online) Collective potential $V(\beta,\gamma)$ for ^{68,70,72}Se. The regions higher than 3 MeV (measured from the oblate HB minima) are drawn by the rose-brown color. 1D collective paths connecting the oblate and prolate local minima are determined by using the ASCC method and depicted with bold red lines.

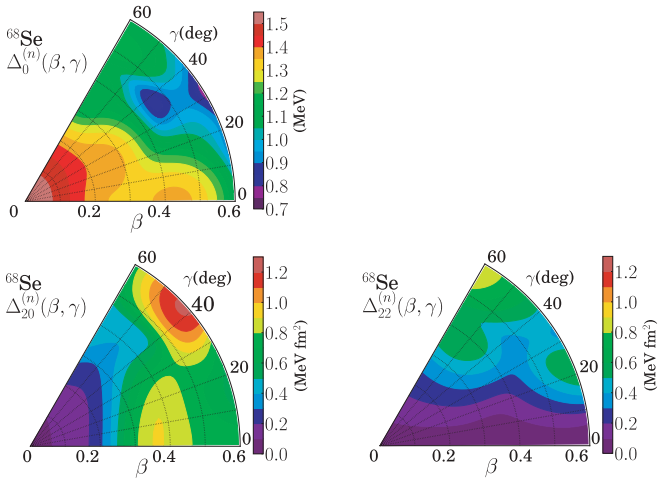

FIG. 2. (Color online) Monopole-pairing and quadrupole-pairing gaps for neutrons of ^{68}Se are plotted in the (β,γ) deformation plane. (upper left) Monopole pairing gap $\Delta_0^{(n)}$. (lower left) Quadrupole pairing gap $\Delta_{20}^{(n)}$. (lower right) Quadrupole pairing gap $\Delta_{22}^{(n)}$. See Ref. [46] for definitions of $\Delta_0^{(n)}$, $\Delta_{20}^{(n)}$, and $\Delta_{22}^{(n)}$.

It may be useful to set up a prescription that works even in a difficult situation where it is not apparent how to choose two collective LQRPA modes. We find that the following prescription always works well for selecting two collective modes among many LQRPA modes. This may be called a minimal metric criterion. At each point on the (β,γ) plane, we evaluate the vibrational part of the metric $W(\beta,\gamma)$ given by Eq. (44) for all combinations of two LQRPA modes, and find the pair that gives the minimum value. We show in Fig. 4 how this prescription actually works. In this figure, the $W(\beta,\gamma)$ values are plotted as functions of β and γ for many pairs of the LQRPA modes. In the situations where the two lowest-frequency LQRPA modes are well separated from other modes, this prescription gives the same results as choosing the two lowest-frequency modes (see the top and middle panels). However, a pair of the LQRPA modes different from the lowest two modes is chosen by this prescription in the region mentioned previously (the bottom panel). This choice may be better than that using the lowest-frequency criterion because we often find that a normal mode of pairing vibrational character becomes the second-lowest LQRPA mode when the monopole-pairing gap significantly decreases in the region of large β. The small values of the vibrational metric implies that the direction of the infinitesimal displacement associated with the pair of the LQRPA modes has a large projection onto the (β,γ) plane. Therefore, this prescription may be well suited to our purpose of deriving the collective Hamiltonian for the (β,γ) variables. It remains as an interesting open question for the future to examine whether or not the explicit inclusion of the pairing vibrational degree of freedom as another collective variable will give us a better description in such situations.

D. Vibrational masses

In Fig. 5 the vibrational masses calculated for ^{68}Se are displayed. We see that their values exhibit a significant

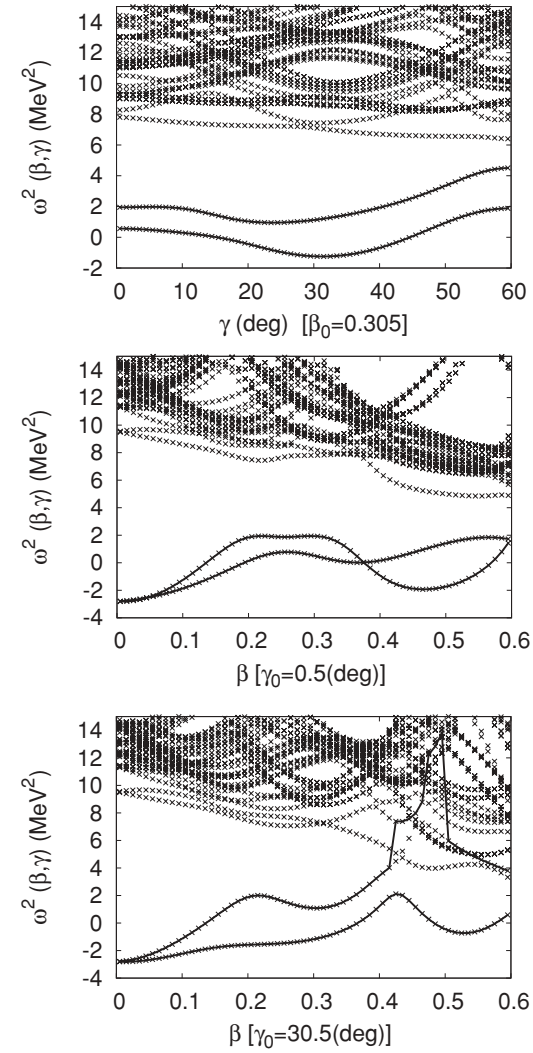

FIG. 3. Frequencies squared ω^2 of the LQRPA modes calculated for ^{68}Se are plotted as functions of β or γ. The LQRPA modes adopted for calculation of the vibrational masses are connected with solid lines. (top) Dependence on γ at $\beta = 0.3$. (middle) Dependence on β along the $\gamma = 0.5^\circ$ line. (bottom) Dependence on β along the $\gamma = 30.5^\circ$ line.

variation in the (β,γ) plane. In particular, the increase in the large β region is remarkable.

Figure 6 shows how the ratios of the LQRPA vibrational masses to the IB vibrational masses vary on the (β,γ) plane. It is clearly seen that the LQRPA vibrational masses are considerably larger than the IB vibrational masses and their ratios change depending on β and γ. In this calculation, the IB vibrational masses are evaluated using the well-known formula

$$D^{(\mathrm{IB})}_{\xi_i\xi_j}(\beta,\gamma) = 2\sum_{\mu\bar{\nu}} \frac{\langle\mu\bar{\nu}|\,\frac{\partial\hat{H}_{\mathrm{CHB}}}{\partial\xi_i}\,|0\rangle\,\langle 0|\,\frac{\partial\hat{H}_{\mathrm{CHB}}}{\partial\xi_j}\,|\mu\bar{\nu}\rangle}{[E_\mu(\beta,\gamma)+E_{\bar{\nu}}(\beta,\gamma)]^3}, \quad (\xi_i = \beta \text{ or } \gamma), \tag{52}$$

where $E_\mu(\beta,\gamma)$, $|0\rangle$, and $|\mu\bar{\nu}\rangle$ denote the quasiparticle energy, the CHB state $|\phi(\beta,\gamma)\rangle$, and the two-quasiparticle state

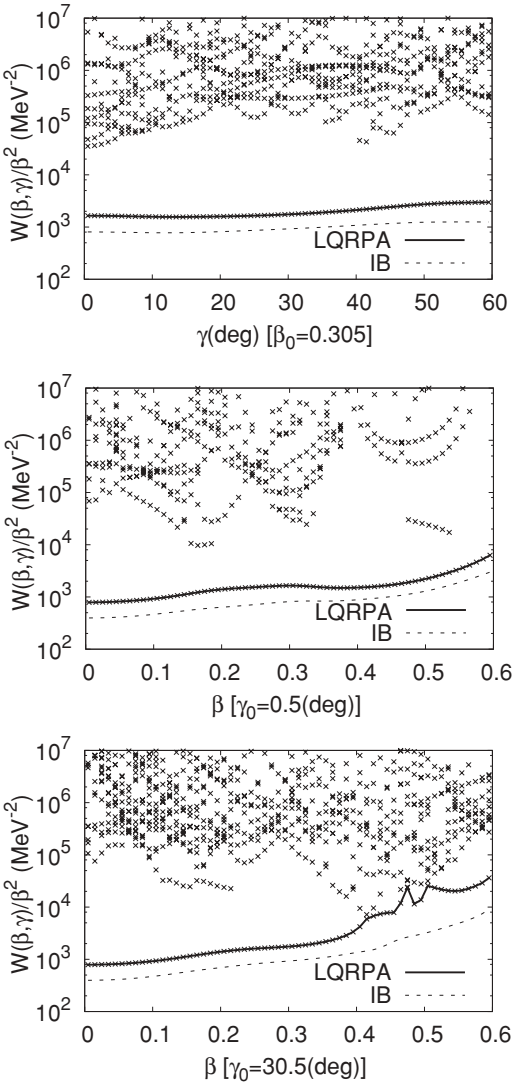

FIG. 4. Dependence on β and γ of the vibrational part of the metric $W(\beta,\gamma)$ calculated for ^{68}Se. (top) Dependence on γ at $\beta = 0.3$. (middle) Dependence on β along the $\gamma = 0.5^\circ$ line. (bottom) Dependence on β along the $\gamma = 30.5^\circ$ line. The cross symbols indicate values of the vibrational metric calculated for various choices of two LQRPA modes from among the lowest 40 LQRPA modes; the lowest mode is always chosen and the other is from the remaining 39 modes. The smallest vibrational metric is shown by solid line. For reference, the vibrational metric calculated using the IB vibrational mass is indicated by broken lines.

$a^\dagger_\mu a^\dagger_{\bar\nu}|\phi(\beta,\gamma)\rangle$, respectively (see Ref. [46] for the meaning of the indices μ and $\bar\nu$).

The vibrational masses calculated for ^{70,72}Se exhibit behaviors similar to those for ^{68}Se.

E. Rotational masses

In Fig. 7, the LQRPA rotational masses $D_k(\beta,\gamma)$ calculated for ^{68}Se are displayed. Similarly to the vibrational masses discussed previously, the LQRPA rotational masses also exhibit a remarkable variation over the (β,γ) plane, indicating a significant deviation from the irrotational property.

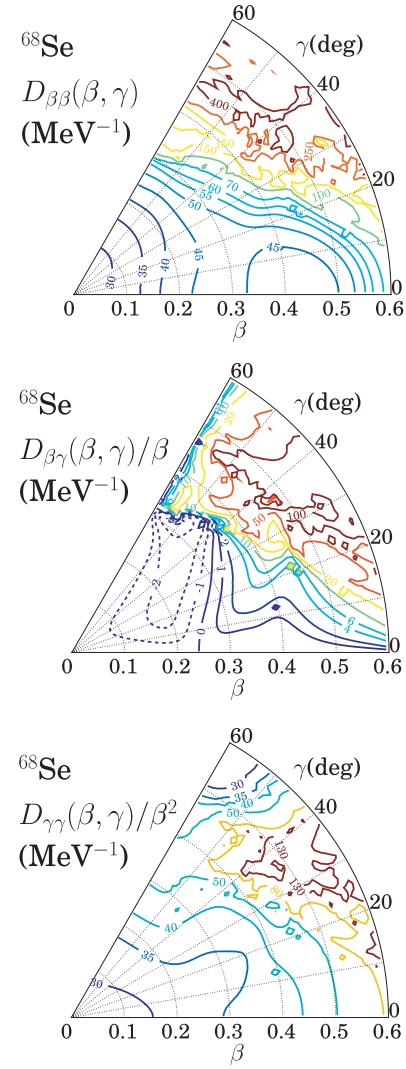

FIG. 5. (Color online) Vibrational masses $D_{\beta\beta}(\beta,\gamma)$, $D_{\beta\gamma}(\beta,\gamma)/\beta$, and $D_{\gamma\gamma}(\beta,\gamma)/\beta^2$, in units of MeV^{-1} calculated for ^{68}Se.

Figure 8 shows how the ratios of the LQRPA rotational masses $D_k(\beta,\gamma)$ to the IB cranking masses $D_k^{(\mathrm{IB})}(\beta,\gamma)$ vary on the (β,γ) plane. The rotational masses calculated for ^{70,72}Se exhibit behaviors similar to those for ^{68}Se.

As we have seen in Figs. 5 through 8, not only the vibrational and rotational masses, but also their ratios to the IB cranking masses exhibit an intricate dependence on β and γ. For instance, it is clearly seen that the ratios, $D_k(\beta,\gamma)/D_k^{(\mathrm{IB})}(\beta,\gamma)$, gradually increase as β decreases. This result is consistent with the calculation by Hamamoto and Nazarewicz [54], where it is shown that the ratio of the Migdal term to the cranking term in the rotational moment of inertia (about the first axis) increases as β decreases. Needless to say, the Migdal term (also called the Thouless-Valation correction) corresponds to the time-odd mean-field contribution taken into account in the LQRPA rotational masses so that the result of Ref. [54] implies that the ratio $D_1(\beta,\gamma)/D_1^{(\mathrm{IB})}(\beta,\gamma)$, increases

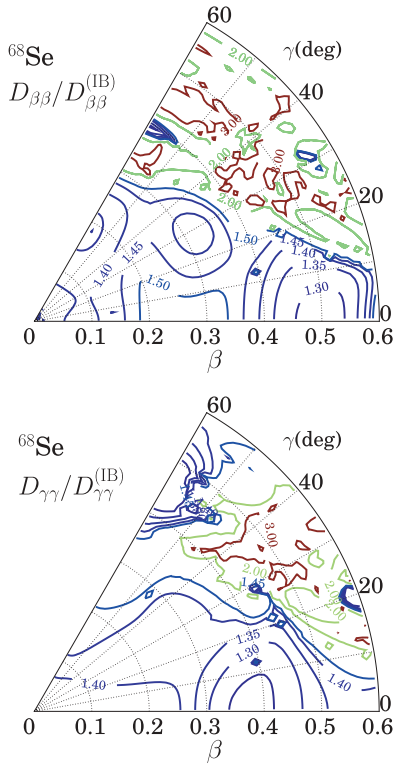

FIG. 6. (Color online) Ratios of the LQRPA vibrational masses to the IB vibrational masses $D_{\beta\beta}/D^{(\mathrm{IB})}_{\beta\beta}$ and $D_{\gamma\gamma}/D^{(\mathrm{IB})}_{\gamma\gamma}$, calculated for ^{68}Se.

as β decreases, in agreement with our result. To understand this behavior, it is important to note that, in the present calculation, the dynamical effect of the time-odd mean-field on $D_1(\beta,\gamma)$ is associated with the $K = 1$ component of the quadrupole-pairing interaction and it always works and increase the rotational masses, in contrast to the behavior of the static quantities like the magnitude of the quadrupole-pairing gaps Δ_{20} and Δ_{22}, which diminish in the spherical shape limit. Obviously, this qualitative feature holds true irrespective of the details of our choice of the monopole-pairing and quadrupole-pairing interaction strengths.

The previous results of the calculation obviously indicate the need to take into account the time-odd contributions to the vibrational and rotational masses by going beyond the IB cranking approximation. In Refs. [29–32], a phenomenological prescription is adopted to remedy the shortcoming of the IB cranking masses; that is, a constant factor in the range 1.40–1.45 is multiplied to the IB rotational masses. This prescription is, however, insufficient in the following points. First, the scaling only of the rotational masses (leaving the vibrational masses aside) violates the symmetry requirement for the 5D collective quadrupole Hamiltonian [1–3] (a similar comment is made in Ref. [4]). Second, the ratios take different values for different LQRPA collective masses ($D_{\beta\beta}$, $D_{\beta\gamma}$, $D_{\gamma\gamma}$, D_1, D_2, and D_3). Third, for every collective mass, the ratio exhibits an intricate dependence on β and γ. Thus, it may be quite insufficient to simulate the time-odd mean-field contributions to the collective masses by scaling the IB cranking masses with a common multiplicative factor.

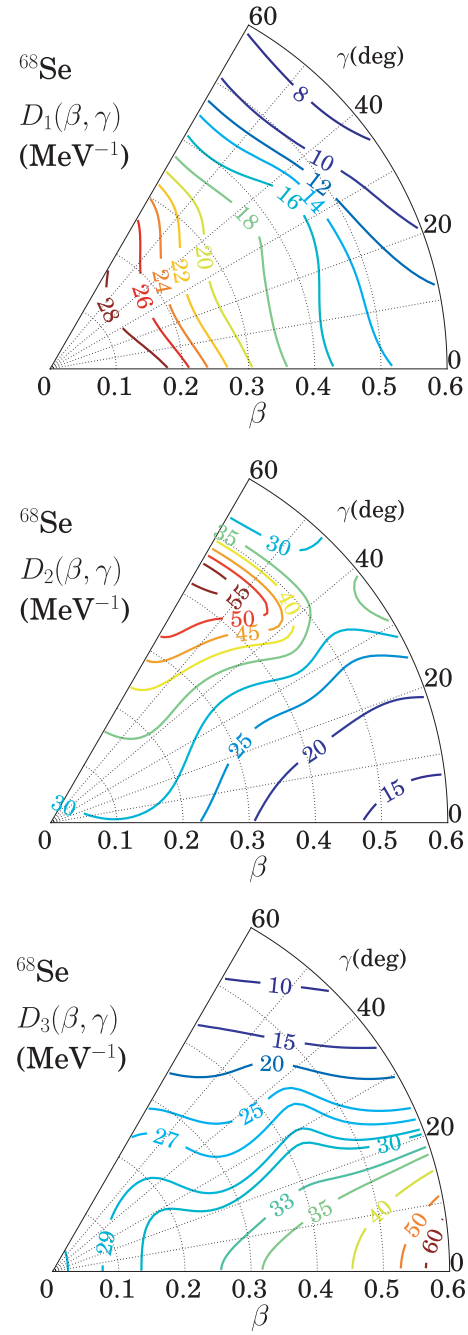

FIG. 7. (Color online) Rotational masses $D_k(\beta,\gamma)$ in units of MeV^{-1}, calculated for ^{68}Se. See Eq. (39) for the relation with the rotational moments of inertia $\mathcal{J}_k(\beta,\gamma)$.

F. Check of self-consistency along the collective path

As discussed in Sec. II, the CHB + LQRPA method is a practical approximation to the ASCC method. It is certainly desirable to examine the accuracy of this approximation by carrying out a fully self-consistent calculation. Although, at the present time, such a calculation is too demanding to carry out for a whole region of the (β,γ) plane, we can check the accuracy at least along the 1D collective path. This is because the 1D collective path is determined by carrying out a fully self-consistent ASCC calculation for a single set of the

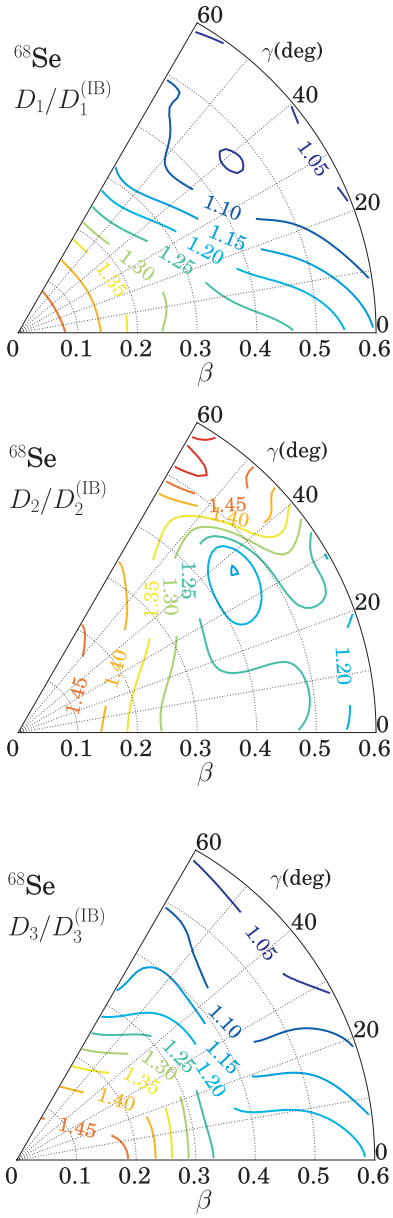

FIG. 8. (Color online) Ratios of the LQRPA rotational masses to the IB rotational masses, $D_k(\beta,\gamma)/D_k^{(\mathrm{IB})}(\beta,\gamma)$, calculated for ^{68}Se.

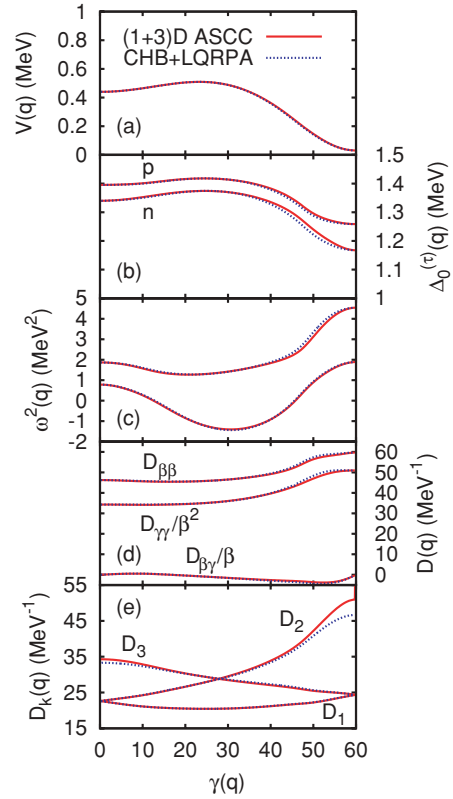

FIG. 9. (Color online) Comparison of physical quantities evaluated with the CHB + LQRPA approximation and those with the ASCC method. Both calculations are carried out along the 1D collective path for ^{68}Se and the results are plotted as a function of $\gamma(q)$. From the top to the bottom: (a) the collective potential, (b) monopole-pairing gaps, $\Delta_0^{(n)}$ and $\Delta_0^{(p)}$, for neutrons and protons, (c) frequencies squared ω^2 of the lowest and the second-lowest modes obtained by solving the moving-frame QRPA and the LQRPA equations, and (d) vibrational masses, $D_{\beta\beta}$, $D_{\beta\gamma}/\beta$, and $D_{\gamma\gamma}/\beta^2$, and (e) rotational masses D_k. In almost all cases, the results of the two calculations are indistinguishable because they agree within the widths of the line.

collective coordinate and momentum. The 1D collective paths projected onto the (β,γ) plane are displayed in Fig. 1. Let us use a notation $|\phi(q)\rangle$ for the moving-frame HB state obtained by self-consistently solving the ASCC equations for a single collective coordinate q [46,47]. To distinguish from it, we write the CHB state as $|\phi(\beta(q),\gamma(q))\rangle$. This notation means that the values of β and γ are specified by the collective coordinate q along the collective path. In other words, $|\phi(\beta(q),\gamma(q))\rangle$ has the same expectation values of the quadrupole operator as those of $|\phi(q)\rangle$. It is important to note, however, that they are different from each other because $|\phi(\beta(q),\gamma(q))\rangle$ is a solution of the CHB equation, which is an approximation of the moving-frame HB equation. Let us evaluate various physical quantities using the two state vectors and compare the results.

In Fig. 9 various physical quantities (the pairing gaps, the collective potential, the frequencies of the local normal modes, the rotational masses, and vibrational masses) calculated using the moving-frame HB state $|\phi(q)\rangle$ and the CHB state $|\phi(\beta(q),\gamma(q))\rangle$ are presented and compared. These calculations are carried out along the 1D collective path for ^{68}Se. Apparently, the results of the two calculations are indistinguishable in almost all cases because they agree within the widths of the line. This good agreement implies that the CHB + LQRPA is an excellent approximation to the ASCC method along the collective path on the (β,γ) plane. As we shall see in the next section, collective wave functions distribute around the collective path. Therefore, it may be reasonable to expect that the CHB + LQRPA method is a good approximation to the ASCC method and suited, at least, for describing the oblate-prolate shape mixing dynamics in ^{68,70,72}Se.

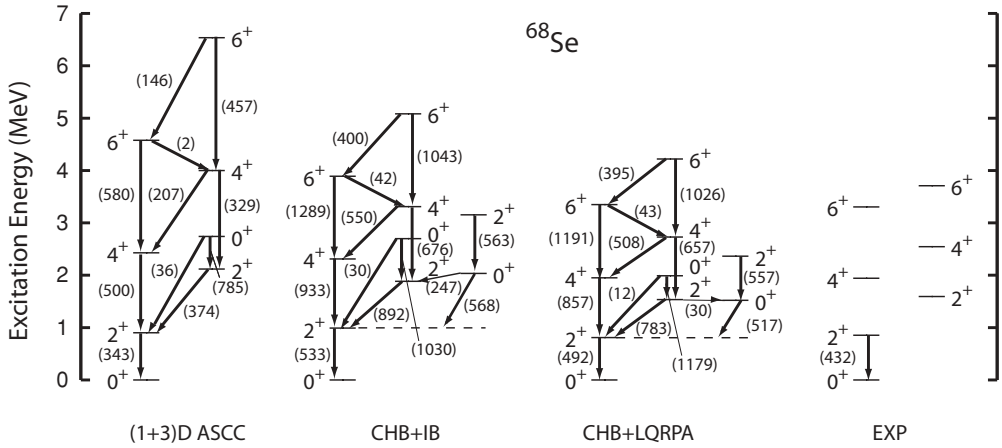

FIG. 10. Excitation spectra and $B(E2)$ values calculated for ^{68}Se by means of the CHB + LQRPA method (denoted CHB + LQRPA) and experimental data [5–7]. For comparison, results calculated using the IB cranking masses (denoted CHB + IB) and those obtained using the (1 + 3)D version of the ASCC method [denoted (1 + 3)D ASCC] are also shown. Only $B(E2)$'s larger than 1 Weisskopf unit [in the (1+3)D ASCC and/or the CHB + LQRPA calculations] are shown in units of e^2fm^4.

IV. LARGE-AMPLITUDE SHAPE-MIXING PROPERTIES OF ^{68,70,72}Se

We calculated collective wave functions solving the collective Schrödinger equation (40) and evaluated excitation spectra, quadrupole transition probabilities, and spectroscopic quadrupole moments. The results for low-lying states in ^{68,70,72}Se are presented in Figs. 10–15.

In Figs. 10, 12, and 14, excitation spectra and $B(E2)$ values for ^{68}Se, ^{70}Se, and ^{72}Se, calculated with the CHB + LQRPA method, are displayed together with the experimental data. The eigenstates are labeled with $I^\pi = 0^+, 2^+, 4^+$, and 6^+. In these figures, results obtained using the IB cranking masses are also shown for the sake of comparison. Furthermore, the results calculated with the (1 + 3)D version of the ASCC method reported in our previous article [47] are shown also for

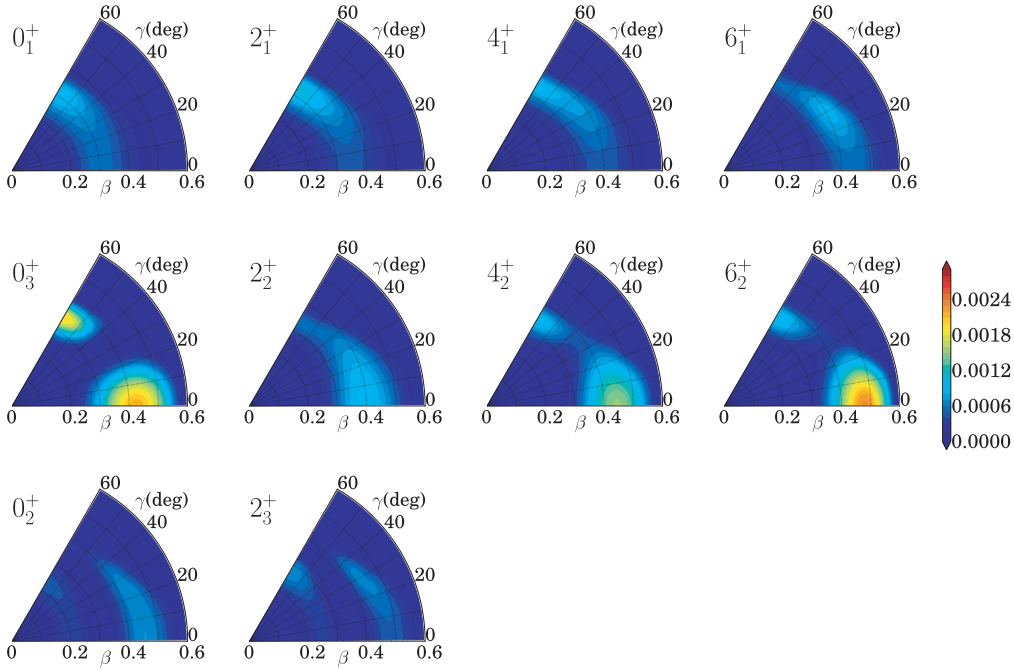

FIG. 11. (Color online) Vibrational wave functions squared $\beta^4|\Phi_{Ik}(\beta,\gamma)|^2$, calculated for ^{68}Se.

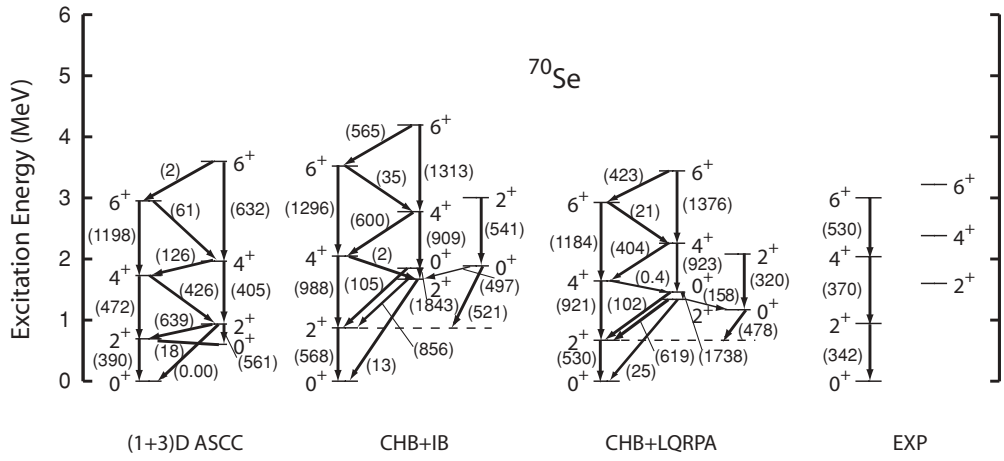

FIG. 12. Same as Fig. 10 but for ^{70}Se. Experimental data are taken from Refs. [8,41].

comparison with the 5D calculations. We use the abbreviation $(1+3)$D to indicate that a single collective coordinate along the collective path describing large-amplitude vibration and three rotational angles associated with the rotational motion are taken into account in these calculations. The classification of the calculated low-lying states into families of two or three rotational bands is made according to the properties of their vibrational wave functions. These vibrational wave functions are displayed in Figs. 11, 13, and 15. In these figures, only the β^4 factor in the volume element (49) are multiplied to the vibrational wave functions squared leaving the $\sin 3\gamma$ factor aside. This is because all vibrational wave functions look triaxial and the probability at the oblate and prolate shapes vanish if the $\sin 3\gamma$ factor is multiplied by them.

Let us first summarize the results of the CHB + LQRPA calculation. The most conspicuous feature of the low-lying states in these proton-rich Se isotopes is the dominance of the large-amplitude vibrational motion in the triaxial shape degree of freedom. In general, the vibrational wave function

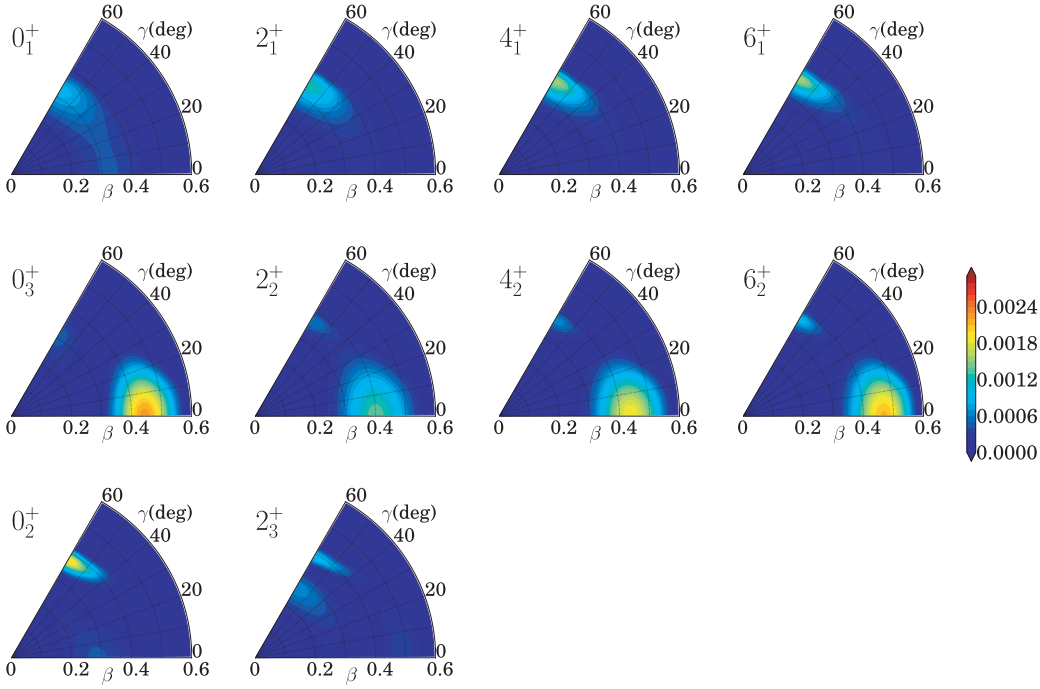

FIG. 13. (Color online) Same as Fig. 11 but for ^{70}Se.

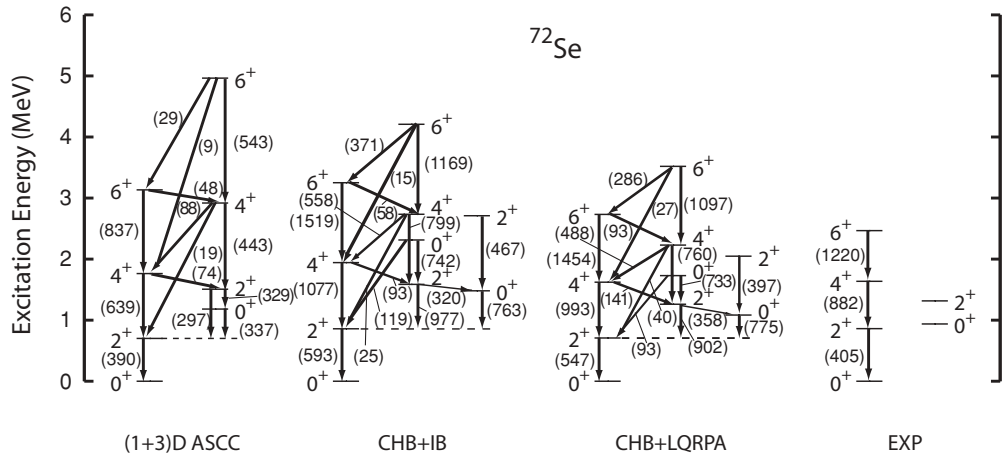

FIG. 14. Same as Fig. 10 but for ^{72}Se. Experimental data are taken from Refs. [8,42].

extends over the triaxial region between the oblate ($\gamma = 60^\circ$) and the prolate ($\gamma = 0^\circ$) shapes. In particular, this is the case for the 0^+ states causing their peculiar behaviors; for instance, we obtain two excited 0^+ states located slightly below or above the 2_2^+ state. Relative positions between these excited states are quite sensitive to the interplay of large-amplitude γ-vibrational modes and the β-vibrational modes. This result of the calculation is consistent with the available experimental data where the excited 0^+ state has not yet been found, but more experimental data are needed to examine the validity of the theoretical prediction. In the following, let us examine the characteristic features of the theoretical spectra more closely for individual nuclei.

For ^{68}Se, we obtain the third band in low energy. The 0_2^+ and 2_3^+ states belonging to this band are also shown in Fig. 10. Their vibrational wave functions exhibit nodes in the β direction (see Fig. 11) indicating that a β-vibrational mode is excited on top of the large-amplitude γ vibrations. As a matter of course, this kind of state is outside of the scope of the $(1 + 3)$D calculation. The vibrational wave functions

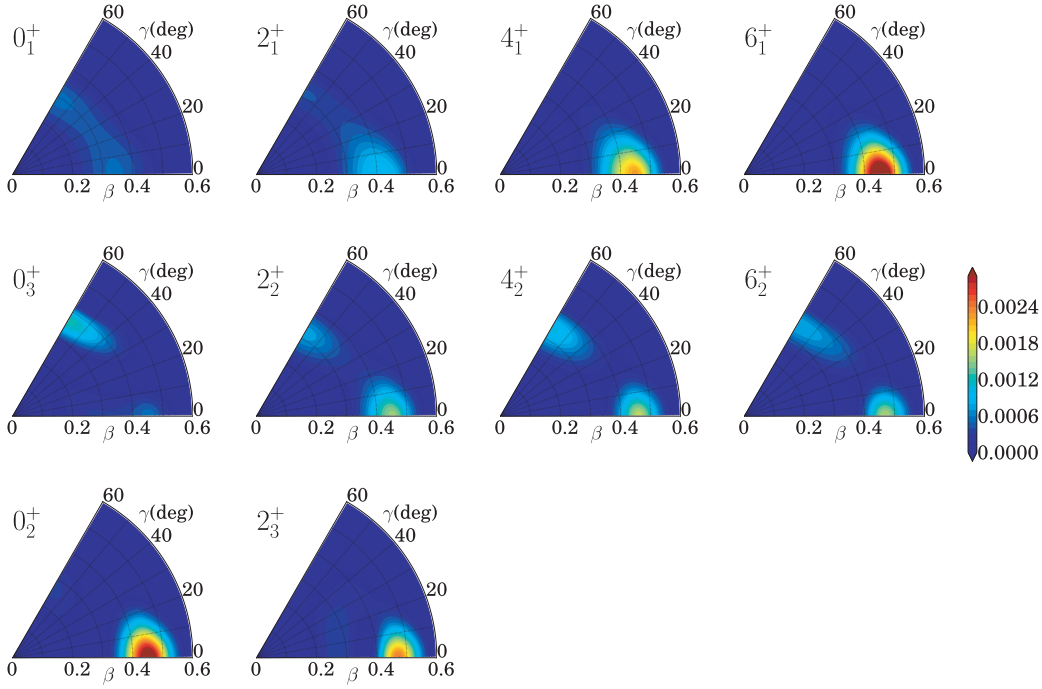

FIG. 15. (Color online) Same as Fig. 11 but for ^{72}Se.

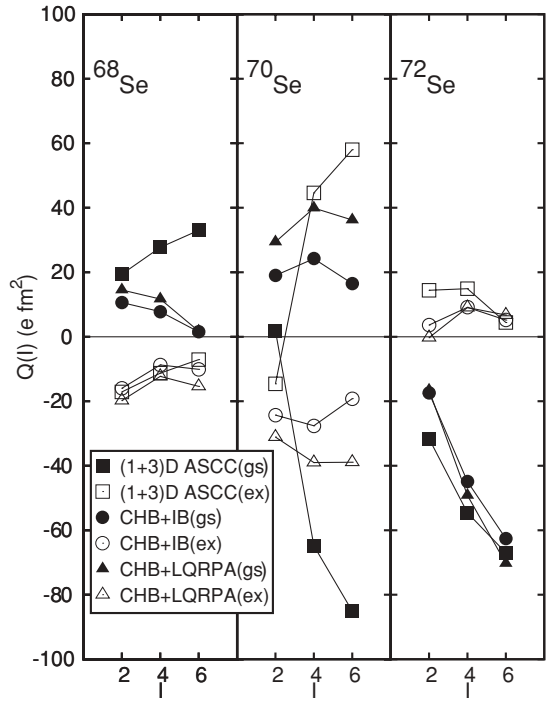

FIG. 16. Spectroscopic quadrupole moments for ^{68,70,72}Se. Values calculated with the LQRPA collective masses are shown with the triangles. For comparison, values calculated with the IB collective masses and those obtained with the $(1+3)$D version of the ASCC method are also shown with the squares and the circles, respectively. The filled symbols show the values for the yrast states, while the open symbols those for the yrare states.

of the yrast 2_1^+ and 4_1^+ states exhibit localization in a region around the oblate shape, while the yrare 2_2^+, 4_2^+, and 6_2^+ states localize around the prolate shape. It is apparent, however, that all the wave functions significantly extend from $\gamma = 0^\circ$ to 60° over the triaxial region, indicating the γ-soft character of these states. In particular, the yrare 4_2^+ and 6_2^+ wave functions exhibit a two-peak structure consisting of the prolate and oblate peaks. The peaks of the vibrational wave function gradually shift toward a region of larger β as the angular momentum increases. This is a centrifugal effect decreasing the rotational energy by increasing the moment of inertia. In the $(1+3)$D calculation, this effect is absent because the collective path is fixed at the ground state. Thus, the 5D calculation yields, for example, a much larger value for $B(E2; 6_1^+ \to 4_1^+)$ in comparison with the $(1+3)$D calculation. Actually, in the 5D CHB + LQRPA calculation, the wave function of the yrast 6_1^+ state localizes in the triaxial region (see Fig. 11) where the moment of inertia takes a maximum value. This leads to a small value for the spectroscopic quadrupole moment (see Fig. 16) because of the cancellation between the contributions from the oblate-like and prolate-like regions. This cancellation mechanism due to the large-amplitude γ fluctuation is effective also in other states; although the spectroscopic quadrupole moments of the yrast 2_1^+ and 4_1^+ (yrare 2_2^+, 4_2^+, and 6_2^+) states are positive (negative) indicating their oblate-like (prolate-like) character, their absolute magnitudes are rather small.

The $E2$-transition probabilities exhibit a pattern reminiscent of the γ-unstable situation; for instance, $B(E2; 6_2^+ \to 6_1^+)$, $B(E2; 4_2^+ \to 4_1^+)$, and $B(E2; 2_2^+ \to 2_1^+)$ are much larger than $B(E2; 6_2^+ \to 4_1^+)$, $B(E2; 4_2^+ \to 2_1^+)$, and $B(E2; 2_2^+ \to 0_1^+)$; see Fig. 10. Thus, the low-lying states in ^{68}Se may be characterized as an intermediate situation between the oblate-prolate shape coexistence and the Wilets-Jean γ-unstable model [55]. Using the phenomenological Bohr-Mottelson collective Hamiltonian, we showed in Ref. [56] that it is possible to describe the oblate-prolate shape coexistence and the γ-unstable situation in a unified way varying a few parameters controlling the degree of oblate-prolate asymmetry in the collective potential and the collective masses. The two-peak structure seen in the 4_2^+ and 6_2^+ states may be considered as one of the characteristics of the intermediate situation. It thus appears that the excitation spectrum for ^{68}Se (Fig. 10) serves as a typical example of the transitional phenomena from the γ-unstable to the oblate-prolate shape coexistence situations.

Let us make a comparison between the spectra in Fig. 10 obtained with the LQRPA collective masses and that with the IB cranking masses. It is obvious that the excitation energies are appreciably overestimated in the latter. This result is as expected from the too low values of the IB cranking masses. The result of our calculation is in qualitative agreement with the HFB-based configuration-mixing calculation reported by Ljungvall *et al.* [8] in that both calculations indicate the oblate (prolate) dominance for the yrast (yrare) band in ^{68}Se. Quite recently, the $B(E2; 2_1^+ \to 0_1^+)$ value was measured in the experiment [7]. The calculated value (492 e^2fm^4) is in fair agreement with the experimental data (432 e^2fm^4).

The result of the calculation for ^{70}Se (Figs. 12 and 13) is similar to that for ^{68}Se. The vibrational wave functions of the yrast 2_1^+, 4_1^+, and 6_1^+ states localize in a region around the oblate shape, exhibiting, at the same time, long tails in the triaxial direction. We note here that, differently from the ^{68}Se case, the 6_1^+ wave function keeps the oblate-like structure. However, the yrare 2_2^+, 4_2^+, and 6_2^+ states localize around the prolate shape, exhibiting, at the same time, small secondary bumps around the oblate shape. For the yrare 2_2^+ state, we obtain a strong oblate-prolate shape mixing in the $(1+3)$D calculation [47]. This mixing becomes weaker in the present 5D calculation, resulting in the reduction of the $B(E2; 4_1^+ \to 2_2^+)$ value. Similarly to ^{68}Se, we obtain two excited 0^+ states in low energy. We see considerable oblate-prolate shape mixings in their vibrational wave functions, but, somewhat differently from those in ^{68}Se, the second and third 0^+ states in ^{70}Se exhibit clear peaks at the oblate and prolate shapes, respectively, Their energy ordering is quite sensitive to the interplay of the large-amplitude γ vibration and the β vibrational modes. The calculated spectrum for ^{70}Se is in fair agreement with the recent experimental data [41], although the $B(E2)$ values between the yrast states are overestimated.

The result of the calculation for ^{72}Se (Figs. 14 and 15) presents a feature somewhat different from those for ^{68}Se and ^{70}Se; that is, the yrast 2_1^+, 4_1^+, and 6_1^+ states localize around the prolate shape instead of the oblate shape. The localization

develops with increasing angular momentum. Nevertheless, similarly to the ^{68,70}Se cases, the yrare 2_2^+, 4_2^+, and 6_2^+ states exhibit the two-peak structure. The spectroscopic quadrupole moments of the 2_1^+, 4_1^+, and 6_1^+ states are negative, and their absolute magnitude increases with increasing angular momentum (see Fig. 16) reflecting the developing prolate character in the yrast band, while those of the yrare states are small because of the two-peak structure of their vibrational wave functions, that is, due to the cancellation of the contributions from the prolate-like and oblate-like regions. Also for ^{72}Se, we obtain two excited 0^+ states in low energy, but they show features somewhat different from the corresponding excited 0^+ states in ^{68,70}Se. Specifically, the vibrational wave functions of the second and third 0^+ states exhibit peaks at the prolate and oblate shape, respectively. As seen in Fig. 14, our results of the calculation for the excitation energies and $B(E2)$ values are in good agreement with the recent experimental data [8] for the yrast 2_1^+, 4_1^+, and 6_1^+ states in ^{72}Se. Experimental $E2$-transition data are awaited for understanding the nature of the observed excited band.

V. CONCLUSION

On the basis of the ASCC method, we developed a practical microscopic approach, called CHFB + LQRPA, of deriving the 5D quadrupole collective Hamiltonian and confirmed its efficiency by applying it to the oblate-prolate shape coexistence/mixing phenomena in proton-rich ^{68,70,72}Se. The results of the numerical calculation for the excitation energies and $B(E2)$ values are in good agreement with the recent experimental data [7,8] for the yrast 2_1^+, 4_1^+, and 6_1^+ states in these nuclei. It is shown that the time-odd components of the moving mean-field significantly increase the vibrational and rotational collective masses and make the theoretical spectra in much better agreement with the experimental data than calculations using the IB cranking masses. Our analysis clearly indicates that low-lying states in these nuclei possess a transitional character between the oblate-prolate shape coexistence and the so-called γ-unstable situation where large-amplitude triaxial-shape fluctuations play a dominant role.

Finally, we would like to list a few issues for the future that seem particularly interesting. First, a fully self-consistent solution of the ASCC equations for determining the 2D collective hypersurface and examination of the validity of the approximations adopted in this article in the derivation of the CHFB + LQRPA scheme. Second, the application to various kinds of collective spectra associated with large-amplitude collective motions near the yrast lines (as listed in Ref. [28]). Third, the possible extension of the quadrupole collective Hamiltonian by explicitly treating the pairing vibrational degrees of freedom as additional collective coordinates. Fourth, the use of the Skyrme energy functionals + density-dependent contact pairing interaction in place of the P + Q force and then modern density functionals currently under active development. Fifth, the application of the CHFB + LQRPA scheme to fission dynamics. The LQRPA approach enables us to evaluate, without the need of numerical derivatives, the collective inertia masses including the time-odd mean-field effects.

ACKNOWLEDGMENTS

Two of the authors (K.S. and N.H.) are supported by the Junior Research Associate Program and the Special Postdoctoral Researcher Program of RIKEN, respectively. The numerical calculations were carried out on Altix3700 BX2 at Yukawa Institute for Theoretical Physics in Kyoto University and RIKEN Cluster of Clusters (RICC) facility. This work is supported by Grants-in-Aid for Scientific Research (Grants No. 20105003, 20540259, and 21340073) from the Japan Society for the Promotion of Science and the JSPS Core-to-Core Program "International Research Network for Exotic Femto Systems."

[1] A. Bohr and B. R. Mottelson, *Nuclear Structure* (Benjamin, Reading, MA, 1975), Vol. II.
[2] S. T. Belyaev, Nucl. Phys. **64**, 17 (1965).
[3] K. Kumar and M. Baranger, Nucl. Phys. A **92**, 608 (1967).
[4] L. Próchniak and S. G. Rohoziński, J. Phys. G **36**, 123101 (2009).
[5] S. M. Fischer, C. J. Lister, and D. P. Balamuth, Phys. Rev. C **67**, 064318 (2003).
[6] S. M. Fischer, D. P. Balamuth, P. A. Hausladen, C. J. Lister, M. P. Carpenter, D. Seweryniak, and J. Schwartz, Phys. Rev. Lett. **84**, 4064 (2000).
[7] A. Obertelli *et al.*, Phys. Rev. C **80**, 031304 (2009).
[8] J. Ljungvall *et al.*, Phys. Rev. Lett. **100**, 102502 (2008).
[9] D. R. Inglis, Phys. Rev. **96**, 1059 (1954).
[10] S. T. Beliaev, Nucl. Phys. **24**, 322 (1961).
[11] K. Kumar, Nucl. Phys. A **231**, 189 (1974).
[12] K. Pomorski, T. Kaniowska, A. Sobiczewski, and S. G. Rohoziński, Nucl. Phys. A **283**, 394 (1977).
[13] S. G. Rohoziński, J. Dobaczewski, B. Nerlo-Pomorska, K. Pomorski, and J. Srebrny, Nucl. Phys. A **292**, 66 (1977).
[14] J. Dudek, W. Dudek, E. Ruchowska, and J. Skalski, Z. Phys. A **294**, 341 (1980).
[15] M. Baranger and M. Véneroni, Ann. Phys. (NY) **114**, 123 (1978).
[16] J. Dobaczewski and J. Skalski, Nucl. Phys. A **369**, 123 (1981).
[17] F. Villars, Nucl. Phys. A **285**, 269 (1977).
[18] K. Goeke and P.-G. Reinhard, Ann. Phys. (NY) **112**, 328 (1978).
[19] D. J. Rowe and R. Bassermann, Can. J. Phys. **54**, 1941 (1976).
[20] T. Marumori, Prog. Theor. Phys. **57**, 112 (1977).
[21] J. Libert, M. Girod, and J.-P. Delaroche, Phys. Rev. C **60**, 054301 (1999).
[22] M. K. Pal, D. Zawischa, and J. Speth, Z. Phys. A **272**, 387 (1975).
[23] N. R. Walet, G. Do Dang, and A. Klein, Phys. Rev. C **43**, 2254 (1991).
[24] D. Almehed and N. R. Walet, Phys. Lett. B **604**, 163 (2004).
[25] T. Marumori, T. Maskawa, F. Sakata, and A. Kuriyama, Prog. Theor. Phys. **64**, 1294 (1980).
[26] M. J. Giannoni and P. Quentin, Phys. Rev. C **21**, 2060 (1980).
[27] G. D. Dang, A. Klein, and N. R. Walet, Phys. Rep. **335**, 93 (2000).
[28] K. Matsuyanagi, M. Matsuo, T. Nakatsukasa, N. Hinohara, and K. Sato, J. Phys. G **37**, 064018 (2010).

[29] T. Nikšić, D. Vretenar, G. A. Lalazissis, and P. Ring, Phys. Rev. Lett. **99**, 092502 (2007).
[30] T. Nikšić, Z. P. Li, D. Vretenar, L. Próchniak, J. Meng, and P. Ring, Phys. Rev. C **79**, 034303 (2009).
[31] Z. P. Li, T. Nikšić, D. Vretenar, J. Meng, G. A. Lalazissis, and P. Ring, Phys. Rev. C **79**, 054301 (2009).
[32] Z. P. Li, T. Nikšić, D. Vretenar, and J. Meng, Phys. Rev. C **81**, 034316 (2010).
[33] M. Girod, J.-P. Delaroche, A. Görgen, and A. Obertelli, Phys. Lett. B **676**, 39 (2009).
[34] J. P. Delaroche, M. Girod, J. Libert, H. Goutte, S. Hilaire, S. Péru, N. Pillet, and G. F. Bertsch, Phys. Rev. C **81**, 014303 (2010).
[35] M. Bender, P.-H. Heenen, and P.-G. Reinhard, Rev. Mod. Phys. **75**, 121 (2003).
[36] M. Matsuo, T. Nakatsukasa, and K. Matsuyanagi, Prog. Theor. Phys. **103**, 959 (2000).
[37] P. Ring and P. Schuck, *The Nuclear Many-Body Problem* (Springer-Verlag, Berlin, 1980).
[38] D. R. Bes and R. A. Sorensen, *Advances in Nuclear Physics* (Plenum Press, New York, 1969), Vol. 2.
[39] M. Baranger and K. Kumar, Nucl. Phys. A **110**, 490 (1968).
[40] N. Hinohara, T. Nakatsukasa, M. Matsuo, and K. Matsuyanagi, Prog. Theor. Phys. **115**, 567 (2006).
[41] G. Rainovski *et al.*, J. Phys. G **28**, 2617 (2002).
[42] R. Palit, H. C. Jain, P. K. Joshi, J. A. Sheikh, and Y. Sun, Phys. Rev. C **63**, 024313 (2001).
[43] M. Baranger and K. Kumar, Nucl. Phys. A **122**, 241 (1968).
[44] K. Kumar and M. Baranger, Nucl. Phys. A **122**, 273 (1968).
[45] N. Hinohara, T. Nakatsukasa, M. Matsuo, and K. Matsuyanagi, Prog. Theor. Phys. **117**, 451 (2007).
[46] N. Hinohara, T. Nakatsukasa, M. Matsuo, and K. Matsuyanagi, Prog. Theor. Phys. **119**, 59 (2008).
[47] N. Hinohara, T. Nakatsukasa, M. Matsuo, and K. Matsuyanagi, Phys. Rev. C **80**, 014305 (2009).
[48] D. J. Thouless and J. G. Valatin, Nucl. Phys. **31**, 211 (1962).
[49] T. Bengtsson and I. Ragnarsson, Nucl. Phys. A **436**, 14 (1985).
[50] S. G. Nilsson and I. Ragnarsson, *Shapes and Shells in Nuclear Structure* (Cambridge University Press, Cambridge, England, 1995).
[51] M. Yamagami, K. Matsuyanagi, and M. Matsuo, Nucl. Phys. A **693**, 579 (2001).
[52] H. Sakamoto and T. Kishimoto, Phys. Lett. B **245**, 321 (1990).
[53] M. Baranger and K. Kumar, Nucl. Phys. **62**, 113 (1965).
[54] I. Hamamoto and W. Nazarewicz, Phys. Rev. C **49**, 2489 (1994).
[55] L. Wilets and M. Jean, Phys. Rev. **102**, 788 (1956).
[56] K. Sato, N. Hinohara, T. Nakatsukasa, M. Matsuo, and K. Matsuyanagi, Prog. Theor. Phys. **123**, 129 (2010).

PHYSICAL REVIEW C **84**, 061302(R) (2011)

Shape fluctuations in the ground and excited 0^+ states of ^{30,32,34}Mg

Nobuo Hinohara,[1,*] Koichi Sato,[1] Kenichi Yoshida,[1,2] Takashi Nakatsukasa,[1] Masayuki Matsuo,[2] and Kenichi Matsuyanagi[1,3]

[1]*Theoretical Nuclear Physics Laboratory, RIKEN Nishina Center, Wako 351-0198, Japan*

[2]*Department of Physics, Faculty of Science, Niigata University, Niigata 950-2181, Japan*

[3]*Yukawa Institute for Theoretical Physics, Kyoto University, Kyoto 606-8502, Japan*

(Received 9 September 2011; published 15 December 2011)

Large-amplitude collective dynamics of shape phase transition in the low-lying states of $^{30-36}$Mg is investigated by solving the five-dimensional (5D) quadrupole collective Schrödinger equation. The collective masses and potentials of the 5D collective Hamiltonian are microscopically derived with use of the constrained Hartree-Fock-Bogoliubov plus local quasiparticle random phase approximation method. Good agreement with the recent experimental data is obtained for the excited 0^+ states as well as the ground bands. For ^{30}Mg, the shape coexistence picture that the deformed excited 0^+ state coexists with the spherical ground state approximately holds. On the other hand, large-amplitude quadrupole-shaped fluctuations dominate in both the ground and the excited 0^+ states in ^{32}Mg, providing a picture that is different from the interpretation of the "coexisting spherical excited 0^+ state" based on the naive inversion picture of the spherical and deformed configurations.

DOI: 10.1103/PhysRevC.84.061302 PACS number(s): 21.60.Ev, 21.10.Re, 21.60.Jz, 27.30.+t

Nuclei exhibit a variety of shapes in their ground and excited states. A feature of the quantum phase transition of a finite system is that the order parameters (shape deformation parameters) always fluctuate and vary with the particle number. Especially, the large-amplitude shape fluctuations play a crucial role in transitional (critical) regions. Spectroscopic studies of low-lying excited states in transitional nuclei are of great interest to observe such unique features of the finite quantum systems.

Low-lying states of neutron-rich nuclei at approximately $N = 20$ attract great interest, as the spherical configurations associated with the magic number disappear in the ground states. In neutron-rich Mg isotopes, the increase of the excitation energy ratio $E(4_1^+)/E(2_1^+)$ [1–3] and the enhancement of $B(E2; 2_1^+ \to 0_1^+)$ from ^{30}Mg to ^{34}Mg [4–6] indicate a kind of quantum phase transition from spherical to deformed shapes taking place around ^{32}Mg. These experiments stimulate microscopic investigations on quadrupole collective dynamics unique to this region of the nuclear chart with various theoretical approaches: the shell model [7–10], the Hartree-Fock-Bogoliubov (HFB) method [11,12], the parity-projected Hartree-Fock (HF) [13], the quasiparticle random phase approximation (QRPA) [14,15], the angular-momentum projected generator coordinate method (GCM) with [16] and without [17,18] restriction to the axial symmetry, and the antisymmetrized molecular dynamics [19].

Quite recently, excited 0^+ states were found in ^{30}Mg and ^{32}Mg at 1.789 MeV and 1.058 MeV, respectively, and their characters are presently under hot discussion [20–23]. For ^{30}Mg, the excited 0_2^+ state is interpreted as a prolately deformed state which coexists with the spherical ground state. For ^{32}Mg, from the observed population of the excited 0_2^+ state in the (t, p) reaction on ^{30}Mg, it is suggested [22] that the 0_2^+ state is a spherical state coexisting with the deformed ground state and that their relative energies are inverted at $N = 20$. However, available shell-model and GCM calculations considerably overestimate its excitation energy (1.4–3.1 MeV) [9,10,16,21]. It is therefore a challenge for modern microscopic theories of nuclear structure to clarify the nature of the excited 0_2^+ states. For understanding shape dynamics in low-lying collective excited states of Mg isotopes near $N = 20$, it is certainly desirable to develop a theory capable of describing various situations in a unified manner, including, at least, (1) an ideal shape coexistence limit where the wave function of an individual quantum state is well localized in the deformation space and (2) a transitional situation where the large-amplitude shape fluctuations dominate.

In this Rapid Communication, we microscopically derive the five-dimensional (5D) quadrupole collective Hamiltonian using the constrained Hartree-Fock-Bogoliubov (CHFB) plus local QRPA (LQRPA) method [24]. The 5D collective Hamiltonian takes into account all the five quadrupole degrees of freedom: the axial and triaxial quadrupole deformations (β, γ) and the three Euler angles. This approach is suitable for our purpose of describing a variety of quadrupole collective phenomena in a unified way. Another advantage is that the time-odd mean-field contributions are taken into account in evaluating the vibrational and rotational inertial functions. In spite of their importance for correctly describing collective excited states, the time-odd contributions are ignored in the widely used Inglis-Belyaev cranking formula for inertial functions. The CHFB + LQRPA method has been successfully applied to various large-amplitude collective dynamics, including the oblate-prolate shaped coexistence phenomena in Se and Kr isotopes [24,25], the γ-soft dynamics in sd-shell nuclei [26], and the shape phase transition in neutron-rich Cr isotopes [27]. A preliminary version of this work was reported in Ref. [28].

The 5D quadrupole collective Hamiltonian is written as

$$\mathcal{H}_{\rm coll} = T_{\rm vib} + T_{\rm rot} + V(\beta, \gamma), \tag{1}$$

$$T_{\rm vib} = \frac{1}{2} D_{\beta\beta}(\beta, \gamma)\dot{\beta}^2 + D_{\beta\gamma}(\beta, \gamma)\dot{\beta}\dot{\gamma} + \frac{1}{2} D_{\gamma\gamma}(\beta, \gamma)\dot{\gamma}^2, \tag{2}$$

*Present address: Department of Physics and Astronomy, University of North Carolina, Chapel Hill, NC 27599-3255.

$$T_{\rm rot} = \frac{1}{2}\sum_{k=1}^{3} \mathcal{J}_k(\beta,\gamma)\omega_k^2, \tag{3}$$

where $T_{\rm vib}$ and $T_{\rm rot}$ are the vibrational and rotational kinetic energies, respectively, and V is the collective potential. The vibrational collective masses $D_{\beta\beta}$, $D_{\beta\gamma}$, and $D_{\gamma\gamma}$ are the inertial functions for the (β,γ) coordinates. The rotational moments of inertia $\mathcal{J}_k$ associated with the three components of the rotational angular velocities ω_k are defined with respect to the principal axes. In the CHFB + LQRPA method, the collective potential is calculated with the CHFB equation with four constraints on the two quadrupole operators and the proton and neutron numbers. The inertial functions in the collective Hamiltonian are determined from the LQRPA normal modes locally defined for each CHFB state in the (β,γ) plane. The equations to find the local normal modes are similar to the well-known QRPA equations, but the equations are solved on top of the nonequilibrium CHFB states. Two LQRPA solutions representing quadrupole shaped motion are selected for the calculation of the vibrational inertial functions. After quantizing the collective Hamiltonian (1), we solve the 5D collective Schrödinger equation and obtain collective wave functions

$$\Psi_{\alpha IM}(\beta,\gamma,\Omega) = \sum_{K=\rm even} \Phi_{\alpha IK}(\beta,\gamma)\langle\Omega|IMK\rangle, \tag{4}$$

where $\Phi_{\alpha IK}(\beta,\gamma)$ are the vibrational wave functions and $\langle\Omega|IMK\rangle$ are the rotational wave functions defined in terms of $\mathcal{D}$ functions $\mathcal{D}^I_{MK}(\Omega)$. We then evaluate $E2$ matrix elements. More details of this approach are given in Ref. [24].

We solve the CHFB + LQRPA equations employing, as a microscopic Hamiltonian, the pairing-plus-quadrupole (P + Q) model including the quadrupole-pairing interaction. As an active model space, the two major harmonic oscillator shells (sd and pf shells) are taken into account for both neutrons and protons. To determine the parameters in the P + Q Hamiltonian, we first perform Skyrme-HFB calculations with the SkM* functional and the surface pairing functional using the HFBTHO code [29]. The pairing strength ($V_0 = -374$ MeV fm^{-3}, with a cutoff quasiparticle energy of 60 MeV) is fixed so as to reproduce the experimental neutron gap of ^{30}Ne (1.26 MeV). We then determine the parameters for each nucleus in the following way. The single-particle energies are determined by means of the constrained Skyrme-HFB calculation at the spherical shape. The resulting single-particle energies (in the canonical basis) are then scaled with the effective mass of the SkM* functional $m^*/m = 0.79$, since the P + Q model is designed to be used for single-particle states whose effective mass is equal to the bare nucleon mass. In ^{32}Mg, the $N = 20$ shell gap between $d_{3/2}$ and $f_{7/2}$ is 3.7 MeV for the SkM* functional, and it becomes 2.9 MeV after the effective mass scaling. This value is appreciably smaller than the standard modified oscillator value 4.5 MeV [30]. This spacing almost stays constant for $^{30-36}$Mg. The strengths of the monopole-pairing interaction are determined to reproduce the pairing gaps obtained in the Skyrme-HFB calculations at the spherical shape. The strength of the quadrupole particle-hole interaction is determined to reproduce the magnitude of the axial quadrupole deformation β of the Skyrme-HFB minimum. The strengths of the quadrupole-pairing interaction are determined so as to fulfill the self-consistency condition [31]. We use the quadrupole polarization charge $\delta e_{\rm pol} = 0.5$ for both neutrons and protons when evaluating $E2$ matrix elements. We solve the CHFB + LQRPA equations at 3600 β-γ mesh points in the region $0 < \beta < \beta_{\rm max}$ and $0^\circ < \gamma < 60^\circ$, with $\beta_{\rm max} = 0.5$ for ^{30}Mg and 0.6 for ^{32,34,36}Mg.

Our theoretical framework is quite general and it can be used in conjunction with various Skyrme forces or modern density functionals going beyond the P + Q model. Then the effects of weakly bound neutrons and coupling to the continuum on the properties of the low-lying collective excitations, discussed in Refs. [14,15], can be taken into account, for example, by solving the CHFB + LQRPA equations in the three-dimensional (3D) coordinate mesh representation. However, it requires a large-scale calculation with modern parallel processors and it remains a challenging future subject. A step toward this goal has recently been carried out for axially symmetric cases [27].

Figure 1 shows the collective potentials $V(\beta,\gamma)$ for $^{30-36}$Mg. It is clearly seen that prolate deformation grows with an increase in the neutron number. The collective potential for ^{30}Mg is very soft with respect to β. It has a minimum at $\beta = 0.11$ and a local minimum at $\beta = 0.33$. The barrier height between the two minima is only 0.24 MeV (measured from the lower minimum). In ^{32}Mg, in addition to the prolate minimum at $\beta = 0.33$, a spherical local minimum (associated with the $N = 20$ spherical shell gap) appears. The barrier height between the two minima is 1.0 MeV (measured from the lower minimum). The spherical local minimum disappears in ^{34}Mg and ^{36}Mg, and the prolate minima become soft in

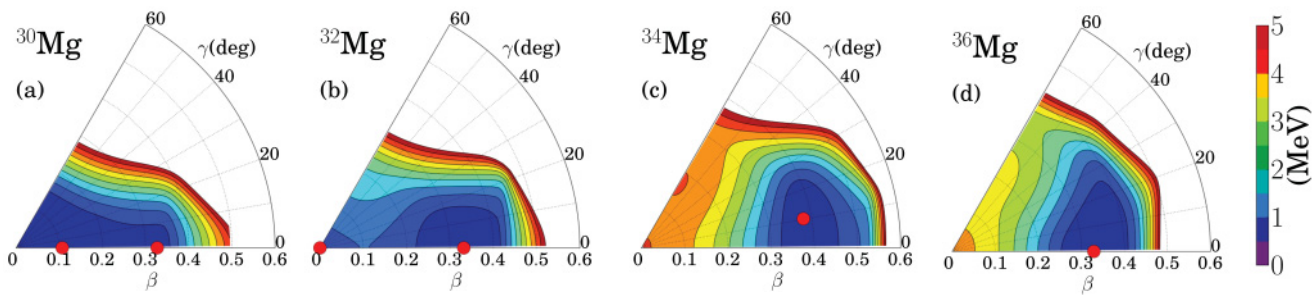

FIG. 1. (Color online) Collective potentials for $^{30-36}$Mg. The HFB equilibrium points are indicated by red circles.

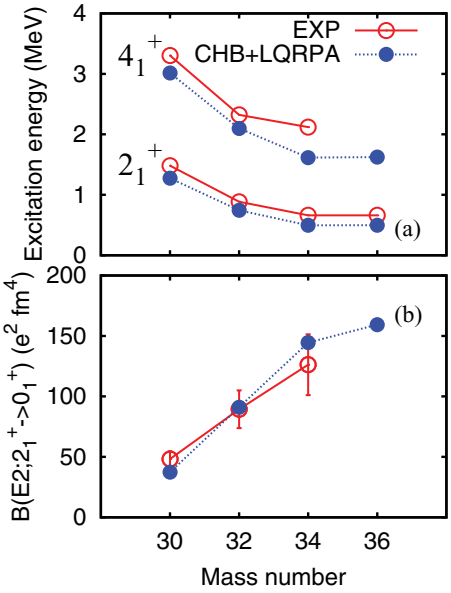

FIG. 2. (Color online) Comparison of calculated excitation energies of the 2_1^+ and 4_1^+ states (upper panel) and $B(E2; 2_1^+ \to 0_1^+)$ values (lower panel) in $^{30-36}$Mg with experimental data [1–6].

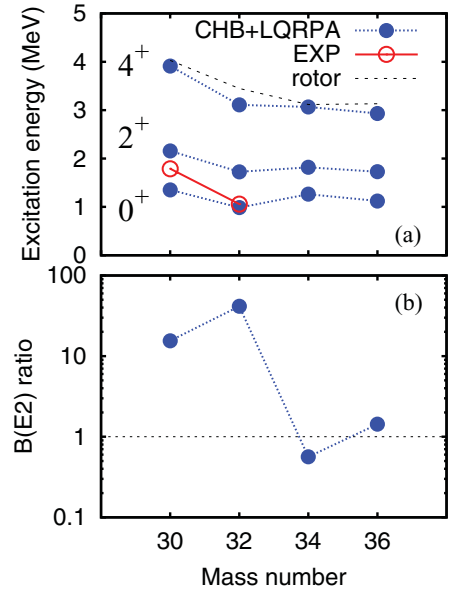

FIG. 3. (Color online) Excitation energies of the excited 0_2^+, $2_{2,3}^+$, and $4_{2,3}^+$ states (upper panel) and the ratio $B(E2; 0_2^+ \to 2_1^+)/B(E2; 0_1^+ \to 2_{2,3}^+)$ of the interband $E2$ transition strengths between the $K = 0_2$ and $K = 0_1$ bands (lower panel). Experimental data are taken from Refs. [21,22]. See text for details.

the direction of triaxial deformation γ. In ^{34}Mg, the potential minimum is located at $\gamma = 10^\circ$.

In Fig. 2, calculated excitation energies and $E2$ transition strengths are compared with the experimental data. The lowering of the excitation energies of the 2_1^+ and 4_1^+ states and the increase of $B(E2; 2_1^+ \to 0_1^+)$ from ^{30}Mg to ^{34}Mg are well described in this calculation. The calculated ratio of the excitation energies $E(4_1^+)/E(2_1^+)$ increases as 2.37, 2.82, 3.26, and 3.26, while the ratio of the transition strengths $B(E2; 4_1^+ \to 2_1^+)/B(E2; 2_1^+ \to 0_1^+)$ decreases as 2.03, 1.76, 1.43, and 1.47, in going from ^{30}Mg to ^{36}Mg. Thus, the properties of the 2_1^+ and 4_1^+states gradually change from vibrational to rotational with increasing neutron number.

Let us next discuss the properties of the 0_2^+ states and the 2^+ and 4^+ states connected to the 0_2^+ states with strong $E2$ transitions. The result of calculation is presented in Fig. 3, together with the recent experimental data. The calculated excitation energies of the 0_2^+ states are 1.353 and 0.986 MeV for ^{30}Mg and ^{32}Mg, respectively, in fair agreement with the experimental data [21,22]. In particular, the very low excitation energy of the 0_2^+ state in ^{32}Mg is well reproduced. In our calculation, more than 90% (80%) of the collective wave functions for the yrast (excited) band members are composed of the $K = 0$ component. Therefore, we denote the ground band by "the $K = 0_1$ band," and the excited band by "the $K = 0_2$ band." The 2^+ and 4^+ states belonging to the $K = 0_2$ band appear as the second 2^+ and 4^+ states in ^{30,32}Mg, while they appear as the third 2^+ and 4^+ states in ^{34,36}Mg. Accordingly, we use $2_{2,3}^+$ and $4_{2,3}^+$ to collectively indicate the second or the third 2^+ and 4^+ states. The calculated ratios of the excitation energies relative to the excited 0_2^+ state $[E(4_{2,3}^+) - E(0_2^+)]/[E(2_{2,3}^+) - E(0_2^+)]$ are 3.18, 2.87, 3.25, and 3.00, for ^{30}Mg, ^{32}Mg, ^{34}Mg, and ^{36}Mg, respectively. In the upper panel of Fig. 3 we also plot the rotor-model prediction for the excitation energies of the 4^+ states estimated from the 0^+–2^+ spacings in the $K = 0_2$ bands. The deviation from the rotor-model prediction is largest in ^{32}Mg, indicating importance of shape-fluctuation effects. Although the calculated excitation spectrum of the $K = 0_2$ band in ^{30}Mg looks rotational, we find a significant deviation from the rotor-model prediction in the $E2$ transition properties. The calculated ratios of the $E2$ transition strengths $B(E2; 4_{2,3}^+ \to 2_{2,3}^+)/B(E2; 2_{2,3}^+ \to 0_2^+)$ are 1.05, 1.54, 1.47, and 1.51 for $^{30-36}$Mg, respectively. The deviation from the rotor-model value (1.43) is largest in ^{30}Mg. The significant deviation from the simple rotor-model pattern of the $K = 0_2$ bands in ^{30}Mg and ^{32}Mg, noticed above, can be seen more drastically in the interband $E2$ transition properties. In the lower panel of Fig. 3, we plot the ratio $B(E2; 0_2^+ \to 2_1^+)/B(E2; 0_1^+ \to 2_{2,3}^+)$ of the interband transition strengths between the $K = 0_1$ and $K = 0_2$ bands. If the $K = 0_1$ and $K = 0_2$ bands are composed of only the $K = 0$ component and the intrinsic structures in the (β, γ) plane are the same within the band members, this ratio should be one. These ratios for ^{34}Mg and ^{36}Mg are close to one, indicating that the change of the intrinsic structure between the 0^+ and 2^+ states is small. In contrast, the ratios for ^{30}Mg and ^{32}Mg are larger than 10, indicating a remarkable change in the shape-fluctuation properties between the 0^+ and 2^+ states belonging to the $K = 0_1$ and $K = 0_2$ bands. The enhancement of the ratios is mainly due to the large $B(E2; 0_2^+ \to 2_1^+)$ values whose origin is discussed below.

Figure 4 shows the vibrational wave functions squared $\sum_K |\Phi_{\alpha IK}(\beta, \gamma)|^2$. Let us first examine the character change of the ground state from ^{30}Mg to ^{34}Mg. In ^{30}Mg, the vibrational wave function of the ground 0_1^+ state is distributed around the spherical shape. In ^{32}Mg, it is extended to the prolately

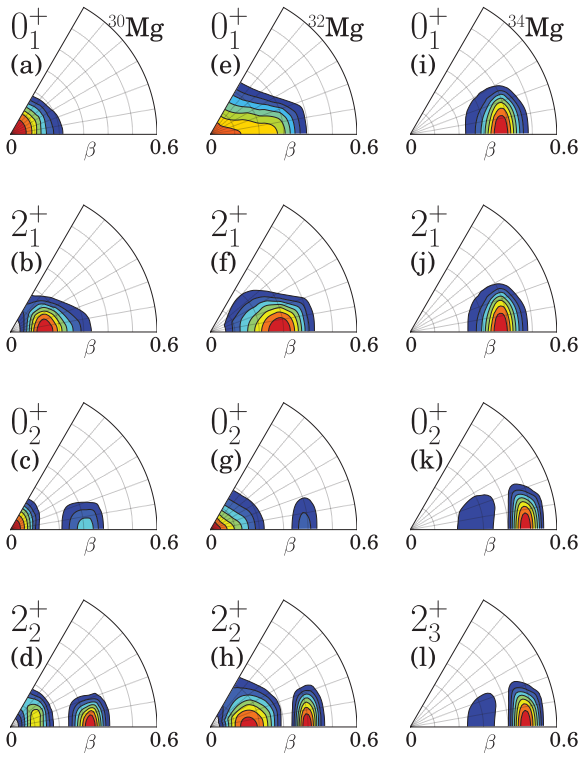

FIG. 4. (Color online) Vibrational wave functions squared $\sum_K |\Phi_{\alpha IK}(\beta,\gamma)|^2$ of the $0_1{}^+$, $2_1{}^+$, $0_2{}^+$, and $2_{2,3}{}^+$ states in $^{30-34}$Mg. Contour lines are drawn at every eighth part of the maximum value.

deformed region. In ^{34}Mg, it is distributed around the prolate shape. From the behavior of the vibrational wave functions, one can conclude that shape fluctuation in the ground $0_1{}^+$ state is largest in ^{32}Mg. To understand the microscopic mechanism of this change from ^{30}Mg to ^{34}Mg, it is necessary to take into account not only the properties of the collective potential in the β direction but also its curvature in the γ direction and the collective kinetic energy (collective masses). This point will be discussed in our forthcoming full-length paper. As suggested from the behavior of the interband $B(E2)$ ratio, the vibrational wave functions of the $2_1{}^+$ state are noticeably different from those of the $0_1{}^+$ state in ^{30}Mg and ^{32}Mg, while they are similar in the case of ^{34}Mg. Next, let us examine the vibrational wave functions of the $0_2{}^+$ and $2_{2,3}{}^+$ states in $^{30-34}$Mg. It is immediately seen that they exhibit one node in the β direction. This is their common feature. In ^{30}Mg and ^{32}Mg, one bump is seen in the spherical to weakly deformed region, while the other bump is located in the prolately deformed region around $\beta = 0.3$–0.4. The bump at the deformed region of the $0_2{}^+$ states and the extended structure of the $2_1{}^+$ states to the deformed region, which lead to an appreciable overlap of their vibrational wave functions, are responsible for the large interband $B(E2; 0_2{}^+ \to 2_1{}^+)$ values. In ^{34}Mg, the node is located near the peak of the vibrational wave function of the $0_1{}^+$ state, suggesting that they have β-vibrational properties.

To further reveal the nature of the ground and excited 0^+ states, it is important to examine not only their vibrational wave functions but also their probability density distributions. Since the 5D collective space is a curved space, the normalization

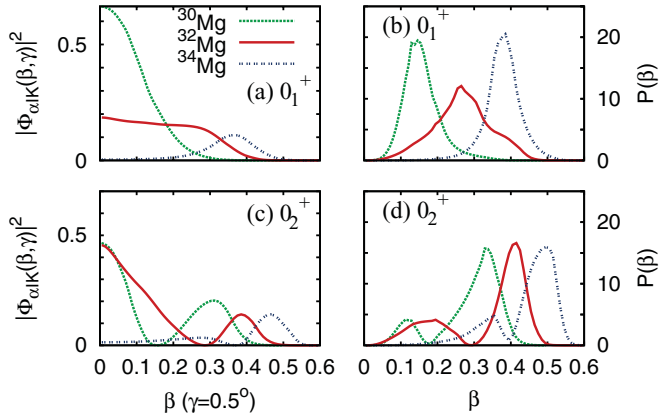

FIG. 5. (Color online) (a) Vibrational wave functions squared $|\Phi_{\alpha,I=0,K=0}(\beta,\gamma=0.5^\circ)|^2$ of the $0_1{}^+$ states in $^{30-34}$Mg. Their values along the $\gamma = 0.5^\circ$ line are plotted as functions of β. (b) Probability densities integrated over γ, $P(\beta) \equiv \int d\gamma |\Phi_{\alpha,I=0,K=0}(\beta,\gamma)|^2 |G(\beta,\gamma)|^{1/2}$, of the $0_1{}^+$ states in $^{30-34}$Mg, plotted as functions of β. (c) Same as (a) but for the $0_2{}^+$ states. (d) Same as (b) but for the $0_2{}^+$ states.

condition for the vibrational wave functions is given by

$$\int \sum_K |\Phi_{\alpha IK}(\beta,\gamma)|^2 |G(\beta,\gamma)|^{1/2} d\beta\, d\gamma = 1, \tag{5}$$

with the volume element

$$|G(\beta,\gamma)|^{1/2} d\beta\, d\gamma = 2\beta^4 \sqrt{W(\beta,\gamma)R(\beta,\gamma)}\, \sin 3\gamma\, d\beta\, d\gamma, \tag{6}$$

$$W(\beta,\gamma) = \{D_{\beta\beta}(\beta,\gamma)D_{\gamma\gamma}(\beta,\gamma) - [D_{\beta\gamma}(\beta,\gamma)]^2\}\beta^{-2}, \tag{7}$$

$$R(\beta,\gamma) = D_1(\beta,\gamma)D_2(\beta,\gamma)D_3(\beta,\gamma), \tag{8}$$

where $D_{k=1,2,3}$ are the rotational masses defined through $\mathcal{J}_k = 4\beta^2 D_k \sin^2(\gamma - 2\pi k/3)$. Thus, the probability density of taking a shape with specific values of (β,γ) is given by $\sum_K |\Phi_{\alpha IK}(\beta,\gamma)|^2 |G(\beta,\gamma)|^{1/2}$. Due to the β^4 factor in the volume element, the spherical peak of the vibrational wave function disappears in the probability density distribution. Accordingly, it will give us a picture that is quite different from that of the wave function. Needless to say, it is important to examine both aspects to understand the nature of individual quantum states.

In Fig. 5, we display the probability density integrated over γ, $P(\beta) \equiv \int d\gamma |\Phi_{\alpha,I=0,K=0}(\beta,\gamma)|^2 |G(\beta,\gamma)|^{1/2}$, of finding a shape with a specific value of β, together with the vibrational wave functions squared $|\Phi_{\alpha,I=0,K=0}(\beta,\gamma)|^2$ for the ground and excited 0^+ states ($\alpha = 1$ and 2). Let us first look at the upper panels for the ground states. We note that, as expected, the spherical peak of the vibrational wave function for ^{30}Mg in Fig. 5(a) corresponds to the peak at $\beta \simeq 0.15$ of the probability density in Fig. 5(b). In Fig. 5(b), the peak position moves toward a larger value of β in going from ^{30}Mg to ^{34}Mg. The distribution for ^{32}Mg is much broader than those for ^{30}Mg and ^{34}Mg.

Next, let us look at the lower panels in Fig. 5 for the excited states. In Fig. 5(c), the vibrational wave functions for

^{30}Mg and ^{32}Mg exhibit the maximum peak at the spherical shape. However, these peaks become small and are shifted to the region with $\beta \simeq 0.1$ and $\beta \simeq 0.2$ in ^{30}Mg and ^{32}Mg, respectively, in Fig. 5(d). On the other hand, the second peaks at $\beta \simeq 0.3$ and $\beta \approx 0.4$ in ^{30}Mg and ^{32}Mg, respectively, seen in Fig. 5(c), become the prominent peaks in Fig. 5(d). In ^{30}Mg, the bump at $\beta \simeq 0.1$ is much smaller than the major bump at $\beta \simeq 0.3$. In this sense, we can regard the $0_2{}^+$ state of ^{30}Mg as a prolately deformed state. In the case of ^{32}Mg, the probability density exhibits a very broad distribution extending from the spherical to deformed regions up to $\beta = 0.5$ with a prominent peak at $\beta \simeq 0.4$ and a node at $\beta \simeq 0.3$. The position of the node coincides with the peak of the probability density distribution of the $0_1{}^+$ state, as expected from the orthogonality condition. The range of the shape fluctuation of the $0_2{}^+$ state in the β direction is almost the same as that of the $0_1{}^+$ state. Thus, the result of our calculation yields a physical picture for the $0_2{}^+$ state in ^{32}Mg that is quite different from the "spherical excited 0^+ state" interpretation based on the inversion picture of the spherical and deformed configurations. A detailed analysis of this point, including the relations with the shell model descriptions [8,9], will be presented in a forthcoming paper. In ^{34}Mg, the peak is shifted to the region with a larger value of β and the tail toward the spherical shape almost disappears.

In summary, we have investigated the large-amplitude collective dynamics in the low-lying states of $^{30-36}$Mg by solving the 5D quadrupole collective Schrödinger equation. The collective masses and potentials of the 5D collective Hamiltonian are microscopically derived with use of the CHFB + LQRPA method. Good agreement with the recent experimental data is obtained for the excited 0^+ states as well as the ground bands. For ^{30}Mg, the shape coexistence picture that the deformed excited 0^+ state coexists with the spherical ground state approximately holds. On the other hand, large-amplitude quadrupole-shaped fluctuations dominate in both the ground and the excited 0^+ states in ^{32}Mg, in contrast to the interpretation of "deformed ground and spherical excited 0^+ states" based on the simple inversion picture of the spherical and deformed configurations. To test these theoretical predictions, an experimental search for the distorted rotational bands built on the excited $0_2{}^+$ states in ^{30}Mg and ^{32}Mg is strongly desired.

One of the authors (N.H.) is supported by the Special Postdoctoral Research Program of RIKEN. The numerical calculations were performed on the RIKEN Integrated Cluster of Clusters (RICC). This work is supported by KAKENHI (Nos. 21340073, 20105003, 23540234, and 23740223).

[1] A. N. Deacon *et al.*, Phys. Rev. C **82**, 034305 (2010).
[2] S. Takeuchi *et al.*, Phys. Rev. C **79**, 054319 (2009).
[3] K. Yoneda *et al.*, Phys. Lett. B **499**, 233 (2001).
[4] O. Niedermaier *et al.*, Phys. Rev. Lett. **94**, 172501 (2005).
[5] T. Motobayashi *et al.*, Phys. Lett. B **346**, 9 (1995).
[6] H. Iwasaki *et al.*, Phys. Lett. B **522**, 227 (2001).
[7] E. K. Warburton, J. A. Becker, and B. A. Brown, Phys. Rev. C **41**, 1147 (1990).
[8] Y. Utsuno, T. Otsuka, T. Mizusaki, and M. Honma, Phys. Rev. C **60**, 054315 (1999).
[9] E. Caurier *et al.*, Nucl. Phys. A **693**, 374 (2001).
[10] T. Otsuka, Eur. Phys. J. A **20**, 69 (2003).
[11] J. Terasaki *et al.*, Nucl. Phys. A **621**, 706 (1997).
[12] P.-G. Reinhard *et al.*, Phys. Rev. C **60**, 014316 (1999).
[13] H. Ohta *et al.*, Eur. Phys. J. A **25**, 549 (2005).
[14] M. Yamagami and N. VanGiai, Phys. Rev. C **69**, 034301 (2004).
[15] K. Yoshida and M. Yamagami, Phys. Rev. C **77**, 044312 (2008).
[16] R. Rodríguez-Guzmán *et al.*, Nucl. Phys. A **709**, 201 (2002).
[17] J. M. Yao *et al.*, Phys. Rev. C **83**, 014308 (2011).
[18] J. M. Yao *et al.*, Int. J. Mod. Phys. E **20**, 482 (2011).
[19] M. Kimura *et al.*, Prog. Theor. Phys. **107**, 33 (2002).
[20] H. Mach *et al.*, Eur. Phys. J. A **25**, 105 (2005).
[21] W. Schwerdtfeger *et al.*, Phys. Rev. Lett. **103**, 012501 (2009).
[22] K. Wimmer *et al.*, Phys. Rev. Lett. **105**, 252501 (2010).
[23] H. T. Fortune, Phys. Rev. C **84**, 024327 (2011).
[24] N. Hinohara, K. Sato, T. Nakatsukasa, M. Matsuo, and K. Matsuyanagi, Phys. Rev. C **82**, 064313 (2010).
[25] K. Sato *et al.*, Nucl. Phys. A **849**, 53 (2011).
[26] N. Hinohara and Y. Kanada-Enyo, Phys. Rev. C **83**, 014321 (2011).
[27] K. Yoshida and N. Hinohara, Phys. Rev. C **83**, 061302 (2011).
[28] N. Hinohara *et al.*, in *International Symposium on New Faces of Atomic Nuclei*, edited by W. Bentz *et al.*, AIP Conf. Proc. No. 1355 (AIP, Melville, NY, 2011), p. 200.
[29] M. Stoitsov *et al.*, Comput. Phys. Commun. **167**, 43 (2005).
[30] T. Bengtsson *et al.*, Nucl. Phys. A **436**, 14 (1985).
[31] H. Sakamoto *et al.*, Phys. Lett. B **245**, 321 (1990).

Shape transition and fluctuations in neutron-rich Cr isotopes around $N = 40$

Koichi Sato,[1] Nobuo Hinohara,[1,2] Kenichi Yoshida,[3,4] Takashi Nakatsukasa,[1] Masayuki Matsuo,[3,4] and Kenichi Matsuyanagi[1,5]

[1]*RIKEN Nishina Center, Wako 351-0198, Japan*

[2]*Department of Physics and Astronomy, University of North Carolina, Chapel Hill, North Carolina 27599-3255, USA*

[3]*Graduate School of Science and Technology, Niigata University, Niigata 950-2181, Japan*

[4]*Department of Physics, Faculty of Science, Niigata University, Niigata 950-2181, Japan*

[5]*Yukawa Institute for Theoretical Physics, Kyoto University, Kyoto 606-8502, Japan*

(Received 1 June 2012; revised manuscript received 27 July 2012; published 29 August 2012)

The spherical-to-prolate shape transition in neutron-rich Cr isotopes from $N = 34$ to 42 is studied by solving the collective Schrödinger equation for the five-dimensional quadrupole collective Hamiltonian. The collective potential and inertial functions are microscopically derived with use of the constrained Hartree-Fock-Bogoliubov plus local quasiparticle random-phase approximation method. Nature of the quadrupole collectivity of low-lying states is discussed by evaluating excitation spectra and electric quadrupole moments and transition strengths. The result of calculation indicates that Cr isotopes around ^{64}Cr are prolately deformed but still possess transitional character; large-amplitude shape fluctuations dominate in their low-lying states.

DOI: 10.1103/PhysRevC.86.024316 PACS number(s): 21.60.Jz, 21.10.Ky, 21.10.Re, 27.50.+e

I. INTRODUCTION

Recent experiments on neutron-rich Cr isotopes show that quadrupole collectivity appreciably develops toward ^{64}Cr with $N = 40$ [1–6]. Going from ^{58}Cr to ^{64}Cr, the excitation energy of the first excited 2_1^+ state decreases and $R_{4/2}$, the ratio of the excitation energy of the 4_1^+ state to that of the 2_1^+ state, increases. These data seem to indicate that a quantum phase transition from the spherical to deformed shapes takes place near $N = 40$. The microscopic origin of the enhanced quadrupole collectivity toward $N = 40$ has been actively discussed from various theoretical approaches: the Hartree-Fock-Bogoliubov (HFB) mean-field calculations using the Skyrme force [8] or the Gogny force [9], the spherical shell-model [7,10], and the projected deformed shell model [11]. These calculations have clarified the important role of the neutron $g_{9/2}$ and $d_{5/2}$ single-particle levels in the emergence of the quadrupole collectivity near $N = 40$. Although the spherical shell model calculations reproduce the experimental data rather well, the character of the quadrupole deformation, especially, the distinction between the equilibrium shape and shape fluctuations around it is not sufficiently clear.

In this paper, we investigate the nature of the quadrupole collectivity in low-lying states of the neutron-rich Cr isotopes $^{58-64}$Cr using an approach that treats the quadrupole deformations as dynamical variables. Thus, the distinction of the equilibrium shape and shape fluctuations is transparent. The deformation energy curve with respect to the axial quadrupole deformation was obtained in the Skyrme HFB mean-field calculation [8], which shows that the quadrupole instability occurs around $N = 38$–42. However, the deformed minima are extremely shallow in these nuclei, suggesting a transitional character. In such transitional situations, one naturally expects that large-amplitude shape fluctuations play an important role in determining the properties of low-lying excited states. Therefore, we take the five-dimensional (5D) quadrupole collective Hamiltonian approach [12], which is capable of describing the large-amplitude quadrupole shape fluctuations associated with the quantum shape transition. It enables us to treat a variety of quadrupole deformation phenomena (vibrational, spherical-prolate transitional, rotational, γ-unstable, triaxial, oblate-prolate shape-coexistent situations, etc.) on an equal footing. Dynamical variables of the 5D quadrupole collective Hamiltonian approach are the magnitude and triaxiality of quadrupole deformation (β, γ) and the three Euler angles. The 5D collective Hamiltonian is characterized by seven functions: the collective potential, three vibrational inertial functions (also called vibrational masses), and three rotational inertial functions. To evaluate the inertial functions, the Inglis-Belyaev (IB) cranking formula has been conventionally used. However, it is well known that the contribution of the time-odd components of the moving mean field is ignored in the IB cranking formula, which leads to the overestimation of excitation energies [14,15].

The constrained Hartree-Fock-Bogoliubov plus local quasiparticle random-phase approximation (CHFB + LQRPA) method [16] is a method which can overcome the shortcoming of the IB cranking formula. This method has been successfully applied to several phenomena: shape coexistence/fluctuation in Se and Kr isotopes [14,16,19], development of triaxial deformation in ^{110}Mo [20], and shape fluctuations in neutron-rich Mg isotopes [21]. Use of the Skyrme energy density functional in solving the CHFB + LQRPA equations has also been initiated for the axially symmetric quadrupole Hamiltonian [22]. In this paper, we solve the LQRPA equations with use of the pairing-plus-quadrupole (P + Q) model [12] including the quadrupole pairing interaction. For the collective Hamiltonian quantized according to the Pauli prescription, we solve the collective Schrödinger equation to obtain the excitation energies, vibrational wave functions, $E2$-transition strengths, and moments.

This paper is organized as follows. We recapitulate the theoretical framework in Sec. II. In Sec. III, we present

results of calculation for $^{58-66}$Cr and discuss the nature of quadrupole collectivity in their low-lying states. We then discuss similarities and differences of the quadrupole shape transition near ^{64}Cr with $N = 40$ and that near ^{32}Mg with $N = 20$. Conclusions are given in Sec. IV.

II. THEORETICAL FRAMEWORK

In this section, we briefly summarize the framework of our collective Hamiltonian approach. See Ref. [16] for details.

A. 5D quadrupole collective Hamiltonian

The 5D quadrupole collective Hamiltonian is given by

$$\mathcal{H}_{\rm coll} = T_{\rm vib} + T_{\rm rot} + V(\beta,\gamma), \tag{1}$$

$$T_{\rm vib} = \frac{1}{2}D_{\beta\beta}(\beta,\gamma)\dot{\beta}^2 + D_{\beta\gamma}(\beta,\gamma)\dot{\beta}\dot{\gamma} + \frac{1}{2}D_{\gamma\gamma}(\beta,\gamma)\dot{\gamma}^2, \tag{2}$$

$$T_{\rm rot} = \frac{1}{2}\sum_{k=1}^{3}\mathcal{J}_k(\beta,\gamma)\omega_k^2, \tag{3}$$

where $T_{\rm vib}$ and $T_{\rm rot}$ represent the vibrational and rotational kinetic energies, while V the collective potential energy. The velocities of the vibrational motion are described in terms of the time derivatives $(\dot{\beta},\dot{\gamma})$ of the quadrupole deformation variables (β,γ) representing the magnitude and the triaxiality of the quadrupole deformation, respectively. The three components ω_k of the rotational angular velocity are defined with respect to the principal axes associated with the rotating nucleus. The moments of inertia are parametrized as $\mathcal{J}_k(\beta,\gamma) = 4\beta^2 D_k(\beta,\gamma)\sin^2\gamma_k$ with $\gamma_k = \gamma - 2\pi k/3$. The inertial functions for vibration (vibrational masses) $D_{\beta\beta}$, $D_{\beta\gamma}$ and $D_{\gamma\gamma}$, and those for rotation (rotational masses) D_k are functions of β and γ.

The collective potential and inertial functions are determined with the CHFB + LQRPA method as explained in the next subsection. Once they are determined as functions of (β,γ), we quantize the collective Hamiltonian according to the Pauli prescription. The collective Schrödinger equation for the quantized collective Hamiltonian is given by

$$\{\hat{T}_{\rm vib} + \hat{T}_{\rm rot} + V\}\Psi_{\alpha IM}(\beta,\gamma,\Omega) = E_{\alpha I}\Psi_{\alpha IM}(\beta,\gamma,\Omega), \tag{4}$$

where

$$\begin{aligned}\hat{T}_{\rm vib} = \frac{-1}{2\sqrt{WR}}\Bigg\{&\frac{1}{\beta^4}\left[\left(\partial_\beta\beta^2\sqrt{\frac{R}{W}}D_{\gamma\gamma}\partial_\beta\right)\right.\\ &\left.-\ \partial_\beta\left(\beta^2\sqrt{\frac{R}{W}}D_{\beta\gamma}\partial_\gamma\right)\right]\\ &+\frac{1}{\beta^2\sin 3\gamma}\left[-\partial_\gamma\left(\sqrt{\frac{R}{W}}\sin 3\gamma\, D_{\beta\gamma}\partial_\beta\right)\right.\\ &\left.+\ \partial_\gamma\left(\sqrt{\frac{R}{W}}\sin 3\gamma\, D_{\beta\beta}\partial_\gamma\right)\right]\Bigg\}\end{aligned} \tag{5}$$

and

$$\hat{T}_{\rm rot} = \sum_k \frac{\hat{I}_k^2}{2\mathcal{J}_k}. \tag{6}$$

Here, $R(\beta,\gamma)$ and $W(\beta,\gamma)$ are defined as

$$R(\beta,\gamma) = D_1(\beta,\gamma)D_2(\beta,\gamma)D_3(\beta,\gamma), \tag{7}$$

$$W(\beta,\gamma) = \{D_{\beta\beta}(\beta,\gamma)D_{\gamma\gamma}(\beta,\gamma) - [D_{\beta\gamma}(\beta,\gamma)]^2\}\beta^{-2}. \tag{8}$$

The collective wave function $\Psi_{\alpha IM}(\beta,\gamma,\Omega)$ is specified by the total angular momentum I, its projection onto the z axis of the laboratory frame M, and α distinguishing the states with the same I and M. It can be written as a sum of products of the vibrational and rotational wave functions:

$$\Psi_{\alpha IM}(\beta,\gamma,\Omega) = \sum_{K={\rm even}}\Phi_{\alpha IK}(\beta,\gamma)\langle\Omega|IMK\rangle, \tag{9}$$

where

$$\langle\Omega|IMK\rangle = \sqrt{\frac{2I+1}{16\pi^2(1+\delta_{K0})}}\left[\mathcal{D}^I_{MK}(\Omega) + (-)^I\mathcal{D}^I_{M-K}(\Omega)\right]. \tag{10}$$

$\mathcal{D}^I_{MK}$ is the Wigner rotation matrix and K is the projection of the angular momentum onto the z axis in the body-fixed frame. The summation over K is taken from 0 to I for even I and from 2 to $I-1$ for odd I.

The vibrational wave functions in the body-fixed frame, $\Phi_{\alpha IK}(\beta,\gamma)$, are normalized as

$$\int d\beta d\gamma |\Phi_{\alpha I}(\beta,\gamma)|^2 |G(\beta,\gamma)|^{\frac{1}{2}} = 1, \tag{11}$$

where

$$|\Phi_{\alpha I}(\beta,\gamma)|^2 \equiv \sum_{K={\rm even}}|\Phi_{\alpha IK}(\beta,\gamma)|^2, \tag{12}$$

and the volume element $|G(\beta,\gamma)|$ is given by

$$|G(\beta,\gamma)| = 4\beta^8 W(\beta,\gamma)R(\beta,\gamma)\sin^2 3\gamma. \tag{13}$$

The symmetries and boundary conditions of the collective Hamiltonian and wave functions are discussed in Ref. [23].

B. The CHFB + LQRPA method

We determine the collective potential and inertial functions with the CHFB + LQRPA method. It is derived on the basis of the adiabatic self-consistent collective coordinate (ASCC) method [15,17,18] by assuming that there is a one-to-one mapping from a point on the collective submanifold embedded in the large-dimensional time-dependent HFB phase space to a point in the (β,γ) deformation space. In the CHFB + LQRPA method, the inertial functions are derived by transforming the local canonical coordinates determined by the LQRPA normal modes to the (β,γ) degrees of freedom.

We first solve the CHFB equation

$$\delta\langle\phi(\beta,\gamma)|\hat{H}_{\rm CHFB}(\beta,\gamma)|\phi(\beta,\gamma)\rangle = 0, \tag{14}$$

$$\hat{H}_{\rm CHFB} = \hat{H} - \sum_\tau \lambda^{(\tau)}\hat{N}^{(\tau)} - \sum_m \mu^{(m)}\hat{D}^{(+)}_{2m} \tag{15}$$

with the constraints on the particle numbers and quadrupole deformation parameters:

$$\langle\phi(\beta,\gamma)|\hat{N}^{(\tau)}|\phi(\beta,\gamma)\rangle = N_0^{(\tau)}, \quad (\tau = n, p), \tag{16}$$

$$\langle\phi(\beta,\gamma)|\hat{D}^{(+)}_{2m}|\phi(\beta,\gamma)\rangle = D^{(+)}_{2m}, \quad (m = 0, 2). \tag{17}$$

Here, $\hat{D}^{(+)}_{2m}$ denotes Hermitian quadrupole operators, $\hat{D}_{20}$ and $(\hat{D}_{22} + \hat{D}_{2-2})/2$ for $m = 0$ and 2, respectively. We define the quadrupole deformation variables (β, γ) in terms of the expectation values of the quadrupole operators

$$\beta\cos\gamma = \eta D^{(+)}_{20} = \eta\langle\phi(\beta,\gamma)|\hat{D}^{(+)}_{20}|\phi(\beta,\gamma)\rangle, \tag{18}$$

$$\frac{1}{\sqrt{2}}\beta\sin\gamma = \eta D^{(+)}_{22} = \eta\langle\phi(\beta,\gamma)|\hat{D}^{(+)}_{22}|\phi(\beta,\gamma)\rangle, \tag{19}$$

where η is a scaling factor (see Ref. [16] for the explicit expression). Then, we solve the LQRPA equations for vibration on top of the CHFB states obtained above,

$$\delta\langle\phi(\beta,\gamma)|[\hat{H}_{\rm CHFB}(\beta,\gamma), \hat{Q}^i(\beta,\gamma)] - \frac{1}{i}\hat{P}_i(\beta,\gamma)|\phi(\beta,\gamma)\rangle = 0, \tag{20}$$

$$\delta\langle\phi(\beta,\gamma)|\left[\hat{H}_{\rm CHFB}(\beta,\gamma), \frac{1}{i}\hat{P}_i(\beta,\gamma)\right] - C_i(\beta,\gamma)\hat{Q}^i(\beta,\gamma)|\phi(\beta,\gamma)\rangle = 0, \quad (i = 1, 2). \tag{21}$$

The infinitesimal generators, $\hat{Q}^i(\beta,\gamma)$ and $\hat{P}_i(\beta,\gamma)$, are locally defined at every point of the (β, γ) deformation space. The quantity $C_i(\beta,\gamma)$ is related to the eigenfrequency $\omega_i(\beta,\gamma)$ of the local normal mode through $\omega_i^2(\beta,\gamma) = C_i(\beta,\gamma)$. It is worth noting that these equations are valid also for regions with negative curvature ($C_i(\beta,\gamma) < 0$) where $\omega_i(\beta,\gamma)$ takes an imaginary value.

The rotational moments of inertia are calculated by solving the LQRPA equation for rotation on each CHFB state. It is an extension of the Thouless-Valatin equation [24] for the HFB equilibrium state to non-equilibrium CHFB states. We call the moments of inertia $\mathcal{J}_k(\beta,\gamma)$ thus determined 'LQRPA moments of inertia.'

We solve the collective Schrödinger equation (4) to obtain excitation energies and vibrational wave functions. Then, electric transition strengths and moments are readily calculated (see Ref. [19] for details).

C. Details of the numerical calculation

The CHFB + LQRPA method can be used in conjunction with any effective interaction (e.g., density-dependent effective interaction such as Skyrme functionals, or other modern nuclear density functionals). In fact, the use of the Skyrme functional for the LQRPA approach has been initiated for axially symmetric quadrupole Hamiltonian [22]. In this study, however, we adopt a version of the pairing-plus-quadrupole (P + Q) model [12] including the quadrupole pairing interaction as well as the monopole pairing interaction for computational simplicity. We take two harmonic-oscillator shells with $N_{sh} = 3, 4$ and $N_{sh} = 2, 3$ for neutrons and protons, respectively. The single-particle energies are determined with the constrained Skyrme-HFB calculations at the spherical shape using the HFBTHO code [25]. The single-particle energies in the canonical basis obtained in the Skyrme-HFB calculations are then scaled with the effective mass of the SkM* functional $m^*/m = 0.79$ for the use of the P + Q model, because it is designed to be used for single particles whose mass is the bare nucleon mass. In these Skyrme-HFB calculations, we employ the SkM* functional and the volume-type pairing with the pairing strength $V_0 = -180$ MeV fm^{-3}. The pairing strength has been adjusted such that the calculated neutron pairing gaps at the HFB minima reproduce the experimental gaps in $^{58-64}$Cr determined from the odd-even mass differences [26].

To determine the quadrupole pairing strengths in the P + Q model, we follow the Sakamoto-Kishimoto prescription [27] to restore the local Galilean invariance broken by the monopole pairing. With this prescription, once we set the values of the monopole pairing strengths $G_0^{(\tau)}(\tau = n, p)$, the quadrupole pairing strengths are self-consistently determined from them at the spherical shape. The other parameters of the P + Q model are determined in the following way. For ^{62}Cr (situated in the middle of the isotopic chain), the monopole pairing strengths and quadrupole particle-hole interaction strength χ are adjusted to approximately reproduce the HFB equilibrium deformation and the pairing gaps at the spherical and HFB equilibrium shapes. For the other nuclei ^{58,60,64,66}Cr, we assume the simple mass number dependence according to Baranger and Kumar [12]: $G_0^{(\tau)} \sim A^{-1}$ and $\chi' \equiv \chi b^4 \sim A^{-5/3}$ (b denotes the oscillator-length parameter). We omit the Fock term as in the conventional treatment of the P + Q model.

The CHFB + LQRPA equations are solved at 60×60 mesh points in the (β, γ) plane defined by

$$\beta_i = (i - 0.5) \times 0.01, \quad (i = 1, \ldots, 60), \tag{22}$$

$$\gamma_j = (j - 0.5) \times 1^\circ, \quad (j = 1, \ldots, 60). \tag{23}$$

For the calculation of the $E2$ transitions and moments, we use the standard values of effective charges $(e^{(n)}_{\rm eff}, e^{(p)}_{\rm eff}) = (0.5, 1.5)$.

III. RESULTS AND DISCUSSION

In this section, we present the numerical results for $^{58-66}$Cr and discuss the nature of quadrupole collectivity in their low-lying states. We furthermore discuss the similarities and differences with Mg isotopes around $N = 20$.

A. Collective potentials and inertial functions

We plot the collective potential $V(\beta,\gamma)$ calculated for $^{58-66}$Cr in Fig. 1. The location of the absolute minimum is indicated by the (blue) circle. In ^{58}Cr, the absolute minimum is located at a nearly spherical shape. Although the minimum shifts to larger deformation in ^{60}Cr, the collective potential is extremely soft in the β direction. A more pronounced local minimum appears at larger deformation in ^{62}Cr, and the minimum becomes even deeper in ^{64}Cr. In ^{66}Cr, the collective

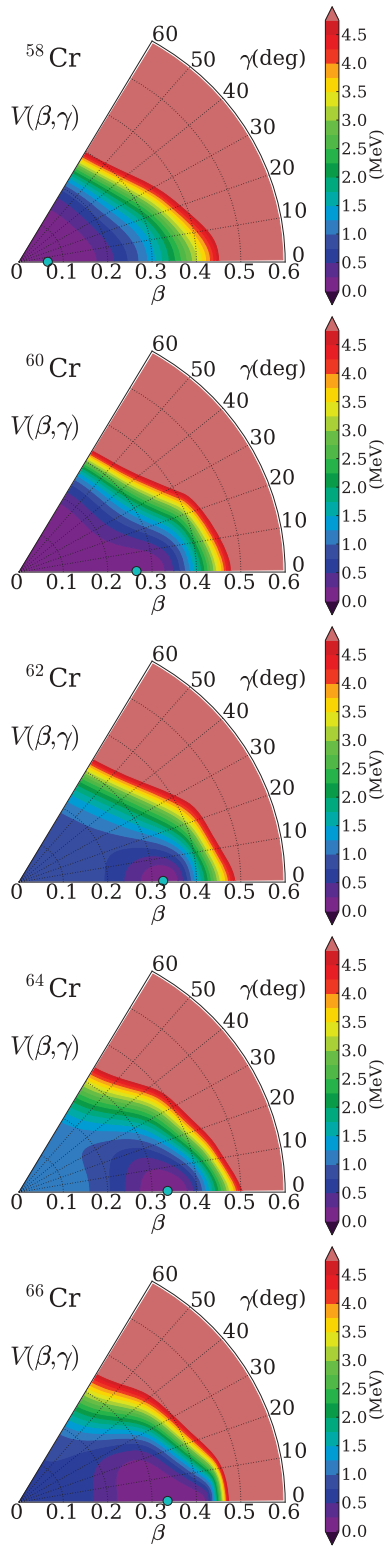

FIG. 1. (Color online) Collective potential energy surfaces $V(\beta, \gamma)$ for $^{58-66}$Cr. The regions higher than 5 MeV (measured from the HFB minima) are colored rosy-brown.

potential becomes slightly softer than in ^{64}Cr. These potential energy surfaces indicate that a quantum shape transition from a spherical to a prolately deformed shape takes place along the isotopic chain toward $N = 40$. In Fig. 2, we plot the Nilsson diagrams of neutrons and protons as functions of β calculated for ^{62}Cr as in Ref. [13]. This is similar to Figs. 5(a) and 5(b) in Ref. [8]. In ^{58}Cr, the neutron and proton shell effects for $N = 34$ and $Z = 24$ are in competition. The appearance of the potential minimum in the slightly deformed region in Fig. 1 suggests that the neutron shell effects dominate over the proton ones. On the other hand, in ^{62}Cr, the deformed shell effects for $N = 38$ and $Z = 24$ are in cooperation and lead to the prolate potential minimum.

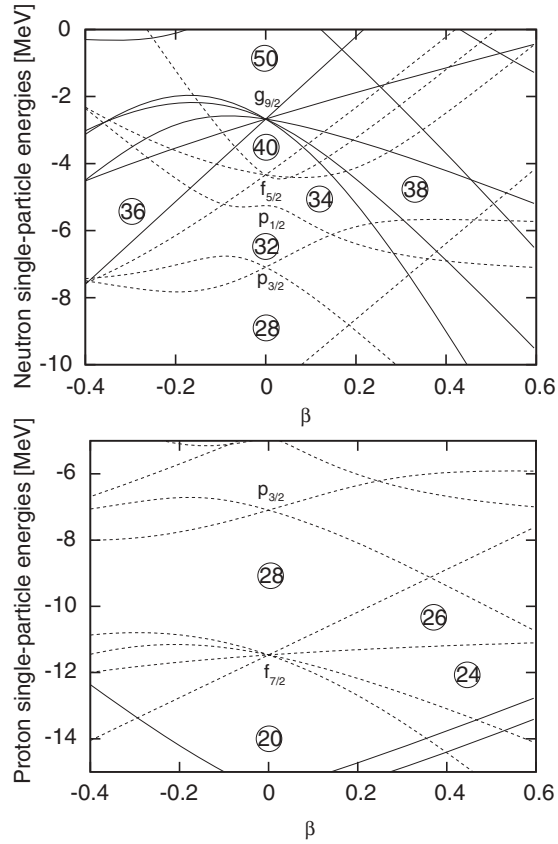

FIG. 2. Nilsson diagrams for neutrons (upper) and protons (lower) in ^{62}Cr as functions of β, calculated as in Ref. [13]. The levels with the positive (negative) parity are plotted with solid (dotted) lines.

In Fig. 3, we plot the neutron and proton monopole pairing gaps $\Delta_0^{(n)}(\beta, \gamma)$ and $\Delta_0^{(p)}(\beta, \gamma)$, the vibrational inertial function $D_{\beta\beta}(\beta, \gamma)$, and the rotational moment of inertia $\mathcal{J}_1(\beta, \gamma)$, calculated for ^{62}Cr. Figure 3(c) clearly shows that the vibrational inertial function is well correlated with the magnitudes of the paring gaps: $D_{\beta\beta}(\beta, \gamma)$ becomes small in the spherical region where $\Delta_0^{(n)}$ and $\Delta_0^{(p)}$ take large values. One might be concerned for complicated behaviors of $D_{\beta\beta}(\beta, \gamma)$ in the strongly deformed region. However, they hardly affect low-lying states, because the collective potential energy is very high there and contributions from this region to the vibrational wave functions are negligibly small. Figure 3(d) clearly indicates that the rotational moment of inertia also has a strong correlation with the pairing gaps. It takes the maximum value in the prolate region around $\beta \simeq 0.35$. Both the neutron and proton pairing gaps become small there due

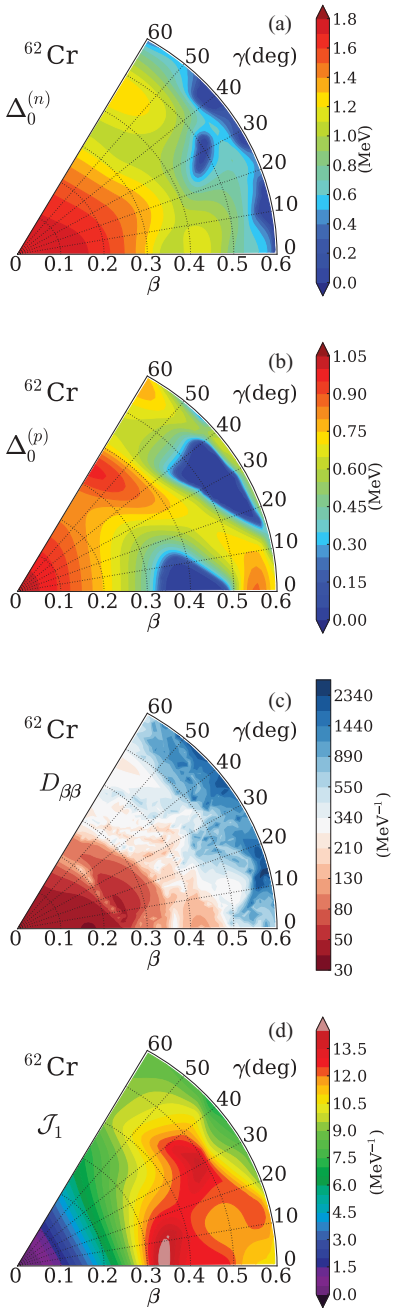

FIG. 3. (Color online) (a) Neutron monopole pairing gap $\Delta_0^{(n)}(\beta,\gamma)$, calculated for ^{62}Cr. (b) Proton monopole pairing gap $\Delta_0^{(p)}(\beta,\gamma)$. (c) Vibrational inertial function $D_{\beta\beta}(\beta,\gamma)$. (d) Rotational moment of inertia $\mathcal{J}_1(\beta,\gamma)$.

to the deformed shell gaps for $N = 38$ and $Z = 24$, see Fig. 2. In particular, the proton pairing gap almost vanishes. It results in the increase of the moment of inertia. As we shall see later, this enhancement promotes the localization of the vibrational wave functions in the (β,γ) plane for excited states with nonzero angular momenta. The rotational and vibrational inertial functions for the other isotopes are qualitatively the same as those for ^{62}Cr. The enhancement of the moments of inertia mentioned above grows gradually with increasing neutron number up to $N = 40$.

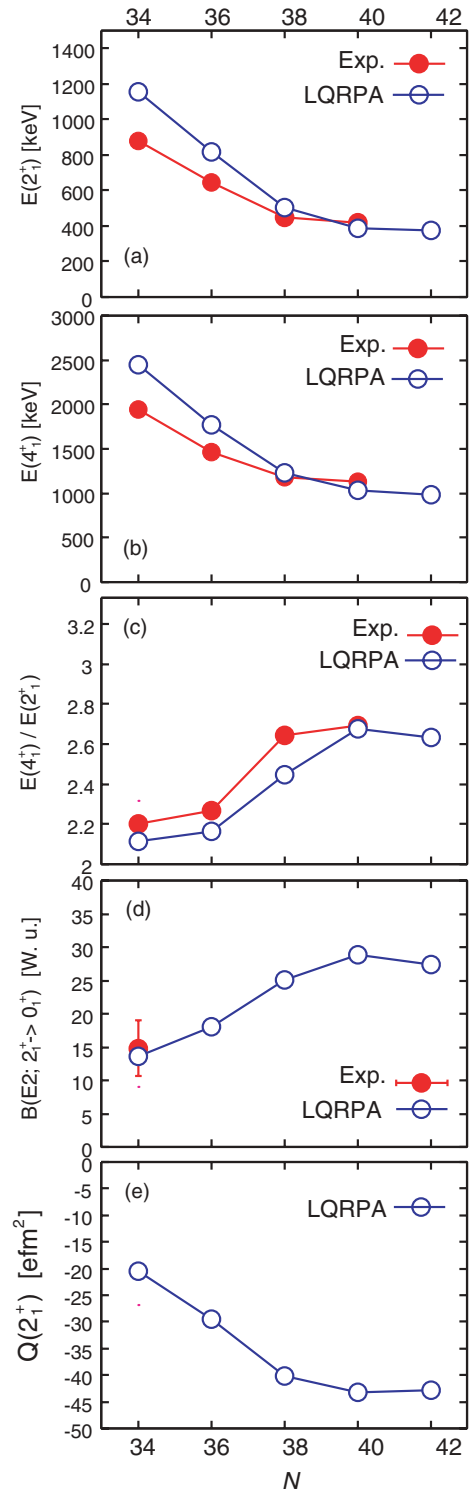

FIG. 4. (Color online) (a) Excitation energies of the 2_1^+ states for $^{58-66}$Cr. (b) Excitation energies of the 4_1^+ states. (c) Ratios of $E(4_1^+)$ to $E(2_1^+)$. (d) Reduced $E2$ transition probabilities $B(E2; 2_1^+ \to 0_1^+)$ in Weisskopf units. (e) Spectroscopic quadrupole moments of the 2_1^+ states. Experimental data are taken from Refs. [2,3,5,6].

B. Yrast states in $^{58-66}$Cr

We show in Fig. 4 the excitation energies of the 2_1^+ and 4_1^+ states, their ratios $R_{4/2}$, the $E2$ transition strengths

TABLE I. Excitation energies of the 2_1^+ state $E(2_1^+)$ in keV, the ratios $R_{4/2}$ of $E(4_1^+)$ to $E(2_1^+)$, and $B(E2; 2_1^+ \to 0_1^+)$ in Weisskopf units for ^{64}Cr and ^{66}Fe. Experimental data are taken from Refs. [6,28].

	Calc.			Exp.		
	$E(2_1^+)$	$R_{4/2}$	$B(E2)$	$E(2_1^+)$	$R_{4/2}$	$B(E2)$
^{64}Cr	386	2.68	28.8	420	2.69	
^{66}Fe	685	2.29	15.5	573	2.47	21.0

$B(E2; 2_1^+ \to 0_1^+)$, and the spectroscopic quadrupole moments of the 2_1^+ states, together with the available experimental data. The decrease in the excitation energies of the 2_1^+ and 4_1^+ states toward $N = 40$ and the increase in their ratio from $N = 36$ to $N = 40$ are well described and indicate that the nature of the quadrupole collectivity gradually changes from vibrational to rotational as the neutron number increases. However, the ratio $R_{4/2}$ at $N = 40$ is still 2.68, which is considerably smaller than the rigid-rotor value 3.33. The $B(E2)$ values and spectroscopic quadrupole moments $Q(2_1^+)$ also suggest the onset of deformation: $B(E2)$ increases and the magnitude of the spectroscopic quadrupole moments, which has a negative sign indicating a prolate shape, increase with increasing neutron number and both of them reach a maximum at $N = 40$.

In Table I, we compare the results for ^{64}Cr with those for ^{66}Fe. (In the calculation for ^{66}Fe, the single-particle energies and the P + Q parameters are determined following the same procedure as explained in Sec. II C. In particular, the latter are exactly the same as those for ^{66}Cr.) Experimental data indicate that the quadrupole collectivity is stronger in ^{64}Cr than in ^{66}Fe: the smaller $E(2_1^+)$ and the larger $R_{4/2}$ and $B(E2)$ values for ^{64}Cr than those for ^{66}Fe. Our calculation reproduces these features quite well.

We depict in Figs. 5 and 6 the squared vibrational wave functions multiplied by β^4 for the 0_1^+, 2_1^+ and 4_1^+ states in $^{58-66}$Cr and those without the β^4 factor for the 0_1^+ and 2_1^+ states in ^{60}Cr and ^{64}Cr, respectively. The β^4 factor comes from the volume element and carries its dominant β dependence [see Eqs. (11) and (13)]. The wave functions look quite different between the two cases. For instance, while the nonweighted 0_1^+ wave function for ^{60}Cr shown in Fig. 6 distributes around the spherical shape, the β^4 factor changes it to the arcuate pattern seen in Fig. 5. In ^{58}Cr and ^{60}Cr, the β^4-weighted 0_1^+ wave functions exhibit arcuate distributions around $\beta = 0.2$ covering the entire γ region. Closely looking, one finds that, while the distribution for ^{58}Cr is almost uniform in the γ direction, it is slightly leaning to the prolate side for ^{60}Cr.

With increasing neutron number, the 0_1^+ wave function localizes more and more on the prolate side, reflecting the deepening of the prolate minima (see the collective potential in Fig. 1). In ^{62}Cr, the 0_1^+ wave function still spreads over the entire γ region, although it has a clear concentration on the prolate side. In ^{64}Cr, one can see a distinct peak around the prolate potential minimum, and the 0_1^+ wave function is most localized at ^{64}Cr. The vibrational wave functions clearly indicate the shape transition from spherical to prolate along the isotopic chain.

For all these isotopes, one can see that the prolate peak grows with increasing angular momentum. This is due to the enhancement of the moments of inertia on the prolate side we have already seen in Fig. 3. Even in ^{58}Cr whose ground state is rather spherical, the 2_1^+ and 4_1^+ states are weakly localized

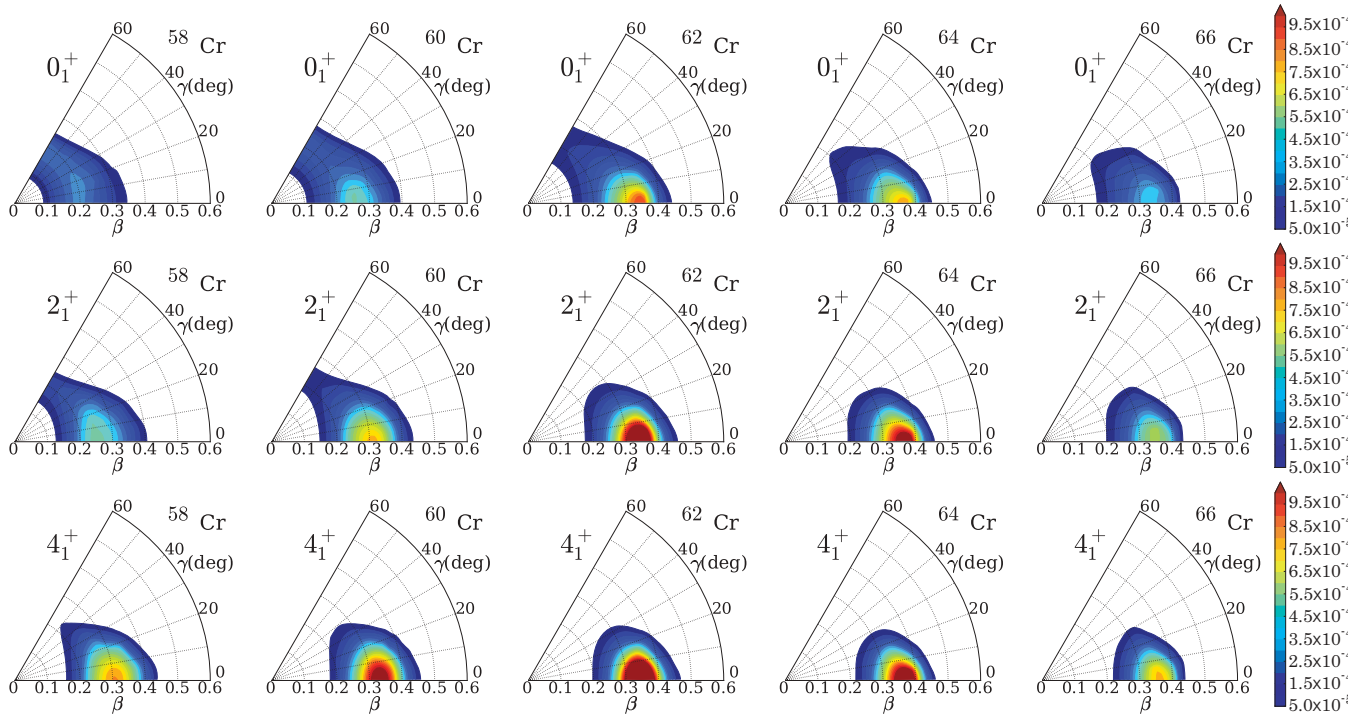

FIG. 5. (Color online) Squared vibrational wave functions multiplied by β^4, $\beta^4 \sum_K |\Psi_{\alpha IK}(\beta, \gamma)|^2$, for the 0_1^+, 2_1^+, and 4_1^+ states in $^{58-66}$Cr.

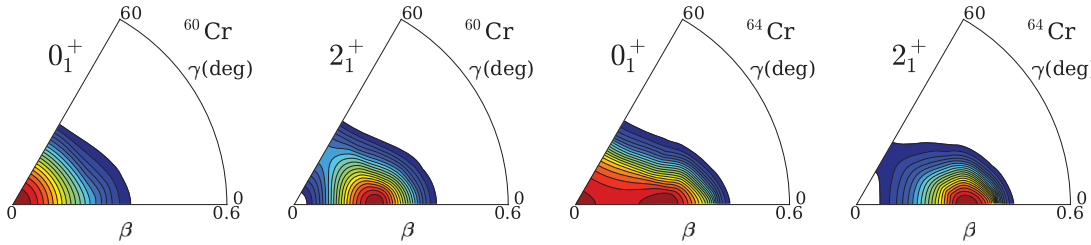

FIG. 6. (Color online) Vibrational wave function squared, $\sum_K |\Psi_{\alpha IK}(\beta, \gamma)|^2$, for the 0_1^+ and 2_1^+ states in ^{60}Cr and ^{64}Cr. The contour lines are drawn at every twentieth part of the maximum value.

on the prolate side, which results in the finite spectroscopic quadrupole moment shown in Fig. 4. In ^{64}Cr, the 2_1^+ and 4_1^+ wave functions are well localized on the prolate side, although the ground state wave function still exhibits non-negligible shape fluctuation in the γ direction. Due to the growth of localization of the wave functions, higher angular momentum states acquire more rotor-like character than the ground state. This fact can be quantified by calculating the ratio

$$R_{6/4/2} \equiv (E(6_1^+) - E(2_1^+))/(E(4_1^+) - E(2_1^+)). \qquad (24)$$

For instance, $R_{6/4/2} = 2.42$ for ^{64}Cr, which is fairly close to the rigid-rotor value 2.57, although the calculated $R_{4/2}$ is 2.67 which is far from the rigid-rotor value 3.33. These results clearly indicate the importance of dynamical effects of rotation on the nuclear shape.

Lenzi *et al.* [7] evaluated the intrinsic quadrupole moments $Q_{\rm int}(I)$ for the yrast states of $^{62-66}$Cr using the spectroscopic quadrupole moments $Q(I)$ obtained in their shell-model calculation and the well-known relation between them for the axially symmetric deformation with $K = 0$. The resulting $Q_{\rm int}(I)$ stay approximately constant along the yrast sequences in ^{62,64,66}Cr, and they interpreted this as a fingerprint of a rigid rotor behavior. We have evaluated $Q_{\rm int}(I)$ in the same way as Lenzi *et al.* but using our calculated $Q(I)$. The resulting $Q_{\rm int}(I)$ values are similar to those of Lenzi *et al.* We feel, however, that this fact is insufficient to conclude that $^{62-66}$Cr are good rotors because $Q(I)$ are average values that are insensitive to the shape fluctuations. We need to examine the properties of nonyrast states which are sensitive to shape fluctuation effects. We also note that $Q(I)$ does not carry direct information about the ground state, and that, according to our calculation, the ground-state vibrational wave function is significantly different from those of the other yrast states with $I \neq 0$.

C. Nonyrast states in $^{58-66}$Cr

To understand the nature of quadrupole collectivity, it is important to examine the properties of the excited bands including their interband transitions to the ground band, although they have not been observed experimentally yet. As typical examples of the calculated results, we display in Figs. 7 and 8 the excitation spectra and the $B(E2)$ values of the low-lying states in ^{60}Cr and ^{64}Cr. (The low-lying states of ^{58}Cr and ^{66}Cr have qualitatively the same features as those of ^{60}Cr and ^{64}Cr, respectively. Those of ^{62}Cr have an intermediate character between ^{60}Cr and ^{64}Cr.)

Let us first discuss the ^{60}Cr case. We notice that the calculated excitation spectrum exhibits some features characteristic of the 5D harmonic oscillator (HO) limit: approximately equal level spacing in the ground band, approximate degeneracy of the 4_1^+ and 2_2^+ states, nearly equal values of $B(E2; 0_2^+ \to 2_1^+)$ and $B(E2; 4_1^+ \to 2_1^+)$, which are about twice of $B(E2; 2_1^+ \to 0_1^+)$, etc. On the other hand, we also notice significant

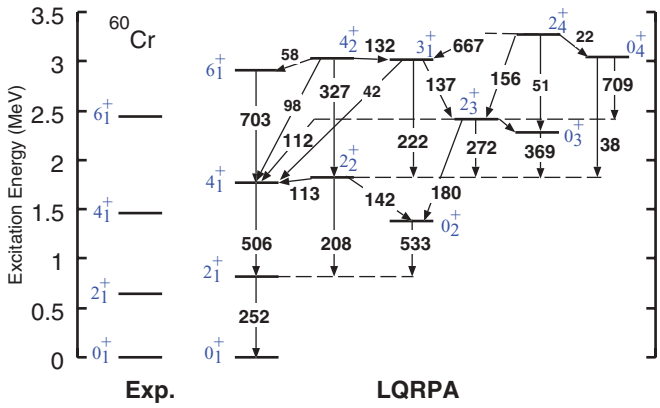

FIG. 7. (Color online) Excitation energies and $B(E2)$ values for ^{60}Cr in comparison with experimental data. Values on arrows indicate $B(E2)$ in units of e^2fm^4. Only $B(E2)$ values larger than 1 Weisskopf unit are shown. Experimental data are taken from Ref. [3].

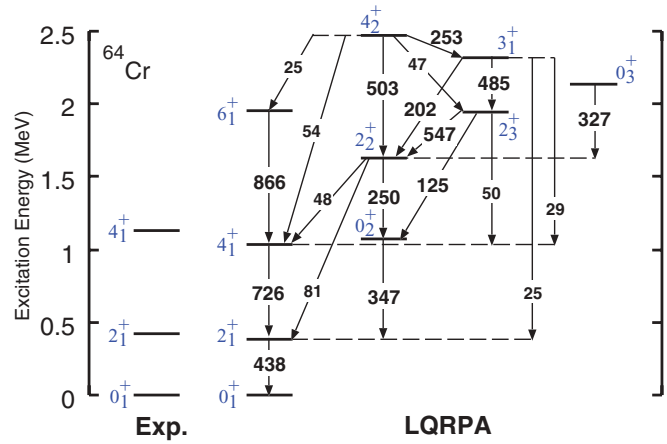

FIG. 8. (Color online) Same as Fig. 7 but for ^{64}Cr. The experimental data are taken from Ref. [6].

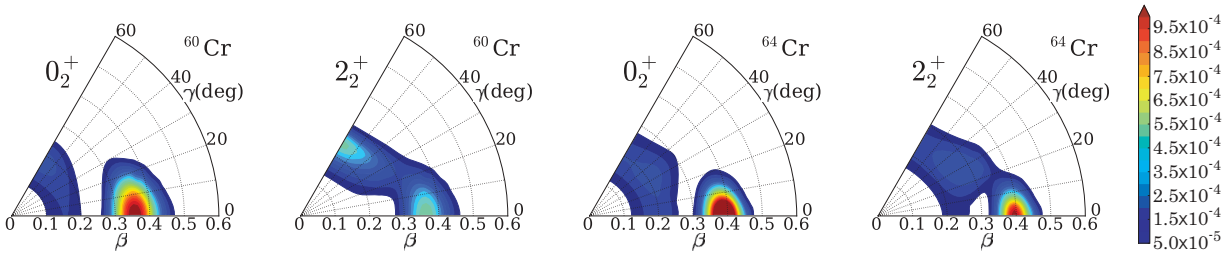

FIG. 9. (Color online) Squared vibrational wave functions multiplied by β^4, $\beta^4 \sum_K |\Psi_{\alpha IK}(\beta,\gamma)|^2$, for the 0_2^+ and 2_2^+ states in ^{60}Cr and ^{64}Cr.

deviations from that limit. First, the 0_2^+ state is considerably lower than the 4_1^+ and 2_2^+ states. Second, the $E2$ transitions forbidden in the HO limit are sizable; e.g., those from the 2_2^+ state to the 4_1^+ and 0_2^+ states are fairly large. Third, the $B(E2)$ value from the 2_2^+ state to the 2_1^+ state is less than half of those from the 4_1^+ and 0_2^+ states.

To examine these anharmonicities, let us look into the vibrational wave functions of the excited states. The β^4-weighted and nonweighted vibrational wave functions of the 0_2^+ and 2_2^+ states are displayed in Figs. 9 and 10, respectively. The 0_2^+ wave function exhibits two components: one around the spherical shape and the other around $\beta = 0.35$. Although it has a β-vibrational feature, i.e., a node in the β direction, it also exhibits a considerable deviation from the 5D HO limit, in which the deformed component concentrating on the prolate side would spread uniformly over the γ direction. We can see a deviation from the 5D HO limit also in the 2_2^+ state. The β^4-weighted 2_2^+ wave function spreads from the prolate to the oblate sides. However, the nonweighted wave function reveals that it also has the β-vibrational component. In fact, this state is a superposition of the large-amplitude γ-vibrational component spreading over the entire γ region and the β-vibrational component. In the 5D HO limit, the 2_3^+ wave function has a node in the β direction, while the 2_2^+ wave function has no node. The calculated 2_2^+ wave functions indicate significant mixing of these components.

Let us proceed to the ^{64}Cr case. We immediately notice some features different from ^{60}Cr. First, the approximate degeneracy of the 4_1^+ and 2_2^+ states seen in ^{60}Cr is completely lifted here. Second, the $E2$ transitions within the ground band are much stronger than those in ^{60}Cr. Third, two low-lying excited bands appear: one consisting of the 0_2^+, 2_2^+ and 4_2^+ states (excited band I), and the other consisting of the 2_3^+, 3_1^+, 4_3^+ states (excited band II, the 4_3^+ state not shown here is at 2.84 MeV). One might be tempted to interpret these excited bands in terms of the conventional concept of the β and γ bands built on a well-deformed prolate ground state, but, in fact, they are markedly different from them. First, there is a strong mixing of the β- and γ-vibrational components, as seen from strong interband $E2$ transitions between the two excited bands. Second, the calculated ratio of the excitation energies relative to $E(0_2^+)$, $(E(4_2^+) - E(0_2^+))/(E(2_2^+) - E(0_2^+))$, is 2.51, which is far from the rigid-body value. Third, the K-mixing effects are strong, e.g., the $K = 0$ ($K = 2$) components of the 2_2^+ (2_3^+) and 4_2^+ (4_3^+) wave functions are at most 60%. To sum up, although the prolate deformation is appreciably developed in the low-lying states of ^{64}Cr, the large-amplitude shape fluctuations play a dominant role and lead to the strong $\beta - \gamma$ coupling and significant interband $E2$ transitions.

In Fig. 11, we plot the vibrational wave functions at $\gamma = 0.5^\circ$ and the probability density $P(\beta)$ of finding a shape with a specific value of β for the ground and excited 0^+ states in $^{60-64}$Cr. Note that the probability density vanishes at the spherical shape because of the β^4 factor in the volume element. It is seen that, while the ground-state wave function for ^{60}Cr distributes around the spherical shape, those for ^{62}Cr and ^{64}Cr extend from the spherical to deformed regions with $\beta \simeq 0.4$ [see Fig. 11(a)]. Accordingly, the peak of the probability distribution moves toward larger β in going from ^{60}Cr to ^{64}Cr [see Fig. 11(b)]. Concerning the excited 0^+ states, their vibrational wave functions exhibit two peaks: a large peak at the spherical shape and a small peak at a prolate shape [see Fig. 11(c)]. In the probability distribution displayed in Fig. 11(d), the spherical peaks move to the $\beta \approx 0.2$ region and the peaks at $\beta = 0.35$–0.4 in turn become prominent.

The above results indicate that large-amplitude shape fluctuations play an important role both in the ground and excited 0^+ states. The growth of the shape fluctuations leads to an enhancement of the calculated $E0$ transition strengths $\rho^2(E0; 0_2^+ \to 0_1^+)$ in going from ^{58}Cr to $^{62-66}$Cr, as displayed in Fig. 12.

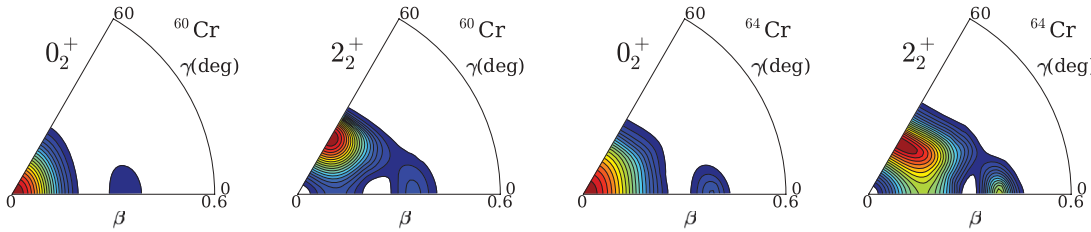

FIG. 10. (Color online) Same as Fig. 6 but for 0_2^+ and 2_2^+ states. The contour lines are drawn at every twentieth part of the maximum value.

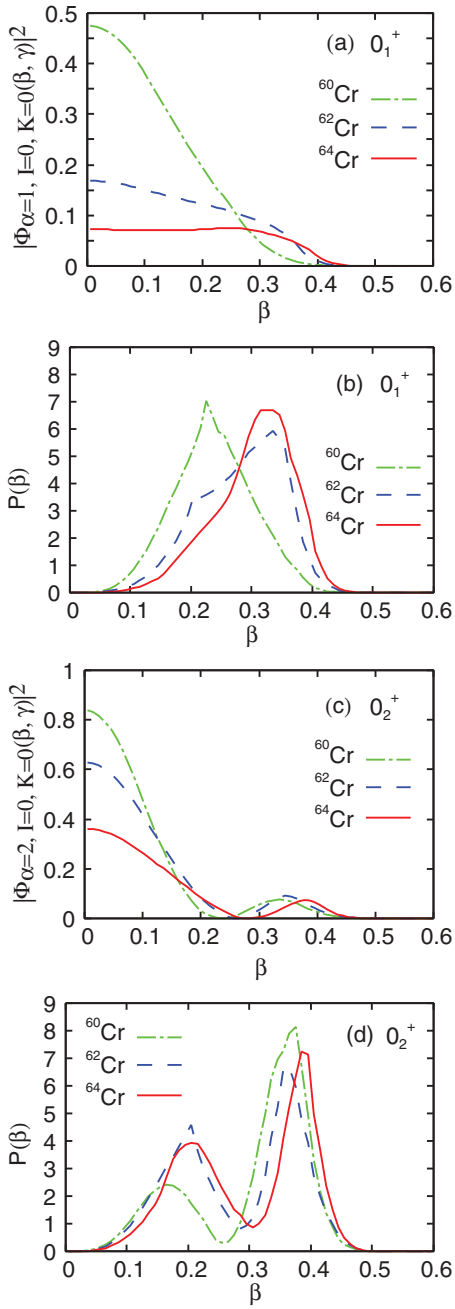

FIG. 11. (Color online) (a) Vibrational wave function squared $|\Phi_{\alpha=1,I=0,K=0}(\beta,\gamma=0.5^\circ)|^2$ of the ground states in $^{60-64}$Cr. (b) Probability densities integrated over γ, $P(\beta)=\int d\gamma |\Phi_{\alpha=1,I=0,K=0}(\beta,\gamma)|^2 |G(\beta,\gamma)|^{1/2}$. (c) Same as (a) but for the 0_2^+ states. (d) Same as (b) but for the 0_2^+ states.

In Ref. [9], Gaudefroy *et al.* studied the collective structure in the $N=40$ isotones and obtained the low-lying states with a vibrational character for ^{64}Cr. Our calculated results indicates that ^{64}Cr is rather deformed but still has a transitional character.

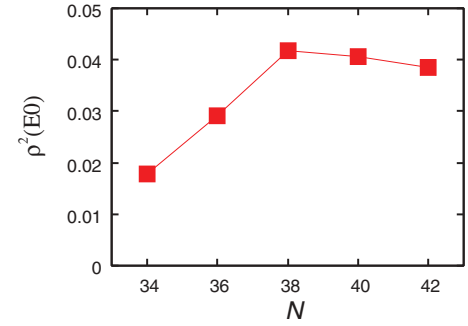

FIG. 12. (Color online) $E0$ transition strengths $\rho^2(E0;0_2^+\rightarrow 0_1^+)$ calculated for $^{58-66}$Cr.

D. Similarities and differences with the Mg isotopes around $N=20$

In Ref. [7], Lenzi *et al.* emphasized similarities between the shell structure of the neutron-rich Cr isotopes near $N=40$ and that of the neutron-rich Mg isotopes around $N=20$: the neutron $g_{9/2}$ and $d_{5/2}$ single-particle levels above the $N=40$ subshell play a similar role to the neutron $f_{7/2}$ and $p_{3/2}$ levels above the $N=20$ shell. The quadrupole matrix elements between these levels are large (because they are spin-nonflip and $\Delta l=2$). The single-particle levels above and below the $N=40$ subshell gap ($N=20$ shell gap) have opposite parities so that the pairing excitations across the gap play an indispensable role to activate the role of the $g_{9/2}$ and $d_{5/2}$ levels ($f_{7/2}$ and $p_{3/2}$ levels) in generating quadrupole collectivity. Also, for protons, the $f_{7/2}$ and $p_{3/2}$ levels in Cr isotopes may play a parallel role to the $d_{5/2}$ and $s_{1/2}$ levels in Mg isotopes.

Indeed, we have found notable similarities between Cr isotopes near $N=40$ and Mg isotopes around $N=20$ in our calculation. First of all, the growth of quadrupole collectivity in going from ^{60}Cr to ^{64}Cr is similar to that from ^{30}Mg to ^{32}Mg. In Fig. 6, while the ground state wave function in ^{60}Cr distributes around the spherical shape, they are considerably extended to the prolately deformed region in ^{64}Cr. The 2_1^+ wave function has a peak on the prolate side in ^{60}Cr and it shifts to larger β in ^{64}Cr. These features are similar to those seen in going from ^{30}Mg to ^{32}Mg in our calculation [21]. Concerning the excited 0_2^+ states in ^{60}Cr and ^{64}Cr, as shown in Figs. 11(c) and 11(d), both vibrational wave functions exhibit a two-hump structure. Similar two-hump structures of the excited 0^+ states have been obtained also in our calculation for ^{30}Mg and ^{32}Mg.

On the other hand, we have also found significant differences between the ^{64}Cr region and the ^{32}Mg region. First of all, the K mixing is strong in the excited bands in the Cr isotopes, whereas they are weak in the Mg region. The shape fluctuations toward the γ direction and the effect of the $\beta-\gamma$ coupling are larger in the Cr isotopes than in Mg. This can be clearly seen, for instance, in the 2_2^+ wave functions displayed in Figs. 9 and 10. Lenzi *et al.* [7] found significant mixture of n-particle–n-hole excitations (n =2,4 and 6) to the wave functions of Cr isotopes in their shell model calculation. This is consistent with the strong K-mixing found in our calculation.

IV. CONCLUSIONS

In this paper, we have investigated the nature of the quadrupole collectivity in the low-lying states of neutron-rich Cr isotopes $^{58-66}$Cr by solving the 5D collective Schrödinger equation. The vibrational and rotational inertial functions and the collective potential in the 5D quadrupole collective Hamiltonian are microscopically derived with use of the CHFB + LQRPA method. The calculated inertial functions include the contributions from the time-odd components of the moving mean field. The results of calculation are in good agreement with the available experimental data. The prolate deformation remarkably develops along the isotopic chain from $N = 36$ to 40. It is not appropriate, however, to characterize the low-lying state of Cr isotopes around ^{64}Cr in terms of the prolate rigid-rotor model: the excitation spectra are still transitional and the large-amplitude shape fluctuations dominate in their low-lying states. The calculated excited bands exhibit strong couplings between the β and γ vibrational degrees of freedom. For close examination of the nature of quadrupole collectivity in these nuclei, experimental exploration of their excited bands is strongly desired.

ACKNOWLEDGMENTS

The numerical calculations were carried out on SR16000 at Yukawa Institute for Theoretical Physics in Kyoto University and RIKEN Integrated Cluster of Clusters (RICC) facility. This work is supported by KAKENHI (Nos. 20105003, 21340073, 23540294, and 23740223).

[1] O. Sorlin *et al.*, Eur. Phys. J. A **16**, 55 (2003).
[2] A. Bürger *et al.*, Phys. Lett. B **622**, 29 (2005).
[3] S. Zhu *et al.*, Phys. Rev. C **74**, 064315 (2006).
[4] N. Aoi *et al.*, Nucl. Phys. A **805**, 400c (2008).
[5] N. Aoi *et al.*, Phys. Rev. Lett. **102**, 012502 (2009).
[6] A. Gade *et al.*, Phys. Rev. C **81**, 051304(R) (2010).
[7] S. M. Lenzi, F. Nowacki, A. Poves, and K. Sieja, Phys. Rev. C **82**, 054301 (2010).
[8] H. Oba and M. Matsuo, Prog. Theor. Phys. **120**, 143 (2008).
[9] L. Gaudefroy, A. Obertelli, S. Péru, N. Pillet, S. Hilaire, J.-P. Delaroche, M. Girod, and J. Libert, Phys. Rev. C **80**, 064313 (2009).
[10] K. Kaneko, Y. Sun, M. Hasegawa, and T. Mizusaki, Phys. Rec. C **78**, 064312 (2008).
[11] Y. Yang, Y. Sun, K. Kaneko, and M. Hasegawa, Phys. Rec. C **82**, 031304(R) (2010).
[12] M. Baranger and K. Kumar, Nucl. Phys. A **110**, 490 (1968).
[13] K. Kumar and M. Baranger, Nucl. Phys. A **110**, 529 (1968).
[14] N. Hinohara, T. Nakatsukasa, M. Matsuo, and K. Matsuyanagi, Prog. Theor. Phys. **119**, 59 (2008).
[15] N. Hinohara, T. Nakatsukasa, M. Matsuo, and K. Matsuyanagi, Phys. Rev. C **80**, 014305 (2009).
[16] N. Hinohara, K. Sato, T. Nakatsukasa, M. Matsuo, and K. Matsuyanagi, Phys. Rev. C **82**, 064313 (2010).
[17] M. Matsuo, T. Nakatsukasa, and K. Matsuyanagi, Prog. Theor. Phys. **103**, 959 (2000).
[18] N. Hinohara, T. Nakatsukasa, M. Matsuo, and K. Matsuyanagi, Prog. Theor. Phys. **117**, 451 (2007).
[19] K. Sato and N. Hinohara, Nucl. Phys. A **849**, 53 (2011).
[20] H. Watanabe *et al.*, Phys. Lett. B **704**, 270 (2011).
[21] N. Hinohara, K. Sato, K. Yoshida, T. Nakatsukasa, M. Matsuo, and K. Matsuyanagi, Phys. Rev. C **84**, 061302 (2011).
[22] K. Yoshida and N. Hinohara, Phys. Rev. C **83**, 061302(R) (2011).
[23] K. Kumar and M. Baranger, Nucl. Phys. A **92**, 608 (1967).
[24] D. J. Thouless and J. G. Valatin, Nucl. Phys. **31**, 211 (1962).
[25] M. V. Stoitsov, J. Dobaczewski, W. Nazarewicz, and P. Ring, Comp. Phys. Comm. **167**, 43 (2005).
[26] National Nuclear Data Center, Brookhaven National Laboratory, http://www.nndc.bnl.gov/.
[27] H. Sakamoto and T. Kishimoto, Phys. Lett. B **245**, 321 (1990).
[28] W. Rother *et al.*, Phys. Rev. Lett. **106**, 022502 (2011).

Existence of an Exotic Torus Configuration in High-Spin Excited States of ^{40}Ca

T. Ichikawa,[1] J. A. Maruhn,[2] N. Itagaki,[1] K. Matsuyanagi,[1,3] P.-G. Reinhard,[4] and S. Ohkubo[5,6]

[1]*Yukawa Institute for Theoretical Physics, Kyoto University, Kyoto 606-8502, Japan*
[2]*Institut für Theoretische Physik, Universität Frankfurt, D-60438 Frankfurt, Germany*
[3]*RIKEN Nishina Center, Wako 351-0198, Japan*
[4]*Institut für Theoretische Physik, Universität Erlangen, D-91058 Erlangen, Germany*
[5]*Department of Applied Science and Environment, University of Kochi, Kochi 780-8515, Japan*
[6]*Research Center for Nuclear Physics, Osaka University, Ibaraki, Osaka 567-0047, Japan*

(Received 26 July 2012; published 5 December 2012)

We investigate the possibility of the existence of the exotic torus configuration in the high-spin excited states of ^{40}Ca. We here consider the spin alignments about the symmetry axis. To this end, we use a three-dimensional cranked Skyrme Hartree-Fock method and search for stable single-particle configurations. We find one stable state with the torus configuration at the total angular momentum $J = 60\,\hbar$ and an excitation energy of about 170 MeV in all calculations using various Skyrme interactions. The total angular momentum $J = 60\,\hbar$ consists of aligned 12 nucleons with the orbital angular momenta $\Lambda = +4$, $+5$, and $+6$ for spin-up or -down neutrons and protons. The obtained results strongly suggest that a macroscopic amount of circulating current breaking the time-reversal symmetry emerges in the high-spin excited state of ^{40}Ca.

DOI: 10.1103/PhysRevLett.109.232503 PACS numbers: 21.60.Jz, 21.60.Ev, 27.40.+z

The investigations of nuclei rotating extremely fast about the symmetry axis provide a good opportunity to severely test the fundamental theory of quantum mechanics. In a classical picture for such rotation, the oblate deformations develop with increasing rotational frequencies due to the strong centrifugal force [1]. However, such a collective rotation about the symmetry axis is quantum-mechanically forbidden. Instead, the spins and the orbital angular momenta of single particles are aligned with the symmetry axis building extremely high angular momenta [2,3]. In this case, the total angular momentum of the nucleus is just the sum of the symmetry-axis components of those of the single particles. Bohr and Mottelson pointed out that in such a nucleus, a ''macroscopic'' amount of circulating current breaking the time-reversal symmetries emerges, which is a fascinating new form of the nuclear matter [4].

A typical example of such phenomena is the high-K oblate isomer states in ^{152}Dy [5]. In the high angular-momentum states above $I = 14\,\hbar$, the observed excited states are irregularly distributed around the average yrast line, which is calculated by assuming a macroscopic nuclear shape with the strongly oblate deformations ($\beta \sim -0.3$). The emergence of these high-spin isomers around the yrast line can be naturally explained by the single-particle alignments [4], because the E2 transitions, which are a characteristic quantity related to the rotational collectivity, are strongly forbidden for those nuclei. In addition, the γ transitions are strongly suppressed due to the large difference of the internal structure between the initial and final states. Those high-spin isomers around the yrast line are thus called ''yrast traps.'' Many experiments have been attempted to produce yrast traps with extremely high spins [6]. The observed highest angular momentum in this category is $I = 49\,\hbar$ in ^{158}Er [7].

In this Letter, we investigate the possibility of the existence of the *torus* configuration as an extreme limit of the high-spin oblate isomers. In such a limit, more nucleons with higher orbital angular momentum are aligned and its density is much denser at the equator. We here consider a special case for the existence of the density only around its equator. We below show that such an exotic state can indeed exist at an extremely high angular momentum in ^{40}Ca.

Many theoretical calculations have been performed to search for the high spin states with strongly oblate deformations in a wide range of nuclei. Those studies have been mainly focused on the nuclei with the oblate deformation at around $\beta \sim -0.3$, heavier than ^{40}Ca [3]. In contrast, Wong discussed the stability of the torus configuration using the macroscopic-microscopic model for a wide range of nuclear systems [8–10]. The calculations using the constraint Hartree-Fock (-Bogoliubov) models have been also performed for heavy-mass systems [11,12]. The calculations using the α cluster model have been attempted to obtain the ring configurations consisting of alpha particles and extra neutrons [13]. However, as shown in the present study, an essential mechanism for the stability of such configuration is the extremely high angular momentum directed to the symmetry axis, resulting in the breaking of the time-reversal symmetry in the intrinsic state.

To investigate the possibility of the existence of the torus configuration in ^{40}Ca with high angular momentum, we use the three-dimensional Skyrme Hartree-Fock (HF) method

with a Lagrange multiplier, which is introduced to obtain the single-particle states aligned with the symmetry axis. To this end, we minimize the HF Hamiltonian, $\hat{H}$, with the Lagrange multiplier, ω. In the present study, we take the z axis as the symmetry axis. We first define the effective Hamiltonian, $\hat{H}'$, given by $\hat{H}' = \hat{H} - \omega\hat{J}_z$, where $\hat{J}_z$ denotes the operator for the sum of the z components of the total angular-momentum for each single particle, $\hat{j}_z$, given by $\hat{J}_z = \sum_i \hat{j^{(i)}}_z$. In the HF approximation, $\hat{H}'$ is rewritten as $\hat{H}' = \sum_i \{\hat{h}_i - \omega \hat{j^{(i)}}_z\}$, where $\hat{h}_i$ denotes the Hamiltonian for each single particle. The eigenvalue of H' is given by $\langle \hat{H}' \rangle = \sum_i \{(e_i - \lambda) - \hbar\omega\Omega_i\}$, where λ denotes the Fermi energy at $\omega = 0$ and e_i and Ω_i denote the energy and the z component of the total angular momentum in the unit of $\hbar$ for each single particle, respectively. In the present study, we search for the stable state using the equivalent cranked Skyrme HF equation, $\delta\langle \hat{H} - \omega\hat{J}_z \rangle = 0$ [14,15], by scanning a large range of ω.

Before the HF calculations, we discuss the shell structure of the torus configuration using the radial displaced harmonic oscillator (RDHO) model [9]. For the torus configuration, not only Ω but also the z component of the orbital angular momentum Λ are good quantum numbers ($\Omega = \Lambda + \Sigma$, where Σ denotes the z component of the spin values, $\pm 1/2$). Two nucleons in each Λ energetically degenerate with the different spin values. At $\hbar\omega = 0$, the lowest configuration for ^{40}Ca is $\Lambda = 0, \pm 1, \pm 2, \pm 3$, and ± 4 and the residual two nucleons can occupy any two states with $\Lambda = \pm 5$. At $\hbar\omega \neq 0$, the possible spin aligned configurations are (i) $\Lambda = 0, \pm 1, \pm 2, \pm 3, \pm 4$, and $+5$ for the total angular momentum $J = 20\hbar$ [$= 5\hbar \times 2$ (spin degeneracy) $\times 2$ (isospin degeneracy)], (ii) $\Lambda = 0, \pm 1, \pm 2, \pm 3, +4, +5$, and $+6$ for $J = 60\hbar$ [$= 15\hbar \times 2 \times 2$], and (iii) $\Lambda = 0, \pm 1, \pm 2, +3, +4, +5, +6$, and $+7$ for $J = 100\hbar$ [$= 25\hbar \times 2 \times 2$].

In the self-consistent calculations, the single-particle wave functions are described on a Cartesian grid with a grid spacing of 1.0 fm. We take $32 \times 32 \times 24$ grid points for the x, y, and z directions, respectively. This was sufficiently accurate to provide converged configurations. The damped-gradient iteration method [16] is used, and all derivatives are calculated using the Fourier transform method. We take three different Skyrme forces which all perform well concerning nuclear bulk properties but differ in details: SLy6 as a recent fit which includes information on isotopic trends and neutron matter [17], and SkI3 and SkI4 as recent fits especially for the relativistic isovector structure of the spin-orbit force [18]. However, except for the effective mass, the bulk parameters (equilibrium energy and density, incompressibility, and symmetry energy) are comparable in the all interactions.

For the initial wave functions, we chose the ring configuration with 10 α particles placed on the x-y plane, as shown in Fig. 1(a). Each α particle is described by the Gaussian function with its center placed on $z = 0$. Using

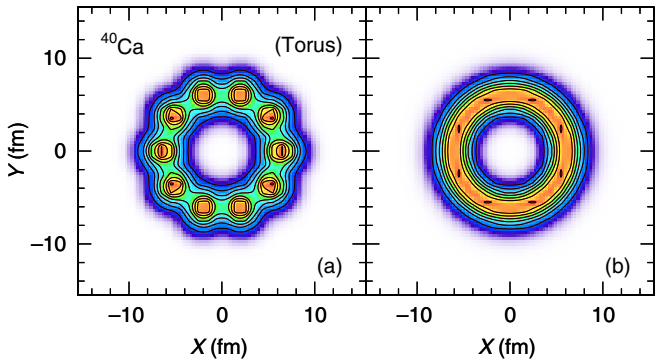

FIG. 1 (color online). Total density for (a) the initial condition of the HF iterations and (b) the calculated result with $\hbar\omega = 1.5$ MeV at the 15 000 HF iterations. The density is integrated in the z direction. The contours correspond to multiple steps of 0.05 fm^{-2}. The color (gray scale) is normalized by the largest density in each plot.

this initial condition, we perform the HF iterations with 15 000 times and investigate the convergence of the calculated results. Figure 2 shows the convergence behaviors of $\langle \hat{J}_z \rangle$ versus the number of the HF iterations with various ω's using the SLy6 interaction. We can see that the result calculated with $\hbar\omega = 1.5$ MeV converges rapidly to $J_z = 60\hbar$. Figure 1(b) shows the density obtained with $\hbar\omega = 1.5$ MeV at the 15 000th iteration step. The calculated result is indeed the torus configuration. The obtained density distribution, $\rho(r, z)$, can be well fitted by $\rho(r, z) = \rho_0 e^{-\{(r-r_0)^2+z^2\}/\sigma^2}$, where $\rho_0 = 0.13$ fm^{-3}, $r_0 = 6.07$ fm, and $\sigma = 1.61$ fm for the SLy6 interaction.

On the other hand, the calculated results with $\hbar\omega = 0.5$ and 1.0 MeV lead to unstable states. That for $\hbar\omega = 2.0$ MeV leads to the fission. Although it seems that

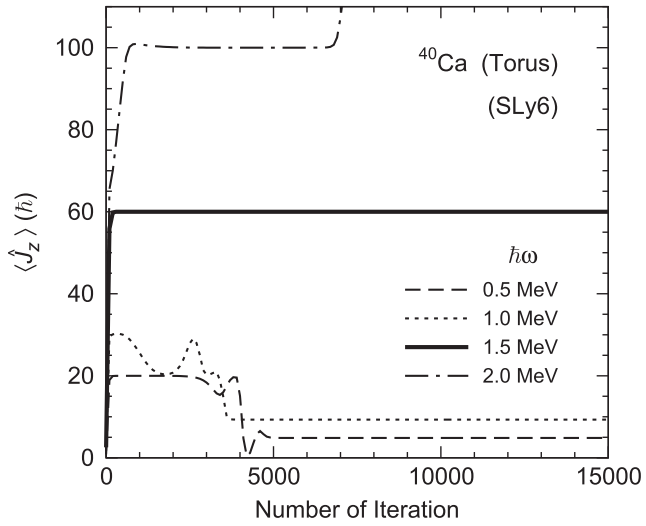

FIG. 2. Convergence behavior of the expectation value of J_z in the HF calculations versus the number of iterations. The dashed, dash-dotted, solid, and dotted lines denote the calculated results with $\hbar\omega = 0.5$, 1.0, 1.5, and 2.0 MeV, respectively.

$\langle \hat{J}_z \rangle$'s with $\hbar\omega = 0.5$ and 1.0 MeV converge at the 15 000th step, those are in fact unstable. In Fig. 2, we can see that these states first converge to a quasistable state. After that, the instability of those states increases. In those quasistable states, J_z is $20\hbar$ for $\hbar\omega = 0.5$, and 1.0 MeV and is $100\,\hbar$ for $\hbar\omega = 2.0$ MeV. Later, we will discuss those quasistable states with $J_z = 20$ and $100\,\hbar$.

We next investigate the region of the Lagrange multipliers where the torus configurations stabilize, using various Skyrme interactions. We find that such region of $\hbar\omega$ for the SLy6 and SkI3 interactions extends from 1.2 to 1.7 MeV. That for the SkI4 interaction is from 1.2 to 1.8 MeV. In such regions, we obtain the only one stable torus configuration at $J_z = 60\,\hbar$ in all calculations. The obtained excitation energies are 170.45, 174.22, and 172.53 MeV for the SLy6, SkI3, and SkI4 interactions, respectively. The fitted radius of the torus configuration is almost the same for all calculations. The dependence of the calculated result on the choice of the interaction is weak. This is mainly because that the spin-orbit forces in the radial directions of the inner and outer surface of the torus configuration almost cancel out each other [see Eq. (4.14) in Ref. [9]]. Thus, the RDHO mode is a good approximation for the present calculations.

Figure 3 shows the single-particle spectrum versus Ω calculated using the SLy6 interaction. The solid and open circles denote the single-particle states with the positive and the negative parities, respectively. The single-particle states with $\Sigma = +1/2$ and $-1/2$ are connected by the dashed and the dotted lines, respectively. These energies connected by each line are well proportional to Λ^2, which is consistent with that of the RDHO model [see Eq. (4.26) in Ref. [9]]. We here define the "sloping" Fermi energy, λ', given by $\lambda' = \lambda + \hbar\omega\Omega$ [3]. Then, the occupied states are obtained by $\langle \hat{H}' \rangle = \sum_i (e_i - \lambda')$ with $e_i < \lambda'$. The solid and the dash-dotted lines denote the sloping Fermi energies with $\hbar\omega = 1.7$ and 1.2 MeV, respectively. The occupied states are denoted by the gray area. In Fig. 3, we can clearly see that the torus configuration can exist at $J_z = 60\,\hbar$ in the region from $\hbar\omega = 1.2$ to 1.7 MeV. The total angular momentum of $J_z = 60\,\hbar$ consists of the spin-up-down pairs of the aligned single particles with the same Λ, (Ω_+, Ω_-), of $(+9/2^+, +7/2^+)$ with $\Lambda = 4$, $(+11/2^-, +9/2^-)$ with $\Lambda = 5$, and $(+13/2^+, +11/2^+)$ with $\Lambda = 6$ (see the solid ellipses in Fig. 3).

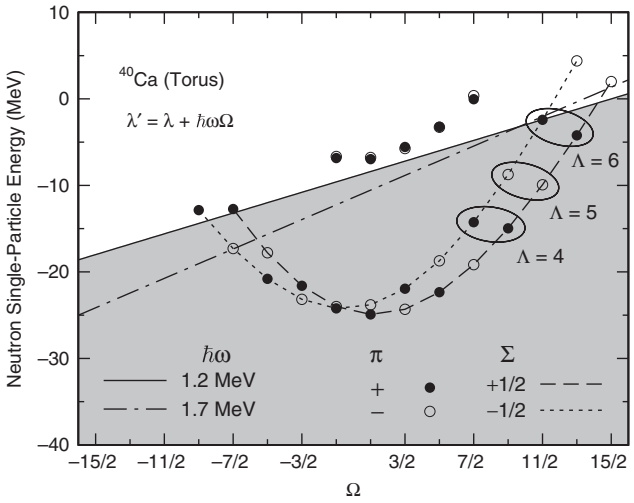

FIG. 3. Single-particle energies versus the z component of the total angular momentum Ω. The solid and open circle denote the single-particle states with the positive and the negative parties, respectively. The single-particle states with the z component of the spin $\Sigma = +1/2$ and $-1/2$ are connected by the dashed and dotted lines, respectively. The solid and the dash-dotted lines denote the sloping Fermi energies with $\hbar\omega = 1.2$ and 1.7 MeV, respectively. The gray area denotes the states below the Fermi energy for $\hbar\omega = 1.2$ MeV.

As discussed in the shell structure of the torus configuration, the states with $J = 20$, 60, and $100\,\hbar$ are the possible combinations of the spin alignment for the RDHO model. For the quasi-stable state with $J = 20\,\hbar$, the centrifugal force is insufficient to stabilize the torus configuration against the strong nuclear attractive force. On the other hand, to build the state with $J = 100\,\hbar$, the unbound states ($e > 0$) with $\Omega = +15/2$ and $+13/2$ are occupied, resulting in the instability for the torus configuration. Only for $J = 60\,\hbar$, the torus configuration can be stabilized. Thus, the stability of the state with $J = 60\,\hbar$ is rather robust. Although we have performed the similar calculations for ^{24}Mg and ^{32}S, we could not find the stable torus states for those nuclei.

As shown in the present study, if the state with the torus configuration is formed at $J = 60\,\hbar$, the macroscopic circulating current of 12 nucleons with $\Lambda = +4$, $+5$, and $+6$ strongly violates the time-reversal symmetry in the intrinsic state (see Fig. 4). It is interesting to investigate how this fascinating new state can be observed in experiments. The state with the torus configuration at $J = 60\,\hbar$ would have

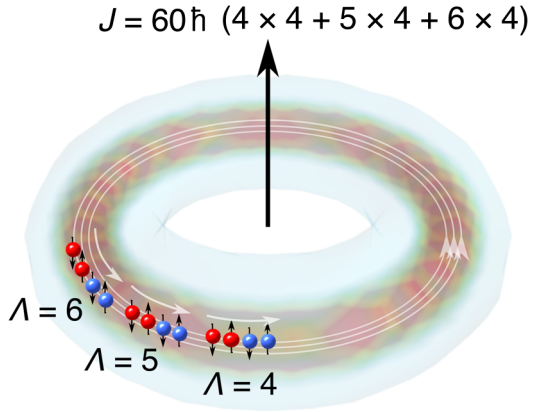

FIG. 4 (color online). Circulating currents of 12 nucleons. The outer layer of the torus surface denotes the half of the total density. The density plot in the inside of the torus surface denotes the calculated density of the aligned 12 single particles.

an extremely large magnetic moment ($\mu = 30\mu_N$). This would lead to a procession motion under an external magnetic field.

A question then arises how such a "femtoscale magnet" rotates spontaneously. When the spherical symmetry is broken, the collective rotation emerges spontaneously, in principle, to restore the broken symmetry. However, it is unclear whether such a state built with significant amount of circulating current can rotate about the perpendicular direction to the symmetry axis or not. If not, such a state would be an anomalous one, which has not yet been recognized in the experiments. Even if the state can rotate, the rotational band built on such a state would show interesting behaviors for their $M1/E2$ transition strengths and moment of inertia, $\mathcal{J}_\perp$. It is intriguing to investigate the extent of the difference between the experimental and the classical rigid-body moments of inertia ($\mathcal{J}_\perp = 20.97\hbar^2 \cdot \mathrm{MeV}^{-1}$ in the case of the SLy6 interaction).

To identify the torus configuration in the experiment, it is also important to discuss the competition to the fission decay channel. The calculation using the macroscopic model with the FRLDM2002 parameter set [19] shows that the fission barrier for the spheroidal deformations vanishes at $J = 32\hbar$ and an excitation energy of 49.27 MeV [20]. Our calculated results for the torus configuration are considerably higher than those values. However, it would be possible that the state with the torus configuration can survive against the fission. One important example for such possibility is the long-lived $K^\pi = 16^+$ isomer in ^{178}Hf with a half-lives of about 31 y [21], which is extremely long compared to other isomers (4 s for the $K^\pi = 8^-$ isomer). In this connection, it is unclear how the collective path from a topologically different torus configuration is connected to the region of the spheroidal deformations leading to the fission [10,12]. A possible decay channel of the torus configuration might be multifragmentation through the sausage mode [10]. Wong indeed showed that the torus configurations are stable from $J \sim 57$ to $74\hbar$ for mass number $A \sim 50$ [10].

In summary, we have suggested the existence of the torus configuration in the extremely high-spin excited states of ^{40}Ca using the three-dimensional cranked Skyrme HF method. We found only one stable state with the torus configuration at $J_z = 60\hbar$ in all the calculations with any Skyrme interactions. The calculated excitation energies of this state are 170.45, 174.22, and 172.53 MeV for the SLy6, SkI3, and SkI4 interactions, respectively. The obtained results are insensitive to the choice of the Skyrme interactions, because the contribution of the spin-orbit force is small in the torus configuration. To build the torus state with $J = 60\hbar$, the 6 nucleons for $\Omega = +9/2^+$ and $+7/2^+$ with $\Lambda = 4$, $\Omega = +11/2^-$ and $+9/2^-$ with $\Lambda = 5$, and $\Omega = +13/2^+$ and $+11/2^+$ with $\Lambda = 6$ are aligned with the symmetry axis for both protons and neutrons. We have shown that such configuration is built on the major shell structure estimated by the RDHO model for the rotating torus shape, indicating that the torus state is robustly stable and the macroscopic amount of the time-reversal symmetry breaking occurs. Although the observation of the torus state would be difficult, exploration for such an exotic state would provide us valuable information on the new frontier of the nuclear matter, which is a big challenge both theoretically and experimentally.

A part of this research has been funded by MEXT HPCI STRATEGIC PROGRAM. This work was undertaken as part by the Yukawa International Project for Quark-Hadron Sciences (YIPQS), and was partly supported by the GCOE program "The Next Generation of Physics, Spun from Universality and Emergence" from MEXT of Japan. J. A. M. and P.-G. R. were supported by BMBF under Contract No. 06ER9063 and No. 06FY9086, respectively. One of the authors (J. A. M.) would like to thank the Japan Society for the Promotion of Science (JSPS) for an invitation fellowship for research in Japan.

[1] S. Cohen, F. Plasil, and W. J. Świątecki, Ann. Phys. (Berlin) **82**, 557 (1974).
[2] A. Bohr, *Proc. Int. Physics 'Enrico Fermi', Cours LXIX*, edited by A. Bohr and R. A. Broglia (North-Holland, Amsterdam, 1977), p. 3.
[3] A. V. Afanasjev, D. B. Fossan, G. J. Lane, and I. Ragnarsson, Phys. Rep. **322**, 1 (1999).
[4] A. Bohr and B. R. Mottelson, Nucl. Phys. **A354**, 303 (1981).
[5] T. L. Khoo, R. Smither, B. Haas, O. Häusser, H. Andrews, D. Horn, and D. Ward, Phys. Rev. Lett. **41**, 1027 (1978).
[6] E. S. Paul *et al.*, Phys. Rev. Lett. **98**, 012501 (2007).
[7] J. Simpson *et al.*, Phys. Lett. B **327**, 187 (1994).
[8] C. Y. Wong, Phys. Lett. **41B**, 446 (1972).
[9] C. Y. Wong, Ann. Phys. (N.Y.) **77**, 279 (1973).
[10] C. Y. Wong, Phys. Rev. C **17**, 331 (1978).
[11] M. Warda, Int. J. Mod. Phys. E **16**, 452 (2007)
[12] A. Staszczak and C. Y. Wong, Acta Phys. Pol. B **40**, 753 (2009).
[13] D. H. Wilkinson, Nucl. Phys. **A452**, 296 (1986).
[14] J. A. Maruhn, M. Kimura, S. Schramm, P.-G. Reinhard, H. Horiuchi, and A. Tohsaki, Phys. Rev. C **74**, 044311 (2006).
[15] T. Ichikawa, J. A. Maruhn, N. Itagaki, and S. Ohkubo, Phys. Rev. Lett. **107**, 112501 (2011).
[16] P.-G. Reinhard and R. Y. Cusson, Nucl. Phys. **A378**, 418 (1982).
[17] E. Chabanat, P. Bonche, P. Haensel, J. Meyer, and R. Schaeffer, Nucl. Phys. **A627**, 710 (1997).
[18] P.-G. Reinhard and H. Flocard, Nucl. Phys. **A584**, 467 (1995).
[19] P. Möller, A. J. Sierk, and A. Iwamoto, Phys. Rev. Lett. **92**, 072501 (2004).
[20] A. J. Sierk, Phys. Rev. C **33**, 2039 (1986); (private communication).
[21] T. L. Khoo, F. M. Bernthal, R. G. H. Robertson, and R. A. Warner, Phys. Rev. Lett. **37**, 823 (1976).

Chapter 1

BCS-pairing and nuclear vibrations

Kenichi Matsuyanagi,[1,2] Nobuo Hinohara[3] and Koichi Sato[1]

[1] *RIKEN Nishina Center, Wako 351-0198, Japan*

[2] *Yukawa Institute for Theoretical Physics, Kyoto University, Kyoto 606-8502, Japan*

[3] *Department of Physics and Astronomy, University of North Carolina, Chapel Hill, North Carolina 27599-3255, USA*

matsuyanagi@riken.jp

On the basis of time-dependent mean-field picture, we discuss the nature of the low-frequency quadrupole vibrations from small-amplitude to large-amplitude regimes as representatives of surface shape vibrations of a superfluid droplet (nucleus). We consider full five-dimensional quadrupole dynamics including three-dimensional rotations restoring the broken symmetries as well as axially symmetric and asymmetric shape fluctuations. We show that the intimate connections between the BCS-pairing and collective vibrations reveal through the inertial masses governing their collective kinetic energies.

1. Introduction

In almost all even-even nuclei consisting of even number of protons and neutrons, aside from the doubly magic nuclei of the spherical shell model, the first excited states possess angular momentum two and positive parity ($I^\pi = 2^+$). Their excitation energies are much lower than the energy gap 2Δ characterizing nuclei with superfluidity (see Fig. 4 in the contribution of Bertsch to this volume), and very large electric quadrupole ($E2$) transition strengths (in comparison with those of single-particle transitions) between these first excited 2^+ states and the ground states have been systematically observed. These experimental data clearly indicate that they are collective excitations of the superfluid system.[1,2] They are genuine quantum vibrations essentially different in character from surface oscillations of a

classical liquid drop, that is, superfluidity and shell structure of nuclei play indispensable roles for their emergence. Unfortunately, this point is quite insufficiently described in several textbooks on nuclear physics.

In a nucleus whose mean field breaks the spherical symmetry but conserves the axial symmetry, its first excited 2^+ state can be interpreted as a uniformly rotating state, provided that the amplitudes of quantum shape fluctuations are smaller than the magnitude of equilibrium deformation. Nuclei exhibiting very small ratios of the excitation energy to the energy gap, $E(2^+)/2\Delta$, (less than about 0.1) belong to this category (see Fig. 4 in the contribution of Bertsch to this volume). The rotational moment of inertia evaluated from $E(2^+)$ turned out to be about half of the rigid-body value. This was one of the most clear evidences leading to the recognition that their ground states are in superfluid phase. Large portion of nuclei exhibiting regular rotational spectra have the prolate shape. Origin of the asymmetry between the prolate and oblate shapes is an interesting fundamental problem still under study.[3]

The first excited 2^+ states other than the rotational states have been regarded as quadrupole vibrations around the spherical shape. Their frequencies are low and decrease as the numbers of neutrons and protons increasingly deviate from the magic numbers of the spherical shell model. Eventually, they turn into the rotational 2^+ states discussed above. Thus, low-frequency quadrupole vibrations may be regarded as soft modes of the quantum phase transitions breaking the spherical symmetry of the mean field. In a finite quantum system like nuclei, however, this phase transition takes place gradually as a function of nucleon number, and there is a wide region of nuclei whose low-energy excitation spectra exhibit characteristics intermediate between the vibrational and the rotational patterns. The softer the mean field toward the quadrupole deformation, the larger the amplitude and the stronger the nonlinearity of the vibration.

In this Chapter, we discuss mainly the low-frequency (slow) quadrupole vibrations rather than summing up the diversity of nuclear vibrational phenomena. The reason is not only because they dominate in low-lying spectra but also because they represent most typically the intimate connection between the BCS-pairing and the emergence of collective vibrational modes in nuclei. Many ideas developed here are applicable also to low-frequency octupole (3^-) vibrations. We here restrict ourselves to the time-dependent mean-field approach, because it provides a clear correspondence between the quantum and classical aspects of the surface shape vibrations. Furthermore, this approach enables us to microscopically derive the collective

coordinates and momenta on the basis of the time-dependent variational principle. We shall show that the inertial masses determining the collective kinetic energies of the low-frequency quadrupole modes clearly reveal their character as surface shape vibrations of a superfluid droplet (nucleus).

We shall start from small-amplitude vibrations around the spherical equilibrium shape and then go to large-amplitude regime where we need to consider full five-dimensional (5D) quadrupole dynamics including three-dimensional rotations restoring the broken symmetries as well as axially symmetric and asymmetric shape fluctuations. Through this Chapter, we would like to stress that construction of microscopic quantum theory of large-amplitude collective motion (LACM) is one of the most challenging open subjects in nuclear structure physics. Nowadays, the dimension of nuclear collective vibrational phenomena awaiting applications of such a microscopic quantum theory is enormously increasing covering wide regions from low to highly excited states, from small to large angular momenta, and from the proton-drip line to the neutron-drip line.

2. Collective motion as moving self-consistent mean field

2.1. *Small-amplitude regime*

Let us consider even-even nuclei whose ground states consist of correlated nucleon pairs occupying time-reversal conjugate single-particle states. The Hartree-Fock-Bogoliubov (HFB) method is a generalized mean-field theory treating the formation of the HF mean field and the nucleon pair condensate in a self-consistent manner,[4] and yields the concept of quasiparticles as single-particle excitation modes in the presence of the pair condensate.

As is well known, Bohr and Mottelson opened the way to a unified understanding of single-particle and collective motions of nuclei by introducing the concept of moving self-consistent mean field.[5–7] The time-dependent extension of the HFB mean field, called the time-dependent HFB (TDHFB) theory, is suitable to formulate their ideas.[8,9] The TDHFB state vector $|\phi(t)\rangle$ can be written in a form of generalized coherent state:

$$|\phi(t)\rangle = e^{i\hat{G}(t)}|\phi(t=0)\rangle = e^{i\hat{G}(t)}|\phi_0\rangle, \tag{1}$$

$$i\hat{G}(t) = \sum_{(ij)}(g_{ij}(t)a_i^\dagger a_j^\dagger - g_{ij}^*(t)a_j a_i), \tag{2}$$

where the HFB ground state $|\phi_0\rangle$ is a vacuum for quasiparticles $(a_i^\dagger, a_j)$,

$$a_i|\phi_0\rangle = 0, \tag{3}$$

with the suffix i distinguishing different quasiparticle states. The functions $g_{ij}(t)$ in the one-body operator $\hat{G}(t)$ is determined by the time-dependent variational principle

$$\delta\langle\phi(t)|i\frac{\partial}{\partial t} - H|\phi(t)\rangle = 0. \tag{4}$$

For small-amplitude vibrations around a HFB equilibrium point, one can make a linear approximation to the TDHFB equations and obtain the quasiparticle random phase approximation (QRPA) which is a starting point of microscopic theory of collective motion.[10,11] Expanding Eq. (4) as a power series of $\hat{G}(t)$ and taking only the linear order, we obtain

$$\delta\langle\phi_0|[H, i\hat{G}] + \frac{\partial\hat{G}}{\partial t}|\phi_0\rangle = 0. \tag{5}$$

Writing $\hat{G}(t)$ in terms of the creation and annihilation operator $(\Gamma^\dagger, \Gamma)$ of the excitation mode as

$$i\hat{G}(t) = \eta(t)\Gamma - \eta^*(t)\Gamma^\dagger, \qquad \eta(t) = \eta e^{-i\omega t}, \tag{6}$$

we obtain the QRPA equation which determines the microscopic structure of $(\Gamma^\dagger, \Gamma)$ as a coherent superposition of many two-quasiparticle excitations. Alternatively, we can write $\hat{G}(t)$ in terms of the collective coordinate and momentum operators $(\hat{Q}, \hat{P})$ and their classical counterparts $(q(t), p(t))$ as

$$\hat{G}(t) = p(t)\hat{Q} - q(t)\hat{P} \tag{7}$$

and obtain the QRPA equation,

$$[\ \hat{H},\ \hat{Q}\ ] = -i\hat{P}/D, \tag{8}$$

$$[\ \hat{H},\ \hat{P}\ ] = iC\hat{Q}, \tag{9}$$

for $(\hat{Q}, \hat{P})$. Here C, D and $\omega^2 = C/D$ respectively denote the stiffness, the inertial mass and the frequency squared of the vibrational mode (with $\hbar = 1$). For Anderson-Nambu-Goldstone (ANG) modes,[12,13] C and ω are zero but D are positive. Note that Eqs. (8) and (9) can be used also for unstable HFB equilibria where C is negative and ω is imaginary. For simplicity, we assumed above that there is only a single collective mode, but in reality $\hat{G}(t)$ is written as a sum over many QRPA normal modes.

The self-consistent mean field of a finite quantum system generates a variety of shell structure dependent on its shape, and single-particle wave functions possess individual characteristics. In addition to rich possibilities of spatial structure, collective excitations associated with the spin-isospin

degrees of freedoms of nucleons occur. Thus, diversity of collective vibrations emerges.[14,15] Even restricting to the 2^+ surface oscillation, there are two modes of different characters. One is the low-frequency mode generated mainly from two-quasiparticle excitations within partly filled major shells (for both protons and neutrons). The other is the high-frequency mode, called giant quadrupole resonance, generated from single-particle excitations across two major shells. While giant resonances are small amplitude vibrations, low-frequency collective modes in open shell nuclei exhibit significant nonlinear effects and we need to go beyond the QRPA. In the QRPA, the quadrupole vibrational modes can be regarded as phonons of 5D harmonic oscillator and excitation spectra are expected to show a simple pattern: e.g., the two-phonon states (double excitations of the 2^+ quanta) will appear as a triplet with $I^\pi = 0^+, 2^+$ and 4^+. Closely examining experimental data, e.g., on their $E2$ transition properties, one finds that they often exhibit significant anharmonicities even when a candidate of such a triplet is seen.[16] The vibrational amplitude becomes very large in transient situations of the quantum phase transition from spherical to deformed, where the spherical mean field is barely stable or the spherical symmetry is broken only weakly. Many nuclei are situated in such transitional regions.

2.2. *Quadrupole collective dynamics*

One of the microscopic approaches to treat nonlinear vibrations is the boson expansion method, where the collective QRPA normal modes at the spherical shape are regarded as bosons and nonlinear effects are evaluated in terms of a power series expansion with respect to the boson creation and annihilation operators. This method has been widely used for low-energy collective phenomena.[17]

In the investigation of low-energy excitation spectra, the pairing-plus-quadrupole (P+Q) model[18,19] and its extension[20] have played a central role. This phenomenological effective interaction represents the competition between the pairing correlations favoring the spherical symmetry and the quadrupole (particle-hole) correlations leading to the quadrupole deformation of the mean field. Combining the P+Q model with the TDHFB theory, Belyaev,[8] Baranger and Kumar[9] microscopically derived the 5D quadrupole collective Hamiltonian describing the quadrupole vibrations and rotations in a unified manner:

$$H = T_{\rm vib} + T_{\rm rot} + V(\beta, \gamma), \tag{10}$$

$$T_{\rm vib} = \frac{1}{2}D_{\beta\beta}(\beta,\gamma)\dot{\beta}^2 + D_{\beta\gamma}(\beta,\gamma)\dot{\beta}\dot{\gamma} + \frac{1}{2}D_{\gamma\gamma}(\beta,\gamma)\dot{\gamma}^2, \tag{11}$$

$$T_{\rm rot} = \sum_k \frac{I_k^2}{2\mathcal{J}_k(\beta,\gamma)}. \tag{12}$$

Here, $T_{\rm vib}$ and $T_{\rm rot}$ denote the kinetic energies of vibrational and rotational motions, while $V(\beta,\gamma)$ represents the collective potential energy defined through the expectation value of an effective interaction with respect to the TDHFB state. The velocities of the vibrational motion are described in terms of the time-derivatives $(\dot{\beta},\,\dot{\gamma})$ of the quadrupole deformation variables $(\beta,\,\gamma)$ representing the magnitude and the triaxiality of the quadrupole deformation, respectively. They are defined in terms of the expectation values of the quadrupole moments or through a parametrization of the surface shape. The three components I_k of the rotational angular momentum and the moments of inertia $\mathcal{J}_k = 4\beta^2 D_k(\beta,\gamma)\sin^2(\gamma - 2\pi k/3)$ in the rotational energy $T_{\rm rot}$ are defined with respect to the intrinsic frame of reference; that is, an instantaneous principal-axis frame of the time-dependent shape-fluctuating mean field.

After quantization with the Pauli prescription, the vibrational kinetic energy takes the following form:[21]

$$\begin{aligned}\hat{T}_{\rm vib} = -\frac{1}{2\sqrt{WR}}\Bigg[&\frac{1}{\beta^4}\frac{\partial}{\partial\beta}\beta^2\sqrt{\frac{R}{W}}\left(D_{\gamma\gamma}\frac{\partial}{\partial\beta} - D_{\beta\gamma}\frac{\partial}{\partial\gamma}\right)\\ &-\frac{1}{\beta^2\sin 3\gamma}\frac{\partial}{\partial\gamma}\sqrt{\frac{R}{W}}\sin 3\gamma\left(D_{\beta\gamma}\frac{\partial}{\partial\beta} - D_{\beta\beta}\frac{\partial}{\partial\gamma}\right)\Bigg],\end{aligned} \tag{13}$$

where

$$W = \beta^{-2}\left[D_{\beta\beta}(\beta,\gamma)D_{\gamma\gamma}(\beta,\gamma) - D_{\beta\gamma}^2(\beta,\gamma)\right], \tag{14}$$

$$R = D_1(\beta,\gamma)D_2(\beta,\gamma)D_3(\beta,\gamma). \tag{15}$$

If the β and γ dependences of the inertial functions, $D_{\beta\beta}, D_{\beta\gamma}, D_{\gamma\gamma}$ and D_k, are ignored, Eq. (13) reduces to a simpler expression used in many papers. However, such an approximation is valid only for small-amplitude vibrations around the spherical shape. It is mandatory to use the above expression to describe large-amplitude vibrations in transitional regions toward the quadrupole deformation.

In an axially deformed nucleus whose collective potential $V(\beta,\gamma)$ has a deep minimum at $\beta \neq 0$ and $\gamma = 0^\circ$ (prolate shape) or $\gamma = 60^\circ$ (oblate shape), a regular rotational spectrum appears. At the same time, one can

identify β and γ bands involving vibrational quanta of fluctuations of the β and γ variables. Close examination of their properties, however, reveals significant nonlinear character of the γ vibration.[22] It has been known that the β vibration couples, often strongly, with the pairing vibration associated with the fluctuation of the pairing gap Δ. Recent experiments reveal further interesting features of the excited 0^+ states[23] upon which we shall touch in Section 3.

2.3. *Quantum shape fluctuations and collective rotations restoring the broken symmetry*

As is well known, the fundamental concept underlying the BCS superconductivity is 'spontaneous symmetry breaking and appearance of collective modes restoring the broken symmetry.'[12,13] Nuclear rotation can be regarded as a manifestation of this dynamics in a finite quantum system; that is, it is a collective motion restoring the spherical symmetry broken by the self-consistently generated mean field.[5,7] It is important, however, to keep in mind that any HFB equilibrium shape inevitably accompanies quantum zero-point fluctuations. The well-known $I(I+1)$ pattern of rotational spectrum will not appear if the fluctuation amplitude is larger than the equilibrium value of $\beta \neq 0$. Even when the minimum in the collective potential $V(\beta, \gamma)$ is deep in the β direction, it may be soft with respect to the γ direction breaking the axial symmetry. In the axially symmetric limit, the rotational motion about the symmetric axis is absent. However, as soon as the axial symmetry is dynamically broken by quantum shape fluctuations, all rotational degrees of freedom about the three principal axes (of the instantaneous shape) are activated. Low energy excitation spectrum in such a situation exhibits a feature more complex than the simple rotational pattern. It seems that many nuclei belong to this category.

2.4. *Microscopic theory of LACM*

The TDHFB theory describes the time evolution of the superfluid mean field without explicitly introducing collective variables. To derive the collective Hamiltonian, we have to assume that the time evolution is governed by a few collective coordinates and momenta. In the work of Baranger and Kumar,[9] the 5D collective Hamiltonian was derived by giving the role of collective coordinates to the quadrupole operators. We note, however, that there are two kinds of 2^+ vibration, and the high frequency quadrupole giant resonance carries the major part (about 90%, see Fig. 5 in the contribution

of Bertsch to this volume) of the energy-weighted sum-rule value for the quadrupole operator. On the other hand, the collective variables are defined in terms of the low-frequency 2^+ QRPA modes in the derivation of the 5D collective Hamiltonian by means of the boson-expansion method.[20] In the QRPA modes, contributions of the two-quasiparticle excitations near the Fermi surface are much larger than those in the quadrupole operators. Therefore, the two definitions are different significantly.

Attempts to construct microscopic theory of LACM on the basis of the TDHFB mean field dates back to the latter half of the seventies (see Refs. 24,25 for reviews). The major challenge was how to extract the collective submanifold embedded in the TDHFB phase space, which is maximally decoupled from other microscopic degrees of freedom.[26] Once such a collective submanifold is extracted, we can set up a local canonical coordinates on it. Such canonical coordinates may be called "collective coordinates." Below we sketch the basic ideas of the LACM theory.

Let us assume that the time evolution of the TDHFB state is determined by the collective coordinate $q(t)$ and momentum $p(t)$. To restore the gauge invariance broken by the HFB mean-field approximation for superfluid nuclei, it is necessary to find a way extending the QRPA procedure to non-equilibrium. For this purpose, we introduce the number fluctuation variable $n(t)$ and the gauge angle $\varphi(t)$ conjugate to it and write the TDHFB state vector in the following form:

$$|\phi(q,p,\varphi,n)\rangle \;\; = e^{-i\varphi\tilde{N}}\,|\phi(q,p,n)\rangle\,, \tag{16}$$

$$|\phi(q,p,n)\rangle = e^{ip\hat{Q}(q)+in\hat{\Theta}(q)}\,|\phi(q)\rangle\,. \tag{17}$$

Here $|\phi(q,p,n)\rangle$ represents an intrinsic state for the pairing rotational degree of freedom parametrized by φ, $|\phi(q)\rangle$ a non-equilibrium HFB state, $\tilde{N}$ nucleon number fluctuation, and $\hat{Q}(q), \hat{\Theta}(q)$ infinitesimal generators. We also define an infinitesimal displacement operator $\hat{P}(q)$ by

$$|\phi(q+\delta q)\rangle = e^{-i\delta q\hat{P}(q)}\,|\phi(q)\rangle\,. \tag{18}$$

Microscopic structures of $\hat{Q}(q), \hat{P}(q), \hat{\Theta}(q)$ and $|\phi(q)\rangle$ are determined on the basis of the time-dependent variational principle:

$$\delta\,\langle\phi(q,p,\varphi,n)|\,i\frac{\partial}{\partial t} - \hat{H}\,|\phi(q,p,\varphi,n)\rangle = 0, \tag{19}$$

where $\hat{H}$ is a microscopic many-body Hamiltonian. (For simplicity, we assume that there is only a single canonical set of collective variables.)

Let us assume that time variation of the mean field is slow (in comparison with the single-particle motion in the mean field), and expand

$|\phi(q,p,n)\rangle$ in powers of p and n. Requiring that the time-dependent variational principle be satisfied at each order, we obtain the equations determining the infinitesimal generators, $\hat{Q}(q), \hat{P}(q)$, and $\hat{\Theta}(q)$, which are a generalization of the QRPA about an HFB equilibrium to non-equilibrium HFB states. Solving these equations in a self-consistent way, we obtain a classical collective Hamiltonian written in terms of canonical variables, which can be readily quantized and yield the collective Schrödinger equation for collective wave functions. The procedure outlined above has been formulated as the adiabatic self-consistent collective coordinate (ASCC) method.[27] Quite recently, we have developed a practical approximation scheme called "constrained HFB+ local QRPA (LQRPA) method" to efficiently carry out such calculations.[28] Examples of numerical application are presented in Figs. 1 and 2. In both cases, we see clear correlations between the β-γ dependence of the paring gap Δ and of the inertial mass $D_{\beta\beta}$; that is, $D_{\beta\beta}$ becomes small in the region where Δ is large.

2.5. *Microscopic mechanism of determining the inertial mass*

The reason why the pairing correlation plays a crucial role in determining the inertia mass of collective motion may be understood in the following way.[29] The single-particle energy levels change following the motion of the mean field and encounter a number of level crossings. When a level crossing occurs near the Fermi surface, the lowest-energy configuration changes. Without the pairing, it is not always easy to rearrange the system to energetically more favorable configurations. In the presence of the pairing correlation, in contrast, it is easy for nucleon pairs to hop from up-sloping levels to down-sloping levels. The easiness/hardness of the configuration rearrangements at the level crossings determines the adiabaticity/diabaticity of the collective motion. Since the inertia represents a property of the system trying to keep a definite configuration, we expect that the stronger the pairing, the smaller the inertial mass.

In this connection, let us note the following fact. The nucleon pair in a deformed mean field is not simply a monopole ($J = 0$) pair but a superposition of different angular momenta J, because the spherical symmetry is broken. Especially, one cannot ignore the quadrupole pairing correlations acting among the $J = 2$ components. For example, when the prolately deformed nucleus develops toward a larger value of β, single-particle energy levels favoring the prolate shape go down while those favoring the oblate

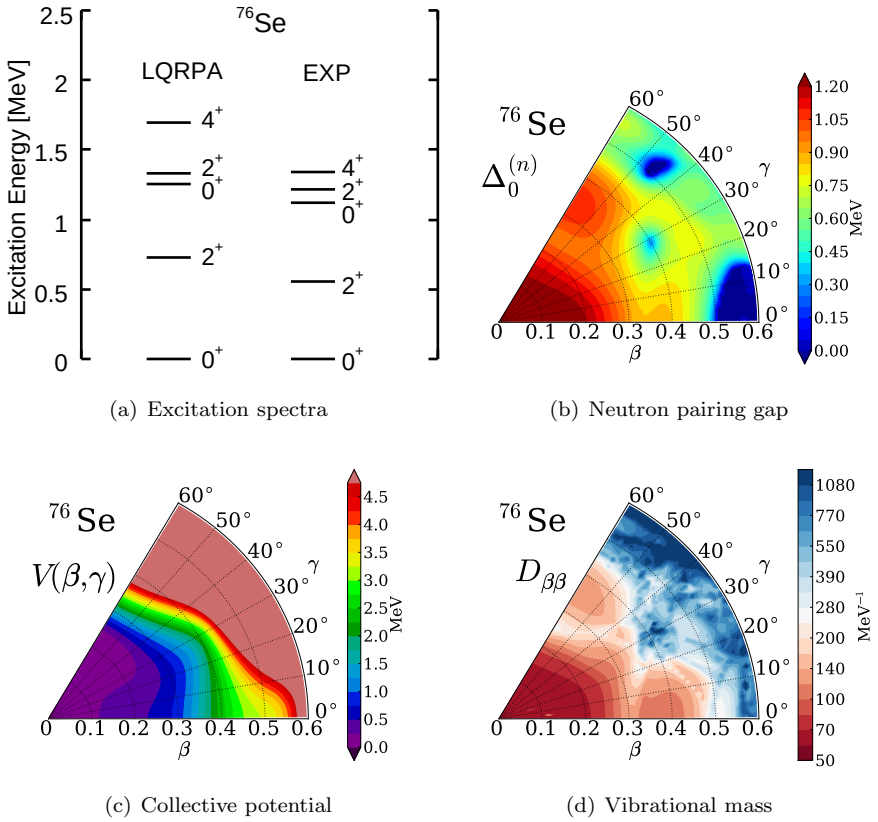

(a) Excitation spectra (b) Neutron pairing gap

(c) Collective potential (d) Vibrational mass

Fig. 1. Application of the LQRPA method to anharmonic quadrupole vibrational excitations in ^{76}Se. Note that the colors are used differently for $\Delta_0^{(n)}$ and $D_{\beta\beta}$.

shape go up. At their level crossing point, the ability of the rearrangement depends on the pairing matrix element between the crossing levels. The spacial overlap between the prolate-favoring and the oblate-favoring single-particle wave functions is smaller than its value at the spherical limit. This effect is taken into account by including the quadrupole pairing correlation. If this effect is ignored, the inertial mass will be underestimated.[28] The interaction strengths of the monopole and quadrupole components are linked by the requirement of Galilean invariance.[20]

3. Remarks on some current topics

3.1. *Shape coexistence and quantum shape fluctuations*

In the situations where two different HFB equilibrium shapes coexist in the same energy region, LACM tunneling through the potential barrier between the two HFB local minima may take place. This a macroscopic tunneling phenomenon where the potential barrier itself is generated as a consequence of the dynamics of the self-bound quantum system. For instance, two strongly distorted rotational bands built on the oblate and prolate shapes have been found in ^{68}Se, which seems to coexist and interact with each other.[30] Figure 2 shows an application of the LQRPA method to this oblate-prolate shape coexistence/fluctuation phenomenon.[28] Such phenomena are widely seen in low-energy spectra from light to heavy nuclei.[23]

One of the recent hot issues related to the shape coexistence/fluctuation is to clarify the nature of deformation in neutron-rich nuclei around ^{32}Mg, where two-particle-two-hole configurations of neutrons across the spherical magic number $N = 20$ play a crucial role.[23] It seems that the pairing and quadrupole correlations act coherently in this situation to generate a large-amplitude quadrupole shape fluctuations.[31]

3.2. *Mysterious 0^+ excited states*

There are only a few nuclei in which the first excited 0^+ state appears below the first excited 2^+ state. An example is the 0^+ state of ^{72}Ge which is known from old days but still poorly understood. This anomaly occurs in the vicinity of $N = 40$ where the $g_{9/2}$ shell starts to be partly filled (due to the pairing). It has been pointed out[32,33] that the neutron pairing vibrations strongly couple with the quadrupole vibrations there and generates such anomalous 0^+ states. It is an open problem whether such 0^+ excited states are describable within the 5D quadrupole dynamics or it is mandatory to extend the dimension of the collective submanifold explicitly treating the pairing gaps as dynamical variables. Closely examining the properties of low-lying excited 0^+ states throughout the nuclear chart, one finds that they exhibit features difficult to understand within the traditional models of nuclear collective motions.[23]

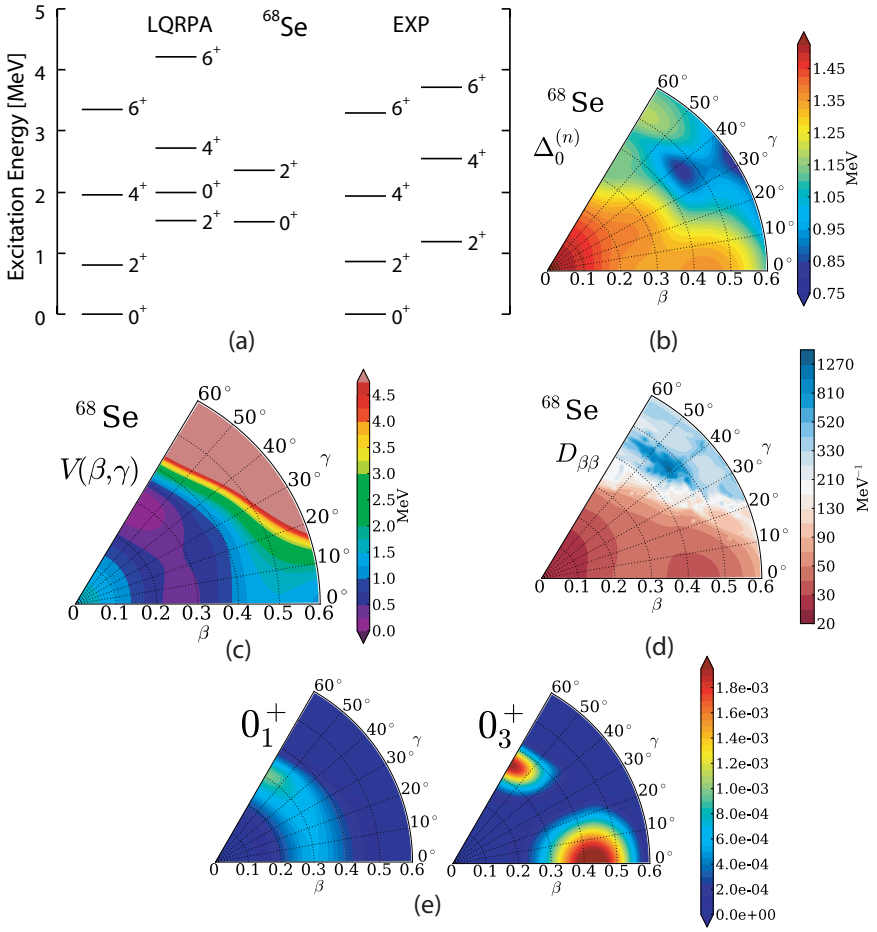

Fig. 2. Application of the LQRPA method[28] to the oblate-prolate shape coexistence/fluctuation phenomenon in ^{68}Se. In the bottom part, vibrational wave functions squared (multiplied by β^4) for the ground 0_1^+ and the (experimentally unknown) third 0_3^+ states are displayed. The β^4 factor takes into account the major β dependence of the volume element for the 5D collective Hamiltonian.

3.3. *Vibrational modes at high angular momentum*

Experimental data for low-frequency vibrations near the high-spin yrast states ('ground' states for given angular momenta) are scarce. As the nucleus rotates more rapidly, excitations of aligned quasiparticles take place step by step,[34,35] the shell structure changes with varying mean-field, and the pair field may eventually disappear.[36] Such drastic changes of the mean-

field and the presence of aligned quasiparticles will significantly modify the properties of vibrational motions. The presence of low-frequency vibrations itself is not self-evident, if we recall that the BCS pairing plays an essential role in the emergence of the low-frequency 2^+ vibrations. On the other hand, we could also expect that vibrations may compete with rotations in high-spin yrast region, because the rotational frequency increases with increasing angular momentum and eventually become comparable to vibrational frequencies.[37]

Discovery of superdeformed bands opened a new perspective to the above open question. We learned that a new shell structure, called superdeformed shell structure, is formed and a new type of soft octupole vibrations simultaneously breaking the axial symmetry and space-reflection symmetry emerge in the near yrast regions of rapidly rotating superdeformed nuclei.[38,39] Quite recently, a number of new data suggesting appearance of γ-vibrations (shape fluctuation modes toward triaxial deformation) at high spin have been reported.[40,41] Appearance of triaxial deformation at high spin due to the weakening of the pairing correlation has been discussed for a long time, but it is only recent years that a variety of experimental data unambiguously indicating the triaxial deformation has been obtained. New rotational modes appearing when the mean field breaks the axial symmetry, called wobbling motions, have been discovered.[42] It is shown that the aligned quasiparticle plays an important role for their emergence.[43] Another new type of rotational spectra expected to appear in triaxially deformed nuclei under certain conditions is the chiral rotation[34] and experimental search for the predicted chiral doublet bands and its precursor phenomena, called chiral vibrations,[44] are now going on.

3.4. *Vibrational modes near the neutron drip line*

The mean field in unstable nuclei near the neutron drip line possesses new features like large neutron-to-proton ratios, formation of neutron skins, weak binding of single-particles states near the Fermi surface, excitations of neutron pair into the continuum.[45] In stable nuclei, overlaps of different single-particle wave functions become maximum at the surface and generate a strong coherence among quasiparticle excitations. In unstable nuclei, weakly bound single-particle wave functions significantly extend to the outside of the half-density surface and acquire strong individualities. It is therefore very interesting to investigate how the pairing correlation in such a situation acts to generate the collectivity of vibrational modes. It is

suggested, for instance, in a recent HFB+QRPA calculation simultaneously taking into account the deformations of the mean field, the pairing correlations and the excitations into the continuum,[46] that a strong coherence of the pairing and shape fluctuations may generate collective vibrations unique to weakly bound neutron-rich nuclei.

3.5. *Concluding remarks*

Quite recently, it becomes possible to carry out fully self-consistent QRPA calculations on the basis of density functional theory for superfluid nuclei and treat low- and high-frequency vibrations as well as the ground states in a unified way for all nuclei from the proton-drip line to the neutron-drip line.[47–49] Fully self-consistent microscopic calculations for large-amplitude vibrations are also initiated.[50] A new era toward understanding vibrational motions of nuclear superfluid droplet is opening.

References

1. G. F. Bertsch and R. A. Broglia, *Oscillations in Finite Quantum Systems* (Cambridge University Press, 1994).
2. D. M. Brink and R. A. Broglia, *Nuclear Superfluidity, Pairing in Finite Systems* (Cambridge University Press, 2005).
3. K. Arita, arXiv:1202.5631, Phys. Rev. C to be published.
4. M. Bender, P.-H. Heenen, and P.-G. Reinhard, Rev. Mod. Phys. **75**, 121 (2003).
5. A. Bohr, Rev. Mod. Phys. **48**, 365 (1976).
6. B. Mottelson, Rev. Mod. Phys. **48**, 375 (1976).
7. A. Bohr and B. R. Mottelson, *Nuclear Structure*, Vol. II, (W. A. Benjamin Inc., 1975; World Scientific 1998).
8. S. T. Belyaev, Nucl. Phys. **64**, 17 (1965).
9. M. Baranger and K. Kumar, Nucl. Phys. A **122**, 241 (1968).
10. M. Baranger, Phys. Rev. **120**, 957 (1960).
11. T. Marumori, Prog. Theor. Phys. **24**, 331 (1960).
12. P. W. Anderson, Phys. Rev. **112**, 1900 (1958).
13. Y. Nambu, Phys. Rev. **117**, 648 (1960).
14. M. N. Harakeh and A van der Woude, *Giant Resonances, High-Frequency Modes of Nuclear Excitation* (Oxford University Press, 2001).
15. P.F. Bortignon, A. Bracco and R. A. Broglia, *Giant Resonances, Nuclear Structure at Finite Temperature* (Harwood academic publishers, 1998).
16. P. E. Garrett and J. L. Wood, J. Phys. G. **37**, 064028 (2010).
17. A. Klein and E. R. Marshalek, Rev. Mod. Phys. **63**, 375 (1991).
18. L. S. Kisslinger and R. A. Sorensen, Rev. Mod. Phys. **35**, 853 (1963).

19. D. R. Bes and R. A. Sorensen, *Advances in Nuclear Physics* vol. 2, (Prenum Press, 1969), p. 129.
20. H. Sakamoto and T. Kishimoto, Nucl. Phys. A **528**, 73 (1991).
21. L. Próchniak and S.G. Rohoziński, J. Phys. G. **36**, 123101 (2009).
22. M. Matsuo and K. Matsuyanagi, Prog. Theor. Phys. **78**, 591 (1987).
23. K. Heyde and J. L. Wood, Rev. Mod. Phys. **83**, 1467 (2011).
24. G. Do Dang, A. Klein, and N.R. Walet, Phys. Rep. **335**, 93 (2000).
25. K. Matsuyanagi, M. Matsuo, T. Nakatsukasa, N. Hinohara, and K. Sato, J. Phys. G. **37**, 064018 (2010).
26. T. Marumori, T. Maskawa, F. Sakata, and A. Kuriyama, Prog. Theor. Phys. **64**, 1294 (1980).
27. M. Matsuo, T. Nakatsukasa, and K. Matsuyanagi, Prog. Theor. Phys. **103**, 959 (2000).
28. N. Hinohara, K. Sato, T. Nakatsukasa, M. Matsuo, and K. Matsuyanagi, Phys. Rev. C **82**, 064313 (2010).
29. F. Barranco, G.F. Bertsch, R.A. Broglia, and E. Vigezzi, Nucl. Phys. A **512**, 253 (1990).
30. S.M. Fisher *et al.*, Phys. Rev. Let. **83**, 4064 (2000).
31. N. Hinohara, K. Sato, K. Yoshida, T. Nakatsukasa, M. Matsuo, and K. Matsuyanagi, Phys. Rev. C **84**, 061302(R) (2011).
32. K. Takada and S. Tazaki, Nucl. Phys. A **448**, 56 (1986).
33. K. J. Weeks, T. Tamura, T. Udagawa, and F.J.W. Hahne, Phys. Rev. C **24**, 703 (1981).
34. S. Frauendorf, Rev. Mod. Phys. **73**, 463 (2001).
35. W. Satula and R.A. Wyss, Rep. Prog. Phys. **68**, 131 (2005).
36. Y. R. Shimizu, J. D. Garrett, R. A. Broglia, M. Gallardo, and E. Vigezzi Rev. Mod. Phys. **61**, 131 (1989).
37. A. Bohr and B. R. Mottelson, Nucl. Phys. A **354**, 303c (1981).
38. T. Nakatsukasa, K. Matsuyanagi, S. Mizutori, and Y.R. Shimizu, Phys. Rev. C **53**, 2213 (1996).
39. D. Roβbach *et al.*, Phys. Lett. B **513**, 9 (2001).
40. J. Ollier *et al.*, Phys. Rev. C **83**, 044309 (2011).
41. L. K. Pattison *et al.*, Phys. Rev. Lett. **91**, 182501 (2003).
42. S. W. Ødegård *et al.*, Phys. Rev. Lett. **86**, 5866 (2001).
43. T. Shoji and Y. R. Shimizu, Prog. Theor. Phys. **121**, 319 (2009).
44. D. Almehed, F. Dönau, and S. Frauendorf, Phys. Rev. C **83**, 054308 (2011).
45. M. Matsuo and T. Nakatsukasa, J. Phys. G. **37**, 064017 (2010).
46. K. Yoshida and M. Yamagami, Phys. Rev. C **77**, 044312 (2008).
47. J. Terasaki, J. Engel, and G. F. Bertsch, Phys. Rev. C **78**, 044311 (2008).
48. S. Ebata, T. Nakatsukasa, T. Inakura, K. Yoshida, Y. Hashimoto, and K. Yabana, Phys. Rev. C **82**, 034306 (2010).
49. K. Yoshida and T. Nakatsukasa, Phys. Rev. C **83**, 021304(R) (2011).
50. K. Yoshida and N. Hinohara, Phys. Rev. C **83**, 061302(R) (2011).

PHYSICAL REVIEW C **88**, 011602(R) (2013)

Damping of quantum vibrations revealed in deep sub-barrier fusion

Takatoshi Ichikawa[1] and Kenichi Matsuyanagi[1,2]
[1]*Yukawa Institute for Theoretical Physics, Kyoto University, Kyoto 606-8502, Japan*
[2]*RIKEN Nishina Center, Wako 351-0198, Japan*
(Received 28 February 2013; revised manuscript received 18 April 2013; published 22 July 2013)

We demonstrate that when two colliding nuclei approach each other, their quantum vibrations are damped near the touching point. We show that this damping is responsible for the fusion hindrance phenomena measured in the deep sub-barrier fusion reactions. To show those, we, for the first time, apply the random-phase-approximation method to the two-body $^{16}O + ^{16}O$ and $^{40}Ca + ^{40}Ca$ systems. We calculate the octupole transition strengths for the two nuclei that adiabatically approach each other. The calculated transition strength drastically decreases near the touching point, which strongly suggests the vanishing of the quantum couplings between the relative motion and the vibrational intrinsic degrees of freedom of each nucleus. Based on this picture, we also calculate the fusion cross section for the $^{40}Ca + ^{40}Ca$ system by using the coupled-channel method with a damping factor that simulates the vanishing of the couplings. The calculated results reproduce the experimental data well, which indicates that the smooth transition from the sudden to the adiabatic processes indeed occurs in the deep sub-barrier fusion reactions.

DOI: 10.1103/PhysRevC.88.011602 PACS number(s): 21.60.Ev, 25.60.Pj, 24.10.Eq, 25.70.Jj

Heavy-ion fusion reactions at low incident energies serve as an important probe for investigating the fundamental properties of the potential tunneling of many-body quantum systems. When two nuclei fuse, a potential barrier, called the Coulomb barrier, is formed because of the strong cancellations between the Coulomb repulsion and the attractive nuclear force. The potential tunneling at incident energies below this Coulomb barrier is called the sub-barrier fusion. One important aspect of the sub-barrier fusion reactions is couplings between the relative motion of the colliding nuclei and the nuclear intrinsic degrees of freedom, such as collective vibrations of the target and/or projectile [1]. Those couplings result in the large enhancement of the fusion cross sections at the sub-barrier incident energies as compared to the estimation of a simple potential model. The coupled-channel (CC) model, which takes the couplings into account, has been successful in explaining this enhancement [2,3].

Recently, it has been possible to measure the fusion cross sections down to extremely deep sub-barrier incident energies [4–7]. The unexpected steep falloff of the fusion cross sections, compared to the standard CC calculations, emerges at the deep sub-barrier incident energies in a wide range of mass systems. These steep falloff phenomena are often called the fusion hindrance. The emergence of the fusion hindrance shows the threshold behavior, which is strongly correlated with the energy at the touching point of the two colliding nuclei [8,9]. In this respect, it has been shown that a key point for understanding this fusion hindrance is the potential tunneling in the density overlap region of the two colliding nuclei (see Fig. 1 in Ref. [8]).

To describe the fusion hindrance phenomena, many theoretical models to extend the standard CC model have been proposed. Based on the sudden picture, Mişicu and Esbensen have proposed that a strong repulsive core exists in the inner part of the Coulomb barrier due to nuclear incompressibility [10]. This model can reproduce the fusion hindrance from the light- to heavy-mass systems well [7,10–12]. Dasgupta *et al*. proposed the concept of the quantum decoherence of the channel couplings [5], but there are only simple calculations with this model [13]. Based on the adiabatic picture, which is the opposite limit to the sudden approach, Ichikawa *et al*. introduced the damping factor in the standard CC calculations to smoothly join between the sudden and the adiabatic processes [14]. This model can reproduce the fusion hindrance better than the sudden model. However, the physical origin of the damping factor was still unclear.

In this Rapid Communication, we show the physical origin of the damping factor proposed in Ref. [14]. In the standard CC model, it has been assumed that the properties of the vibrational modes do not change, even when two colliding nuclei touch with each other. However, in fact, the single-particle wave functions drastically change in the two nuclei by approaching each other. This results in the damping of the vibrational excitations, that is, the vanishing of the couplings between the relative motion and the vibrational excitations of each nucleus. To show this, we, for the first time, apply the random-phase-approximation (RPA) method to the two-body $^{16}O + ^{16}O$ and $^{40}Ca + ^{40}Ca$ systems and calculate the octupole transition strength $B(E3)$ as a function of the distance between the two nuclei. We below show that the obtained $B(E3)$ values for the individual nuclei are indeed damped near the touching point.

To illustrate our main idea, we first discuss a disappearance of the octupole vibration during the $^{16}O + ^{16}O$ fusion process. We calculate the mean-field potential with the folding procedure that uses the single Yukawa function to conserve its inner volume [15]. In the two-body system before the touching point, we assume the two sharp-surface spherical nuclei. After the touching point, we describe the nuclear shapes with the lemniscatoids parametrization as shown in Ref. [16]. By using this, we can describe the smooth transition from the two- to the one-body mean-field potentials. The depths of the neutron and proton potentials are taken from Ref. [17]. We use the radius for the proton and neutron potentials R_0 with

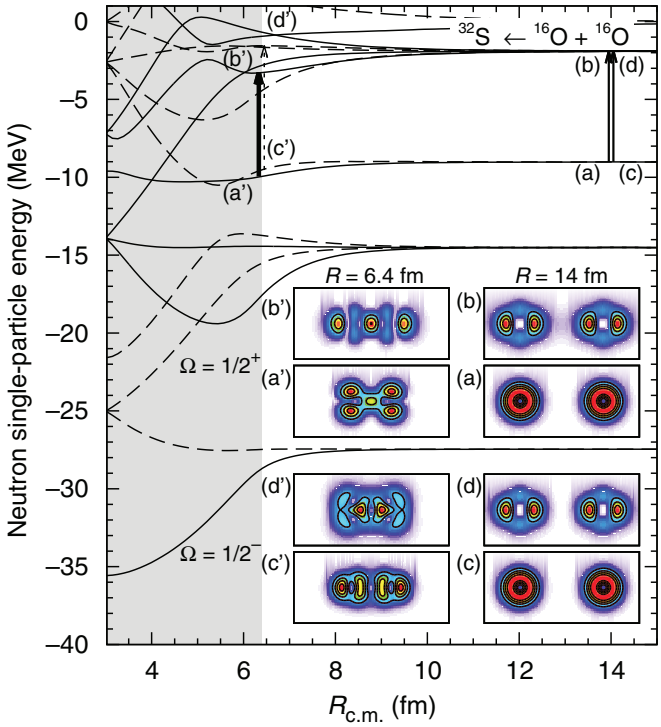

FIG. 1. (Color online) Nilsson diagram for the neutron single-particle states versus the distance between $^{16}O + {}^{16}O$. The solid and dashed lines denote the positive- and negative-parity states, respectively. The gray area denotes the overlap region of $^{16}O + {}^{16}O$. The solid and dashed arrows denote the main p-h excitations that generate the octupole vibration. The single-particle density distributions for these p and h states are given in the insets from (a) to (d) and (a′) to (d′).

$R_0 = 1.26A^{1/3}$ fm, where A is the total nucleon number. In the calculations, the origin is located at the center-of-mass position of the two nuclei. The above procedure works well because Umar and Oberacker found that the double-folding potential with the frozen density agrees almost perfectly with the density-constrained time-dependent Hartree-Fock (TDHF) approach for distances $R \geqslant 6$ fm [18].

By using the obtained mean-field potentials, we solve the axially symmetric Schrödinger equation with the spin-orbit force. Then, the parity π and the z component of the total angular momentum Ω are the good quantum numbers. The details of the model and the parameters are similar to those in Refs. [15,17]. We calculate the single-particle wave functions of both the projectile and the target by using the one-center single Slater determinant. We expand the total single-particle wave function by many deformed harmonic-oscillator bases in the cylindrical coordinate representation. The deformation parameter of the basis functions is determined so as to cover the target and projectile. The basis functions are taken with their energy lower than $25\hbar\omega$.

Figure 1 shows the Nilsson diagram for the obtained neutron single-particle energies versus the distance between $^{16}O + {}^{16}O$. The solid and dashed lines denote the positive- and negative-parity states, respectively. The gray area denotes the overlap region of the two nuclei. The distance $R = 6.4$ fm corresponds to the touching point. Some densities for the obtained single particles at $R = 14$ and 6.4 fm are given in the insets from (a) to (d) and (a′) to (d′) in Fig. 1, respectively. At $R = 14$ fm, we see that the positive (negative) parity indicates the symmetric (asymmetric) combinations of the single-particle states that refer to the right- and left-sided ^{16}O. Thus, the positive- and negative-parity single-particle states are degenerate for large R. With decreasing R, these single-particle states smoothly change to those for the composite ^{32}S system.

We can now easily extend the RPA method [19] to the two-body system because the wave functions of both the one- and the two-body systems are described with the one-center Slater determinant. We can directly superpose all combinations of the particle (p) and hole (h) states for the obtained single particles in a unified manner for both the one- and the two-body systems. We solve the RPA equation at each center-of-mass distance between $^{16}O + {}^{16}O$. At large R values, the RPA solutions with $\Omega^\pi = 0^+$ and 0^- represent the symmetric and asymmetric combinations of the states where the RPA modes are excited in either the right- or the left-sided ^{16}O. When the R values decrease below the touching point, they smoothly change to excitation modes in the composite ^{32}S system. In the calculations, we only take into account the p-h states with the excitation energies below 30 MeV. We use the residual interaction as the density-dependent contact one taken from Ref. [20]. The strength of the residual interaction is determined at each R such that the lowest $\Omega^\pi = 0^-$ solution of the RPA appears at zero energy. We have developed a new scheme based on the Tomonaga theory of collective motion [21,22] that enables us to separate the center of mass, the relative motion, and the intrinsic degrees of freedom. It is a generalization of the known procedure in the RPA [23]. It is also interesting to compare our results with the TDHF dynamics [24].

For the calculated results, the obtained first excited state of the right-sided ^{16}O is the octupole (3^-) one with a large $B(E3)$ value. At $R = 15$ fm, the excitation energy and the $B(E3, 3_1^- \rightarrow 0_1^+)$ value are 5.29 MeV and 102.07 e^2 fm^6, respectively. We have checked that those values are consistent with the calculated results of the one-body ^{16}O. Figure 2(a) shows the calculated transition densities and currents [19] for the first excited state with $\Omega^\pi = 0^+$ at $R = 14$ fm. In Fig. 2(a), we can clearly see the octupole vibrations in both ^{16}O's. At $R = 8.0$ fm, the transition density of the neck part between two ^{16}O's develops [see Fig. 2(b)]. At $R = 6.4$ fm, the octupole vibrations of each ^{16}O become weak [see Fig. 2(c)]. The degenerating excitation energies of the first excited states with $\Omega^\pi = 0^+$ and 0^- split below $R = 8$ fm. They become 5.82 and 4.83 MeV at $R = 6.4$ fm.

To more clearly see the damping of the octupole vibrations, we calculate the $B(E3)$ value for the right-sided ^{16}O. We can easily calculate it by taking a symmetric linear combination of the octupole transition amplitudes for the positive- and negative-parity RPA solutions. Figure 3(a) shows the calculated $B(E3, 3_1^- \rightarrow 0_1^+)$ values versus the distance between $^{16}O + {}^{16}O$. In Fig. 3(a), we can see that the $B(E3)$ value for the right-sided ^{16}O (the solid line) falls off at around $R = 8$ fm with decreasing R, which indicates that the octupole vibrations are strongly suppressed near the touching point.

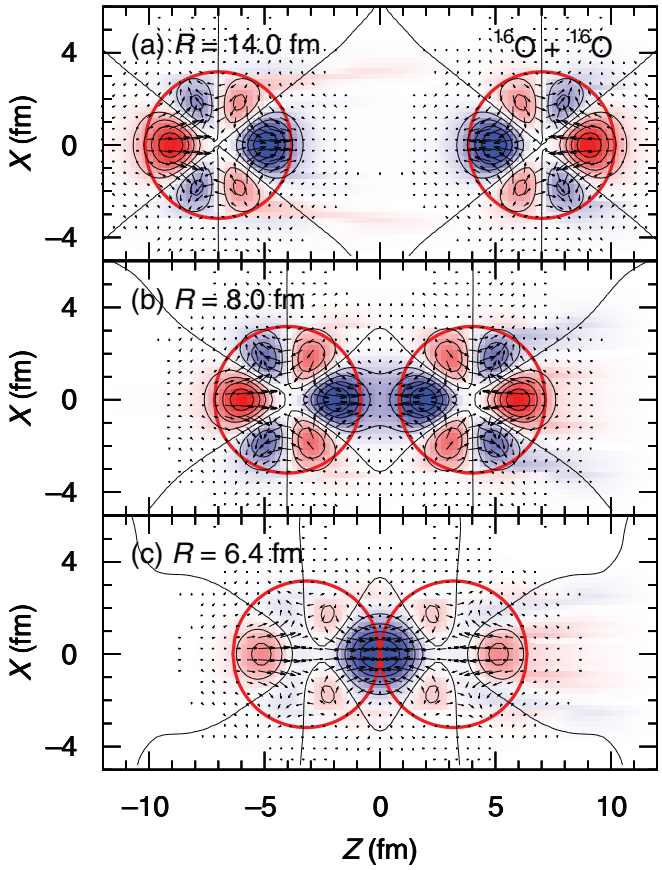

FIG. 2. (Color online) Transition densities and currents for the first excited 3^- state with $\Omega^\pi = 0^+$ at (a) $R = 14.0$ fm, (b) $R = 8.0$ fm, and (c) $R = 6.4$ fm. The contour lines denote the transition density. The arrows denote the current density. These two values are normalized in each plot. The (red) thick solid line denotes the half depth of the mean-field potential.

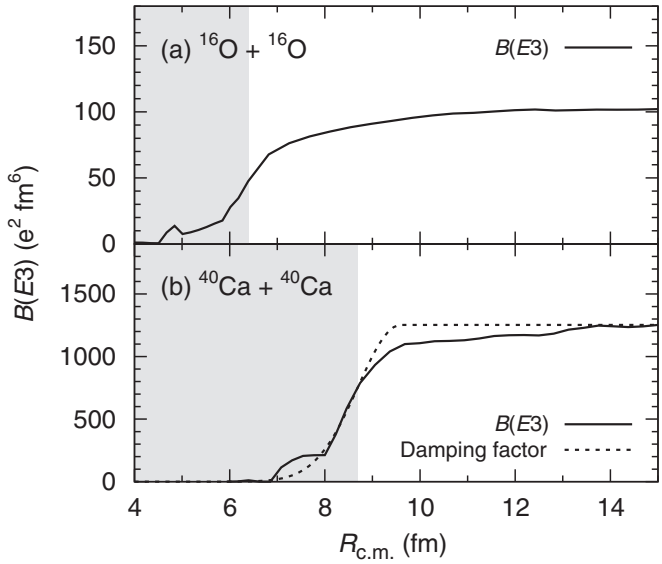

FIG. 3. Transition strengths $B(E3)$ for the first excited state versus the distance between (a) $^{16}O + ^{16}O$ and (b) $^{40}Ca + ^{40}Ca$. The solid line denotes the calculated results. The gray area denotes the overlap region of the two colliding nuclei. In the bottom panel (b), the dotted line denotes the damping factor of Eq. (2) in Ref. [14], estimated from the experimental data of the fusion cross section.

The damping of the vibrations originates from the change in the single-particle wave functions. At $R = 14$ fm, the major p-h excitations that generate the octupole vibration are those from the $p_{1/2}$ to the $d_{5/2}$ single-particle states in ^{16}O. In these states, the degenerating positive- and negative-parity doublet states contribute equally to generate the octupole vibration. Those can be seen in the density distributions of the $\Omega^\pi = 1/2^+$ and $1/2^-$ states given in the insets from (a) to (d) in Fig. 1. The corresponding p-h excitations are denoted by the solid arrows from (a) to (b) and (c) to (d) in Fig. 1. When the two nuclei approach each other, the features of these single-particle wave functions drastically change. At $R = 6.4$ fm, the neck formation takes place in the positive-parity states, whereas, it is forbidden for the negative-parity states (that have nodes at the touching point). Thus, the density distributions of those parity partners become quite different from each other. [See the insets from (a′) to (d′).] In the RPA calculation, the contributions from the negative-parity states to the octupole vibration become small at the touching point [see the solid and dotted arrows from (a′) to (b′) and (c′) to (d′), respectively], which results in the decreases in the $B(E3)$ value.

The mechanism for the damping of the quantum vibration is a general one, which is also valid for heavier-mass systems. We have also performed the RPA calculations for the $^{40}Ca + ^{40}Ca$ and $^{56}Ni + ^{56}Ni$ systems. In the calculations, we use $R_0 = 1.27\,A^{1/3}$. We obtained the similar damping of the $B(E3)$ values for the both systems. In Fig. 3(b), the solid line denotes the calculated result for the $^{40}Ca + ^{40}Ca$ system. The calculated excitation energy and the $B(E3, 3^-_1 \to 0^+_1)$ value for the $^{40}Ca + ^{40}Ca$ system are 3.24 MeV and 1253.17 e^2 fm^6 at $R = 15.0$ fm, respectively.

As shown above, the octupole vibrations are damped near the touching point, which results in the vanishing of the couplings between the relative motion and the vibrational intrinsic degrees of freedom. This vanishing would lead to the smooth transition from the sudden to the adiabatic process as shown in Ref. [14]. It is clear that such an effect has not been taken into account in the standard CC model. One candidate to include is the introduction of the damping factor proposed in Ref. [14]. To clearly see the effect of the vanishing of the couplings, we calculate the fusion cross section for the $^{40}Ca + ^{40}Ca$ system by using the computer code CCFULL [25] coupled with the damping factor based on the model of Ref. [14].

In the calculations, we include the couplings to only the low-lying 3^- and 2^+ states and to single-phonon and all mutual excitations of these states. We take the energies and the deformations of each state taken from Ref. [7] to reproduce the experimental data well. We use the same deformation parameters for the Coulomb and nuclear couplings. For the parameters of the Yukawa-plus-exponential (YPE) model, we use $r_0 = 1.191$ and $a = 0.68$ fm.

It is remarkable that the damping factor strongly correlates with the calculated $B(E3)$ value for the $^{40}Ca + ^{40}Ca$ system. To show this, we take $\lambda_\alpha = 0$ in the damping factor of Eq. (2)

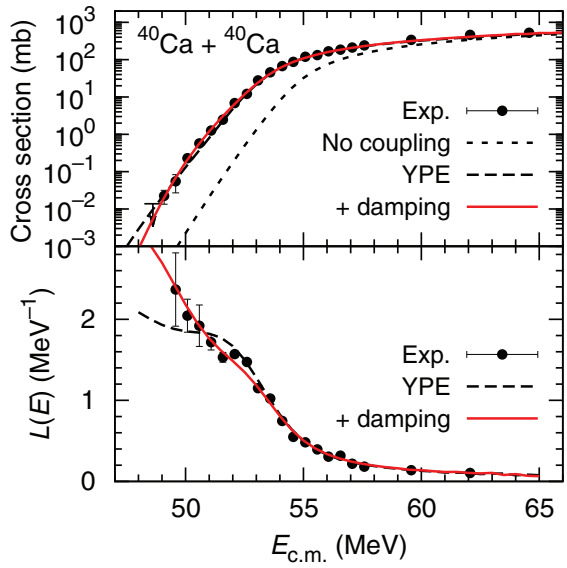

FIG. 4. (Color online) Fusion cross section (upper panel) and its logarithmic derivative (lower panel) for the ^{40}Ca + ^{40}Ca system versus the incident energies. The solid circles denote the experimental data taken from Ref. [7]. The solid and dashed lines denote the calculated results of the coupled-channel method by using the YPE potential with and without the damping factor, respectively. The dotted line denotes the calculated result without the couplings.

in Ref. [14] for simplicity. We tune the parameters R_d and a_d in the damping factor so as to reproduce the experimental data of the fusion cross section. We obtain $R_d = 9.6$ and $a_d = 0.9$ fm as the best fits to the data. In Fig. 3(b), the dotted line denotes the obtained damping factor normalized at $R = 15$ fm.

Figure 4 shows the calculated fusion cross section (upper panel) and its logarithmic derivative $d\ \ln(E_{\rm c.m.}\sigma_{\rm fus})/dE_{\rm c.m.}$ (lower panel) for the ^{40}Ca + ^{40}Ca system. The solid and dashed lines denote the calculation with and without the damping factor, respectively. The dotted line denotes the calculation without the couplings. In Fig. 4, we can see that the calculated results with the damping factor reproduce the experimental data well, which is better than the sudden model [7,12]. In our model, the calculated astrophysical S factor has a peak structure. We also performed the CC calculation for the ^{48}Ca + ^{48}Ca system, and the calculated result reproduces the experimental data well. The CC calculations with the damping factor also already reproduced the experimental data for the ^{64}Ni + ^{64}Ni, ^{58}Ni + ^{58}Ni, and ^{16}O + ^{208}Pb systems well [14].

To summarize, we have demonstrated the damping of the quantum vibrations when two nuclei adiabatically approach each other. To show this, we, for the first time, applied the RPA method to the two-body ^{16}O + ^{16}O and ^{40}Ca + ^{40}Ca systems and calculated the $B(E3)$ values of each nucleus. We have shown that the calculated $B(E3)$ value is indeed damped near the touching point. We have also shown that the damping factor proposed in Ref. [14] strongly correlates with the calculated $B(E3)$ values and the calculations of the fusion cross section coupled with the damping factor reproduce the experimental data well. This indicates that the fusion hindrance originates from the damping of the quantum couplings and strongly suggests that the smooth transition from the sudden to the adiabatic processes occurs near the touching point.

The authors thank K. Hagino and A. Iwamoto for useful discussions. A part of this research was funded by the MEXT HPCI STRATEGIC PROGRAM. This work was supported by JSPS KAKENHI Grant Number 25800145.

[1] M. Dasgupta *et al.*, Annu. Rev. Nucl. Part. Sci. **48**, 401 (1998).
[2] A. B. Balantekin and N. Takigawa, Rev. Mod. Phys. **70**, 77 (1998).
[3] K. Hagino and N. Takigawa, Prog. Theor. Phys. **128**, 1061 (2012).
[4] C. L. Jiang *et al.*, Phys. Rev. Lett. **89**, 052701 (2002); **93**, 012701 (2004); C. L. Jiang, B. B. Back, H. Esbensen, R. V. F. Janssens, and K. E. Rehm, Phys. Rev. C **73**, 014613 (2006); C. L. Jiang, B. B. Back, R. V. F. Janssens, and K. E. Rehm, *ibid.* **75**, 057604 (2007); C. L. Jiang, K. E. Rehm, B. B. Back, and R. V. F. Janssens, *ibid.* **79**, 044601 (2009).
[5] M. Dasgupta *et al.*, Phys. Rev. Lett. **99**, 192701 (2007).
[6] A. M. Stefanini *et al.*, Phys. Rev. C **78**, 044607 (2008); Phys. Lett. B **679**, 95 (2009).
[7] G. Montagnoli *et al.*, Phys. Rev. C **85**, 024607 (2012).
[8] T. Ichikawa, K. Hagino, and A. Iwamoto, Phys. Rev. C **75**, 064612 (2007).
[9] E. S. Zin Thein, N. W. Lwin, and K. Hagino, Phys. Rev. C **85**, 057602 (2012).
[10] Ş Mişicu and H. Esbensen, Phys. Rev. Lett. **96**, 112701 (2006); Phys. Rev. C **75**, 034606 (2007).
[11] H. Esbensen, C. L. Jiang, and A. M. Stefanini, Phys. Rev. C **82**, 054621 (2010).
[12] Ş Mişicu and F. Carstoiu, Phys. Rev. C **84**, 051601(R) (2011).
[13] A. Diaz-Torres, D. J. Hinde, M. Dasgupta, G. J. Milburn, and J. A. Tostevin, Phys. Rev. C **78**, 064604 (2008).
[14] T. Ichikawa, K. Hagino, and A. Iwamoto, Phys. Rev. Lett. **103**, 202701 (2009); EPJ Web Conf. **17**, 07001 (2011).
[15] M. Bolsterli *et al.*, Phys. Rev. C **5**, 1050 (1972).
[16] T. Ichikawa, K. Hagino, and A. Iwamoto, Phys. Rev. C **75**, 057603 (2007).
[17] P. Möller *et al.*, At. Data Nucl. Data Tables **59**, 185 (1995).
[18] A. S. Umar and V. E. Oberacker, Phys. Rev. C **74**, 021601(R) (2006).
[19] P. Ring and P. Schuck, *The Nuclear Many-Body Problem* (Springer-Verlag, Berlin, 1980).
[20] S. Shlomo and G. Bertsch, Nucl. Phys. A **243**, 507 (1975).
[21] S. Tomonaga, Prog. Theor. Phys. **13**, 468 (1955).
[22] T. Ichikawa and K. Matsuyanagi (to be published).
[23] S. Kamerdzhiev, R. J. Liotta, E. Litvinova, and V. Tselyaev, Phys. Rev. C **58**, 172 (1998).
[24] R. Keser, A. S. Umar, and V. E. Oberacker, Phys. Rev. C **85**, 044606 (2012).
[25] K. Hagino, N. Rowley, and A. T. Kruppa, Comput. Phys. Commun. **123**, 143 (1999).

PHYSICAL REVIEW C **89**, 011305(R) (2014)

Pure collective precession motion of a high-spin torus isomer

T. Ichikawa,[1] K. Matsuyanagi,[1,2] J. A. Maruhn,[3] and N. Itagaki[1]
[1]*Yukawa Institute for Theoretical Physics, Kyoto University, Kyoto 606-8502, Japan*
[2]*RIKEN Nishina Center, Wako 351-0198, Japan*
[3]*Institut fuer Theoretische Physik, Universitaet Frankfurt, D-60438 Frankfurt, Germany*
(Received 17 November 2013; published 16 January 2014)

We investigate the precession motion of the exotic torus configuration in high-spin excited states of ^{40}Ca. For this aim, we use the three-dimensional time-dependent Hartree-Fock (TDHF) method. Although the high-spin torus isomer is a unique quantum object characterized by the alignment of angular momenta of independent single-particle motions, we find that the obtained moment of inertia for rotations about an axis perpendicular to the symmetry axis is close to the rigid-body value. We also analyze the microscopic structure of the precession motion using the random-phase approximation (RPA) method for high-spin states. In the RPA calculation, the precession motion of the torus isomer is generated by coherent superposition of many one-particle–one-hole excitations across the sloping Fermi surface that strongly violates the time-reversal symmetry. By comparing results of the TDHF and the RPA calculations, we find that the precession motion obtained by the TDHF calculation is a pure collective motion well decoupled from other collective modes.

DOI: 10.1103/PhysRevC.89.011305 PACS number(s): 21.60.Jz, 21.60.Ev, 27.40.+z

Nuclear rotation is a collective motion that restores the symmetry spontaneously broken in the self-consistent mean field. When deformed nuclei break the spherical symmetry but preserve the axial symmetry, the rotation about the symmetry (z) axis is quantum mechanically forbidden. For instance, in high-spin oblate isomer states, the total angular momentum about the symmetry axis is constructed not by the collective rotation but the alignments of the angular momenta of individual nucleons [1,2]. However, even such a state can rotate about an axis perpendicular to the symmetry axis, because the density distribution breaks the rotational symmetry about that axis. Below we call this (x or y) axis a perpendicular axis. This rotational degree of freedom causes the *precession* motion of the system as a whole [3].

In our previous paper [4], we showed the existence of a stable torus configuration in high-spin excited states of ^{40}Ca, whose z component of the total angular momentum, K, is $K = 60\ \hbar$. This large angular momentum is generated by alignment of single-particle angular momenta of a total of twelve nucleons; the z components of the orbital angular momenta, $\Lambda = +4$, $+5$, and $+6\ \hbar$ for spin-up or -down neutrons and protons, are summed up to $K = 60\ \hbar$. Thus, this torus isomer has a significant amount of circulating current. A question then arises how such a "femto-scale magnet" rotates collectively to restore the broken symmetry about a perpendicular axis.

A key physical quantity to understand fundamental properties of nuclear rotation is the moment of inertia about a perpendicular axis. It is theoretically known that an independent-particle configuration in a deformed harmonic-oscillator potential rotates with rigid moment of inertia, provided that the self-consistency between the potential and the density distribution is fulfilled [5]. In reality, however, measured moments of inertia for deformed nuclei largely deviate from the rigid-body values. For instance, measured moments of inertia for precession motions of high-K prolate isomers are significantly smaller than rigid-body values [6,7]. This reduction has been seen at high spin where pairing correlations are negligible, and is attributed to shell effects [6]. For high-K oblate isomers, precession modes have not yet been observed. A possible reason is that their moments of inertia are much reduced from rigid-body values due to oblate shell structure at small deformation [8]. Then excitation energies of precession motion become higher. This would be a reason why the search for precession modes of a high-K oblate isomer is difficult and remains as an experimental challenge. The high-K torus isomer can be regarded as an extreme limit of the high-K oblate isomer. Therefore, dynamical properties of the high-K torus isomer revealed in its moment of inertia about a perpendicular axis will provide a fresh insight into dynamical properties of high-K oblate isomers as well.

In this Rapid Communication, we present a periodic numerical solution of the precession motion of the high-K torus isomer in ^{40}Ca described by the three-dimensional time-dependent Hartree-Fock (TDHF) equation. We trigger the precession motion by applying a certain amount of angular momentum in the direction of a perpendicular axis. We estimate the moment of inertia characterizing such an exotic mode of nuclear collective rotation. We find that the obtained moment of inertia is close to the rigid-body value. This result is surprising, because the high-K torus isomer is created by aligned angular momenta of independent particle motion and possesses strong time-odd components in the self-consistent mean field. We shall also analyze the microscopic structure of the precession motion using the random-phase approximation (RPA) method and compare with the result of the TDHF calculation.

Since the TDHF method describes time evolution of a wave packet, quantization is necessary to obtain quantum spectra. If we succeed in obtaining periodic numerical solutions in real-time evolution of the TDHF mean field, then we can adopt the semiclassical quantization procedure. It is, however, very difficult to obtain the periodic solutions, because nonlinear effects tend to destroy the periodic motion and lead to chaotic

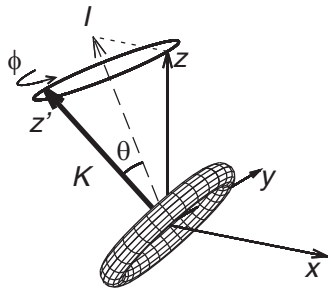

FIG. 1. Schematic picture of the precession motion of a high-K torus isomer. The bold solid arrow denotes the symmetry axis of the density distribution. The dashed arrow denotes the precession axis. The symbols θ and ϕ denote the tilting and the rotation angles, respectively.

motion. Thus, up to now, periodic solutions have been found only for a few relatively simple cases such as large-amplitude monopole vibrations in ^{4}He and ^{16}O [9]. Periodic solutions for rotational modes have not yet been reported. In this Rapid Communication, we will also show that the precession frequency obtained in the TDHF calculation agrees with that of the RPA method in good approximation. That is, we have, for the first time, succeeded in obtaining the quantum excitation energy of the precession motion by the numerical application of the TDHF method.

Figure 1 shows a schematic picture for the precession motion of a high-K torus isomer. In the figure, the bold solid arrow denotes the symmetry (z') axis of the density distribution in the body-fixed frame. At $t = 0$, this axis is identical to the z axis in the laboratory frame and the torus isomer has the angular momentum, K, along this axis. When we give an angular momentum to the (negative) direction of the x axis (the dotted line) at $t = 0$, the total angular momentum changes to $\vec{I}$. Then, the precession motion starts. The symmetry (z') axis rotates about a fixed axis (the dashed arrow) that coincides with the direction of the total angular momentum $\vec{I}$. We call this axis the precession axis. In the precession motion, the value K is conserved. The tilting angle, θ, is defined as the angle between the symmetry (z') axis and the precession axis (the direction of the total angular momentum). The symbol ϕ denotes the rotation angle of the z' axis rotating about the precession axis. The moment of inertia for the rotation about a perpendicular axis of the torus configuration, $\mathcal{I}_{\perp}$, is then given by $\mathcal{I}_{\perp} = I/\omega_{\rm prec}$, where $\omega_{\rm prec}$ denotes the rotational frequency of the precession motion. The first excited state of the precession motion is the state with $I = K + 1$. Since the torus isomer of ^{40}Ca has $K = 60\,\hbar$, we calculate the precession motion with $I = 61\,\hbar$.

To calculate the precession motion by means of the TDHF method, we use the code SKY3D [10]. We calculate the initial state of the torus configuration for ^{40}Ca with the z component of the total angular momentum $K = 60\ \hbar$ by the cranked HF method using this code. The details are given in Ref. [4]. In the calculations, the single-particle wave functions are described on a Cartesian grid with a grid spacing of 1.0 fm. We take $32 \times 32 \times 24$ grid points for the x, y,

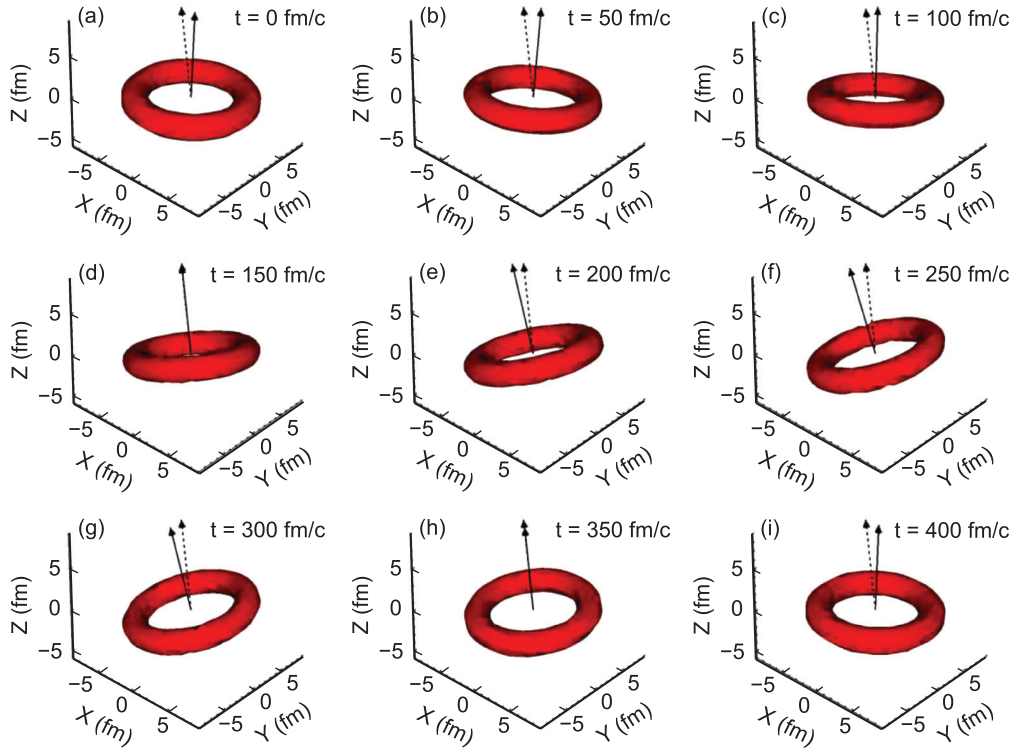

FIG. 2. (Color online) Snapshots of the time evolution of the density distribution of the high-K torus isomer in ^{40}Ca obtained by the TDHF calculations. The (red) surface indicate that the density is half of the maximum value there. The time step of each snapshot is 50 fm/c. The solid and the dotted lines denote the symmetry and the precession axes, respectively.

and z directions, respectively. In all the calculations, we use the SLy6 interaction [11]. As shown in Ref. [4], the interaction dependence is negligible, because the spin-orbit force effects are weak in the torus configuration. The obtained density distribution on the plane at $z = 0$ is well fitted by $\rho(r) = \rho_0 e^{-(r-R_0)^2/\sigma^2}$, where $\rho_0 = 0.12$ fm^{-3}, $R_0 = 6.06$ fm, and $\sigma = 1.64$ fm. The rigid-body moment of inertia calculated using the obtained density distribution is $\mathcal{I}_\perp^{\rm rid} = 21.1\ \hbar^2/\text{MeV}$.

To excite the precession motion, we provide an impulsive force at $t = 0$ fm/c by the external potential given by $V_{\rm ext}(r,\varphi,z) = V_0 z \cos\varphi \exp[-(r - R_0)^2/\sigma^2]$. The parameter V_0 is chosen such that the total angular momentum becomes $I = 61\ \hbar$, that is, the x component of the total angular momentum, I_x, is $I_x = -11.0\ \hbar$ at $t = 0$ [$I = \sqrt{60^2 + (-11)^2}\ \hbar = 61\ \hbar$]. Here, we use $V_0 = 0.12757$ MeV. We determine the time evolution of the density distribution by solving the TDHF equation of motion, $i\hbar\dot{\rho} = [h,\rho]$, where h is the single-particle Hamiltonian and ρ is the one-body density matrix. To solve the TDHF equation, we take a Taylor expansion to the time-development operator up to the 12th order in the code. The time step of the TDHF calculations is 0.2 fm/c. We calculate the time evolution until 3000 fm/c. Thus, we obtain about 7.5 periods of the precession motion.

Figure 2 shows snapshots of the time-evolution of the density distribution obtained by the TDHF calculations. In the figure, we plot the surface at the half of the maximum value of the density distribution. The time step of each snapshot is 50 fm/c. We can clearly see in this figure about one period of the precession motion of the high-K torus isomer of ^{40}Ca.

Figure 3 shows the time evolution of (a) the total angular momentum I, (b) the tilting angle θ, and (c) the rotational angle ϕ. In Fig. 3(a), we see that the value of the total angular momentum converges to about 61 $\hbar$, indicating that the TDHF calculations work well for long duration. The total energy also converges well. By the impulsive force, $-\partial V_{\rm ext}/\partial z$, exerted at $t = 0$, not only the precession motion but also other collective motions such as the γ vibrations might be excited. However, the tilting angle fluctuates only slightly between 10° and 11° [see Fig. 3(b)]. This indicates that the coupling effects between the precession motion and other collective modes are rather weak. In Fig. 3(c), we see that the rotational angle linearly increases in each period. The obtained periods are 401.4, 403.5, 404.6, 405.4, 403.5, 400.9, and 401.5 fm/c. The fluctuations of the period indicate the extent of the effects due to the couplings with other collective modes and/or precision of numerical calculation. They are much smaller (less than 1%) than the time scale of the precession motion. The average period, $T_{\rm prec}$, is 403.0 fm/c. Thus, the average frequency is $\omega_{\rm prec} = 2\pi/T_{\rm prec} = 3.08\,\text{MeV}/\hbar$. We can identify $\hbar\omega_{\rm prec}$ with the $\Delta I = 1$ excitation energy of the precession mode of the high-K torus isomer. We shall later confirm this interpretation in connection with the RPA treatment of this mode. The moment of inertia obtained in this way is $\mathcal{I}_\perp^{\rm TDHF} = I/\omega_{\rm prec} = 19.8\ \hbar^2/\text{MeV}$, which is very close to the rigid-body value $\mathcal{I}_\perp^{\rm rid} = 21.1\ \hbar^2/\text{MeV}$. The high-$K$ torus isomer is a unique quantum object characterized by the alignment of angular momenta of independent single-particle motions. The alignment causes a significant amount of circulating current and, as a consequence, the self-consistent mean field strongly violates the time-reversal symmetry. Although these features are essentially different from the classical rigid body, we find that the high-K torus isomer performs a collective rotation about a perpendicular axis with the moment of inertia close to the rigid-body value.

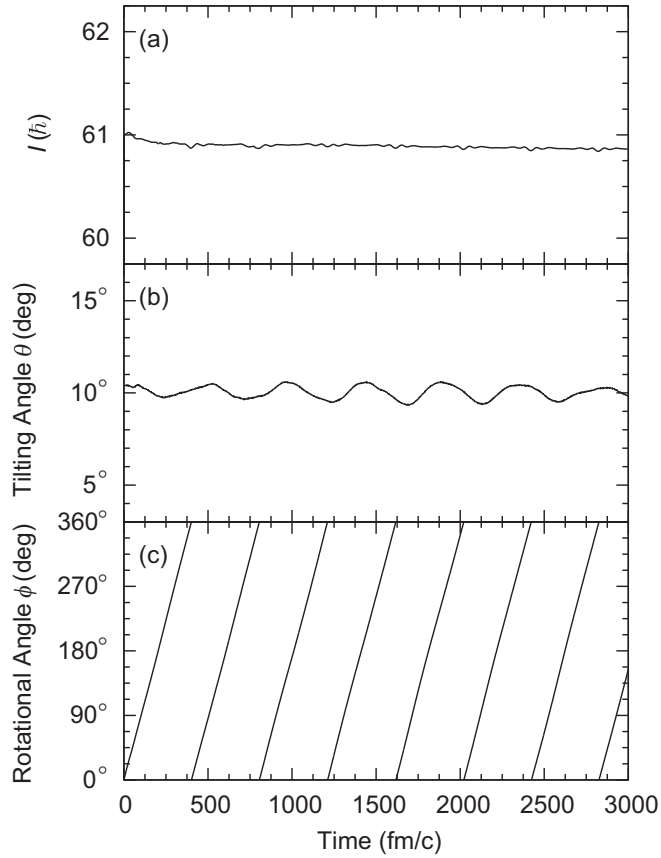

FIG. 3. Time-evolution of (a) total angular momentum I, (b) the tilting angle θ, and (c) the rotational angle ϕ of the precession motion for the high-K torus isomer in ^{40}Ca.

To obtain a deeper understanding of the microscopic particle-hole structure generating the collective precession motion, we have performed an RPA calculation with the radial displaced harmonic-oscillator (RDHO) model [12]. We also confirm the validity of the relation $\mathcal{I}_\perp^{\rm TDHF} = I/\omega_{\rm prec}$ used to extract the moment of inertia from the real-time TDHF evolution. The RDHO model represents the major features of the torus isomer and works well, because effects of the spin-orbit force are negligible in the torus configuration. We can also avoid the complications for the treatment of unbound single-particle states by using this model. In the RDHO model for the torus configuration, the single-particle potential V is given, in the cylindrical coordinates, by $V(r,z) = \frac{1}{2}m\omega_0^2(r - R_0)^2 + \frac{1}{2}m\omega_0^2 z^2$, where m and R_0 denote the nucleon mass and the torus radius, respectively. The Coulomb potential is ignored for simplicity. The harmonic-oscillator frequency ω_0 is determined such that the density distribution calculated with this model agrees, in good approximation, with that of the torus isomer obtained by the cranked HF calculation. The rigid-body moment of inertia calculated with the RDHO

density distribution is $\mathcal{I}_\perp^{\rm RDHO} = 21.1\ \hbar/{\rm MeV}$, which agrees with the rigid-body value, $\mathcal{I}_\perp^{\rm rid}$, for the torus isomer.

We can easily determine the frequency of the precession motion by solving the RPA dispersion equation [7], $\mathcal{I}_\perp^{\rm RPA}(\omega) = K/\omega$, where the moment of inertia, $\mathcal{I}_\perp^{\rm RPA}$, is a function of ω defined by

$$\mathcal{I}_\perp^{\rm RPA}(\omega) = \frac{\hbar^2}{2}\sum_{ph}\left\{\frac{|J_+^{ph}|^2}{(\epsilon_{ph}-\hbar\omega)} + \frac{|J_-^{ph}|^2}{(\epsilon_{ph}+\hbar\omega)}\right\}. \quad (1)$$

Here the sum is taken over the one-particle–one-hole (1p-1h) excitations across the sloping Fermi surface (see Fig. 3 in Ref. [4]) and ϵ_{ph} denote their excitation energies. The quantities $J_\pm^{ph}$ represent the matrix elements of the angular momentum raising and lowering operators, $J_\pm^{ph} = \langle ph|\hat{J}_\pm|0\rangle$, between the torus configuration $|0\rangle$ and the 1p-1h excited states $|ph\rangle$. This RPA dispersion equation is valid for velocity-independent residual interactions, and it yields the classical relation, $\mathcal{I}_\perp^{\rm rid} = I/\omega$, except that anharmonic effects higher order in $1/K$ are ignored and, accordingly, I is approximated by K. By solving the RPA dispersion equation, we can simultaneously determine the frequency, ω, and the moment of inertia, $\mathcal{I}_\perp$, of the precession motion. The lowest eigenfrequency that satisfies the above equation is just the RPA precession frequency of interest. We denote this solution $\omega_{\rm RPA}$. The precession motion is generated by coherent superposition of many 1p-1h excitations across the sloping Fermi surface. The value of $\mathcal{I}_\perp^{\rm RPA}$ at $\omega_{\rm RPA}$ is the RPA moment of inertia for the precession motion. In the limit $\omega_{\rm RPA} = 0$, $\mathcal{I}_\perp^{\rm RPA}$ reduces to the adiabatic cranking formula, $\mathcal{I}_\perp^{\rm crank}$. Using the single-particle wave functions obtained by the RDHO model, we determine $\omega_{\rm RPA}$ and $\mathcal{I}_\perp^{\rm RPA}$. In the calculations, we take all 1p-1h excitations whose energies are below $\epsilon_{ph} \leqslant 30$ MeV. We obtain $\omega_{\rm RPA} = 3.02\ {\rm MeV}/\hbar$ and $\mathcal{I}_\perp^{\rm RPA} = 19.6\ \hbar^2/{\rm MeV}$. This value of the RPA moment of inertia is different from the adiabatic cranking value $\mathcal{I}_\perp^{\rm crank} = 20.0\ \hbar^2/{\rm MeV}$ only slightly, indicating that the effect of the finite frequency ($\omega_{\rm RPA} \neq 0$) is rather small for the precession motion under consideration.

The RPA frequency $\omega_{\rm RPA}$ and the moment of inertia $\mathcal{I}_\perp^{\rm RPA}$ agree with the TDHF results for $\omega_{\rm prec}$ and $\mathcal{I}_\perp^{\rm TDHF}$ in very good approximation. If K is replaced with $I = K + 1$ in the RPA dispersion equation, the agreement becomes even better ($\omega_{\rm RPA} = 3.07\ {\rm MeV}/\hbar$). This almost perfect agreement clearly indicates that the periodic numerical solution obtained in the real-time TDHF evolution describes the collective rotation well decoupled from other collective modes. The agreement between the TDHF and RPA results furthermore suggests that the net effect of the velocity-dependent interactions such as the spin-orbit interaction is small, despite the presence of a significant amount of circulating current which strongly violates the time-reversal symmetry in the self-consistent mean field. As we have seen in [4], the effects of the spin-orbit potential almost cancel out between the inside and outside of the torus radius R_0. This suggests that the velocity-dependent interaction effects are almost canceled out for the precession motion under consideration. The results of the TDHF and the RPA calculations thus suggest that basic physical conditions for the occurrence of the rigid precession motion are (1) the independent-particle configuration is pure and stable, (2) the symmetry breaking about a perpendicular axis is sufficiently strong, and (3) the net effect of the velocity-dependent interactions is small.

In summary, we have obtained a periodic numerical solution in the TDHF time evolution that describes the precession motion of the high-K torus isomer with $K = 60\ \hbar$ in ^{40}Ca. Although the high-K torus isomer is a unique quantum object characterized by the alignment of angular momenta of independent single-particle motions, we find that the torus isomer performs a collective rotation about an axis perpendicular to the symmetry axis with the moment of inertia close to the classical rigid-body value. We have also performed the RPA calculation for the precession motion with the RDHO model. By comparing the results of the TDHF and the RPA calculations, we have confirmed that the periodic TDHF solution corresponds to the precession mode generated by coherent superposition of many 1p-1h excitations across the sloping Fermi surface. This exotic mode of rotation at high spin is ideally decoupled from other collective modes.

A part of this research has been funded by the MEXT HPCI STRATEGIC PROGRAM. This work was undertaken as part by the Yukawa International Project for Quark-Hadron Sciences (YIPQS). J.A.M. was supported by BMBF under Contracts No. 06FY9086 and No. 05P12RFFTG.

[1] A. Bohr, in *Elementary Modes of Excitation in Nuclei*, *Proceedings of the International School of Physics "Enrico Fermi", Course LXIX*, edited by A. Bohr and R. A. Broglia (North-Holland, Amsterdam, 1977), p. 3.
[2] A. V. Afanasjev *et al.*, Phys. Rep. **322**, 1 (1999).
[3] A. Bohr and B. R. Mottelson, Nucl. Phys. A **354**, 303c (1981).
[4] T. Ichikawa *et al.*, Phys. Rev. Lett. **109**, 232503 (2012).
[5] A. Bohr and B. R. Mottelson, *Nuclear Structure*, Vol. II (World Scientific, Singapore, 1998).
[6] M. A. Deleplanque, S. Frauendorf, V. V. Pashkevich, S. Y. Chu, and A. Unzhakova, Phys. Rev. C **69**, 044309 (2004).
[7] Y. R. Shimizu, M. Matsuzaki, and K. Matsuyanagi, Phys. Rev. C **72**, 014306 (2005).
[8] C. G. Anderson *et al.*, Nucl. Phys. A **361**, 147 (1981).
[9] J.-S. Wu, M. R. Strayer, and M. Baranger, Phys. Rev. C **60**, 044302 (1999).
[10] J. A. Maruhn *et al.*, arXiv:1310.5946.
[11] E. Chabanat *et al.*, Nucl. Phys. A **627**, 710 (1997).
[12] C. Y. Wong, Ann. Phys. (NY) **77**, 279 (1973).

Observation of Low- and High-Energy Gamow-Teller Phonon Excitations in Nuclei

Y. Fujita,[1,2,†] H. Fujita,[1] T. Adachi,[1] C. L. Bai,[3] A. Algora,[4,5] G. P. A. Berg,[6] P. von Brentano,[7] G. Colò,[8] M. Csatlós,[5] J. M. Deaven,[9] E. Estevez-Aguado,[4] C. Fransen,[7] D. De Frenne,[10,*] K. Fujita,[1] E. Ganioğlu,[11] C. J. Guess,[9,‡] J. Gulyás,[5] K. Hatanaka,[1] K. Hirota,[1] M. Honma,[12] D. Ishikawa,[1] E. Jacobs,[10] A. Krasznahorkay,[5] H. Matsubara,[1,§] K. Matsuyanagi,[13,14] R. Meharchand,[9,‖] F. Molina,[4,¶] K. Muto,[15] K. Nakanishi,[1,**] A. Negret,[16] H. Okamura,[1,*] H. J. Ong,[1] T. Otsuka,[17] N. Pietralla,[7,††] G. Perdikakis,[9,18] L. Popescu,[19] B. Rubio,[4] H. Sagawa,[12,13] P. Sarriguren,[20] C. Scholl,[7,‡‡] Y. Shimbara,[21,§§] Y. Shimizu,[1,‖‖] G. Susoy,[11] T. Suzuki,[1] Y. Tameshige,[1] A. Tamii,[1] J. H. Thies,[22] M. Uchida,[1] T. Wakasa,[1,¶¶] M. Yosoi,[1] R. G. T. Zegers,[9] K. O. Zell,[7] and J. Zenihiro[1,‖‖]

[1]*Research Center for Nuclear Physics, Osaka University, Ibaraki, Osaka 567-0047, Japan*
[2]*Department of Physics, Osaka University, Toyonaka, Osaka 560-0043, Japan*
[3]*Department of Physics, Sichuan University, Chengdu 610065, China*
[4]*Instituto de Física Corpuscular, CSIC-Universidad de Valencia, E-46071 Valencia, Spain*
[5]*Institute for Nuclear Research (MTA-Atomki), H-4001 Debrecen, Post Office Box 51, Hungary*
[6]*Department of Physics and JINA, University of Notre Dame, Notre Dame, Indiana 46556, USA*
[7]*Institut für Kernphysik, Universität zu Köln, D-50937 Köln, Germany*
[8]*Dipartimento di Fisica, Università degli Studi di Milano, and INFN, Sezione di Milano, via Celoria 16, 20133 Milano, Italy*
[9]*National Superconducting Cyclotron Laboratory, Michigan State University, East Lansing, Michigan 48824-1321, USA*
[10]*Vakgroep Subatomaire en Stralingsfysica, Universiteit Gent, B-9000 Gent, Belgium*
[11]*Department of Physics, Istanbul University, Istanbul 34134, Turkey*
[12]*Center for Mathematical Sciences, University of Aizu, Aizu-Wakamatsu, Fukushima 965-8580, Japan*
[13]*RIKEN, Nishina Center, Wako Saitama 351-0198, Japan*
[14]*Yukawa Institute for Theoretical Physics, Kyoto University, Kyoto 606-8502, Japan*
[15]*Department of Physics, Tokyo Institute of Technology, Ohokayama, Meguro, Tokyo 152-8551, Japan*
[16]*Horia Hulubei National Institute for Physics and Nuclear Engineering, 077125 Bucharest-Magurele, Romania*
[17]*Department of Physics, University of Tokyo, Hongo, Bunkyo, Tokyo 113-0033, Japan*
[18]*Department of Physics, Central Michigan University, Mt. Pleasant, Michigan 48859, USA*
[19]*SCK-CEN, Belgian Nuclear Research Center, B-2400 Mol, Belgium*
[20]*Instituto de Estructura de la Materia, IEM-CSIC, Serrano 123, E-28006 Madrid, Spain*
[21]*Graduate School of Science and Technology, Niigata University, Nishi, Niigata 950-2181, Japan*
[22]*Institut für Kernphysik, Westfälische Wilhelms-Universität, D-48149 Münster, Germany*

(Received 29 January 2014; published 18 March 2014)

Gamow-Teller (GT) transitions in atomic nuclei are sensitive to both nuclear shell structure and effective residual interactions. The nuclear GT excitations were studied for the mass number $A = 42$, 46, 50, and 54 "f-shell" nuclei in (^{3}He, t) charge-exchange reactions. In the ^{42}Ca $\rightarrow$ ^{42}Sc reaction, most of the GT strength is concentrated in the lowest excited state at 0.6 MeV, suggesting the existence of a low-energy GT phonon excitation. As A increases, a high-energy GT phonon excitation develops in the 6–11 MeV region. In the ^{54}Fe $\rightarrow$ ^{54}Co reaction, the high-energy GT phonon excitation mainly carries the GT strength. The existence of these two GT phonon excitations are attributed to the 2 fermionic degrees of freedom in nuclei.

DOI: 10.1103/PhysRevLett.112.112502 PACS numbers: 24.30.Cz, 25.55.Kr, 27.40.+z

Atomic nuclei are the "quantum finite many-body system" consisting of correlated nucleons, i.e., protons and neutrons. However, the independent particle model called the shell model (SM), has succeeded in describing single "particle (p)" or single "hole (h)" properties of a proton (π) or a neutron (ν). By introducing a spin-orbit ($L \cdot S$) force, whose effect is stronger than in atoms, the shell closures at "magic numbers" (the proton number Z or neutron number N of 2, 8, 20, 28, and so forth [see, e.g., Ref. [1]]) were reproduced. The "doubly magic nuclei" such as ^{4}He with $N = Z = 2$, ^{16}O with $N = Z = 8$, or ^{40}Ca with $N = Z = 20$ behave like an atomic inert gas, and can work as inert cores.

Nucleons can also form strongly correlated pairs [2,3]. These nuclear correlations can be treated as effective residual interactions (ERIs). The collective excitations caused by ERIs are commonly observed in many-body systems. In nuclei, giant resonances (GRs) with specific total angular momentum and parity (J^π values) are examples. They are visualized as one-phonon vibrations from a macroscopic view point, or as collective excitations of particle-hole (p-h) or particle-particle (p-p) configurations from a microscopic view point [4]. Note that nucleons have a spin degree of freedom. In addition, they have two "faces," i.e., π and ν. In 1932, Heisenberg introduced the isospin quantum number T to describe phenomena caused

by the 2 fermionic degrees of freedom. Therefore, GRs as well as ERIs can be specified by their spin nonflip and spin flip nature and, also, by the isoscalar (IS) and the isovector (IV) characters. In IV excitations, πs and νs vibrate out of phase. Note that they are found only in systems having 2 fermionic degrees of freedom. In this respect, Gamow-Teller (GT) excitations specified by both spin and IV excitations are characteristic of nuclei.

Only a few configurations are involved in GT transitions caused by the GT operator $\sigma\tau$ having no radial or angular momentum component [5,6]. In a SM picture, where the nucleons are in an orbit with angular momentum ℓ and spin $s = \pm 1/2$, GT transitions can connect only the orbits with the $j_>$ $(= \ell + 1/2)$ and $j_<$ $(= \ell - 1/2)$ values, where the former is energetically lower than the latter due to the $L \cdot S$ force. Therefore, without ERIs, a transition between $j_>$ orbits causes an excitation at zero energy, while a $j_> \rightarrow j_<$ transition occurs at 3 to 7 MeV [1].

Absolute values of GT transition strength B(GT) can be obtained in β-decay studies. The accessible excitation energy (E_x), however, is limited by the decay Q value [6]. In the 1980s, it was found that charge-exchange (CE) reactions at intermediate incident energies ($E >$ 100 MeV/nucleon) and the scattering angle $\Theta = 0°$ are good tools for the study of GT excitations [4]. In the studies using (p, n) reactions [7], bumplike GT resonances (GTRs), i.e., high-energy GT phonon excitations, with a few MeV width were commonly observed at $E_x = 9$–18 MeV in nuclei with mass A larger than about 60 [7,8]. The main part of the GT strength was carried by the GTRs containing $\approx$ 50–60% of the GT sum-rule strength [8]. Note that GTRs were always observed at E_xs higher than the energy difference of the $j_<$ and $j_>$ orbits. Because of the neutron excess in these nuclei, the main configurations of the GTRs are of p-h nature. It is well established that the ERIs among the p-h configurations in IV excitations, such as the GT or IV dipole excitations, have a repulsive nature, and thus, IV GRs are pushed up relative to the unperturbed p-h energies [4]. On the contrary, in lighter nuclei with mass number $A \leq 40$, prominent high-energy GTRs are not observed; the GT strength is mainly carried by states at lower energies [6,7]. This raises a question of how these two features of GT strength distributions can be understood consistently.

In order to reconcile these observations, we studied the GT excitations for the "f-shell" nuclei in the transitional mass region of $40 < A < 60$ using the (p, n)-type (^{3}He, t), CE reaction. The orbits $f_{5/2}$ and $f_{7/2}$ with $\ell = 3$ represent the $j_<$ and $j_>$ orbits, respectively, where the single particle energy of the former is about 6 MeV higher than that of the latter [1]. For a systematic study, we selected target nuclei with even Z and N numbers and neutron excesses of two, i.e., $T_z = +1$, where $T_z = (N - Z)/2$ is the z component of isospin T. They were ^{42}Ca, ^{46}Ti, ^{50}Cr, and ^{54}Fe. The final nuclei are ^{42}Sc, ^{46}V, ^{50}Mn, and ^{54}Co with odd Z and N numbers and $T_z = 0$, respectively.

It has been shown that GT excitations dominate the spectra of the (^{3}He, t), CE reaction at 0° and an intermediate beam energy of 140 MeV/nucleon [6]. In addition, although there were exceptions, a close proportionality between the cross sections at 0° and the B(GT) values

$$\sigma(0°) \simeq \hat{\sigma}^{\mathrm{GT}}(0°) B(\mathrm{GT}), \tag{1}$$

has been empirically established [6,9–13], where $\hat{\sigma}^{\mathrm{GT}}(0°)$ is the unit GT cross section at 0°.

The (^{3}He, t) experiments were performed at the high resolution facility of RCNP, consisting of a beam line WS course [14] and the Grand Raiden spectrometer [15] using the ^{3}He beam from the $K = 400$ Ring Cyclotron [16]. The targets consisted of enriched self-supporting ^{42}Ca, ^{46}Ti, ^{50}Cr, and ^{54}Fe metal foils with thicknesses of 0.8–1.8 mg/cm^2. The outgoing tritons were momentum analyzed within the full acceptance of the spectrometer at 0° and detected with a focal-plane detector system [17].

Energy resolutions of $\Delta E = 21$–33 keV (FWHM), much better than the energy spread of the beam of about 120 keV, were realized by applying both dispersion matching and focus matching techniques [6,18,19]. These resolutions are about 1 order of magnitude better than those in the pioneering (p, n) works [7,20,21]. This high energy resolution makes a detailed study of GT excitations possible. A good angular resolution of $\Delta\Theta \leq$ 5 mr (FWHM) was achieved by applying the angular dispersion matching technique [18] and the overfocus mode of the spectrometer [22].

The acceptance of the spectrometer was subdivided into four scattering-angle regions of $\Theta = 0°$–0.5°, 0.5°–1.0°, 1.0°–1.5°, and 1.5°–2.0° using the tracking information. The $J^\pi = 1^+$, GT states excited by $\Delta L = 0$, GT transitions can be identified by their maximum intensity at $\Theta = 0°$ (for detail, see [23]). Figure 1 shows the "0° spectra" that include the events with $\Theta \leq 0.5°$. The ^{46}V, ^{50}Mn, and ^{54}Co spectra are from Refs. [23–25], and the ^{42}Ca(^{3}He, t)^{42}Sc spectrum was newly measured in this study. The angular distribution analysis shows that most of the prominent states are excited with $\Delta L = 0$. Among them, the ground states are all $J^\pi = 0^+$ isobaric analog states (IASs), each forming an isospin multiplet with the target ground state. Therefore, it is suggested that the $\Delta L = 0$ excited states are $J^\pi = 1^+$, GT states [6]. The B(GT) values were derived using Eq. (1). The $\hat{\sigma}^{\mathrm{GT}}$ values were deduced by using the information on the $T_z = -1 \rightarrow 0$, β^+ decay [25,26] assuming that $T_z = \pm 1 \rightarrow 0$ mirror GT transitions have the same B(GT) values on the basis of isospin symmetry [6]. The gradual decrease of $\hat{\sigma}^{\mathrm{GT}}$ as a function of E_x [9] was corrected using distorted wave Born approximation calculations (see, e.g., [23]).

The remarkable feature in Fig. 1 is the completely different strength distributions in these four systems although the neutron excess in the initial nuclei is always

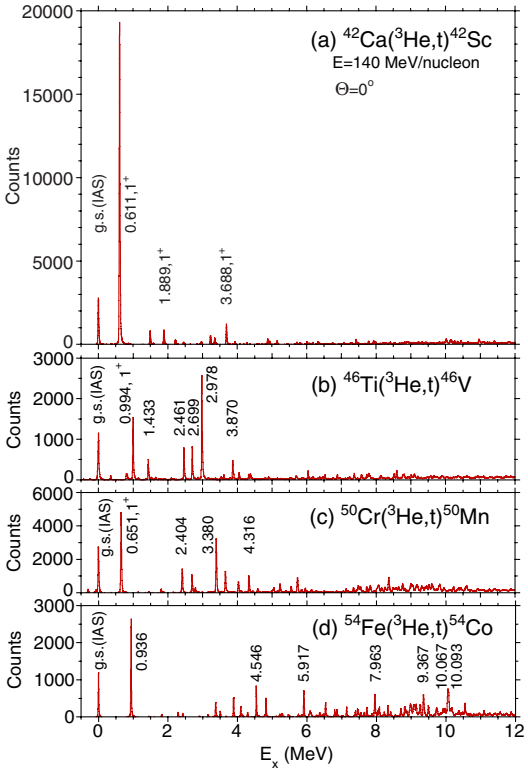

FIG. 1 (color online). High energy-resolution spectra of (^{3}He, t) reaction on $A = 42$–54, $T_z = +1$ target nuclei. The vertical scales are normalized so that the heights of all GT peaks are approximately proportional to the B(GT) values. The GT strength is concentrated in one low-energy state in ^{42}Sc [panel (a)]. The fine structures of GTRs in the 6–11 MeV region are observed in panels (c) and (d).

two. In ^{42}Sc, most of the GT strength, in agreement with [20], is concentrated in the excitation of the lowest GT state at 0.611 MeV. In ^{46}V and ^{50}Mn, however, the low-energy strength becomes fragmented and at the same time the bumplike structure of the GTR in the 6–11 MeV region begins to develop [Figs. 1(b) and 1(c)]. A fragmentation of GT strength was also observed in the ^{44}Ca → ^{44}Sc reaction [27], suggesting that the concentration of the strength is also hampered by a larger neutron excess of four in ^{44}Ca. Finally in ^{54}Co [Fig. 1(d)], the GT strength is mainly in the GTR.

The cumulative sum of the experimental B(GT) values is shown in Fig. 2(a) up to $E_x = 12$ MeV. A shift in the strength to higher energy with increasing A is again clearly seen. The total sum in ^{42}Sc is 2.7(4), with 80% of the GT strength carried by the lowest GT state. The observed sum gradually increases with A and it is 3.9(6) in ^{54}Co [23], where ≈75% of the GT strength is found in the high-energy GTR structure.

In a SM picture, the $j_>$ valence orbits, $\pi f_{7/2}$ and $\nu f_{7/2}$, outside the inert ^{40}Ca core ($Z = N = 20$) will be gradually filled in the $T_z = +1$, $A = 42$–54 nuclei as A increases (see Fig. 3). On the other hand, the $j_<$, $\pi f_{5/2}$ and $\nu f_{5/2}$ orbits

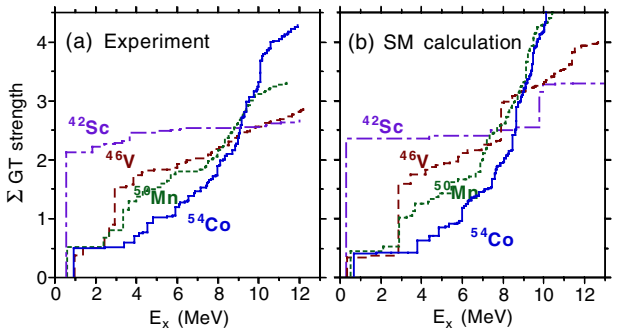

FIG. 2 (color online). (a) Cumulative-sum strengths of the experimental B(GT) values in the final nuclei ^{42}Sc, ^{46}V, ^{50}Mn, and ^{54}Co. They are shown by dotted-dashed, dashed, dotted, and solid lines, respectively. (b) Cumulative sums from SM calculations [28] including the quenching factor of $(0.74)^2$.

remain unpopulated. In this picture, without ERIs, we expect a low-energy GT excitation originating from the $\nu f_{7/2} \rightarrow \pi f_{7/2}$ transition and a high-energy one from the $\nu f_{7/2} \rightarrow \pi f_{5/2}$, where the latter is expected ≈6 MeV higher than the former due to the strong $L \cdot S$ force [1]. The single particle strengths of these GT excitations are similar, namely $B(\mathrm{GT}) = 9/7$ and $12/7$, respectively [9]. Taking into account the occupation and vacancy factors of the $f_{7/2}$ and $f_{5/2}$ shells, the relative strengths between the $\nu f_{7/2} \rightarrow \pi f_{7/2}$ and $\nu f_{7/2} \rightarrow \pi f_{5/2}$ transitions are 9:12 and 9:48 in the ^{42}Ca → ^{42}Sc and ^{54}Fe → ^{54}Co reactions, respectively. Therefore, we can, to some extent, understand the larger high-energy strength in the $A = 54$ system. However, from this simple picture, we cannot understand the concentration of GT strength to the low-energy 0.611 MeV state in the ^{42}Ca → ^{42}Sc reaction.

Figure 2(b) shows the cumulative sum of the GT strengths from SM calculations. The modern GXPF1J interaction used in the calculation was derived to reproduce various experimental data [28]. We see that the A dependence of the GT strength distribution, including the

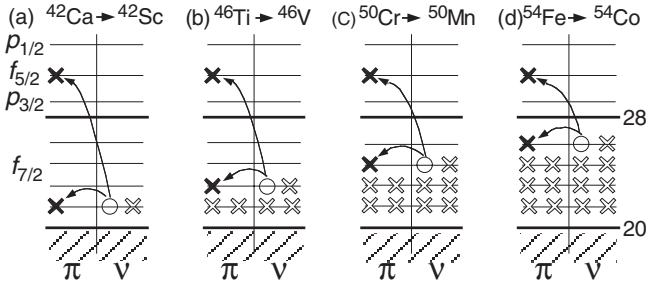

FIG. 3. The SM configurations before and after the β^--type GT transitions in $A = 42$–54, f-shell nuclei. Positions occupied by protons (π) and neutrons (ν) are shown by open crosses. Positions that are newly occupied by protons and unoccupied by neutrons after making GT transitions (shown by the arrows) are indicated by filled crosses and open circles, respectively. The shell closures at $Z = N = 20$ and 28 are indicated by thick solid lines.

concentration of the GT strength in the lowest GT state in ^{42}Sc, is well reproduced. However, we notice that this concentration of the GT strength is reproduced even in a SM calculation using the classical Kuo-Brown interaction [29], suggesting that it contains the essential ERI components that make the GT strength concentrate in the lowest GT state of ^{42}Sc.

Further calculations were performed using a quasiparticle random phase approximation (QRPA) framework based on a self-consistent Hartree-Fock mean field with Skyrme interactions. First, we performed standard calculations including proper IV ERIs in both the p-h and the p-p configurations. Within this framework, GT strengths and GTR structures in nuclei heavier than $A \approx 60$ have been well reproduced [30]. As an extension, the observed GT strength in the GTR region of ^{54}Co was well reproduced. Note that closed shells are formed at Z or $N = 28$. Then, the main transition $\nu f_{7/2} \rightarrow \pi f_{5/2}$ makes a p-h type ($\pi f_{5/2}$, $\nu f_{7/2}^{-1}$) configuration in ^{54}Co [see Fig. 3(d)]. Here, we see the established scenario that the main part of the GT strength is pushed up to the GTR region, higher than the p-h energy of $\approx$6 MeV, by the repulsive IV interaction that is active in p-h configurations. However, the concentration of GT strength in one low-energy state in ^{42}Sc could not be reproduced; about half of the total GT strength always remained in the GTR region.

In the SM picture, the final nucleus ^{42}Sc has one π and one ν outside the inert ^{40}Ca core. As shown in Fig. 3(a), p-p configurations of ($\pi f_{7/2}$, $\nu f_{7/2}$) and ($\pi f_{5/2}$, $\nu f_{7/2}$), are formed after the transitions $\nu f_{7/2} \rightarrow \pi f_{7/2}$ and $\nu f_{7/2} \rightarrow \pi f_{5/2}$, respectively. Taking the antisymmetrization into account, a π-ν pair can couple to the spin $S = 0$ and $T = 1$ (spin-singlet, IV) or $S = 1$ and $T = 0$ (spin-triplet, IS) states, and the analysis of ERIs in these states shows that the spin-triplet IS ERI is attractive and stronger than the spin-singlet IV ERI [31]. Note that the IS, ERI cannot act in the IV-type π-π or ν-ν pairs. In addition, it is discussed that p-p type configurations are sensitive to the IS pairing interaction [32,33], and the attraction is strong if both nucleons of the π-ν pair are in the same shell [3,31]. It is known that this attractive IS ERI makes the deuteron bound [34].

In newly performed spherical QRPA calculations [35], the spin-triplet IS ERI was also included, which changed the results drastically; in the ^{42}Ca $\rightarrow$ ^{42}Sc calculation, a strong concentration of the GT strength in the lowest GT state appeared as the IS coupling constant f [35] was increased from null to $f = 1$. In addition, at $f = 1$ the contributions of the main p-p type configurations ($\pi f_{5/2}$, $\nu f_{7/2}$) and ($\pi f_{7/2}$, $\nu f_{7/2}$) of the lowest 1^+ state were in phase, increasing the collectivity [35].

As discussed, the configurations of GTRs are p-h type in heavier nuclei with neutron excess. Since ERIs of p-h configurations are repulsive in IV excitations, the GTRs are pushed to a higher E_x region. However, we observed that the GT excitations can be shifted to a lower energy if the configurations of the final nucleus have πp-νp nature where the attractive IS ERI can be active. We saw that the 0.611 MeV GT state in ^{42}Sc collects 80% of the total GT strength in the region up to 12 MeV. The GT transition to this state has a large B(GT) value of 2.2, which can be deduced from the small log ft value of 3.25 of the isospin analogous GT transition in the ^{42}Ti β decay to ^{42}Sc [36]. Therefore, in the sense that this low-energy GT state has the collective nature and carries most of the observed GT strength, it is comparable to the high-energy GTR in heavy $N > Z$ nuclei.

In the limit of null $L \cdot S$ force, Wigner proposed the existence of SU(4) symmetry and the "super-multiplet state" [37]. In this limit, (a) the GT strength is concentrated in a low-energy GT state, and, also, (b) excitation energies of both the IAS and the GT state are identical. From Fig. 1, we see a broken SU(4) symmetry in the $A = 54$ system, while a good symmetry is observed in the $A = 42$ system. We found that the attractive IS ERI plays the role of restoring the SU(4) symmetry and the 0.611 MeV GT state in ^{42}Sc has a character close to that of a super-multiplet state. Therefore, we can call this state the "low-energy super GT" (LESGT) state. Note that "zero-energy" πp-νp configurations that are essential for the formation of LESGT states are realized only in CE excitations (and β decays).

The LESGT state is expected if the relevant configurations of the final GT state are of πp-νp nature. Indeed, strong GT transitions to the ground states of the $N = Z$ nuclei ^{6}Li and ^{18}F have been observed in the β-decay studies of ^{6}He and ^{18}Ne, respectively [38,39]. The transitions have very small log ft values of 2.9 and 3.1. In addition, we can confirm the concentration of the main GT strength in the ground state of ^{18}F from the ^{18}O(p, n) measurement [40]. Since ^{4}He and ^{16}O can act as inert cores, we expect that these ground states in ^{6}Li and ^{18}F have πp-νp configurations, and thus, they are also LESGT states.

In summary, in the high-resolution (^{3}He, t) measurements for f-shell nuclei, we observed low- and high-energy collective GT excitations, i.e., two kinds of GT phonon states. In ^{42}Sc, a concentration of the GT strength was observed in the lowest GT state, which we call the LESGT state. We found that the attractive IS ERI that is active in πp-νp configurations pulls the GT strength to a lower excitation energy and that LESGT states are the extreme structure carrying most of the GT strength. In ^{46}V and ^{50}Mn, transitional features were observed; the low-energy phonon strength became fragmented and weaker, while the strength in the high-energy GTR region increased. In ^{54}Co, the main part of the GT strength was concentrated in the GTR phonon structure. As is known, GTRs are formed by the repulsive IV ERI that is active in the πp-νh configurations. Note that the existence of IS and IV ERIs, and thus, low- and high-energy GT phonon excitations, are attributed

to the 2 fermionic degrees of freedom, which is a unique feature in atomic nuclei.

The (^{3}He, t) experiments were performed at RCNP, Osaka under the Experimental Programs No. E197, No. E214, and No. E307. Y. F. acknowledges discussions with Professors H. Toki (Osaka), I. Hamamoto (University of Lund), M. H. Harakeh (KVI), and W. Gelletly (Surrey). This work was in part supported by MEXT, Japan (Grants No. 13002001, No. 15540274, and No. 18540270); MICINN, Spain (Grant No. FPA200806419-C02-01); DFG, Germany (Contracts No. Br 799/12-1, No. Jo 391/2-1, and No. Pi 393/1-2); the FWO-Flanders, OTKA Foundation, Hungary (Grant No. K106035); and RIKEN-CNS joint research project on large-scale nuclear-structure calculations. Y. F. and B. R. acknowledge the support of the Japan-Spain collaboration program by JSPS and CSIC.

[*]Deceased.
[†]fujita@rcnp.osaka-u.ac.jp
[‡]Present address: Department of Physics and Applied Physics, University of Massachusetts Lowell, Lowell, Massachusetts 01854, USA.
[§]Present address: NIRS, Inage, Chiba 263-8555, Japan.
[‖]Present address: Los Alamos National Laboratory, Los Alamos, New Mexico 87545, USA.
[¶]Present address: Comisión Chilena de Energía Nuclear, Post Office Box 188-D, Santiago, Chile.
[**]Present address: Central Customs Laboratory, Ministry of Finance, Kashiwa, Chiba 277-0882, Japan.
[††]Present address: IKP, TU-Darmstadt, Darmstadt, Germany.
[‡‡]Present address: Institute for Work Design of North Rhine-Westphalia, Radiation Protection Services, 40225 Düsseldorf, Germany.
[§§]Present address: CYRIC, Tohoku University, Aramaki, Aoba, Sendai 980-8578, Japan.
[‖‖]Present address: RIKEN, Nishina Center, Wako, Saitama 351-0198, Japan.
[¶¶]Present address: Department of Physics, Kyushu University, Higashi, Fukuoka 812-8581, Japan.

[1] A. Bohr and B. R. Mottelson, *Nuclear Structure* (Benjamin, New York, 1969), Vol. 1.
[2] R. A. Broglia and V. Zelevinsky, *Fifty Years of Nuclear BCS, Pairing in Finite Systems* (World Scientific, Singapore, 2013).
[3] R. Subedi *et al.*, Science **320**, 1476 (2008), and references therein.
[4] M. N. Harakeh and A. van der Woude, *Giant Resonances*, *Oxford Studies in Nuclear Physics* (Oxford University Press, Oxford, 2001), and references therein.
[5] F. Osterfeld, Rev. Mod. Phys. **64**, 491 (1992), and references therein.
[6] Y. Fujita, B. Rubio, and W. Gelletly, Prog. Part. Nucl. Phys. **66**, 549 (2011), and references therein.
[7] J. Rapaport and E. Sugarbaker, Annu. Rev. Nucl. Part. Sci. **44**, 109 (1994), and references therein.
[8] C. Gaarde, Nucl. Phys. **A396**, 127c (1983).
[9] T. N. Taddeucci, C. A. Goulding, T. A. Carey, R. C. Byrd, C. D. Goodman, C. Gaarde, J. Larsen, D. Horen, J. Rapaport, and E. Sugarbaker, Nucl. Phys. **A469**, 125 (1987), and references therein.
[10] Y. Fujita *et al.*, Phys. Rev. C **59**, 90 (1999).
[11] Y. Fujita *et al.*, Phys. Rev. C **67**, 064312 (2003).
[12] R. Zegers *et al.*, Phys. Rev. C **74**, 024309 (2006).
[13] Y. Fujita *et al.*, Phys. Rev. C **75**, 057305 (2007).
[14] T. Wakasa *et al.*, Nucl. Instrum. Methods Phys. Res., Sect. A **482**, 79 (2002).
[15] M. Fujiwara *et al.*, Nucl. Instrum. Methods Phys. Res., Sect. A **422**, 484 (1999).
[16] http://www.rcnp.osaka-u.ac.jp.
[17] T. Noro *et al.*, in Research Center Nuclear Physics (Osaka University) Annual Report, 1991, p. 177.
[18] Y. Fujita, K. Hatanaka, G.P.A. Berg, K. Hosono, N. Matsuoka, S. Morinobu, T. Noro, M. Sato, K. Tamura, and H. Ueno, Nucl. Instrum. Methods Phys. Res., Sect. B **126**, 274 (1997), and references therein.
[19] H. Fujita *et al.*, Nucl. Instrum. Methods Phys. Res., Sect. A **484**, 17 (2002).
[20] C. D. Goodman *et al.*, Phys. Lett. **107B**, 406 (1981).
[21] J. Rapaport *et al.*, Nucl. Phys. **A410**, 371 (1983).
[22] H. Fujita *et al.*, Nucl. Instrum. Methods Phys. Res., Sect. A **469**, 55 (2001).
[23] T. Adachi *et al.*, Phys. Rev. C **85**, 024308 (2012).
[24] T. Adachi *et al.*, Phys. Rev. C **73**, 024311 (2006).
[25] Y. Fujita *et al.*, Phys. Rev. Lett. **95**, 212501 (2005).
[26] F. Molina, B. Rubio, Y. Fujita, and W. Gelletly, AIP Conf. Proc. **1423**, 23 (2012).
[27] Y. Fujita *et al.*, Phys. Rev. C **88**, 014308 (2013).
[28] M. Honma, T. Otsuka, T. Mizusaki, M. Hjorth-Jensen, and B. A. Brown, J. Phys. Conf. Ser. **20**, 7 (2005), and references therein.
[29] H. Toki and G. F. Bertsch, Phys. Rev. C **26**, 2330 (1982).
[30] P. Sarriguren, Phys. Rev. C **87**, 045801 (2013).
[31] G. F. Bertsch and Y. Luo, Phys. Rev. C **81**, 064320 (2010), and references therein.
[32] J. Engel, M. Bender, J. Dobaczewski, W. Nazarewicz, and R. Surman, Phys. Rev. C **60**, 014302 (1999).
[33] E. Moya de Guerra, A. A. Raduta, L. Zamick, and P. Sarriguren, Nucl. Phys. **A727**, 3 (2003).
[34] A. O. Macchiavelli, in *Fifty Years of Nuclear BCS*, edited by R. A. Broglia and V. Zelevinsky (World Scientific, Singapore, 2013), Chap. 32, p. 432.
[35] C. L. Bai, H. Sagawa, M. Sasano, T. Uesaka, K. Hagino, H. Q. Zhang, X. Z. Zhang, and F. R. Xu, Phys. Lett. B **719**, 116 (2013); C. L. Bai *et al.* (private communication).
[36] T. Kurtukian Nieto *et al.*, Phys. Rev. C **80**, 035502 (2009).
[37] E. P. Wigner, Phys. Rev. **51**, 106 (1937).
[38] D. R. Tilley, C. M. Cheves, J. L. Godwin, G. M. Hale, H. M. Hofmann, J. H. Kelley, C. G. Sheu, and H. R. Weller, Nucl. Phys. **A708**, 3 (2002).
[39] D. R. Tilley, H. R. Weller, C. M. Cheves, and R. M. Chasteler, Nucl. Phys. **A595**, 1 (1995).
[40] B. D. Anderson *et al.*, Phys. Rev. C **27**, 1387 (1983).

High-spin torus isomers and their precession motions

T. Ichikawa,[1] K. Matsuyanagi,[1,2] J. A. Maruhn,[3] and N. Itagaki[1]
[1]*Yukawa Institute for Theoretical Physics, Kyoto University, Kyoto 606-8502, Japan*
[2]*RIKEN Nishina Center, Wako 351-0198, Japan*
[3]*Institut für Theoretische Physik, Universität Frankfurt, D-60438 Frankfurt, Germany*
(Received 2 August 2014; published 22 September 2014)

Background: In our previous study, we found that an exotic isomer with a torus shape may exist in the high-spin, highly excited states of ^{40}Ca. The z component of the total angular momentum, $J_z = 60\hbar$, of this torus isomer is constructed by totally aligning 12 single-particle angular momenta in the direction of the symmetry axis of the density distribution. The torus isomer executes precession motion with the rigid-body moments of inertia about an axis perpendicular to the symmetry axis. The investigation, however, has been focused only on ^{40}Ca.
Purpose: We systematically investigate the existence of exotic torus isomers and their precession motions for a series of $N = Z$ even-even nuclei from ^{28}Si to ^{56}Ni. We analyze the microscopic shell structure of the torus isomer and discuss why the torus shape is generated beyond the limit of large oblate deformation.
Method: We use the cranked three-dimensional Hartree-Fock method with various Skyrme interactions in a systematic search for high-spin torus isomers. We use the three-dimensional time-dependent Hartree-Fock method for describing the precession motion of the torus isomer.
Results: We obtain high-spin torus isomers in ^{36}Ar, ^{40}Ca, ^{44}Ti, ^{48}Cr, and ^{52}Fe. The emergence of the torus isomers is associated with the alignments of single-particle angular momenta, which is the same mechanism as found in ^{40}Ca. It is found that all the obtained torus isomers execute the precession motion at least two rotational periods. The moment of inertia about a perpendicular axis, which characterizes the precession motion, is found to be close to the classical rigid-body value.
Conclusions: The high-spin torus isomer of ^{40}Ca is not an exceptional case. Similar torus isomers exist widely in nuclei from ^{36}Ar to ^{52}Fe and they execute the precession motion. The torus shape is generated beyond the limit of large oblate deformation by eliminating the 0s components from all the deformed single-particle wave functions to maximize their mutual overlaps.

DOI: 10.1103/PhysRevC.90.034314 PACS number(s): 21.60.Jz, 21.60.Ev, 27.40.+z

I. INTRODUCTION

Nuclear rotation is a key phenomenon to study the fundamental properties of finite many-body quantum systems. In particular, the rotation about the symmetry (z) axis produces a unique quantum object with its density distribution of a torus shape, as shown in our previous studies for ^{40}Ca [1,2]. In a classical picture for such rotation the oblate deformation develops with increasing rotational frequency due to the strong centrifugal force [3]. However, such a collective rotation about the symmetry axis is quantum-mechanically forbidden. Instead, it is possible to construct extremely high-spin states by aligning individual angular momenta of single-particle motion in the direction of the symmetry axis [4,5].

A drastic example is a high-spin torus isomer in ^{40}Ca [1], where 12 single particles with the orbital angular momenta $\Lambda = +4$, $+5$, and $+6$ align in the direction of the symmetry axis and construct a z component of the total angular momentum of $J_z = 60\hbar$. Thus, a "macroscopic" amount of circulating current emerges in the torus isomer state, which may be regarded as a fascinating new form of the nuclear matter suggested by Bohr and Mottelson [6].

Another important kind of rotation is a collective motion that restores the symmetry spontaneously broken in the self-consistent mean field. The density distribution of the torus isomer largely breaks the symmetry about an (x or y) axis perpendicular to the symmetry axis [2]. Below, we call this axis a perpendicular axis. Thus, the torus isomer can rotate about a perpendicular axis, although the collective rotation about the symmetry axis is quantum-mechanically forbidden. This rotational degree of freedom causes the precession motion of the system as a whole. Then, an interesting question arises how such a "femtoscale magnet" rotates collectively to restore the broken symmetry about a perpendicular axis.

A physical quantity characterizing such a collective rotation is the moment of inertia about a perpendicular axis. It has been theoretically recognized that an independent-particle configuration in a deformed harmonic-oscillator potential rotates with the rigid-body moment of inertia when the self-consistency between the mean-field potential and the density is fulfilled [7]. However, measured moments of inertia for the case of the precession motion of prolately deformed nuclei are often much smaller than the rigid-body values even when pairing correlations are negligible [8,9]. This is because of shell effects in high-K prolate isomers [8]. Although precession modes of high-K oblate isomers have not been observed yet, their moments of inertia would be much reduced from the rigid-body values due to oblate shell structures at small deformations [10].

From these observations, it might be conjectured that the moment of inertia about a perpendicular axis for the torus isomer also significantly deviates from the classical rigid-body value, because the torus isomer is a unique quantum object characterized by the alignment of angular momenta of independent-particle motions. It is thus surprising that the

moment of inertia about a perpendicular axis, evaluated with the time-dependent Hartree-Fock (TDHF) method, from the rotational period of the precession motion of the torus isomer in ^{40}Ca takes a value close to the classical rigid-body value [2]. We analyzed the microscopic structure of the precession motion by using the random-phase approximation (RPA) method. In the RPA calculation, the precession motion of the torus isomer is generated by a coherent superposition of many one-particle-one-hole excitations across the sloping Fermi surface. We found that the precession motion obtained by the TDHF calculation is a pure collective motion well decoupled from other collective modes. In our previous studies, however, we focused only on the torus isomer of ^{40}Ca. It is thus important to investigate whether torus isomers exist also in other nuclei and the properties of the precession motion found there are universal or not.

In this paper, we first perform a systematic investigation of the high-spin torus isomers for a series of $N = Z$ even-even nuclei from ^{28}Si to ^{56}Ni. We show that the high-spin torus isomer of ^{40}Ca is not an exceptional case. About 40 years ago, Wong suggested, using a macroscopic-microscopic method, the possible existence of torus isomers at highly excited states of a wide region of nuclei [12]. Quite recently, Staszczak and Wong systematically explored the existence of torus isomers using the constrained cranked Hartree-Fock (HF) method and found some torus isomers at highly excited states in several nuclei [11]. However, they use the harmonic-oscillator basis expansion method, which is insufficient to treat unbound states. It is therefore difficult to examine the stability of the torus isomers against the nucleon emission in their calculation, although some of them would contain single particles in unbound states.

We then perform a systematic TDHF calculation to investigate the properties of the precession motion. For all the high-spin torus isomers obtained by the cranked HF calculation, we find the periodic solutions of the TDHF equation of motion, which describe the precession motions. Among them, the precession motion of the $60\hbar$ torus isomer of ^{40}Ca is particularly stable and continues for many periods.

To understand the microscopic origin of appearance of the torus isomers, we analyze the process during which the shell structure of the large oblate shape and that of the torus shape grow up from that of the spherical shape. Using the radially displaced harmonic-oscillator (RDHO) model [12] and the oblately deformed harmonic-oscillator potential, we finally discuss why the lowest $0s$ components disappear from all the single-particle wave functions of the occupied states and how a large 'hole' region is created in the center of the nucleus to generate the torus shape.

This paper is organized as follows. In Sec. II, we describe the theoretical framework and parameters of the numerical calculation. In Sec. III, we present results of the systematic calculation for static and dynamical properties of the high-spin torus isomers including their precession motions. In Sec. IV, we analyze microscopic shell structures of the torus isomers and discuss the reason why the torus shape emerges beyond the limit of large oblate deformation. Finally, we summarize our studies in Sec. V.

II. THEORETICAL FRAMEWORK

A. Cranked HF calculation

To investigate systematically the existence of high-spin torus isomer states in a wide range of nuclei, we use the cranked three-dimensional Skyrme HF method. To build high-spin states rotating about the symmetry axis of the density distribution (z axis), we add a Lagrange multiplier, ω, to the HF Hamiltonian, $\hat{H}$. Then, the effective HF Hamiltonian, $\hat{H}'$, is written as $\hat{H}' = \hat{H} - \omega\hat{J}_z$, where $\hat{J}_z$ denotes the z component of the total angular momentum. We minimize this effective HF Hamiltonian with a given Lagrange multiplier, which is equivalent to the cranked HF equation given by $\delta\langle\hat{H} - \omega\hat{J}_z\rangle = 0$.

For this purpose, we slightly modify the code SKY3D. The details of the code are given in Ref. [13]. In the code, the single-particle wave functions are described on a Cartesian grid with a grid spacing of 1.0 fm, which is a good approximation for not only bound states but also unbound states in contrast to the harmonic-oscillator basis expansion. We take $32 \times 32 \times 24$ grid points for the x, y, and z directions, respectively. This is sufficiently accurate to provide converged configurations. The damped-gradient iteration method [14] is used, and all derivatives are calculated with the Fourier transformation method.

In the calculation, we use the SLy6, SkI3, and SkM* Skyrme forces to check the interaction dependence of the calculated results. These effective interactions were well constructed based on nuclear bulk properties but differ in details; SLy6 as a fit which includes information on isotopic trends and neutron matter [15], SkI3 as a fit taking into account the relativistic isovector properties of the spin-orbit force [16], and SkM* as a widely used traditional standard [17]. However, except for the effective mass, the bulk properties (equilibrium energy and density, incompressibility, and symmetry energy) are comparable to each other. In the energy density functional, we omit terms depending on the spin density, because it may be necessary to extend the standard form of the Skyrme interaction in order to properly take into account the spin-density dependent effects [18] (see also a review [19]), but such effects are inessential to the torus isomers.

B. Setting of initial configurations

In the cranked HF calculations, we first search for stable torus configurations in a series of $N = Z$ even-even nuclei from ^{28}Si to ^{56}Ni. We use, as an initial configuration of the HF calculation, an α-cluster ring configuration placed on the x-y plane, as shown in Fig. 1 of Ref. [1]. The α-cluster wave function is described by a Gaussian function with the width of 1.8 fm. The center positions of the Gaussian functions are placed equiangularly along a circle with a radius of 6.5 fm on the (x,y) plane. Only for the calculations of ^{52}Fe with the SkM* interaction, we use a radius of 7.55 fm and a width of 1.63 fm. Using these initial configurations, we perform 15 000 HF iterations. We search for stable torus solutions varying ω from 0.5 to 2.5 MeV/$\hbar$ with a step of 0.1 MeV/$\hbar$. After these calculations, we check the convergence of the total energies, the density distributions, and the total angular momenta. In the calculations of the excitation energies, we

subtract the expectation value of the center-of-mass motion in both the ground and the torus isomer states.

We next calculate all single-particle states including those above the Fermi energy. To calculate those, we use, as initial wave functions of the HF calculation, the single-particle wave functions of the RDHO model [12]. This model is a good approximation to the mean-field of torus-shaped isomers. In this model, the single-particle potential is given by

$$V(r,z) = \tfrac{1}{2}m\omega_0^2(r - R_0)^2 + \tfrac{1}{2}m\omega_0^2 z^2, \quad (1)$$

where m denotes the nucleon mass, ω_0 the oscillator frequency, r and z the radial and the z components of the cylindrical coordinate system, and R_0 the radius parameter of the torus shape. Since the radial wave function of the lowest energy in the RDHO model is described by a shifted Gaussian function with the width $d = \sqrt{\hbar/m\omega_0}$, we determine ω_0 from the radius of a cross section of a torus ring. The optimal values of R_0 and d are determined through the global investigation mentioned above. Using this initial condition and a value of ω_0 obtained by the global investigation, we perform the HF iteration over 20 000 times and calculate the single-particle states up to the 40th for both protons and neutrons.

C. Sloping Fermi surface

It is important to note that the cranking term $-\omega\hat{J}_z$ does not change the single-particle wave functions for rotation about the symmetry axis. Thus, it is useful to introduce the concept of "sloping" Fermi surface. As usual, the single-particle Hamiltonian is given by $\hat{H}' = \sum_i(\hat{h}_i - \omega\hat{j}_z^{(i)})$, where $\hat{h}_i$ and $\hat{j}_z^{(i)}$ denote the mean-field Hamiltonian and the z component of the total angular momentum for each single particle, respectively. The eigenvalue of $\hat{H}'$ is written as $E' = \sum_i[(e_i - \lambda) - \hbar\omega\Omega_i]$, where λ denotes the Fermi energy at $\omega = 0$. The symbols e_i and Ω_i denote the single-particle energy and the eigenvalue of $\hat{j}_z^{(i)}$, respectively. By introducing the sloping Fermi surface defined by $\lambda'(\Omega) = \lambda + \hbar\omega\Omega$, we can rewrite E' as $E' = \sum_i\{e_i - \lambda'(\Omega_i)\}$. Therefore, aligned configurations can be easily constructed by plotting the single-particle energies as a function of Ω and tilting the Fermi surface in the (e,Ω) plane. It is important to note that the value of ω to specify an aligned configuration is not unique. As we can immediately see in Figs. 3–7 below, individual configurations do not change for a finite range of ω.

D. Optimally aligned torus configurations

Let us focus on optimally aligned torus configurations where all the single-particle states below the sloping Fermi surface are occupied. They are expected to be more stable than other aligned configurations involving particle-hole excitations across the sloping Fermi surface. Before carrying out the cranked HF calculations, we can easily presume candidates of optimally aligned torus configurations. Since the effects of the spin-orbit potential are negligibly weak in the torus configurations, not only Ω but also the z component of the orbital angular momentum, Λ, are good quantum numbers ($\Omega = \Lambda + \Sigma$, where Σ denotes the z component of the spin, $\pm 1/2$) [1]. Single-particle states having the same Λ value with different spin directions are approximately degenerated and simultaneously occupied. Thus, the lowest-energy configurations for the torus shapes at $\omega = 0$ are $\Lambda = 0$, ± 1, ± 2, and ± 3 for ^{28}Si, $\Lambda = 0, \pm 1, \pm 2, \pm 3$, and $+4$ or -4 for ^{32}S, $\Lambda = 0, \pm 1, \ldots, \pm 4$ for ^{36}Ar, $\Lambda = 0, \pm 1, \ldots, \pm 4$, and $+5$ or -5 for ^{40}Ca, $\Lambda = 0, \pm 1, \ldots, \pm 5$ for ^{44}Ti, $\Lambda = 0, \pm 1, \ldots, \pm 5$, and $+6$ or -6 for ^{48}Cr, $\Lambda = 0, \pm 1, \ldots, \pm 6$ for ^{52}Fe, and $\Lambda = 0, \pm 1, \ldots, \pm 6$, and $+7$ or -7 for ^{56}Ni.

For instance, in ^{40}Ca, possible aligned configurations at $\omega \neq 0$ are (i) $\Lambda = 0, \pm 1, \ldots, \pm 4$, and $+5$ for $J_z = 20\hbar$ [$=5\hbar \times 2$ (spin degeneracy) $\times 2$ (isospin degeneracy)], (ii) $\Lambda = 0, \pm 1, \pm 2, \pm 3, +4$, and $+5$ for $J_z = 60\hbar$ [$=15\hbar \times 2 \times 2$], and (iii) $\Lambda = 0, \pm 1, \pm 2, +3, +4, +5, +6$, and $+7$ for $J_z = 100\hbar$ [$=25\hbar \times 2 \times 2$]. However, we could not obtain stable HF solutions for the configurations (i) and (iii): the centrifugal force is insufficient for stabilizing the configuration (i), while the last occupied single-particle state with $\Lambda = 7$ is unbound for the configuration (iii). Indeed, we confirmed that the torus isomer configuration (iii) with $J_z = 100\hbar$ slowly decays. In the systematic calculations, it is often difficult to discuss the stability of torus isomers when such unbound states are included. To avoid this difficulty, in this paper, we focus on torus configurations without involving unbound single-particle states.

E. TDHF calculation for the precession motion

For the stable torus isomers obtained above, we performed TDHF calculations to investigate their precession motions. The time evolution of the density distribution is determined by solving the TDHF equation of motion $i\hbar\dot{\rho} = [\hat{H}, \rho]$. When an impulsive force is provided in a direction perpendicular to the symmetry axis at $t = 0$, the torus isomer starts to execute the precession motion. This precession motion is associated with a rotation about a perpendicular axis, i.e., an axis perpendicular to the symmetry axis. In Ref. [2], we already showed that this precession motion is a pure collective motion to restore the broken symmetry and well described as coherent superpositions of many 1p-1h excitations across the sloping Fermi surface. We investigate whether other torus isomers also execute the precession motion well decoupled from other collective modes and whether their moments of inertia are close to the rigid-body values or not. In this way, we can also check the stability of the obtained torus isomers against given impulsive forces.

Figure 1 illustrates the schematic picture of the precession motion taken from Ref. [2]. At $t = 0$, the torus isomer is placed on the x-y plane with the angular momentum K ($=J_z$) along the z axis in the laboratory frame. When an impulsive force is provided in the negative x direction (the dotted line) at $t = 0$, the total angular momentum becomes $\vec{I}$ (the dashed line). We call this vector the precession axis. After that, the symmetry axis of the density distribution in the body-fixed frame (the bold solid line) starts to rotate about the precession axis with the rotational angle ϕ. In the precession motion, the value K is conserved and its direction is identical to the bold solid line. The tilting angle θ is defined as the angle between the bold solid and the dashed lines. Then, the moment of inertia for the rotation about a perpendicular axis, $\mathcal{J}_\perp$, can be estimated by $\mathcal{J}_\perp = I/\omega_{\rm prec}$, where $\omega_{\rm prec}$ denotes the rotational frequency of

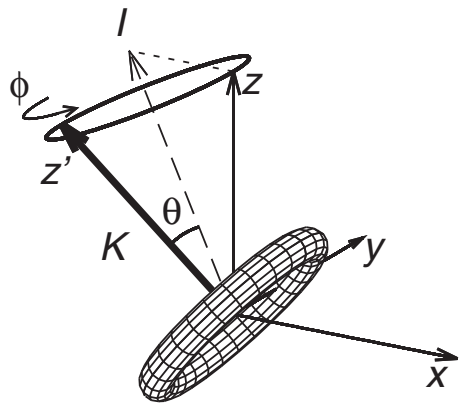

FIG. 1. Schematic picture for the precession motion of torus isomers taken from Ref. [2]. The bold solid line denotes the symmetry axis of the density distribution. The dashed line denotes the precession axis. The symbols θ and ϕ denote the tilting and the rotational angles, respectively.

the precession motion. To build the first excited state of the precession motion, we provide an impulsive force such that the total angular momentum becomes $I = K + 1$.

To solve the TDHF equation, we use the code SKY3D and take the Taylor expansion of the time-development operator up to the 12th order. The setups of spatial grid points and interactions are the same as those of the cranked HF calculations described above. We start to perform calculations from the initial density distribution obtained by the cranked HF calculations. The time step of the TDHF calculations is 0.2 fm/c. We calculate the time evolution until 3000 fm/c. To excite the precession motion, we provide an impulsive force at $t = 0$ by the external potential given by $V_{\rm ext}(r,\varphi,z) =$

TABLE I. Stable torus isomers obtained in the cranked HF calculation with various Skyrme interactions. The excitation energy, $E_{\rm ex}$, is measured from the ground state. The calculated density distributions are fitted to the Gaussian function $\rho(r,z) = \rho_0 e^{-[(r-R_0)^2+z^2]/d^2}$ and the resulting values of the parameters, ρ_0, R_0, and d, are listed. The symbols, $\mathcal{I}_\perp^{\rm rid}$ and $\mathcal{I}_\parallel^{\rm rid}$, denote the rigid-body moments of inertia for the rotations about a perpendicular and the symmetry axes, respectively.

System	J_z ($\hbar$)	$E_{\rm ex}$ (MeV)	ρ_0 (fm^{-3})	R_0 (fm)	d (fm)	$\mathcal{I}_\perp^{\rm rid}$ ($\hbar^2$/MeV)	$\mathcal{I}_\parallel^{\rm rid}$ ($\hbar^2$/MeV)
(SLy6)							
^{36}Ar	36	123.89	0.137	5.12	1.62	14.3	26.4
^{40}Ca	60	169.71	0.129	6.07	1.61	21.0	39.6
^{44}Ti	44	151.57	0.137	6.30	1.61	24.6	46.5
^{48}Cr	72	191.25	0.132	7.19	1.60	33.8	64.7
^{52}Fe	52	183.70	0.138	7.47	1.60	39.1	75.1
(SkI3)							
^{36}Ar	36	125.15	0.146	5.01	1.58	13.7	25.3
^{40}Ca	60	173.52	0.138	5.90	1.58	19.9	37.5
^{44}Ti	44	153.02	0.146	6.17	1.58	23.6	44.6
^{48}Cr	72	193.66	0.141	7.00	1.57	32.0	61.3
^{52}Fe	52	183.70	0.147	7.31	1.57	37.5	71.9
(SkM*)							
^{36}Ar	36	124.80	0.131	5.16	1.65	14.6	26.9
^{40}Ca	60	167.84	0.122	6.17	1.64	21.8	41.0
^{44}Ti	44	152.20	0.131	6.36	1.64	25.1	47.5
^{48}Cr	72	192.40	0.125	7.30	1.63	34.9	66.7
^{52}Fe	52	187.08	0.132	7.55	1.63	40.0	76.7

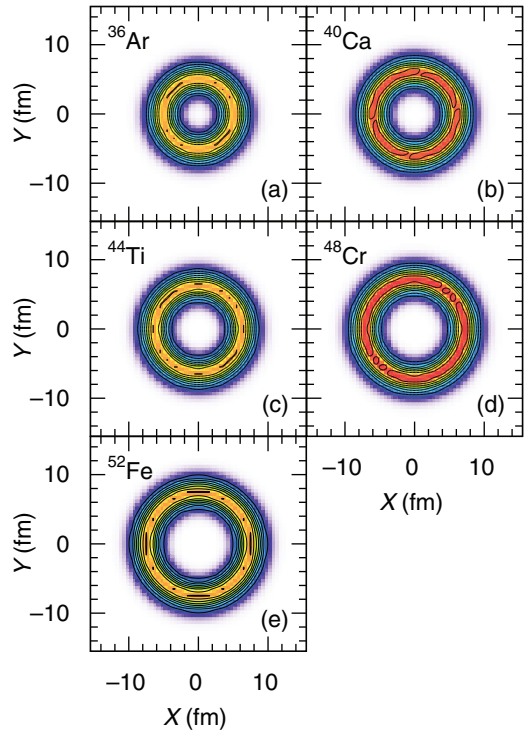

FIG. 2. (Color online) Density distributions on the $z = 0$ plane of the obtained stable torus isomers. The contours correspond to multiple steps of 0.015 fm^{-3}. The color is normalized by the largest density in each plot.

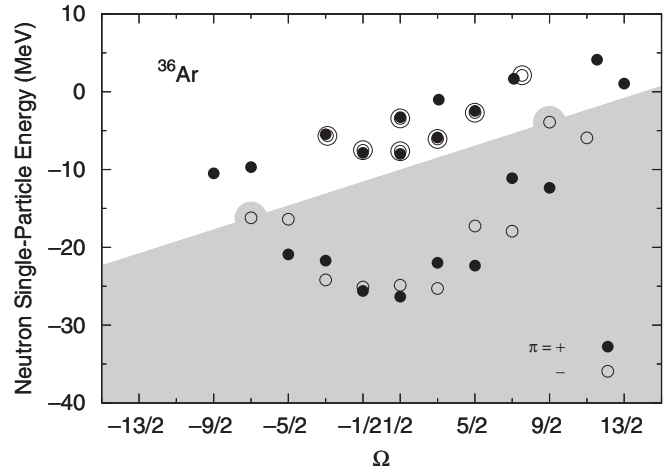

FIG. 3. Single-particle energies versus the z component of the total angular momentum, Ω, for ^{36}Ar. Solid and open circles denote the single-particle energies of the positive- and negative-parity states, respectively. To illustrate the degeneracy of positive- and negative-parity states, some negative-parity states are shown by double open circles.

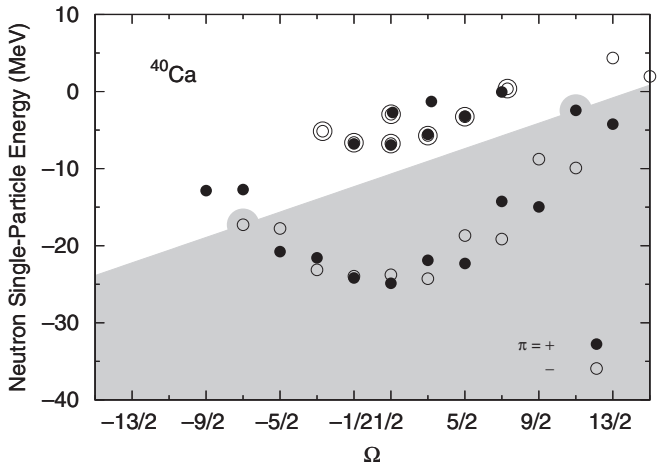

FIG. 4. Single-particle energies versus Ω for ^{40}Ca. All symbols are the same as in Fig. 3.

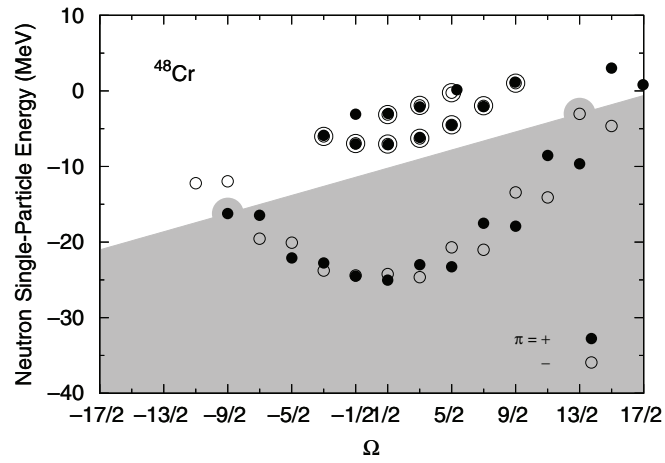

FIG. 6. Single-particle energies versus Ω for ^{48}Cr. All symbols are the same as in Fig. 3.

$V_0 z \cos\varphi \exp[-(r - R_0)^2/d^2]$. This impulsive force gives an angular momentum in the negative x direction at $t = 0$. The parameter V_0 is chosen such that the total angular momentum becomes $I = K + 1$.

III. RESULTS OF CALCULATION

A. Static properties

We have carried out a systematic search for stable torus isomers for the $N = Z$ even-even nuclei from ^{28}Si to ^{56}Ni. The result of the calculation is summarized in Table I. We obtain the stable torus isomers in ^{36}Ar for $J_z = 36\ \hbar$, ^{40}Ca for $J_z = 60\hbar$, ^{44}Ti for $J_z = 44\ \hbar$, ^{48}Cr for $J_z = 72\ \hbar$, and ^{52}Fe for $J_z = 52\ \hbar$ with all the three Skyrme interactions used in this study. On the other hand, we have not found any stable torus isomer in ^{28}Si, ^{32}S, and ^{56}Ni. In Fig. 2, we plot the total density distributions of the torus isomers obtained in the cranked HF calculation with the SLy6 interaction.

The total density distribution of each of the torus isomers obtained in the cranked HF calculation is well fitted by the Gaussian function $\rho(r,z) = \rho_0 e^{-[(r-R_0)^2+z^2]/d^2}$, where ρ_0, R_0, and d denote the maximum value of the nucleon density, the radius of the torus ring, and the width of a cross section of the torus ring, respectively. The resulting values of the parameters, ρ_0, R_0, and d, are tabulated in the middle part of Table I. We see that the values ρ_0 and d are almost constant for all the torus isomers. The interaction dependence of these values is weak. It is interesting that, in all the results, ρ_0 is smaller than the saturation nuclear density ($\rho_{\rm sat} \sim 0.17$ fm^{-3}) and d is close to the width of an α particle used in Brink's α-cluster model ($d_\alpha \sim 1.46$ fm) [20].

Using the total density distribution, we also calculate the rigid-body moments of inertia for rotation about a perpendicular axis, $\mathcal{T}_\perp^{\rm rid}$, and the symmetry axis, $\mathcal{T}_\parallel^{\rm rid}$. The results are also shown in Table I. Later, we shall compare these values for $\mathcal{T}_\perp^{\rm rid}$ with those obtained by an analysis of the precession motions in the TDHF time evolution.

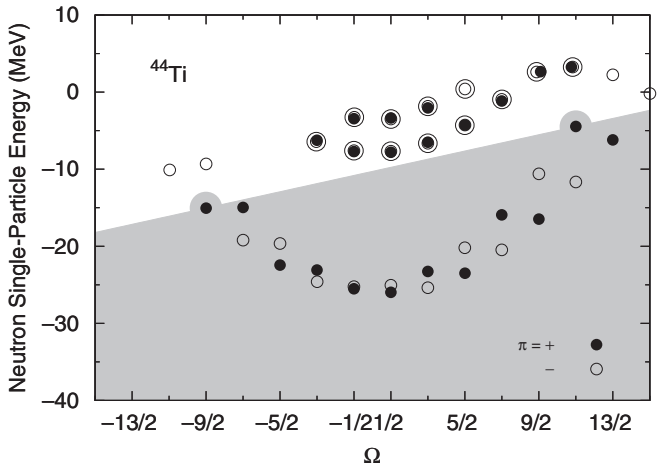

FIG. 5. Single-particle energies versus Ω for ^{44}Ti. All symbols are the same as in Fig. 3.

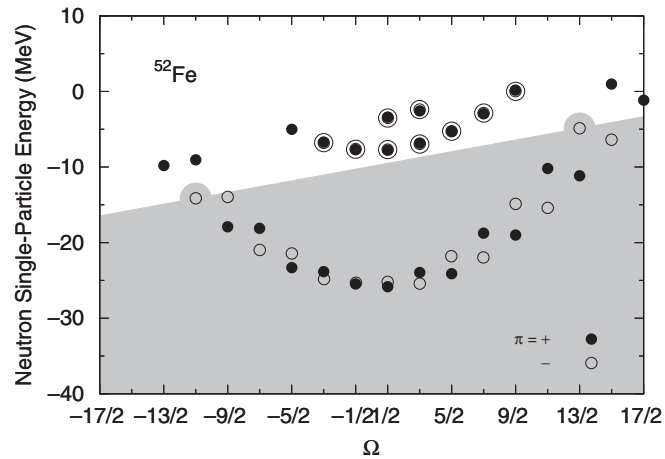

FIG. 7. Single-particle energies versus Ω for ^{52}Fe. All symbols are the same as in Fig. 3.

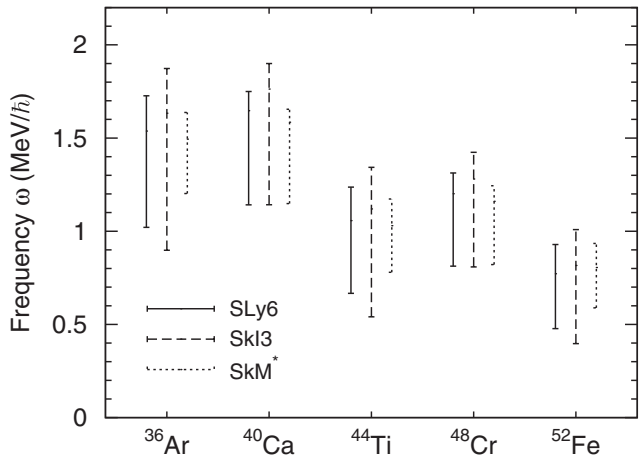

FIG. 8. Regions of ω for which each of the torus isomers stably exists. The solid, dashed, and dotted lines denote the results calculated with the SLy6, SkI3, and SkM* interactions, respectively.

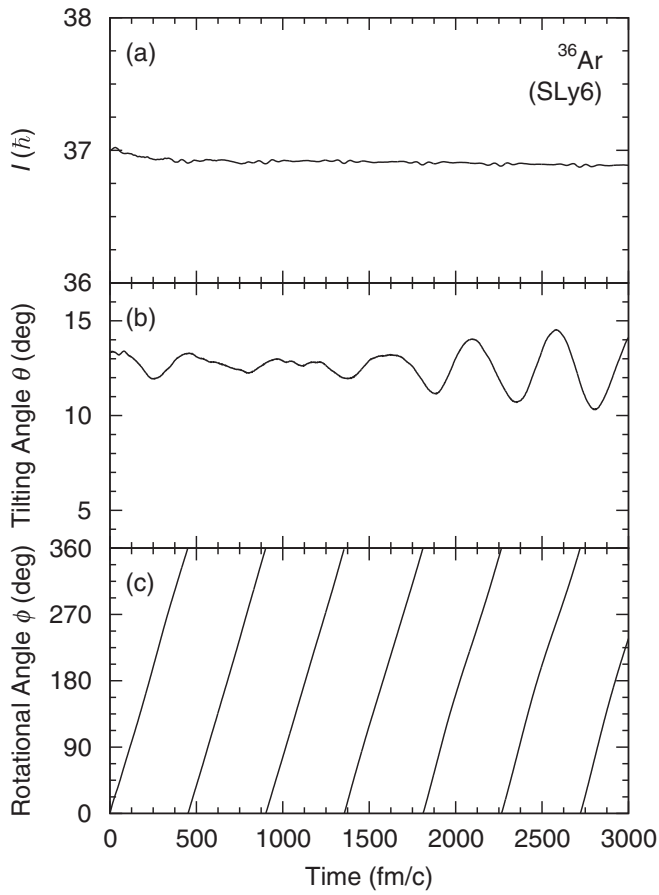

FIG. 9. Time evolution of the precession motion for the torus isomers of ^{36}Ar calculated by solving the TDHF equation of motion for the SLy6 interaction. In the plot, panels (a), (b), and (c) denote the total angular momentum I, the tilting angle θ, and the rotational angle ϕ, respectively.

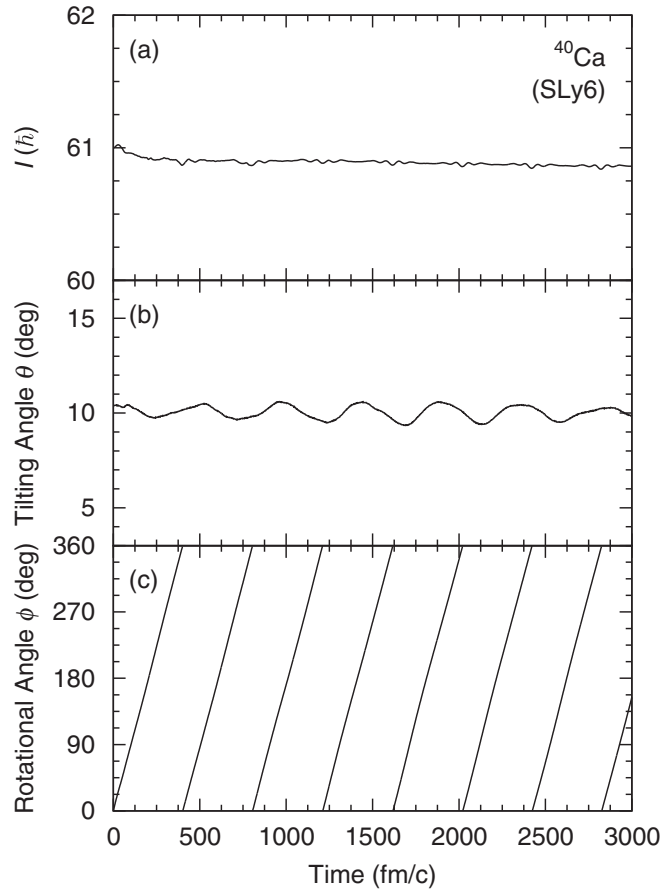

FIG. 10. Time evolution of the precession motion for the torus isomers of ^{40}Ca. All symbols are the same as Fig. 9.

To investigate microscopic structures of the torus isomers, we plot in Figs. 3–7 neutron single-particle energies versus Ω for each torus isomer calculated with the SLy6 interaction. In the figures, the solid and the open circles denote the positive- and negative-parity states, respectively. The gray area in each plot denotes the occupied states. In each plot, we see that the single-particle energies with the same Λ are almost degenerate. This indicates that the effects of the spin-orbit force are negligibly small and Λ is approximately a good quantum number in all the torus isomers. One may also notice that the Kramer's degeneracy for a pair of single-particle states with $\pm\Lambda$ is lifted. This is due to the time-odd components (dependent on the current density) of the cranked HF mean fields associated with the macroscopic currents, which are produced by the alignment of the single-particle angular momenta with large values of Λ.

Because of the negligible spin-orbit splittings, the spin-orbit partners are always occupied simultaneously. Therefore, the J_z values of the optimally aligned configurations are easily determined by summing up the Λ values of the occupied single-particle states: they are $\Lambda = 0, \pm1, \pm2, \pm3, +4, +5$ [$J_z = 9\,\hbar \times 2$ (spin degeneracy) $\times 2$ (isospin degeneracy) $= 36\,\hbar$] for ^{36}Ar, $\Lambda = 0, \pm1, \pm2, \pm3, +4, +5, +6$ [$J_z = 15\,\hbar \times 2 \times 2 = 60\,\hbar$] for ^{40}Ca, $\Lambda = 0, \pm1, \ldots, \pm4, +5, +6$ [$J_z = 11\,\hbar \times 2 \times 2 = 44\,\hbar$] for ^{44}Ti, $\Lambda = 0, \pm1, \ldots, \pm4, +5, +6, +7$

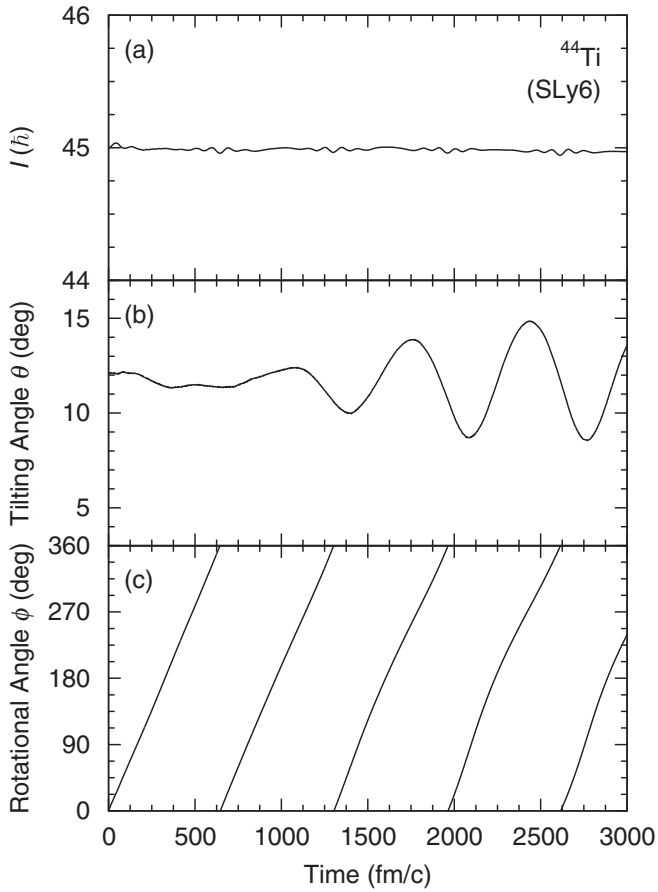

FIG. 11. Time evolution of the precession motion for the torus isomers of ^{44}Ti. All symbols are the same as Fig. 9.

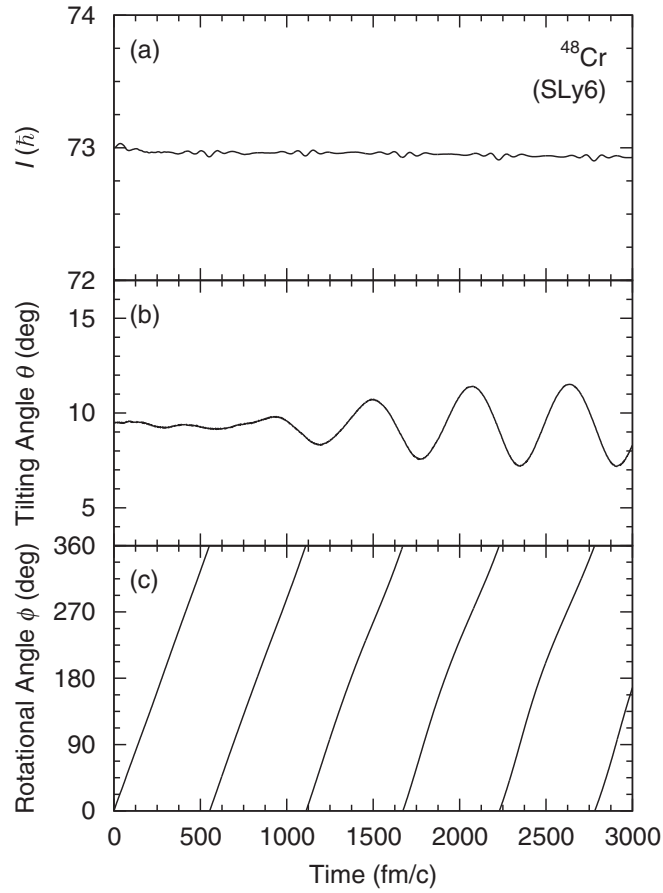

FIG. 12. Time evolution of the precession motion for the torus isomers of ^{48}Cr. All symbols are the same as Fig. 9.

$[J_z = 18\ \hbar \times 2 \times 2 = 72\ \hbar]$ for ^{48}Cr, and $\Lambda = 0, \pm 1, \ldots, \pm 5, +6, +7$ $[J_z = 13\ \hbar \times 2 \times 2 = 52\ \hbar]$ for ^{52}Fe.

We can estimate from the figures a region of ω for which each of the torus isomers stably exist. This is done by determining the steepest and the most gradual slopes of the Fermi surface for which the occupied single-particle configuration remains the same. The results are plotted in Fig. 8. The solid, dashed, and dotted lines denote the regions of ω for each of the stable torus isomers obtained with the SLy6, SkI3, and SkM* interactions, respectively. We see that the result does not strongly depend on the Skyrme interaction employed, although the width is weakly dependent on it.

B. Dynamic properties

We carried out a systematic TDHF calculation for each of the torus isomers and found that that the TDHF time evolution of the density distribution is quite similar to that displayed in Fig. 2 of [2]. Figures 9–13 show the calculated time evolution of the precession motion for each of the torus isomers obtained with the SLy6 interaction. In each plot in the figures, panels (a), (b), and (c) denote the total angular momentum, I, the tilting angle, θ, and the rotational angle, ϕ, respectively. In panel (a) in each plot, we can see that the total angular momentum is conserved very well. This indicates that the TDHF calculations are sufficiently accurate. We find that the precession motion of the ^{40}Ca torus isomer is especially stable [see panel (b) in each plot], where the rotational angle ϕ lineally increases with time, indicating that the rotation of the symmetry axis about the precession axis keeps a constant velocity through all the periods. This indicates that the strong shell effects responsible for the appearance of the torus isomer in ^{40}Ca also stabilize the precession motion. We find that the precession motions emerge also for other torus isomers and they are stable at least for two periods. After that, however, the tilting angle gradually starts to fluctuate. Correspondingly, the rotational angle ϕ also starts to deviate from the linear time evolution [see panel (c) in each plot]. We have also carried out similar TDHF calculations with the use of the SkI3 and SkM* interactions. The results are similar to those shown above for the SLy6 interaction, which implies that the properties of the precession motion are robust and depend on the choice of the Skyrme interaction only weakly.

To evaluate the moment of inertia for the rotation about a perpendicular axis, we take the average of the two periods starting from $t = 0$ during which the precession motion is especially stable. The results are tabulated in the third column of Table II. Using these values, we calculate the frequency of the precession motion by $\omega_{\rm prec} = 2\pi / T_{\rm prec}$ and the moment of inertia for the rotation about a perpendicular axis by $\mathcal{I}_{\perp}^{\rm TDHF} =$

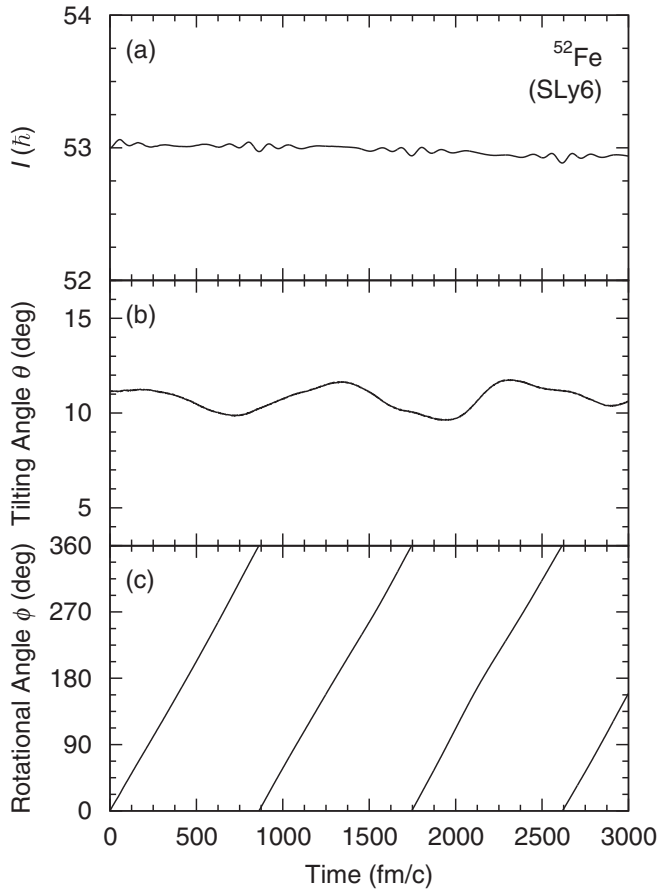

FIG. 13. Time evolution of the precession motion for the torus isomers of ^{52}Fe. All symbols are the same as Fig. 9.

$I/\omega_{\rm prec}$. The results are tabulated in the forth and fifth columns of Table II. The obtained moments of inertia are very close to the rigid-body values tabulated in Table I for all the Skyrme interactions employed. As discussed in Ref. [2], these results indicate that the precession motions under consideration are pure collective motions generated by coherent superpositions of many 1p-1h excitations across the sloping Fermi surface.

TABLE II. Results of the TDHF calculation for the precession motions of the torus isomers from ^{36}Ar to ^{52}Fe. The symbol I denotes the resulting total angular momentum after an impulsive force is provided. The symbol $T_{\rm prec}$ denotes the average over the two periods from $t = 0$ for the precession motion. The symbol $\omega_{\rm prec}$ denotes the precession frequency estimated by $\omega_{\rm prec} = 2\pi/T_{\rm prec}$. The symbol $\mathscr{T}_\perp^{\rm TDHF}$ denotes the moment of inertia for the rotation about a perpendicular axis estimated by $\mathscr{T}_\perp^{\rm TDHF} = I/\omega_{\rm prec}$.

System	I ($\hbar$)	$T_{\rm prec}$ (MeV/$\hbar$)	$\omega_{\rm prec}$ (MeV)	$\mathscr{T}_\perp^{\rm TDHF}$ ($\hbar^2$/MeV)
(SLy6)				
^{36}Ar	37	450.1	2.75	13.5
^{40}Ca	61	402.5	3.08	19.8
^{44}Ti	45	651.0	1.90	23.7
^{48}Cr	73	554.5	2.24	32.6
^{52}Fe	53	872.8	1.42	37.3
(SkI3)				
^{36}Ar	37	427.9	2.90	12.8
^{40}Ca	61	378.6	3.28	18.6
^{44}Ti	45	624.4	1.99	22.7
^{48}Cr	73	524.5	2.36	30.9
^{52}Fe	53	839.0	1.48	35.9
(SkM*)				
^{36}Ar	37	464.2	2.67	13.9
^{40}Ca	61	418.2	2.96	20.6
^{44}Ti	45	666.1	1.86	24.2
^{48}Cr	73	572.8	2.16	33.7
^{52}Fe	53	894.8	1.39	38.3

IV. DISCUSSION

A. Radial density distributions of individual single-particle states

Let us examine the radial density distributions of individual single-particle wave functions on the $z = 0$ plane for the torus isomer of ^{40}Ca. For this purpose, we interpolate the density distributions described with a Cartesian coordinate in the cranked HF calculations by means of a third-order B-spline function. After that, we transform those to a cylindrical coordinate representation $[\rho_i(x,y) \to \rho_i(r,\varphi)]$. We then integrate $\rho_i(r,\varphi)$ in the φ direction and obtain $\rho_i(r)$. The calculated results are plotted in the upper panel of Fig. 14.

As shown in Refs. [1,2], the RDHO model can describe well the microscopic structures of torus isomers. To illustrate this, we solve the Schrödinger equation with the RDHO potential, Eq. (1), by means of the deformed harmonic-oscillator basis expansion and calculate $\rho_i(r)$. In the calculation, we take $R_0 = 6.07$ fm and $d = 1.61$ fm for the RDHO model and the same aligned single-particle configuration as that obtained by the cranked HF calculation for ^{40}Ca. The obtained radial density distributions of the individual single-particle states are plotted in the lower panel of Fig. 14. Using these density distributions, we calculate the rigid-body moments of inertia about a perpendicular axis and the symmetry axis: they are $\mathscr{T}_\perp^{\rm RDHO} = 21.3\ \hbar^2$/MeV and $\mathscr{T}_\parallel^{\rm RDHO} = 40.2\ \hbar^2$/MeV, respectively. These values are in good agreement with those obtained by the cranked HF calculation.

In Fig. 14, it is clearly seen that the radial density distributions of the individual single-particle states in the RDHO model are quite similar to those obtained by the cranked HF calculations. In particular, the peak positions of each radial density distribution are in good agreement between the two calculations. As a matter of fact, the peak position of each density distribution shifts to a larger r with increasing orbital angular momentum. Looking into details of the density distributions obtained by the cranked HF calculations, one may notice that some radial density distributions with high angular momentum slightly shift due to the spin-orbit potential. In Fig. 4, the degeneracy of single-particle energies with the same high Λ is indeed slightly broken for the spin-orbit partner with $\Omega^\pi = 9/2^-$ and $11/2^-$ ($\Lambda = 5$) and that with $\Omega^\pi = 11/2^+$ and $13/2^+$ ($\Lambda = 6$). These spin-orbit effects are absent in the RDHO model.

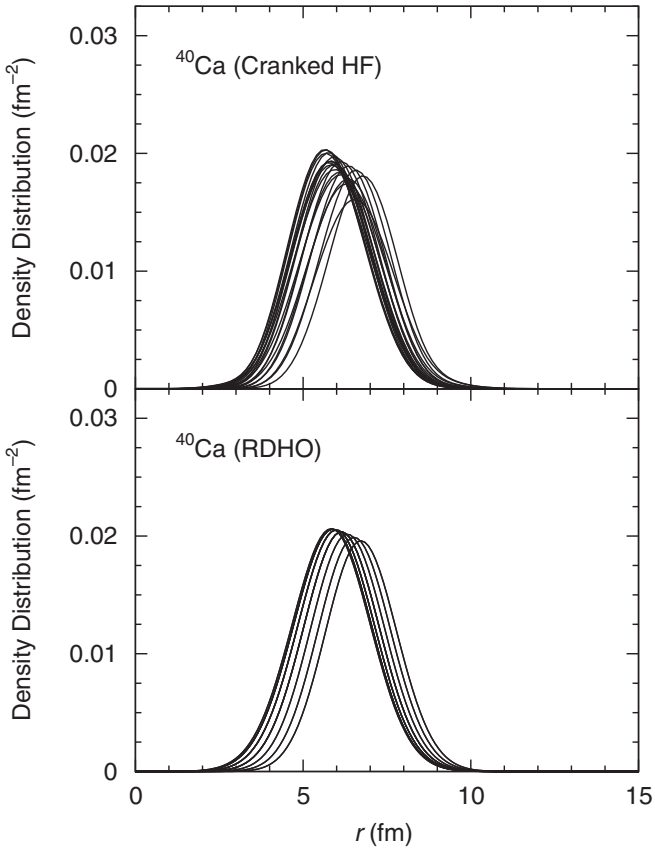

FIG. 14. Radial density distributions of individual single-particle states on the $z = 0$ plane for ^{40}Ca obtained by the cranked HF calculations (upper panel) and the RDHO model (lower pannel). The densities for the ϕ direction in cylindrical coordinates are integrated.

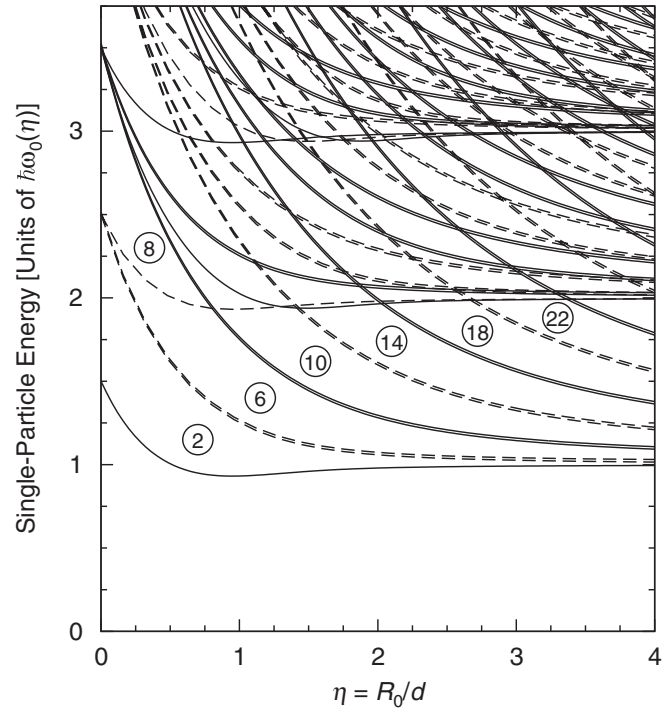

FIG. 15. Nilsson diagram versus $\eta = R_0/d$ of the RDHO model for ^{40}Ca. The solid and dashed lines denote the single-particle states with positive and negative parities, respectively. The single-particle energies are plotted in units of $\hbar\omega_0(\eta)$. To illustrate the degeneracy of the levels, the single-particle energies with higher Ω are slightly shifted.

B. Shell structure of torus nucleus

Using the RDHO model, we next investigate shell structures of a torus isomer and examine how single-particle configurations change from spherical to torus shapes. Figure 15 shows a Nilsson diagram versus the parameter $\eta = R_0/d$ for ^{40}Ca. At $\eta = 0$, the nuclear shape is spherical. At $\eta = 4$, a torus shape is well developed, which is a size similar to that obtained by the cranked HF calculations. Note that we take into account volume conservation inside an equipotential surface of a torus isomer (see Ref. [12] and the Appendix for the volume conservation in $0 \leqslant \eta \leqslant 1$). To eliminate the volume effect, we plot the single-particle energies in unit of $\hbar\omega_0(\eta)$. In this figure, we slightly shift the single-particle energies with higher Ω in order to illustrate the degeneracy of the states.

In Fig. 15, we see the spherical major shell with $E = \hbar\omega_0(N_{\rm sh} + 3/2)$ at $\eta = 0$, where $N_{\rm sh}$ denotes the total number of oscillator quanta. With increasing η, the single-particle energies with $\Omega = 1/2$ approach the asymptotic value given by $E = \hbar\omega_0(N'_{\rm sh} + 1)$, where $N'_{\rm sh} = n_r + n_z$, n_z and n_r denote the quantum number for oscillations in the z and the radial directions, respectively. The energies of other single-particle states with larger Ω in the same $N_{\rm sh}$ shell steeply decrease as a function of η. At $\eta = 4$, the tenth and 11th (from the bottom) single-particle states with $\Omega^p = 11/2^-$ and $13/2^-$ ($\Lambda = 6$) become lower than the 14th level with $N'_{\rm sh} = 1$ (the $1\hbar\omega_0$ state). These two single-particle states originate from those with a spherical harmonic-oscillator quantum number of $N_{\rm sh} = 5$ (the $5\hbar\omega_0$ state).

It is easy to understand these behaviors. As Wong showed in Ref. [12], the single-particle energies for large R_0 are approximately given by $E \sim \hbar\omega_0(N'_{\rm sh} + 1) + \hbar^2\Lambda^2/2mR_0^2$. Thus, the single-particle energies belonging to the same $N'_{\rm sh}$ shell are proportional to Λ^2 at lager R_0.

Figure 16 shows the single-particle energies in the RDHO model versus Ω from $\eta = 0$ to 4. At $\eta = 0$ [Fig. 16(a)], the familiar shell structure of the spherical harmonic-oscillator is seen. With increasing η [Figs. 16(b)–16(d)], single-particle energies with high Ω rapidly decrease. Then, the single-particle energies start to form parabolic structures. At $\eta = 4$ [Fig. 16(e)], two important properties emerge: (i) the curvature of the parabolic structure becomes large, and (ii) the single-particle energies within the same $N'_{\rm sh}$ shell are proportional to Λ^2. These two properties play an essential role in stabilizing the torus isomers when single particles are aligned in the direction of the symmetry axis.

It is surprising that the single-particle shell structure of the RDHO model at $\eta = 4$ is very similar to that of Fig. 5 obtained by the cranked HF calculation. The RDHO model is therefore a good approximation for describing the microscopic structures of the torus isomers.

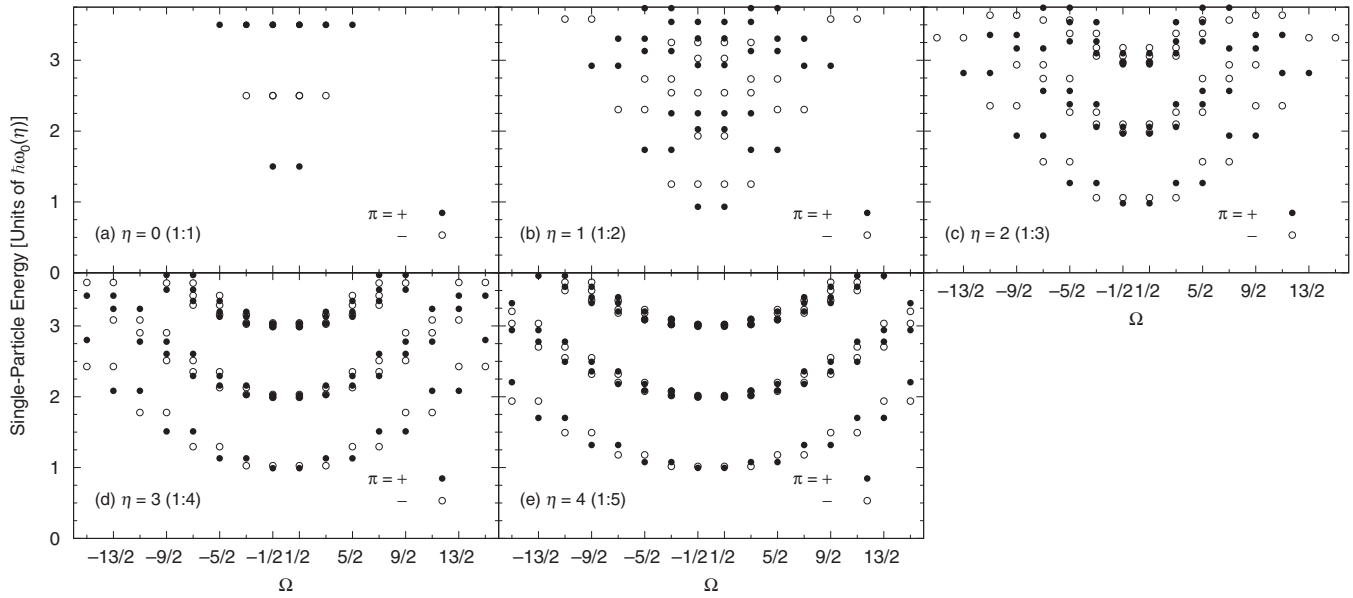

FIG. 16. Single-particle energies of the RDHO model versus Ω at various values of $\eta = R_0/d$. The solid and open circles denote the single-particle states with positive and negative parities, respectively.

C. Emergence of the torus shape beyond the limit of oblate deformation

Lastly, let us discuss the reason why the torus nucleus emerges beyond the limit of large oblate deformation. In the spherical harmonic-oscillator potential, the radial wave function of the lowest single-particle state is given by a Gaussian function peaked at the center (the 0*s* state): accordingly, the central part of the total density distribution is quite stable. Then, a question arises why such a stable and robust wave function vanishes and how the torus shape emerges.

To investigate why the 0*s* state disappears, we calculate the single-particle energies for the deformed harmonic-oscillator potential as a function of oblate deformation. Figure 17 shows the obtained Nilsson diagram versus the aspect ratio of the short (the z direction) to the long (the radial direction) axes for an ellipsoidal nuclear surface (oblate deformation). The aspect ratio 1 : 1 corresponds to the spherical shape. The aspect ratio 1 : 5 corresponds to an oblate shape with the same aspect ratio as that of the torus isomer of ^{40}Ca obtained by the cranked HF calculation. The single-particle energies are plotted in unit of $\hbar\omega_0(\epsilon)$, where $\omega_0(\epsilon)$ denotes the frequency of the harmonic-oscillator potential depending on the Nilsson perturbed-spheroid parameter ϵ to describe ellipsoidal nuclear shapes. In $\omega_0(\epsilon)$, the volume conservation inside an equipotential surface is taken into account [21]. In the figure, we see that some single-particle energies associated with high $N_{\rm sh}$ spherical major shells rapidly decrease with increasing oblate deformation. At the aspect ratio 1 : 5, the last occupied state for ^{40}Ca ($N = 20$) originates from that with a spherical harmonic-oscillator quantum number of $N_{\rm sh} = 3$ (the $3\hbar\omega_0$ state).

In Fig. 18, the single-particle energies are plotted versus Ω at each aspect ratio. We see that the shell gaps of the single-particle energies decrease with increasing oblate deformation. However, the basic pattern of deformed shell structure does not change, in contrast to that of the RDHO model shown in Fig. 16. In Fig. 18(e), the dashed line denotes the Fermi level for $N = 20$ at $\omega = 0$. The neutron density distribution,

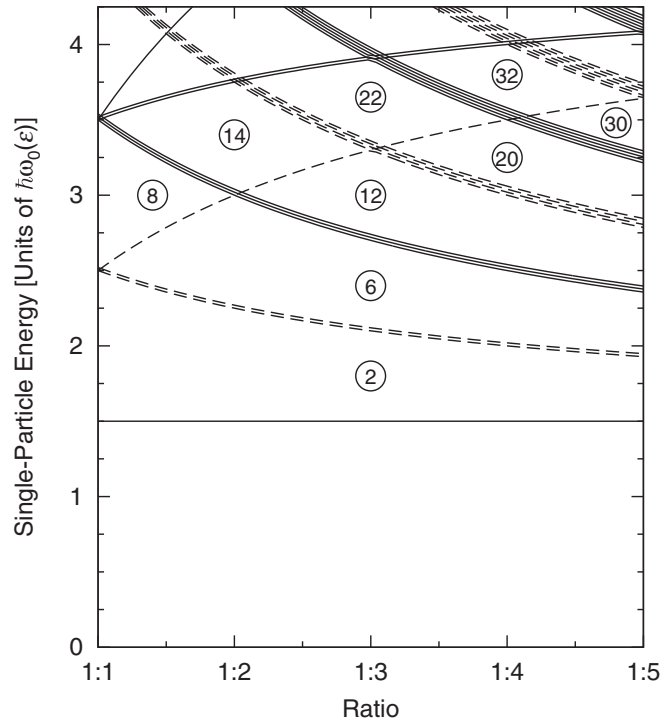

FIG. 17. Nilsson diagram versus the aspect ratio of the short (the z direction) to long (the radial direction) axes for an ellipsoidal nuclear surface (oblate deformations). The solid and dashed lines denote the single-particle states with positive and negative parities, respectively. The aspect ratio 1 : 1 corresponds to the spherical shape. The aspect ratio 1 : 5 is close to that of a torus isomer obtained by the cranked HF calculation.

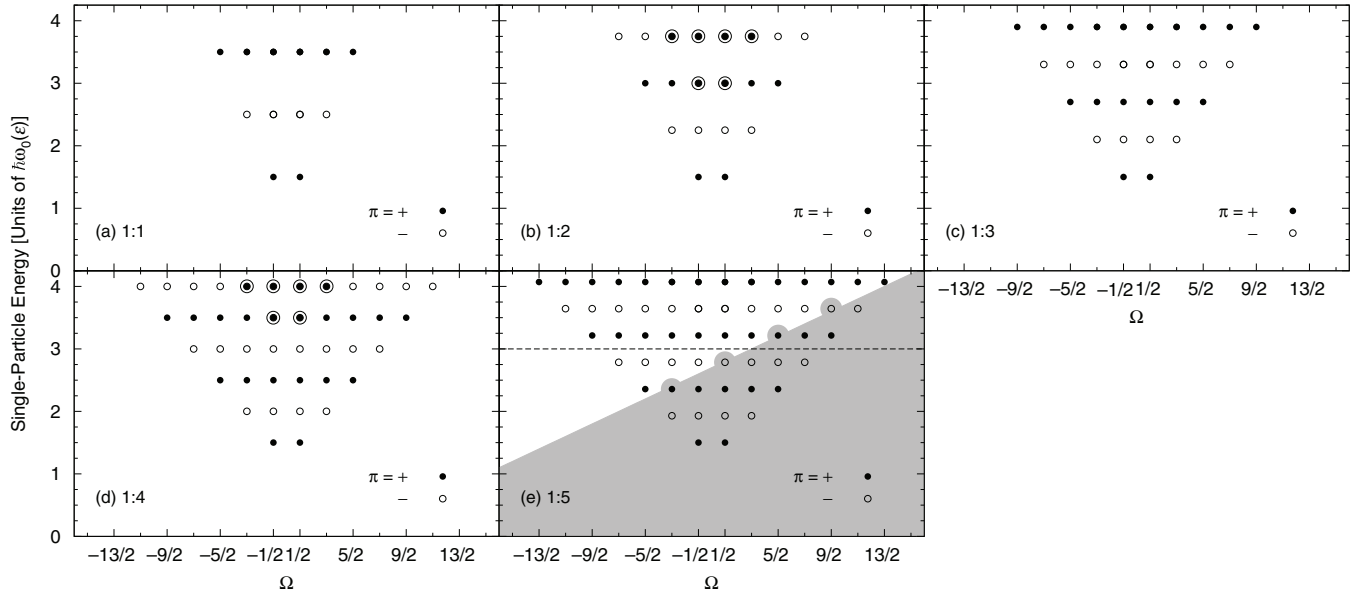

FIG. 18. Single-particle energies of the deformed harmonic-oscillator versus Ω at various oblate deformations. In (e), the dashed line denotes the Fermi surface for ^{40}Ca ($N = 20$) at $\omega = 0$. The gray area denotes the occupied states in ^{40}Ca at $\omega = 1.6$ MeV/$\hbar$ for rotation about the symmetry axis.

$\rho(r,z)$, for the occupied configuration is shown in Fig. 19(a). The densities in the φ direction are integrated. Two prominent peaks are seen in the density distribution. We next consider an aligned single-particle configuration at $\omega = 1.6$ MeV/$\hbar$. This ω corresponds to a value for the torus isomer of ^{40}Ca. The occupied states at this ω are shown by the gray area in Fig. 18(e). By the alignments, totally five single-particle states with $11/2^-[505]$ and $9/2^-[505]$ ($\Lambda = 5$), $9/2^+[404]$ and $7/2^+[404]$ ($\Lambda = 4$), and $5/2^+[402]$ ($\Lambda = 2$) are occupied (the asymptotic Nilsson label $\Omega^\pi[Nn_z\Lambda]$ is used here). On the other hand, the single particle states with $-7/2^-[303]$ and $-5/2^-[303]$ ($\Lambda = 3$), $-5/2^+[202]$ ($\Lambda = 2$), and $-3/2^-[301]$ and $-1/2^-[301]$ ($\Lambda = 1$) become unoccupied. Summing up the aligned single-particle angular momenta, we obtain the neutron contribution to the z component of the total angular momentum $J_z = 31\hbar$. Taking into account the proton contribution as well, we finally obtain the total angular momentum $J_z = 62\ \hbar$ for this oblate configuration, which is close to that of the torus isomer for ^{40}Ca obtained by the cranked HF calculation. The neutron density distribution at $\omega = 1.6$ MeV/$\hbar$ is shown in Fig. 19(b). The two peaks seen in Fig. 19(a) vanish and densities in the central region become flat and stretch to radial direction, as the single-particle states with high Ω are occupied.

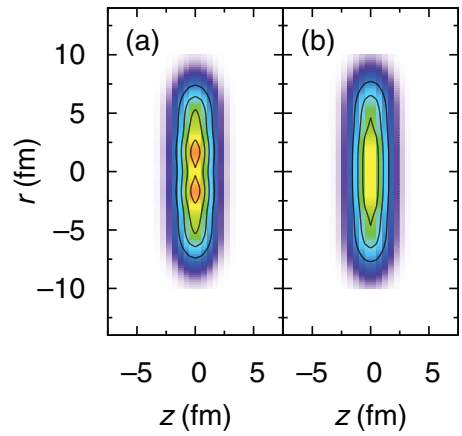

FIG. 19. (Color online) (a) Density distributions of neutrons in ^{40}Ca calculated for the deformed harmonic-oscillator model at an oblate deformation of the aspect ratio 1 : 5 with $\omega = 0$. The contours correspond to multiple steps of 0.05 fm^{-2}. The densities for the ϕ direction in the cylindrical coordinate are integrated. (b) The same as (a) but with $\omega = 1.6$ MeV/$\hbar$. The colors are normalized by the largest density of (a).

Figure 20 shows the density distributions of individual single-particle states of special interest at aspect ratio 1 : 5. The densities for the φ direction in the cylindrical coordinate are integrated. The dashed line shows the density distribution of the lowest $\Lambda = 0$ state. On the other hand, the solid lines depict those of the aligned $\Lambda = 2$, 4, and 5 states mentioned above that are occupied at $\omega = 1.6$ MeV/$\hbar$. The single-particle density distributions of these aligned states peak around $r = 6$ fm. Apparently, the overlap between the aligned nucleons and the nucleons in the lowest $\Lambda = 0$ state is very small. Namely, the lowest $\Lambda = 0$ state largely containing the spherical $0s$ component is rather isolated from the others. To gain the attractive interactions between nucleons, the total system tends to maximize the overlaps between the density distributions of individual single particles. Thus, it would be energetically favorable to concentrate the densities of individual nucleons around $r = 6$ fm. In this way, the nucleus with extremely large oblate deformation may start to generate the torus shape. This seems to be the basic reason why a large 'hole' is created in the central region of the nucleus by eliminating the spherical $0s$ wave function.

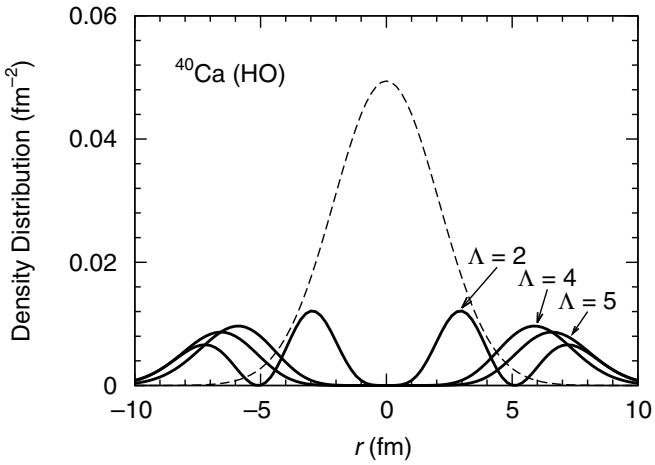

FIG. 20. Density distributions of the single-particle states of special interest for ^{40}Ca on the $z = 0$ plane in an oblate deformation of the aspect ratio 1 : 5 calculated with the deformed harmonic-oscillator model. The densities in the ϕ direction in the cylindrical coordinate are integrated. The solid lines show the density distributions of the aligned single-particle states with $\Lambda = 2$, 4, and 5 that are occupied at $\omega = 1.6$ MeV/$\hbar$. The dashed line shows the density distribution of the lowest $\Lambda = 0$ state.

V. SUMMARY

We have systematically investigated the existence of high-spin torus isomers for a series of $N = Z$ even-even nuclei from ^{28}Si to ^{56}Ni using the cranked HF method. We found the stable torus isomers from ^{36}Ar to ^{52}Fe for all the Skyrme interactions used in this study. In the obtained torus isomers, the z components of the total angular momentum are $J_z = 36\hbar$ for ^{36}Ar, $60\hbar$ for ^{40}Ca, $44\hbar$ for ^{44}Ti, $72\hbar$ for ^{48}Cr, and $52\hbar$ for ^{52}Fe. We fitted the density distribution of each of the obtained torus isomers with the Gaussian function. We also analyzed the microscopic structure of the obtained torus isomers by plotting the single-particle energies versus Ω and using the concept of sloping Fermi surface. We determined the regions of ω for which the obtained torus isomers can stably exist in each Skyrme interaction. The dependence of the obtained results on the Skyrme interactions employed is found to be weak.

We have also performed TDHF calculations to explore the properties of the precession motion rotating with angular momentum $I = K + 1$, which is built on each of the obtained torus isomer with $I = K$. For all the obtained torus isomers, the precession motion emerges and the symmetry axis rotates about the precession axis for at least two periods. It was found that the precession motion of the $60\hbar$ isomer in ^{40}Ca is especially robust and stably rotates for many periods, We obtained similar results for all the Skyrme interactions used, We also estimated the moment of inertia for the rotation about a perpendicular axis from the calculated rotational periods of the precession motion. The obtained moments of inertia are close to the rigid-body values for all the obtained torus isomers.

We have discussed the radial density distribution of each single-particle wave function in the high-spin torus isomer of ^{40}Ca. We showed that the density distributions are well approximated by those of the RDHO model. We then discussed how the shell structure develops from spherical to torus shapes. There are two important mechanisms for stabilizing torus isomers: (i) the development of the major shells consisting of single-particle states whose energies are given by $E = (N'_{\rm sh} + 1) + \hbar^2\Lambda^2/2mR_0^2$, where $N'_{\rm sh} = n_r + n_z$ and Λ is the z component of orbital angular momentum. (ii) a large value of R_0 that reduces the energies of high Ω single-particle states. We finally discussed why the $0s$ components of all the single-particle wave functions vanish and generate a torus shape. We showed that in an aligned single-particle configuration with extremely large oblate deformation, the overlaps between the density distributions of the lowest $\Lambda = 0$ single-particle state and the aligned high-Ω single-particle states become very small due to the strong centrifugal force. To gain the attractive interaction energy as much as possible, nucleons tend to maximize the overlaps of their wave functions. An optimal configuration beyond the limit of large oblate deformation is the one creating the localization of single-particle density distributions around a torus ring. This seems to be a basic mechanism of the emergence of high-spin torus isomers.

ACKNOWLEDGMENTS

T.I. was supported in part by MEXT SPIRE and JICFuS. This work was undertaken as part by the Yukawa International Project for Quark-Hadron Sciences (YIPQS). J.A.M. was supported by BMBF under Contract Nos. 06FY9086 and 05P12RFFTG, respectively.

APPENDIX: PARAMETERS AND VOLUME CONSERVATION IN THE RDHO MODEL

In the RDHO model, we take the oscillator frequency, ω_0, to conserve the inner volume of an equipotential energy surface. It is given by

$$\left(\frac{\omega_0}{\mathring{\omega}_0}\right)^3 = \begin{cases} \left(1+\frac{\eta^2}{2}\right)\sqrt{1-\eta^2} + \frac{3}{4}\pi\eta\left(1+\frac{2}{\pi}\arctan\frac{\eta}{\sqrt{1-\eta^2}}\right) & (0 \leqslant \eta < 1) \\ \frac{3}{2}\pi\eta & (\eta \geqslant 1), \end{cases} \tag{A1}$$

where $\eta = R_0/d$ and $\mathring{\omega}_0$ denotes the oscillator frequency in the spherical limit. Here, we take $\hbar\mathring{\omega}_0 = 41A^{-1/3}\rho_{\rm torus}/\rho_{\rm gr}$ MeV, where A is the number of nucleons, and $\rho_{\rm torus}$ and $\rho_{\rm gr}$ denote the average densities of a torus isomer and the ground state, respectively [11]. In the calculations, we use $\rho_{\rm torus} = (2/3)\rho_{\rm gr}$.

[1] T. Ichikawa, J. A. Maruhn, N. Itagaki, K. Matsuyanagi, P.-G. Reinhard, and S. Ohkubo, Phys. Rev. Lett. **109**, 232503 (2012).
[2] T. Ichikawa, K. Matsuyanagi, J. A. Maruhn, and N. Itagaki, Phys. Rev. C **89**, 011305(R) (2014).
[3] S. Cohen, F. Plasil, and W. J. Świątecki, Ann. Phys. (NY) **82**, 557 (1974).
[4] A. Bohr, in *Elementary Modes of Excitation in Nuclei, Proceedings of the International School of Physics "Enrico Fermi", Course LXIX*, edited by A. Bohr and R. A. Broglia (North-Holland, Amsterdam, 1977), p. 3.
[5] A. V. Afanasjev, D. B. Fossan, G. J. Lane, and I. Ragnarsson, Phys. Rep. **322**, 1 (1999).
[6] A. Bohr and B. R. Mottelson, Nucl. Phys. A **354**, 303c (1981).
[7] A. Bohr and B. R. Mottelson, *Nuclear Structure*, Vol. II (World Scientific, Singapore, 1998).
[8] M. A. Deleplanque, S. Frauendorf, V. V. Pashkevich, S. Y. Chu, and A. Unzhakova, Phys. Rev. C **69**, 044309 (2004).
[9] Y. R. Shimizu, M. Matsuzaki, and K. Matsuyanagi, Phys. Rev. C **72**, 014306 (2005).
[10] C. G. Andersson, J. Krumlinde, G. Leander, and Z. Szymański, Nucl. Phys. A **361**, 147 (1981).
[11] A. Staszczak and C. Y. Wong, arXiv:1312.3413.
[12] C. Y. Wong, Ann. Phys. (NY) **77**, 279 (1973).
[13] J. A. Maruhn, P.-G. Reinhard, P. D. Stevenson, and A. S. Umar, Comp. Phys. Comm. **185**, 2195 (2014).
[14] P.-G. Reinhard and R. Y. Cusson, Nucl. Phys. A **378**, 418 (1982).
[15] E. Chabanat, P. Bonche, P. Haensel, J. Meyer, and R. Schaeffer, Nucl. Phys. A **627**, 710 (1997).
[16] P.-G. Reinhard and H. Flocard, Nucl. Phys. A **584**, 467 (1995).
[17] J. Bartel, P. Quentin, M. Brack, C. Guet, and H.-B. Hakansson, Nucl. Phys. A **386**, 79 (1982).
[18] P. Wen, L.-G. Cao, J. Margueron, and H. Sagawa, Phys. Rev. C **89**, 044311 (2014).
[19] J. R. Stone and P.-G. Reinhard, Prog. Part. Nucl. Phys. **58**, 587 (2007).
[20] D. Brink, in *Proceedings of the International School of Physics "Enrico Fermi", Course 36, Varenna, 1965*, edited by C. Bloch (Academic Press, London, 1966), pp. 247–277.
[21] S. G. Nilsson and I. Ragnarsson, *Shapes and Shells in Nuclear Structure* (Cambridge University Press, Cambridge, 1995).